International
Progress Report

IPR-01-13

Äspö Hard Rock Laboratory

Bonded-particle simulations of the in-situ failure test at Olkiluoto

David Potyondy
Peter Cundall

Itasca Consulting Group. Inc.

March 2000

Svensk Kärnbränslehantering AB
Swedish Nuclear Fuel
and Waste Management Co
Box 5864
SE-102 40 Stockholm Sweden
Tel 08-459 84 00
+46 8 459 84 00
Fax 08-661 57 19
+46 8 661 57 19

Äspö Hard Rock
Laboratory

Report no.	No.
IPR-01-13	F19K
Author	Date
Potyondy, Cundall	00-03-30
Checked by	Date
Christer Svemar	
Approved	Date
Christer Svemar	02-01-28

Äspö Hard Rock Laboratory

Bonded-particle simulations of the in-situ failure test at Olkiluoto

David Potyondy
Peter Cundall

Itasca Consulting Group. Inc.

March 2000

Keywords: Failure test, Rock failure, failure modelling, particle flow code, PFC, Crack propagation

ABSTRACT

The *PFC* ^{2D} Model for Rock is employed to predict damage formation adjacent to a circular test hole in gneissic tonalite subjected to compressive loading produced by the pressurization of two horizontal slots located above and below the test hole. The results of this work demonstrate that plausible predictions of excavation-induced damage formation can be made by employing the *PFC* ^{2D} Model for Rock. The predictions provide information about the detailed distribution of microcracks, including microcrack intensity, location and orientation as well as the time evolution of such damage. The failure mechanisms exhibited by the *PFC* ^{2D} model include the formation of notches (in compressive regions) and tensile fractures (in tensile regions) adjacent to the excavation. The lack of a clear understanding of the details of the physical mechanisms that drive the failure processes forces us to hypothesize as to what constitutes the relevant set of laboratory-scale properties to which the *PFC* ^{2D} material must be calibrated. In this study, we have calibrated the *PFC* ^{2D} material to match elastic modulus, crack-initiation stress and unconfined compressive strength, as well as the anisotropy in modulus and strength exhibited by gneissic tonalite. We have not attempted to match the complete strength envelope (including the Brazilian tensile strength) or the fracture toughness of the material. However, it is not clear if these material properties will actually influence the damage that forms adjacent to an excavation.

SAMMANFATTNING

Koden PFC^{2D} för berg används för att förutsäga skador som åstadkoms runt ett cirkulärt testhål i gnejsisk tonalit vilken utsätts för tryckbelastning via två horisontella skåror i berget lokaliserade över och under testhålet. Resultatet av här presenterat arbete visar att goda prediktioner av brytningsinducerade skador kan göras med hjälp av koden PFC^{2D}. Prediktionerna lämnar information om den detaljerade fördelningen av mikrosprickor inklusive intensitet, lokalisering och orientering liksom tidsförloppet för varje sådan skada. Brottmekanismerna som visas av koden PFC^{2D} inkluderar bildningen av kilar (i tryckregioner) och dragsprickor (i dragregioner) i närheten av testhålet. Avsaknaden av en tydlig förståelse för den fysikaliska mekanismen som driver brottsprocessen tvingar oss att anta vad som utgör en relevant uppsättning data i laboratorieskala för kalibrering av PFC^{2D}–materialet. I denna studie har PFC^{2D}–materialet kalibrerats för att matcha elasticitetsmodul, sprickinitieringstryck och enaxlig tryckhållfasthet liksom spridning i modul och hållfasthet hos gnejsisk tonalit. Vi har inte försökt matcha den kompletta hållfasthetsenveloppen (inklusive draghållfasthet vid brasilianska provet) eller bergsprickors ytråhet. Det är emellertid inte klart om dessa materialegenskaper verkligen påverkar den skada som utbildas runt ett hål i berg.

TABLE OF CONTENTS

1 BACKGROUND AND INTRODUCTION

As part of the development of disposal technology of spent nuclear fuel, an in-situ failure test is planned for execution in the experimental full-scale deposition hole number 2 in the Research Tunnel at Olkiluoto, Finland. In the proposed test (Autio *et al.*, 1999a), two horizontal slots located approximately 350 mm above and below a 100 mm diameter test hole are pressurized via expansive grout. The combination of in-situ stresses and the stresses induced by slot pressurization is expected to cause damage to form around the inner surface of the test hole. The damage is expected to take the form of 1) sidewall breakout on both opposing sides in the horizontal direction and 2) radial tensile fractures on both opposing sides in the vertical direction. The objective of this work is to simulate the in-situ failure test by numerical modelling using the *PFC* ^{2D} (Itasca, 1999) code and thereby predict the damage adjacent to the test hole. The damage prediction includes intensity, location and orientation of the microcracks (and possible coalescence into macrofractures). After the physical test has been completed, the microcracking and failure patterns adjacent to the test hole will be studied in detail (by impregnating the rock with resin and studying overcored sections) and compared to the simulation results.

Although 3D continuum-based numerical modelling performed with an elastic/plastic constitutive law using *FLAC* ^{3D} (Itasca, 1997) has already provided a general picture of the test-hole response (Autio *et al.*, 1999b), the detailed distribution of microcracks and macrofractures that comprise the damage cannot be predicted from such an analysis. Instead, a discontinuum model, in which cracks are represented explicitly, is required to obtain such information about the damage including microcrack intensity, location and orientation. The discontinuum model used here is referred to as the *PFC* Model for Rock.

1.1 THE PFC MODEL FOR ROCK

An effort was begun in 1995 to extend and refine previous modelling of the observed notch formation in the Mine by Experiment test tunnel (Read and Martin, 1996) at the Underground Research Laboratory in Pinawa, Manitoba. That work has evolved into an effort to develop and verify the *"PFC* Model for Rock" — a mechanistically based numerical model for predicting excavation-induced rock-mass damage and long-term strength in Lac du Bonnet granite. The present status of these efforts is summarized in the following abstract from Potyondy and Cundall (1999). Additional published material related to this model includes Itasca (1999), Potyondy and Fairhurst (1999), Potyondy and Cundall (1998), Potyondy *et al.*(1996), and Cundall *et al.*(1996).

> *The calibration of the PFC* ^{2D} *model of rock is extended to include both short-term laboratory response (elastic modulus, crack-initiation stress, strength envelope and crack-damage stress) and long-term laboratory response (static-*

fatigue response including the effect of confinement) as well as field-scale response (evolution and extent of damage around three excavations at the 42-level of the URL). The work has included: development of a parallel-bonded synthetic material, reformulation of the micromodel for stress corrosion based more closely on known mechanisms of subcritical crack growth (than was that of the Phase III-study (Potyondy et al., 1997)), and development of a thermal formulation accounting for transient heat flow and thermal-mechanical loading. Extensive attempts to match the strength envelope for Lac du Bonnet granite were only partially successful. Simulations of unconfined static-fatigue tests correspond well with laboratory results for Lac du Bonnet granite; however, simulations of confined static-fatigue tests, using the same set of microparameters as were used in the unconfined tests, do not correspond well with laboratory results for Barre granite. For one set of stress-corrosion parameters, resulting patterns of cracks and failure mechanisms match quite well the breakout observed in the field for all three tunnels; however, the damage-formation times are much too large. Finally, the present simulations reveal a richer structure of crack formation than do those of the Phase III study including a crude replication of the slabbing observed in the field.

Ongoing efforts (Cundall and Potyondy, 1999) are aimed at producing by March 2001 both

1) a definitive report on the *PFC* Model for Rock that will include detailed instructions on the calibration procedure and comparison of *PFC* ^{2D} results and measured excavation-disturbed zone characteristics; and
2) a report on the integration of *PFC* ^{2D} simulations and field measurements of acoustic properties of rock (in collaboration with R. Paul Young, a seismologist from Liverpool University).

Potyondy *et al.*(1996) provide additional discussion of the *PFC* Model for Rock and its relation to other particle-based models. The material in the following two paragraphs is taken from that discussion.

Rock is a brittle heterogeneous material that exhibits inelastic deformation because of the existence and formation of numerous microcracks. Under increasing load, these microcracks coalesce into macrocracks, or fractures. The approaches for modelling this inelastic deformation and fracture can be classified into two categories, depending on whether damage is represented indirectly via its effect on constitutive relations, or directly by the formation and tracking of a large number of microcracks. Most indirect approaches idealize the material as a continuum and utilize average measures of material degradation in constitutive relations to represent irreversible microstructural damage, while most direct approaches idealize the material as a collection of structural units (springs, beams, etc.) or separate particles bonded together at their contact points and utilize the breakage of individual structural units or bonds to represent damage. Typically, direct approaches have not been applied to the solution of boundary-value problems involving complicated deformation patterns. Instead, their use has been limited to helping develop the constitutive relations required by indirect methods to solve boundary-value problems. However, increases in computing power have made it feasible to model entire boundary-value problems with direct

approaches, thereby simulating the physical micromechanisms directly and bypassing development of complex constitutive laws. The PFC model of a solid is an example of one such direct modelling approach. It is especially applicable to the class of problems (such as rock fracture) for which the complex constitutive behaviour (arising from extensive micro- and macro-cracking) is difficult to characterize accurately in terms of a continuum formulation.

In summary, the *PFC* Model for Rock simulates the mechanical behaviour (both static and dynamic) of rock by representing it as a bonded assembly of circular or spherical particles. The *PFC* model can be categorized as a direct, damage-type numerical model, where the deformation is not a function of prescribed relations between stresses and strains, but of the changing microstructure. The *PFC* model can reproduce the evolution of damage within the synthetic material as it progresses from essentially solid, intact material to broken, granular material with accompanying dilation and, in the process, the effective strength and moduli of the body change as the cracks grow and interact, producing a non-linearity in the macroscopic stress-strain curves.

Rock is a complex material comprised of numerous cemented grains, and the mechanical behaviour of rock involves crack growth that depends on the heterogeneous nature of the local stress distribution within the material. The fact that the *PFC* model of rock can reproduce much of this complex behaviour at both a micro- and a macro-level implies that this model captures in some way the essential features of the heterogeneity in rock deformation and failure. If this statement is accepted, then the *PFC* model can provide a single framework within which a large spectrum of behaviours exhibited by rock-like materials can be captured. This allows postulation and testing of micromechanisms and, if successful, prediction of behaviours that cannot yet be encompassed by existing continuum theories.

1.1.1 Calibrating the PFC Material

Although it is relatively easy to assign chosen properties to a PFC model, it is often difficult to choose such properties so that the behaviour of the resulting synthetic material resembles that of an intended physical material. For codes that model continua, the input properties (such as modulus and strength) can be derived directly from measurements performed on laboratory specimens. For codes such as PFC that synthesize macro-scale material behaviour from the interactions of micro-scale components, the input properties of the microscopic constituents are usually not known. In this case, we must first determine the relevant behaviours (and response set that best characterizes these behaviours) of our intended physical material, and then choose the appropriate microproperties by means of a calibration process in which the responses of the synthetic material are compared directly with the relevant measured responses of the intended physical material. This comparison can be made at both laboratory scale (e.g., triaxial and static-fatigue response) and field scale (e.g., evolution and extent of damage around various excavations) depending upon the intended application of the PFC model.

The laboratory-scale properties typically chosen to characterize the short-term response of hard rock are the elastic modulus (E), crack-initiation stress (σ_{ci}) and strength envelope ($\sigma_f = \sigma_f (P_c)$, where σf and Pc are peak stress and confining pressure, respectively). The crack-damage stress (σ_{cd}) can be reproduced using a clustered PFC^{2D}

material. Procedures to allow one to reproduce these laboratory-scale properties are described in Section 3.5 of the FISH in PFC^{2D} volume of Itasca (1999). It should be noted that our current understanding of this calibration process is still incomplete — i.e., we still do not know how to construct a PFC material that reproduces a given strength envelope or one that reproduces a given ratio of unconfined compressive strength to Brazilian tensile strength. But we can reproduce a given modulus, crack-initiation stress and peak strength at a given confinement, and we can then obtain the strength envelope and Brazilian tensile strength by performing biaxial and Brazilian tests upon the synthetic material.

1.1.2 Predicting Damage Adjacent to the Test Hole

The objective of the present work is to simulate the in-situ failure test using the PFC ^{2D} code and thereby predict the damage that will form adjacent to the test hole. This requires that we first perform a calibration step, in which a PFC ^{2D} material is created that reproduces (in a best-fit sense) what are believed to be the relevant set of laboratory responses of the physical rock. Then, this best-fit PFC ^{2D} material is assigned to the boundary-value model of the in-situ failure test, and the bond breakages that occur in this model provide a direct damage prediction. The simulation process involves creation of an analogue material that —when subjected to the same boundary conditions as the real rock —will exhibit damage that is similar to what will occur in the real rock. The accuracy of such a damage prediction hinges upon how closely the analogue material can reproduce the physical mechanisms that are driving the failure process.

During the past four years the authors of the present report have been developing and verifying the PFC ^{2D} model of rock with the goal of predicting excavation-induced rock-mass damage and long-term strength of the rock at the Canadian URL (Potyondy and Cundall, 1999). Thus, we have established a certain level of confidence in the ability of the present PFC ^{2D} model of rock to reproduce the essential features of the physical mechanisms occurring in this type of hard, brittle rock (Lac du Bonnet granite) during both short- and long-term loading tests, further discussion of the calibration process and support for this assertion can be found in Sections 3.2 and 3.5 of the FISH in PFC^{2D} volume of Itasca (1999).

The in-situ failure test will be carried out in one of the full-scale experimental deposition holes in the research tunnel at Olkiluoto. The main rock type found in these holes is gneissic tonalite. The gneissic tonalite appears to be similar to the granite and granodiorite found at the Canadian URL, with the primary difference being its schistosity (see Section 2.1). Thus, a part of the present effort has been directed toward extending the PFC ^{2D} model of rock such that it can reproduce the observed anisotropy in the modulus and peak strength of the gneissic tonalite. Procedures already exist (described in Section 3.5 of the FISH in PFC^{2D} volume of Itasca (1999)) to create an isotropic PFC ^{2D} material. It is this isotropic material that has been assigned to the boundary-value models of the excavations at the Canadian URL.

The attempt to develop an anisotropic PFC ^{2D} material has been only partially successful. As is described in Section 2.2, we have developed both a smeared and a

discrete anisotropy material representation. Although it could be argued that the discrete representation mimics more closely the physical behaviours exhibited during uniaxial tests than does the smeared representation (compare Figures 40 and 45), model-size limitations make it impractical to assign the discrete representation to the boundary-value model of the in-situ test. Therefore, the uniaxial-test behaviour of the discrete representation is documented, but the effect of material anistropy upon damage formation adjacent to the test hole is only investigated for the smeared representation.

1.2 OUTLINE OF REPORT CONTENTS

The calibration of the *PFC* ^{2D} material is presented in Section 2.0. First, we summarize the relevant set of laboratory responses of the gneissic tonalite. The calibration process involves creating a *PFC* ^{2D} material that reproduces this set of responses. Because the responses include anisotropic behaviour, we describe two approaches to creating an anisotropic *PFC* ^{2D} material. Then, we describe the synthetic specimens and the procedures used to create and test them. Finally, the behaviours of the best-fit *PFC* ^{2D} materials are compared both quantitatively and qualitatively with the observed laboratory behaviours of the gneissic tonalite.

Predictions of damage adjacent to the test hole are presented in Section 3.0. First, the boundary-value model of the in-situ test is described as are the coarse- and fine-resolution instances of that model. Then, the simulation results are presented (predominantly in the form of damage plots depicting the evolution of microcracking adjacent to the test hole for progressively increasing grout pressures) for the anisotropic and the two isotropic material representations. The discussion includes an examination of the effects of model resolution, material representation, and bond-failure mechanism (all micro-tensile failure or a mix of micro-tensile and micro-shear failure) upon the resulting damage patterns. Finally, a prediction of the expected damage is made, based on the results of the different cases.

The report concludes in Section 4.0 with an evaluation of our current ability to make explicit predictions of damage formation adjacent to excavations using the *PFC* Model for Rock and includes some caveats that should be kept in mind when comparing model predictions with field observations.

The work described in this report was performed by David Potyondy, Peter Cundall and Carlos Carranza-Torres.

2 CALIBRATION OF THE PFC MATERIAL

The following three laboratory-scale properties are chosen to characterize the response of the gneissic tonalite: elastic modulus (E), crack-initiation stress (σ_{ci}), and unconfined compressive strength (σ_f). Each of these properties exhibits a dependence upon schistosity angle, which is defined as the angle that the schistosity planes make with the uniaxial-loading axis (see Figure 1). The *PFC* ^{2D} calibration is performed by simulating sets of unconfined compression tests for which the schistosity angle is varied and attempting to match the observed dependence of these properties upon schistosity angle (see Figures 2 and 3).

Best-fit anisotropic materials were created that best match the schistosity-angle dependence of these properties, and two best-fit isotropic materials were created that bound the schistosity-angle dependence of these properties. In addition, two variants of most materials were created in which the bond-failure mode is forced to be either tensile only or a mixture of tensile and shear. We do this by setting the micro-shear strength equal to infinity in the first case, and by setting the micro-shear strength equal to the micro-normal strength in the second case. These two variants have been created, because these two types of materials exhibit different failure mechanisms at the microlevel, and we wish to investigate what effect, if any, this has upon the macroscopic failure mechanisms that develop in both the synthetic laboratory specimens and in the material surrounding the test-hole.

The following naming convention is employed to describe the different best-fit materials. Each *PFC* ^{2D} material is given a name of the form **AB**, in which **A** ={ST, T} denotes the bond-failure mode, either *shear & tensile* or *tensile only*; and **B** ={As, Ad, U, L} denotes the material representation, either *smeared anisotropic*, *discrete anisotropic*, *upper-bound isotropic* or *lower-bound isotropic*. Thus, for example, the lower-bound isotropic material in which both shear and tensile bond failure may occur would be designated as **STL**, while the corresponding upper-bound isotropic material would be designated as **STU**, and the corresponding smeared and discrete anisotropic materials would be designated as **STAs** and **STAd**, respectively.

2.1 LABORATORY RESPONSES: MECHANICAL PROPERTIES OF GNEISSIC TONALITE

The in-situ failure test will be carried out in one of the full-scale experimental deposition holes in the research tunnel at Olkiluoto. The main rock type found in these holes is gneissic tonalite, which can be described as follows (Bates and Jackson, 1984). Tonalite is a synonym for quartz diorite, a group of plutonic rocks having the composition of diorite but with an appreciable amount of quartz; quartz diorite grades into granodiorite as the alkali feldspar content increases. Gneissic indicates that the rock possesses the texture and structure typical of gneisses, with foliation that is more widely

spaced, less marked, and often more discontinuous than that of a schistose texture or structure.

The gneissic tonalite exhibits clear schistosity, or parallel arrangement of mineral grains, which is evident from the banding that is visible to the naked eye. The banding arises from the oriented nature of the oblong grains of biotite and hornblende, which comprise approximately 34% of the mineral composition by volume (with quartz and plagioclase comprising the bulk of the remainder). Grains are subhedral, meaning that they are bounded partly by their own rational faces and partly by surfaces formed against pre-existing grains as a result of crystallization or recrystallization. The grain sizes range from 0.3 to 3.0 mm. The undisturbed rock matrix is solid and intragranular fissures are sparse; however, there exist oriented clusters of mafic minerals (especially biotite and hornblende) with higher porosity. The average bulk porosity is approximately 0.25%. The hornblende and quartz are stiffer (by a factor of 1.5 to 2) than the biotite and plagioclase. This stiffness contrast between grains will tend to induce micro-tensions oriented perpendicular to the direction of maximum compression. Under increasing load, these micro-tensions will induce microcracks that are aligned parallel with the direction of maximum compression. The mechanical properties of the gneissic tonalite are similar to the granite and granodiorite found at the Canadian Underground Research Laboratory (Everitt *et al.*, 1993). However, the mica content of the gneissic tonalite is much higher than that of the URL granite and granodiorite, and the gneissic tonalite exhibits more clearly defined schistosity (Autio, 2000).

Laboratory testing (Autio *et al.*, 1999a) indicates that the schistosity affects the mechanical properties. Define the angle that the schistosity planes make with the uniaxial-loading axis as the schistosity angle, α (see Figure 1). Test specimens were obtained from the full-scale experimental deposition holes in the research tunnel at Olkiluoto. The specimens were right circular cylinders with L/D ratios of 2.6 and diameters of 41, 54 and 99 mm. Uniaxial loading tests (at a loading rate of 0.75 MPa/s) were performed for different schistosity angles to obtain values of Young's modulus, Poisson's ratio, crack-initiation stress, crack-damage stress and peak strength. These parameters were then plotted versus schistosity angle for the three different diameters (see Figures 2 and 3).*

* * In these figures, the Young's modulus is given by the second-order curve of Autio *et al.*(1999a) Figure 3.4-5 (which fits the average values at each of three orientations), the peak strength is given by either the second-order curve of Autio *et al.*(1999a) Figure 3.4-13 (which fits the average values at each of three orientations) or of Autio *et al.*(1999a) Figure 3.4-1 (which fits the test results for all orientations), and the crack-initiation and crack-damage stresses are from Autio *et al.*(1999a) Table 3.4-1.

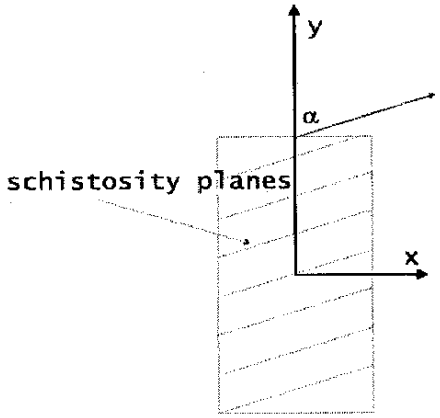

Figure 1. *Definition of schistosity angle (y-axis is uniaxial-loading axis).*

The results of the laboratory testing can be summarized as follows.

a) The properties do not depend upon specimen diameter, except for the case in which α=0 for which the smaller-diameter specimens are stronger.

b) The rock strengths (all three values) and the Young's modulus depend upon schistosity angle, whereas the Poisson's ratio does not (at least not within the experimental scatter) and can be taken as approximately 0.28 (Autio *et al.*, 1999a, Figure 3.4-9).

c) The four properties that depend upon schistosity angle all exhibit the same general relation. They are largest for a schistosity angle of zero, decline to a minimum at approximately 60 degrees and remain near this minimum up to 90 degrees, with a nearly flat curve from 30 to 90 degrees. Theoretical analyses for the effects of planar anisotropy in which the rock is assumed to possess a set of parallel planes of weakness (Jaeger and Cook, 1979, page 107) suggest a symmetric shape with a minimum at approximately 30 degrees. The measured strength properties differ from this by not possessing the expected strength increase as the schistosity angle approaches 90 degrees. A mechanism to explain the observed anisotropy of the gneissic tonalite is described in Section 2.2.2.

d) Loading the lab-conditioned specimens at a slow loading rate of 0.0075 MPa/s only reduced the unconfined compressive strength by about five percent for a schistosity angle of 11 degrees. If stress corrosion were occurring, these tests would not show its effect because internal saturation was not controlled.

e) Loading fully saturated specimens at the normal rate of 0.75 MPa/s reduced the unconfined compressive strength by 23 percent for a schistosity angle of 35 degrees. If stress corrosion were occurring, one would expect an even greater strength reduction if these same specimens were subjected to the slow loading rate.

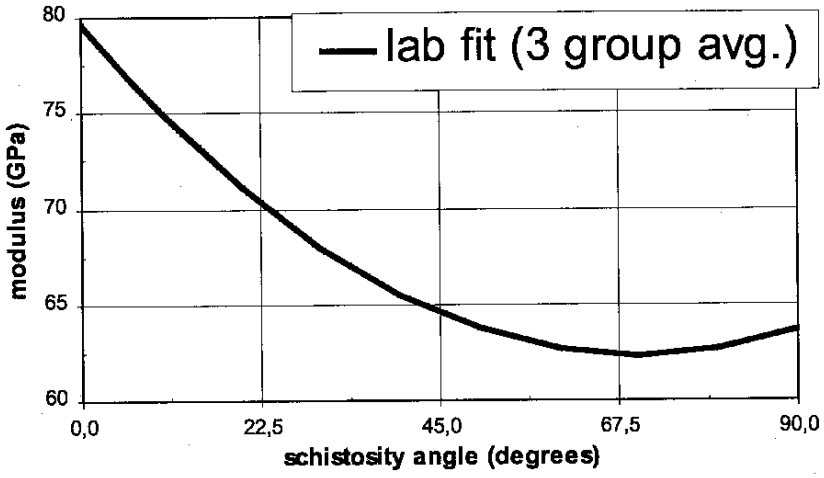

Figure 2. *Variation of modulus with schistosity angle (54 mm specimens).*

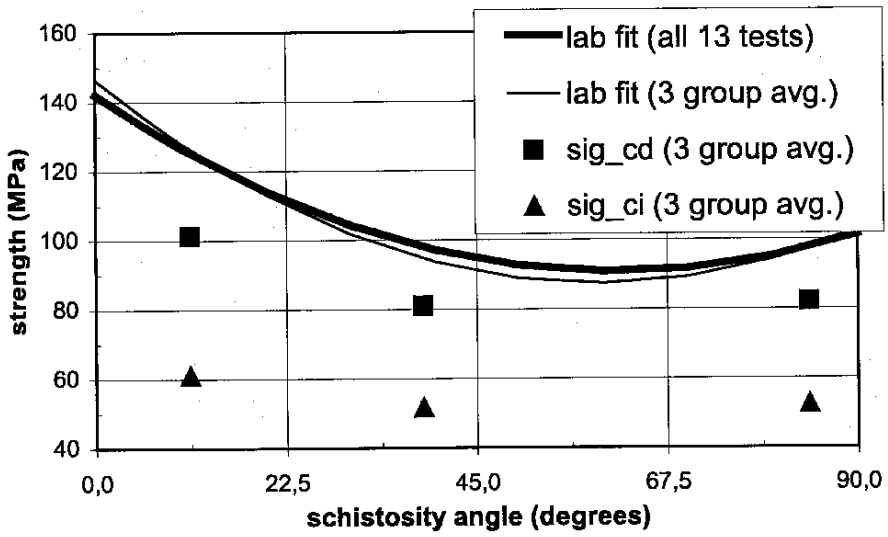

Figure 3. *Variation of strengths with schistosity angle (54 mm specimens).*

2.2 SIMULATING MATERIAL ANISOTROPY WITH PFC^{2D}

The mechanical responses (which are interpreted as material properties, such as modulus and peak strength) exhibited by a material may be said to be either isotropic or anisotropic. An isotropic material exhibits responses that are identical in all directions, while an anisotropic material exhibits direction-dependent responses. An example of an anisotropic material is wood, which exhibits greater strength in a direction parallel with the grain than perpendicular to the grain.

In our previous work with *PFC* ^{2D} , we have developed a specimen-genesis procedure and a set of microparameters that produce a *PFC* ^{2D} material that exhibits an isotropic mechanical response. As part of the present project, we have extended the set of microparameters such that the *PFC* ^{2D} material exhibits an anisotropic mechanical response that can be made to match the response of the gneissic tonalite.

Two different approaches have been developed. The first approach utilizes a smeared representation in which the anisotropy in strength is introduced at the microlevel by varying the parallel-bond strengths as a function of the bond orientation relative to the schistosity direction. The second approach utilizes a discrete representation in which the anisotropy in both modulus and strength is introduced at the macrolevel by first identifying a set of finite-sized, discrete, elongated regions of material (joint sets) aligned with the schistosity planes and embedded within the base material, and then varying the relative stiffnesses and strengths of the two materials. (The best-fit discrete anisotropic material has a joint-set material that is significantly softer and weaker than the base material.)

The following notation is employed to describe both approaches. The *PFC* ^{2D} model cross section (defined by the xy-plane) is assumed to be oriented perpendicular to the schistosity planes such that the orientation of the schistosity planes relative to the xy-system can be defined by either the schistosity plane normal vector p_i or the schistosity direction s_i (see Figure 4). The schistosity orientation within a particular *PFC* ^{2D} model is set by specifying the schistosity direction. Note that the schistosity direction need not be aligned with the y-axis. schistosity planes

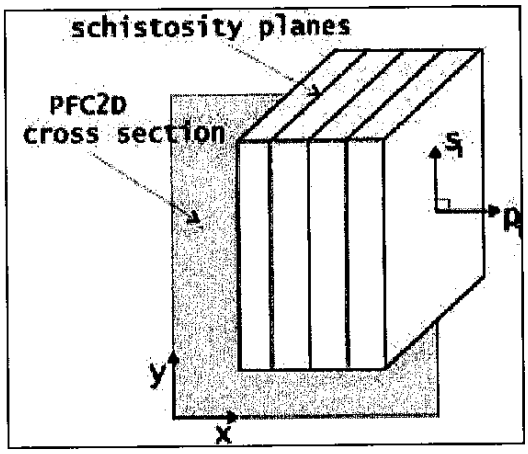

Figure 4. *Unit vectors used to define the orientation of schistosity planes relative to the PFC^{2D} cross section.*

2.2.1 Implementation of Smeared Representation

In the smeared representation of material anisotropy, it is assumed that the strength anisotropy observed at the macroscale arises from a similar strength anisotropy at the microscale. There are two microscale strengths: the parallel-bond normal strength, σ_c , and the parallel-bond shear strength, τ_c ; thus, two failure modes must be considered.

For the case of micro-tensile failure, we assume that the strength in direction n_i is controlled by the parallel-bond normal strength of bonds oriented parallel with n_i . For the case of micro-shear failure, we assume that the strength in direction n_i is controlled by the parallel-bond shear strength of bonds oriented at 45 degrees to n_i.

These assumptions arise from the observation that the primary mode of microcracking that develops during compression tests consists of sets of tensile microcracks that are predominantly aligned parallel with the loading direction and sets of shear microcracks that are predominantly aligned at 45 degrees to the loading direction (see Figure 30). The effect of applying these assumptions to a PFC ^{2D} material that has been constructed so as to allow only micro-tensile failure is described with the aid of Figure 5, which depicts two sets of bonds, or potential crack sites. In order to produce a synthetic material that is stronger when loaded parallel with the schistosity planes than when loaded perpendicular to the schistosity planes, we will assign larger strength values to the red bonds than to the blue bonds.*

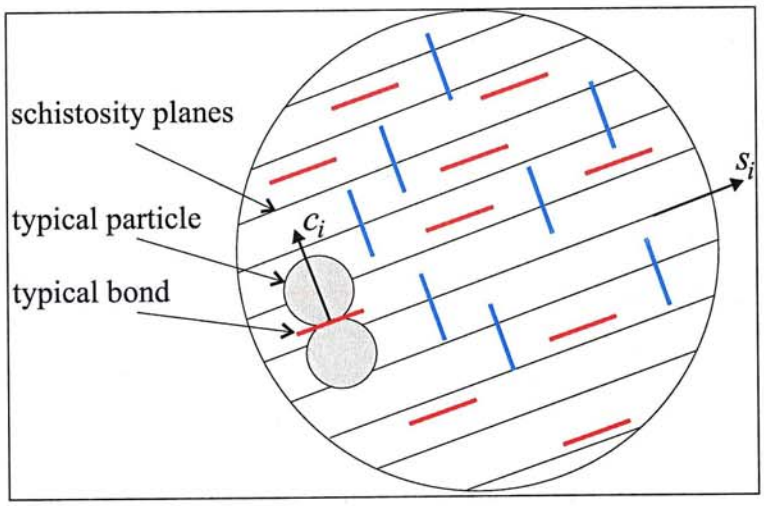

Figure 5. *Two sets of bonds oriented parallel with the schistosity planes (in red) and perpendicular to the schistosity planes (in blue).*

The smeared representation of material anisotropy requires the following two inputs. The first input is a table of xy-pairs that describes the variation of the normalized macroscopic unconfined compressive strength with respect to α . The strength values

* * This may seem contrary to the common-sense notion that schistosity planes are likely to be weaker rather than stronger for tension perpendicular to the planes. The paradox probably indicates that the conceptual model of induced micro-tension in a particle assembly is inappropriate in this case. Rather, the directional and non-uniform distribution of stiffness (and possibly also strength) as-sociated with the schistosity planes may induce local tensions. When loading direction is varied, these local tensions may develop differently and thereby activate different failure modes. (Compare Figures 40 and 45, and note how the discrete material exhibits a two-stage failure process of band localization followed by secondary cracking in the base material, whereas the smeared material exhibits no band localization.) Ideally, such a representation of the schistosity planes as discrete bands of softer and weaker material should form the basis of our micromodel of the material. In fact, this approach is explored in Sections 2.2.3, 2.4.3, and 2.5.3 but a truly comprehensive study would involve a significant extension to the state of the art in micromodeling, and is well beyond the scope of the present contract. For these reasons, and because of model-size limitations, the smeared representation is used here in spite of its deficiencies.

are normalized by the strength for α =0. (This input is the normalized version of Figure 3.) The second input is a strength-reduction factor, f_s , which serves to adjust each table value such that the adjusted value, υ' , satisfies

$$\upsilon' = 1 - (1 - \upsilon) f_s \qquad (1)$$

where υ is the original value. Both the original and adjusted input tables used in the present work are shown in Figure 6.

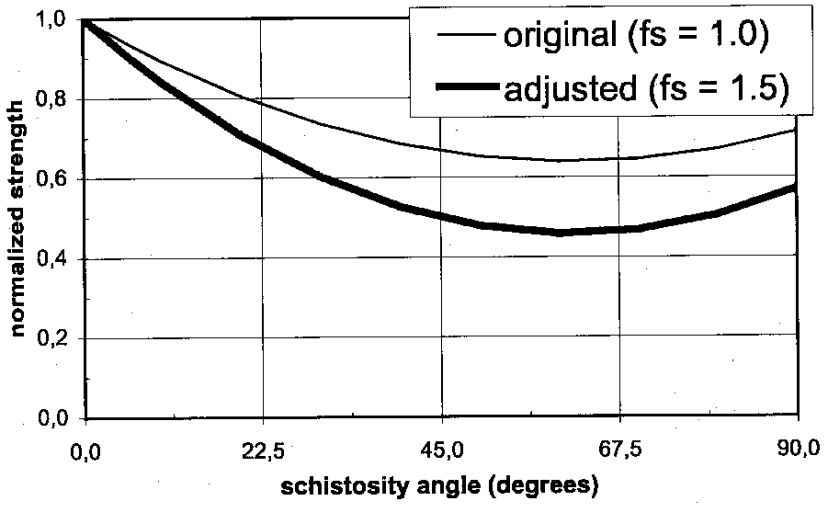

Figure 6. *Normalized macrostrength tables (original and adjusted).*

The parallel-bond normal and shear strengths are set as follows. First, the parallel-bond normal and shear strengths are assigned based on the input parameters describing an isotropic PFC ^{2D} material. (The strengths will then satisfy a Gaussian (normal) distribution.) Then, the two strength values at each parallel bond are adjusted as follows.

1. Define the orientation of the bond by c_i (see Figure 5).
2. Define the minimum angle between the lines formed by c_i and s_i as α_c . (Note that $0<\alpha_c<90^\circ$.)
3. Set the parallel-bond normal strength to satisfy

$$\sigma_c = (\sigma_c)_o S(90 - \alpha_c) \qquad (2)$$

   where $(\sigma_c)_o$ is the original strength value, and S is the value from the adjusted normalized macrostrength table evaluated at an angle of $90 - \alpha_c$.

4. Set the parallel-bond shear strength to satisfy

$$\tau_c = (\tau_c)_o \begin{cases} S(\alpha_c + 45), \alpha_c < 45 \\ S(\alpha_c - 45), \alpha_c > 45 \end{cases} \qquad (3)$$

   where $(\tau_c)_o$ is the original strength value, and S is the value from the adjusted normalized macrostrength table evaluated at the specified angles.

2.2.2 Hypothesized Anisotropic Material

Before describing the discrete representation of material anisotropy, a brief discussion of the hypothesis that guided its development will be provided. This hypothesis provides a mechanism to explain the observed anisotropy of the gneissic tonalite. The modulus anisotropy follows directly from the hypothesized mechanism; however, the strength anisotropy is more complex, and may require extension of the hypothesis to provide a full explanation.

The following hypothetical material will reproduce the observed modulus anisotropy. The hypothetical material consists of discrete bands of softer and weaker material aligned with the schistosity planes. The modulus of such a material will exhibit the general anisotropy trend of Figure 2 — i.e., largest modulus for α =0, smallest modulus for α =90 and decreasing modulus for increasing α . The stiffness response of such a material can be idealized by a set of stiff springs for the base material and a set of softer springs for each band. For α =0 (i.e., when the bands are aligned with the loading direction), these two sets of springs act in parallel. For α =90 (i.e., when the bands are perpendicular to the loading direction), these two sets of springs act in series. Thus, the modulus will be less when α =90, and the amount by which it will be less is determined by the stiffness ratio of the base material and the bands.

This hypothetical material will also exhibit a strength anisotropy, although it is difficult to determine its exact form. Macroscopic shear failure is activated in the bands when they are oriented at angles (perhaps 20 to 60 degrees) to the loading direction. But note that microscopic failure may be tensile (see Figure 7). At these angles, shear strain is concentrated in the bands, because they are "in series" with the more competent minerals that comprise the base material.

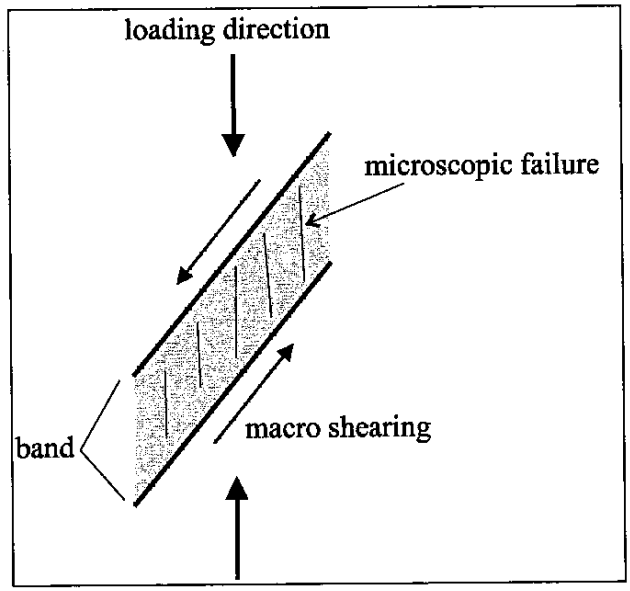

***Figure** 7. Strain localization in hypothetical material.*

If all of the damage occurred solely within the bands, then this material would exhibit the strength anisotropy observed in foliated rocks such as slates — i.e., a symmetric shape with a minimum at approximately 30 degrees. However, if we allow damage to also occur within the base material, then the strength anisotropy could differ. Specifically, if we postulate the existence of a different failure mode for large values of α (perhaps 60 degrees or more), then such a material may possess the same sort of strength anisotropy as does the gneissic tonalite. This alternate failure mode consists of the formation of tensile fractures that emanate from the top/bottom of certain bands and propagate parallel with the loading direction (see Figure 45). Such fractures might be induced by a sort of beam-bending process whereby the softer bands, when loaded in series (i.e., approximately perpendicular to the bands), induce bending in the stiffer base material comprising the band "roof/floor."

Evidence that some such alternate failure mode (although perhaps not exactly this beam-bending process) may be causing the observed strength anisotropy in the gneissic tonalite is provided by studying the failure mechanisms of other materials that exhibit a similar strength anisotropy. One such material is wood, which exhibits greater strength in a direction parallel with the grain than perpendicular to the grain. We postulate that wood is weaker when loaded perpendicular to the grain because of the alternate failure mode of crushing, which does not occur for small values of α.

Another such material is Cordova Cream, a mildly laminated, highly permeable oolitic limestone, which is weaker (with average uniaxial compressive strengths of 21 and 13 MPa) and softer (with average moduli of 22 and 17 GPa) when loaded perpendicular to the bedding planes (Haimson and Song, 1993).* We postulate that Cordova Cream is weaker when loaded perpendicular to the bedding planes because of the alternate failure mode of pore collapse, which does not occur for smaller values of α . Note that Cordova Cream is an *oolitic* limestone, which means that it is made up chiefly of ooliths (small rounded accretionary bodies, generally formed of calcium carbonate, resembling fish eggs with a diameter of 0.25 to 2.0 mm) cemented together (Bates and Jackson, 1984). Thus, it is reasonable to postulate a pore-collapse mechanism for this material. The mechanism is activated at large values of α when shear strain concentrates in the bedding layers.

2.2.3 Implementation of Discrete Representation

In the discrete representation of material anisotropy, it is assumed that both the modulus and strength anisotropies observed at the macroscale arise from the existence of a set of discrete bands of softer and weaker material aligned with the schistosity planes. Refer to Section 2.2.2 for a discussion of why such a hypothetical material was chosen.

---

* Haimson and Song (1993) subjected vertical boreholes drilled in cubical specimens of Cordova Cream with vertical bedding (parallel to the drilled borehole) to monotonically increasing uniform far-field horizontal loading (1 = σ 3) until breakout failure occurred. They report that: "The surprising result was that the breakouts were randomly distributed, exhibiting no apparent bedding plane effect on the orientation of the spallings, despite the bedding-related anisotropy at low confining pressures." If one accepts the similarity between the Cordova Cream and the gneissic tonalite being argued here, then these results support the assertion that the effect of anisotropy upon damage formation during the in-situ test will also be minimal.

We have developed a means to construct a PFC ^{2D} material that replicates the microstructure of a homogeneous base material full of penny-shaped clusters of biotite (which is weaker and less stiff than the base material). We do this by first constructing an isotropic PFC ^{2D} material to serve as the base material, and then introducing finite-width, discontinuous bands of biotite that are aligned with the schistosity planes. The bands are characterized by the following six input parameters, which can be divided into two groups.

(1) **Band geometry.** All bands have the same thickness (t) and spacing (s). Each band is comprised of a group of band segments that are created as follows. A band-segment length (l) is specified, and then band segments are placed at random locations along each band until the ratio of the total segment length to the total band length equals a specified value (herein referred to as the discontinuity ratio, dr). Segment overlap is not considered; thus, the discontinuity ratio is only an approximation to the fraction of each band actually occupied by the band segments. (The implementation makes use of the **JSET** command, which is described in Itasca (1999).) Thus, in summary, the band geometry is fully described by the four parameters t, s, l and d_r.

(2) **Band material properties.** After the particles and parallel bonds comprising the bands have been identified, the modulus and strength of the material represented by these particles and parallel bonds is reduced relative to the modulus and strength of the base material by the factors E_f and S_f , respectively. This is done by modifying the properties of all identified particles and parallel bonds as follows. The normal and shear stiffnesses of each particle and of each parallel bond are set equal to E_f times their current values. The normal and shear strengths of each parallel bond are set equal to S_f times their respective mean values (that were input to the specimen-genesis procedure). (In retrospect, it may have been more consistent to simply set these values equal to Sf times their current values, because then the strengths of the material within each band would satisfy the same Gaussian distribution as does the base material.) Thus, in summary, the band material properties are fully described by the two parameters E_f and S_f

2.3 CREATION AND TESTING OF THE SYNTHETIC SPECIMENS

All *PFC* ^{2D} specimens used during the calibration process have a height of 142 mm and a width of 54 mm and possess a uniform particle-size distribution bounded by R_{min} and R_{max} with R_{max} =1.66 min and R_{min} = 0.5 mm. Each specimen contains approximately 40 particles across its width. Different packing arrangements are produced by varying the seed of the random-number generator used during specimen genesis. Brazilian tests are performed on some of these specimens by trimming them into a circular shape. Typical specimens, and the walls used to load them, are shown in Figures 8 and 9.

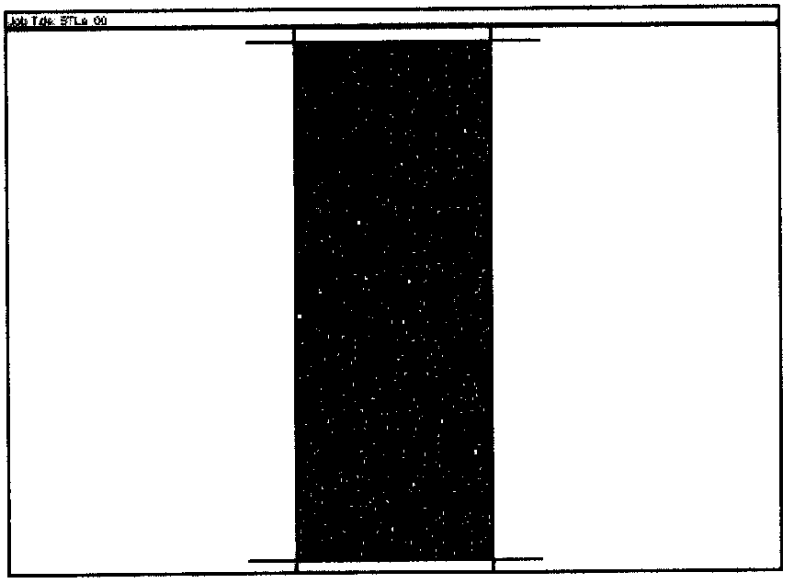

Figure 8. *Representative specimen used during the calibration process (4634 particles; 8974 parallel bonds).*

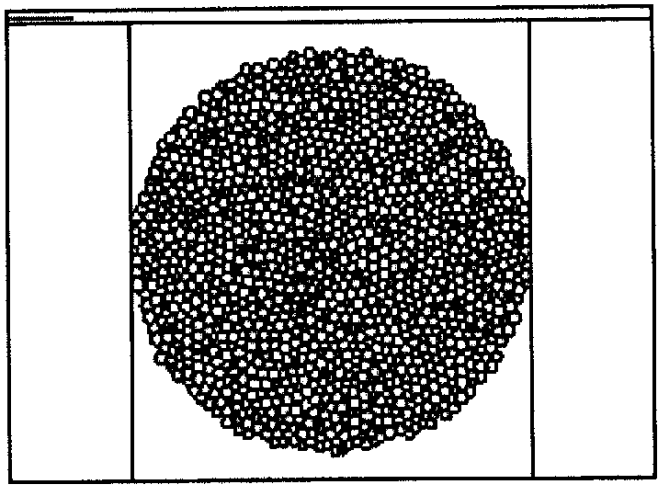

Figure 9. *Brazilian disk trimmed from the representative specimen (1386 particles; 2664 parallel bonds).*

All PFC ^{2D} specimens were created using the specimen-genesis procedure (Itasca, 1999), which produces a rectangular specimen containing a densely packed, bonded particle assembly with low locked-in stress. The microparameters that characterize the parallel-bonded material are given by Eq. (3.17) in the FISH in PFC^{2D} volume of Itasca (1999). These specimen-genesis procedures and microparameters produce a PFC ^{2D} material that exhibits an isotropic mechanical response. The additional procedures and microparameters used to produce an anisotropic PFC ^{2D} material are described in Section 2.2. Biaxial and Brazilian tests were performed on all PFC ^{2D} specimens using

the biaxial and Brazilian-test environments (Itasca, 1999), in which each specimen is confined and loaded by four enclosing walls (see Figures 10 and 11). All biaxial tests were performed with a confinement of 0.1 MPa, which is assumed to be an adequate representation of unconfined conditions.

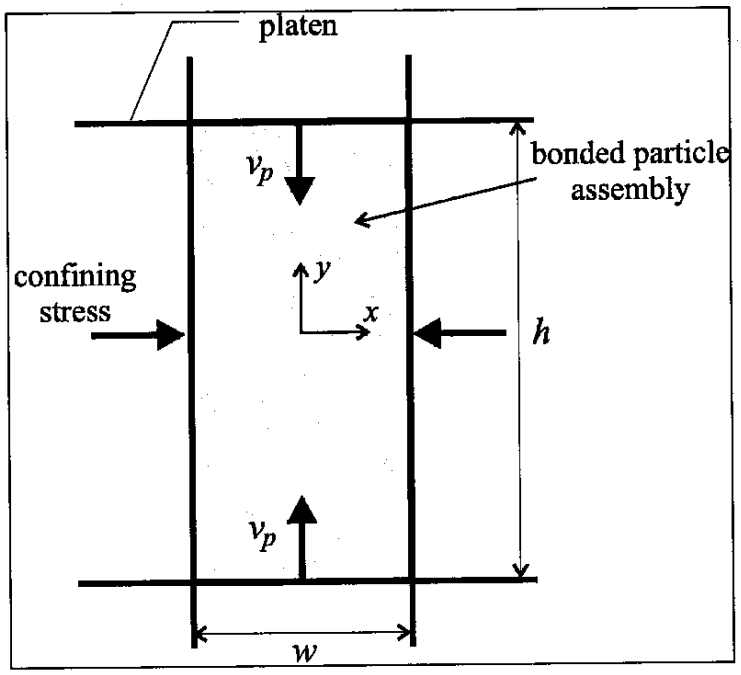

Figure 10. *Sketch of biaxial-test environment.*

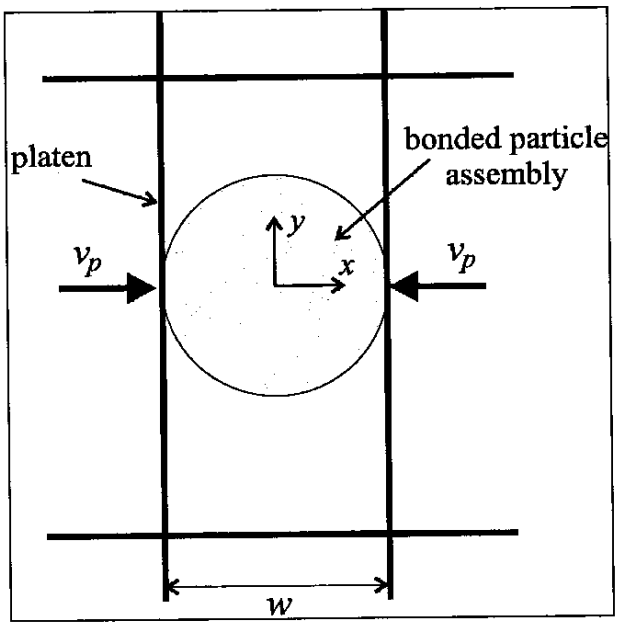

Figure 11. *Sketch of Brazilian-test environment.*

The results of the biaxial and Brazilian tests were determined using the procedures described in the FISH in PFC^{2D} volume of Itasca (1999). The results include:

(1) the Young's modulus, E (This value is computed as the ratio of axial stress to axial strain using stress and strain values corresponding to the point when one-half of the peak stress has been obtained.)

(2) the unconfined compressive strength, σ_f (This value is taken as the peak stress on a plot of axial stress versus axial strain.)

(3) the crack-initiation stress, σ_{ci} (This value is taken as the axial stress at the point during the test at which one percent of the total number of cracks existing at peak stress have been formed. The rationale for using this procedure to determine σ_{ci} is described in Section 2.2 of Potyondy and Cundall (1999).)

(4) the Brazilian tensile strength, σ_t (This value is computed by

$$\sigma_t = F_f / \pi R t \qquad (4)$$

where F_f is the peak force acting on the platens, and R and t are the radius and thickness, respectively, of the Brazilian disk (Goodman 1980). For all tests described in this report, the disk radius was equal to twice the specimen width, and the disk thickness was unity.)

(5) the total number and type of cracks, N_{ft} and N_{fs}, existing in the biaxial or Brazilian specimen at the point when the peak load has been obtained.

The same set of control parameters were used when creating and testing all of the PFC ^{2D} specimens. (The microparameters that characterize the particular PFC ^{2D} materials examined in this project are listed in Section 2.4.) The following control parameter values were assigned (see Tables 3.1 and 3.5 in the FISH in PFC^{2D} volume of Itasca (1999)):

B =1.1
σ_o=-1.0 MPa (specimen-genesis control parameters)
N_f=3
n_f/N=0.0 **(5)**
β_x=0 001
β_y=1.0(biaxial-test control parameters)
v_p=0.05 m/s
N_p=400 cycles
S_p=10 stages **(6)**
β_x=1.0
v_p=0.05 m/s (Brazilian-test control parameters)
N_p=400 cycles
S_p=10 stages **(7)**

2.4 SIMULATED RESPONSES (BEST-FIT MATERIALS)

The PFC ^{2D} specimens are the same size (54 by 142 mm) as the laboratory 54 mm specimens and are calibrated to match the schistosity-angle relationships exhibited by the 54 mm specimens (because these results seem to lie between those of the 41 and 99 mm specimens and are thus taken to be representative for this rock). The laboratory results to which the PFC ^{2D} models have been calibrated are shown in Figures 2 and 3. The six PFC ^{2D} materials described in the following two sections were assigned to the test-hole models. The discrete anisotropic material described in Section 2.4.3 was not assigned to the test-hole models.

2.4.1 Isotropic Materials

Because the response of the isotropic PFC ^{2D} material does not vary with schistosity angle, we have created two best-fit isotropic materials to bound the laboratory response set. The upper-bound material matches the maximum modulus and strength ($E \approx 80$ GPa and $\sigma_f \approx 140$ MPa), while the lower-bound material matches the minimum modulus and strength ($E \approx 62$ GPa and $\sigma_f \approx 90$ MPa). Also, two variants of each material were created in which the bond-failure mode is forced to be either tensile only or a mixture of tensile and shear. Thus, there are a total of four isotropic materials.

The microparameters that characterize these four best-fit isotropic materials, designated as STU, TU, STL and TL, are given by Eq. (3.17) in the FISH in PFC^{2D} volume of Itasca (1999). The following parameter values were assigned to these materials. The upper-bound materials were assigned larger micro-modulus values than were the lower-bound materials.

$$\begin{array}{lll} \rho & = 2810 \text{ kg/m}^3 & \\ E_c & = 53 \text{ GPa} & \\ k_n / k_s & = 1.0 & \\ \lambda & = 1.0 & \text{(materials STU and TU)} \\ E_c & = 53 \text{ GPa} & \\ k^n / k^s & = 1.0 & \\ \mu & = 0.50 & \end{array} \qquad (8)$$

$$\begin{array}{lll} \rho & = 2810 \text{ kg/m}^3 & \\ E_c & = 41 \text{ GPa} & \\ k_n / k_s & = 1.0 & \\ \lambda & = 1.0 & \text{(materials STL and TL)} \\ E_c & = 41 \text{ GPa} & \\ k^n / k^s & = 1.0 & \\ \mu & = 0.50 & \end{array} \qquad (9)$$

The micro-strengths of all four materials were assigned the following four separate sets of values.

$$\begin{aligned} \bar{\sigma}_c \text{ (mean)} &= 113 \text{ MPa} \\ \bar{\sigma}_c \text{ (std. dev.)} &= 21 \text{ MPa} \\ \bar{\tau}_c \text{ (mean)} &= 113 \text{ MPa} \\ \bar{\tau}_c \text{ (std. dev.)} &= 21 \text{ MPa} \end{aligned} \qquad \text{(material STU)} \tag{10}$$

$$\begin{aligned} \bar{\sigma}_c \text{ (mean)} &= 90 \text{ MPa} \\ \bar{\sigma}_c \text{ (std. dev.)} &= 16 \text{ MPa} \\ \bar{\tau}_c \text{ (mean)} &= 10000 \text{ MPa} \\ \bar{\tau}_c \text{ (std. dev.)} &= 0 \text{ MPa} \end{aligned} \qquad \text{(material TU)} \tag{11}$$

$$\begin{aligned} \bar{\sigma}_c \text{ (mean)} &= 74 \text{ MPa} \\ \bar{\sigma}_c \text{ (std. dev.)} &= 13 \text{ MPa} \\ \bar{\tau}_c \text{ (mean)} &= 74 \text{ MPa} \\ \bar{\tau}_c \text{ (std. dev.)} &= 13 \text{ MPa} \end{aligned} \qquad \text{(material STL)} \tag{12}$$

$$\begin{aligned} \bar{\sigma}_c \text{ (mean)} &= 58 \text{ MPa} \\ \bar{\sigma}_c \text{ (std. dev.)} &= 11 \text{ MPa} \\ \bar{\tau}_c \text{ (mean)} &= 10000 \text{ MPa} \\ \bar{\tau}_c \text{ (std. dev.)} &= 0 \text{ MPa} \end{aligned} \qquad \text{(material TL)} \tag{13}$$

Note that the ST and T materials differ only in the values assigned to the parallel-bond normal and shear strengths. The parallel-bond normal and shear strengths of materials TU and TL have been assigned a very large value in order to prevent micro-shear failure and thereby force the material to fail only in a micro-tensile mode.

Because these are isotropic materials, it is only necessary to construct and test a single 54 by 142 mm specimen of each material. The reproducibility of the results is investigated by creating five original specimens of each material that have different packing arrangements, and then subjecting each of these specimens to both a biaxial and a Brazilian test.

The results are presented in Figures 12 and 13. The upper- and lower-bounding properties of these materials are evident in Figures 14 and 15, which depict the average values of modulus and strength for each material. Note that these isotropic responses plot as straight lines.

STU	upper-bound isotropic, shear & tensile fail					
packing	E (GPa)	sig_f (MPa)	sig_ci (MPa)	N_fn	N_fs	sig_t (MPa)
A	80.1	135.9	51.8	58	53	31.3
B	79.8	141.4	69.8	81	67	32.7
C	79.8	138.0	72.2	142	84	31.8
D	78.9	134.9	76.6	78	57	34.6
E	79.7	145.9	78.0	110	95	31.2
average	79.7	139.2	69.7	NA	NA	32.3

TU	upper-bound isotropic, tensile only fail					
packing	E (GPa)	sig_f (MPa)	sig_ci (MPa)	N_fn	N_fs	sig_t (MPa)
A	80.3	148.0	77.0	204	0	26.9
B	79.7	141.2	82.7	340	0	29.1
C	79.7	154.1	60.4	255	0	28.4
D	79.0	147.3	70.7	210	0	32.1
E	79.7	140.2	73.9	393	0	33.5
average	79.7	146.2	72.9	NA	NA	30.0

Figure 12. *Biaxial- and Brazilian-test results for the two upper-bound isotropic materials.*

STL	lower-bound isotropic, shear & tensile fail					
packing	E (GPa)	sig_f (MPa)	sig_ci (MPa)	N_fn	N_fs	sig_t (MPa)
A	61.7	89.1	49.0	101	53	23.5
B	62.0	87.6	44.7	86	47	21.1
C	63.0	94.8	58.1	118	64	21.1
D	61.4	90.4	46.0	69	54	22.3
E	61.1	92.9	43.0	106	58	20.2
average	61.8	91.0	48.2	NA	NA	21.6

TL	lower-bound isotropic, tensile only fail					
packing	E (GPa)	sig_f (MPa)	sig_ci (MPa)	N_fn	N_fs	sig_t (MPa)
A	61.6	88.5	39.0	196	0	19.8
B	62.1	89.6	40.9	245	0	17.1
C	63.2	93.4	46.2	273	0	19.5
D	61.4	91.3	55.4	408	0	18.9
E	61.1	92.4	36.0	372	0	20.7
average	61.9	91.0	43.5	NA	NA	19.2

Figure 13. *Biaxial- and Brazilian-test results for the two lower-bound isotropic materials.*

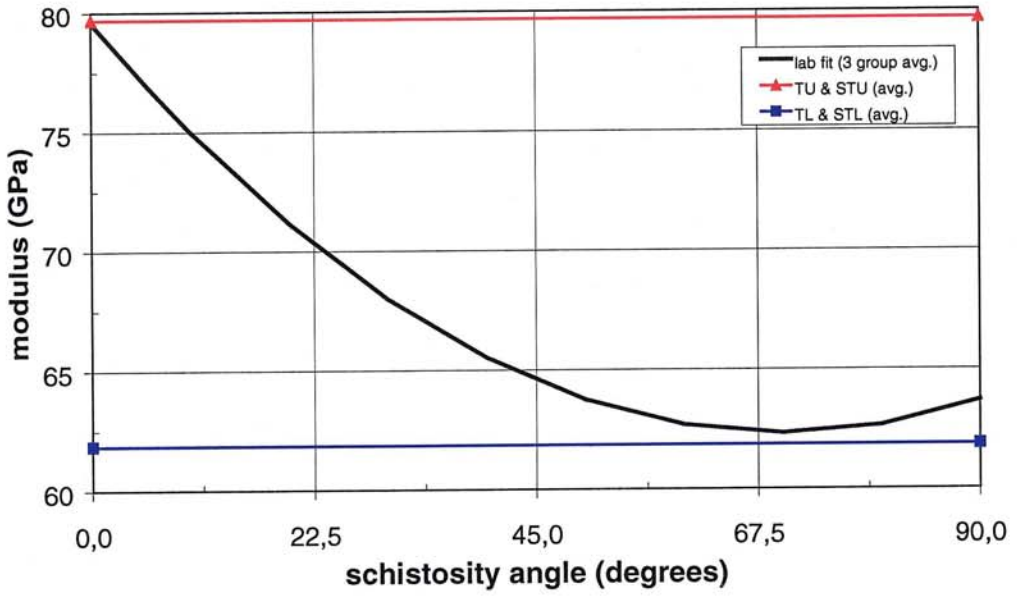

Figure 14. Variation of modulus with schistosity angle (all four isotropic materials).

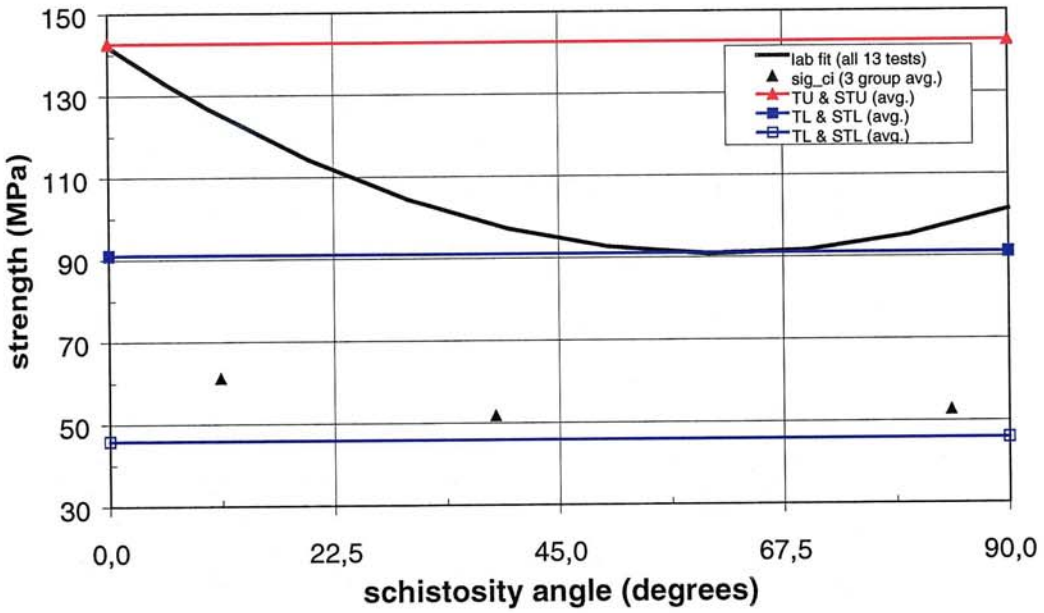

Figure 15. Variation of strengths with schistosity angle (all four isotropic materials).

2.4.2 Smeared Anisotropic Materials

In an attempt to match the observed strength variation with schistosity angle, we have created a best-fit smeared anisotropic material. The current implementation of the smeared approach does not address modulus variation, therefore, this material produces an isotropic modulus. Also, two variants of this material were created in which the

bond-failure mode is forced to be either tensile only or a mixture of tensile and shear. Thus, there are two smeared anisotropic materials.

The microparameters that characterize the two best-fit smeared anisotropic materials, designated as STAs and TAs, are given by Eq. (3.17) in the FISH in PFC^{2D} volume of Itasca (1999), and by the strength-reduction factor, f_s ,in Section 2.2.1. The following parameter values were assigned to these materials.

$$\begin{aligned} \rho &= 2810 \text{ kg/m}^3 \\ E_c &= 46 \text{ GPa} \\ k_n/k_s &= 1.0 \\ \bar{\lambda} &= 1.0 \qquad \text{(materials STAs and TAs)} \\ \bar{E}_c &= 46 \text{ GPa} \\ \bar{k}^n/\bar{k}^s &= 1.0 \\ \mu &= 0.50 \\ f_s &= 1.5 \end{aligned} \tag{14}$$

$$\begin{aligned} \bar{\sigma}_c \text{ (mean)} &= 140 \text{ MPa} \\ \bar{\sigma}_c \text{ (std. dev.)} &= 25 \text{ MPa} \qquad \text{(material STAs)} \\ \bar{\tau}_c \text{ (mean)} &= 140 \text{ MPa} \\ \bar{\tau}_c \text{ (std. dev.)} &= 25 \text{ MPa} \end{aligned} \tag{15}$$

$$\begin{aligned} \bar{\sigma}_c \text{ (mean)} &= 97 \text{ MPa} \\ \bar{\sigma}_c \text{ (std. dev.)} &= 17 \text{ MPa} \qquad \text{(material TAs)} \\ \bar{\tau}_c \text{ (mean)} &= 10000 \text{ MPa} \\ \bar{\tau}_c \text{ (std. dev.)} &= 0 \text{ MPa} \end{aligned} \tag{16}$$

Note that these materials differ only in the values assigned to the parallel-bond normal and shear strengths. The parallel-bond shear strength of material TAs has been assigned a very large value in order to prevent micro-shear failure and thereby force the material to fail only in a micro-tensile mode.

One way to obtain the modulus and strength variations for these anisotropic materials would be to create one large specimen of each material, and then perform biaxial tests upon a set of extracted cores oriented at different directions relative to the schistosity direction. Such an approach would most closely mimic the way in which the laboratory results are generated. However, we can minimize the scatter in such results (produced by testing different samples of rock — the samples are not identical to one another) by employing the following alternate procedure.

We create a single 54 by 142 mm specimen and assign it isotropic properties. Then, from this original specimen, we generate a set of final specimens for which the schistosity angle is varied from 0 to 90 degrees (by utilizing the procedure described in Section 2.2.1, which modifies the parallel-bond strengths as a function of bond

orientation relative to the schistosity direction). All other model components, including particle packing, are identical for all of these final specimens. We then perform an unconfined biaxial test upon each of these final specimens to obtain the modulus and strength variations. Brazilian tests were not performed upon the anisotropic materials. In addition, the reproducibility of the results is investigated by creating five original specimens that have different packing arrangements, and testing the set of final specimens generated from each of these five original specimens.

The resulting modulus variations for both materials is shown in Figure 16, which depicts the average values for the five different original specimens. The smeared anisotropic material exhibits an isotropic modulus. This is to be expected, because only the parallel-bond strengths were modified by the smeared anisotropy installation procedure. An attempt was made to modify the effective micro-modulus at each bond as a function of the bond orientation relative to the schistosity direction (in the same way as is being done for the bond strengths); however, the macroscopic modulus remained essentially isotropic. It appears that some sort of discrete approach may be necessary to produce a PFC ^{2D} material with an anisotropic macromodulus; the results in Section 2.4.3 support this assertion (see Figure 23).

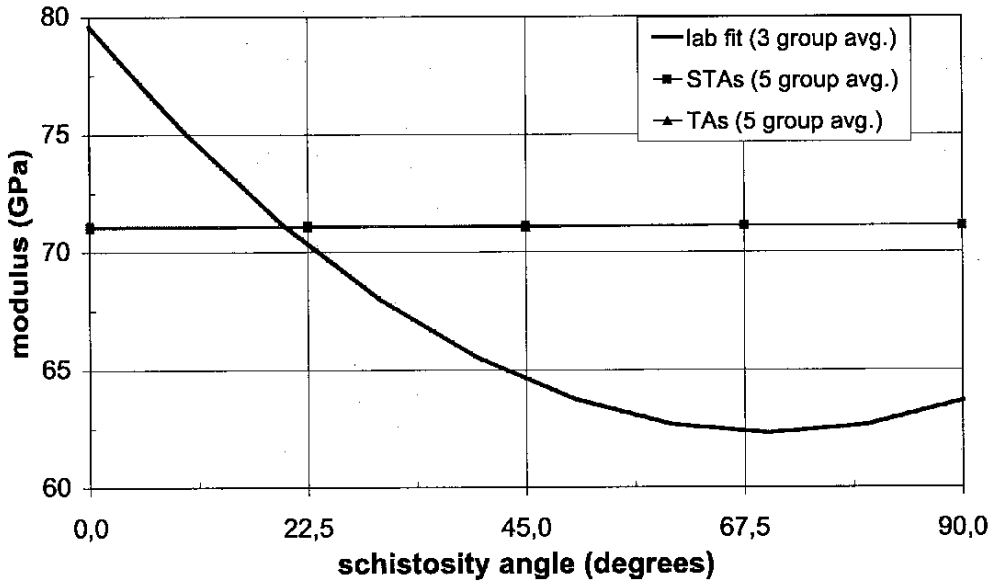

Figure 16. *Variation of modulus with schistosity angle (smeared anisotropic materials STAs and TAs).*

The resulting strength variations for both materials are shown in Figures 17, 18 and 19. The effect of particle packing arrangement on result reproducibility is illustrated in Figures 17 and 18, which depict the peak-strength results for the five different original specimens of both materials. The average response that is representative of each material is shown in Figure 19, which depicts the average values of both peak strength and crack-initiation stress for each set of tests. These results indicate that the smeared anisotropic material does exhibit the correct trend in its strength anisotropy — i.e., a larger value for $\alpha = 0$ than for $\alpha = 90$, and a nearly flat response for $\alpha > 45$.

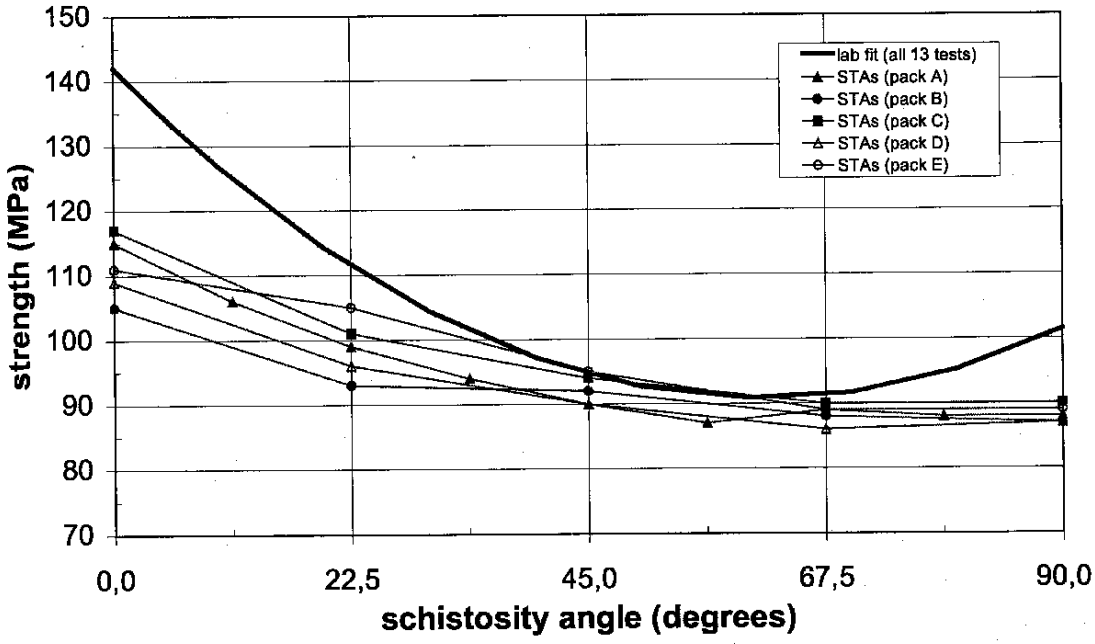

Figure 17. *Variation of strength with schistosity angle (effect of packing; smeared anisotropic material STAs).*

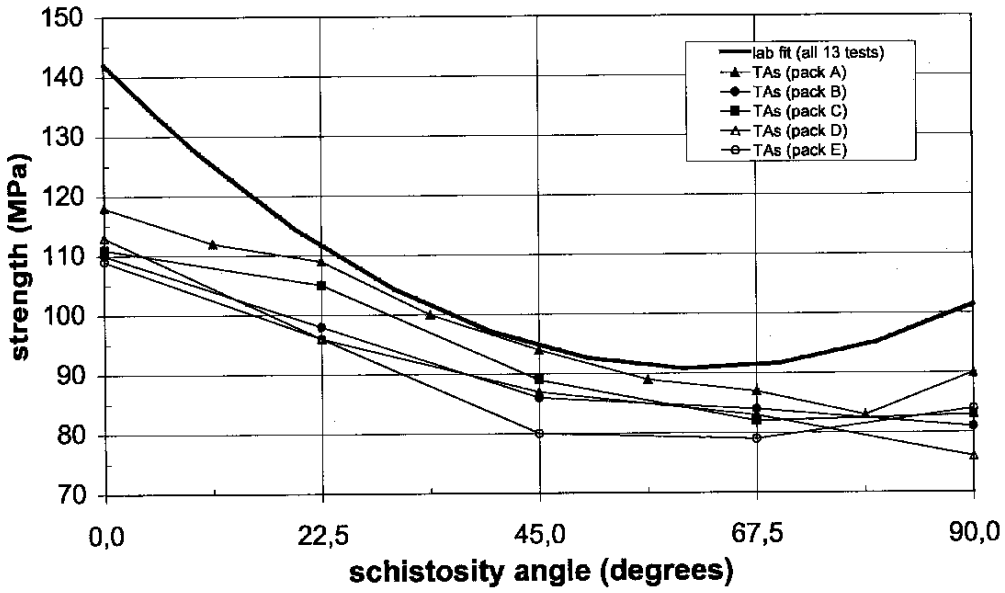

Figure 18. *Variation of strength with schistosity angle (effect of packing; smeared anisotropic material TAs).*

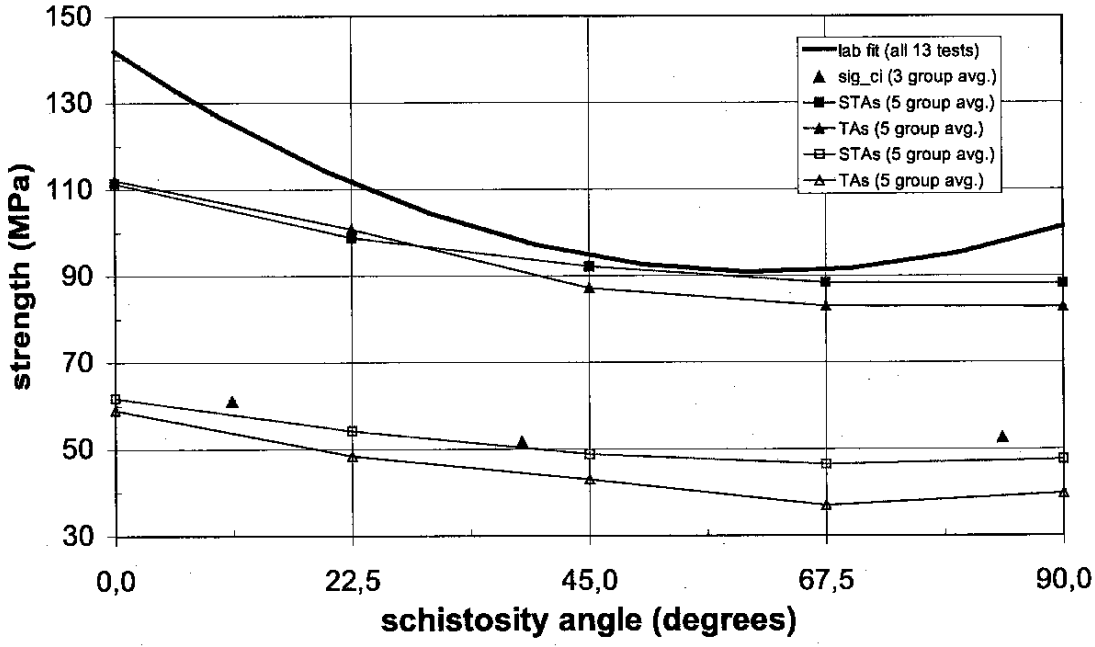

Figure 19. *Variation of strengths with schistosity angle (smeared anisotropic materials STAs and TAs).*

2.4.3 Discrete Anisotropic Material

In an attempt to match the observed variation of both modulus and strength with schistosity angle, we have created a best-fit discrete anisotropic material. The bond-failure mode of this material is forced to be a mixture of tensile and shear. The microparameters that characterize this material, designated as STAd, are given by Eq. (3.17) in the FISH in PFC^{2D} volume of Itasca (1999), and by the additional six parameters in Section 2.2.3. The following parameter values were assigned to this material. (Note that some of the band properties are specified in terms of $\bar{D}$, the average particle diameter in the specimen.)

ρ =2810 kg/m^3
E_c =69 GPa
k_n/k_s =1.0 (base material STAd) **(17)**
λ =1.0
E_c =69 GPa
k^n/k^s =1.0
μ =0.50

$$\begin{aligned} \bar{\sigma}_c \text{ (mean)} &= 163 \text{ MPa} \\ \bar{\sigma}_c \text{ (std. dev.)} &= 30 \text{ MPa} \qquad \text{(base material STAd)} \\ \bar{\tau}_c \text{ (mean)} &= 163 \text{ MPa} \\ \bar{\tau}_c \text{ (std. dev.)} &= 30 \text{ MPa} \end{aligned} \tag{18}$$

$$\begin{aligned} t &\approx 2\tilde{D} \approx 2.6 \text{ mm} \\ s &= 8\tilde{D} = 10.5 \text{ mm} \\ l &= 8\tilde{D} = 10.5 \text{ mm} \qquad \text{(band material STAd)} \\ d_r &= 0.85 \\ E_f &= 0.05 \\ S_f &= 0.20 \end{aligned} \tag{19}$$

One way to obtain the modulus and strength variations for this anisotropic material would be to create one large specimen, and then perform biaxial tests upon a set of extracted cores oriented at different directions relative to the schistosity direction. Such an approach would most closely mimic the way in which the laboratory results are generated. However, we can minimize the scatter in such results (produced by testing different samples of rock — the samples are not identical to one another) by employing the following alternate procedure.

We create a single 54 by 142 mm specimen and assign it isotropic properties. Then, from this original specimen, we generate a set of final specimens for which the schistosity angle is varied from 0 to 90 degrees (by utilizing the procedure described in Section 2.2.3, which modifies the material properties of the set of particles and parallel bonds that comprise the bands). All other model components, including particle packing, are identical for all of these final specimens. We then perform an unconfined biaxial test upon each of these final specimens to obtain the modulus and strength variations. (Brazilian tests were not performed upon the anisotropic materials.) In addition, the reproducibility of the results is investigated by creating five original specimens that have the same packing arrangement but different band-segment locations within each band (by varying the seed of the random-number generator used to locate the segments within each band), and testing the set of final specimens generated from each of these five original specimens.

The band geometries of two of the STAd specimens are shown in Figures 20 and 21, which depict the lower half of each specimen for α =22.5. In these figures, the particles comprising the base and band materials are drawn in yellow and white, respectively, and the parallel bonds comprising the bands are drawn as red filled circles. Notice how these two specimens have different band-segment locations, which are here designated as band A and band B.

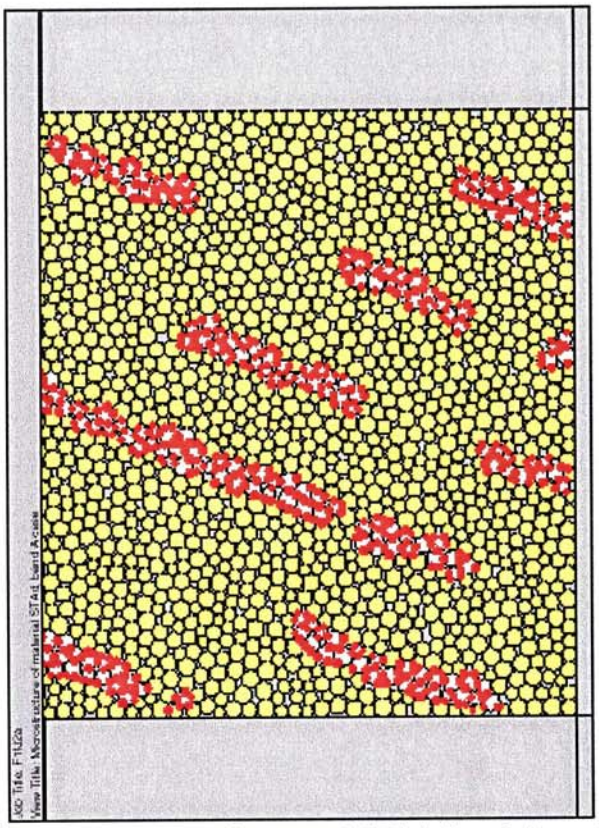

Figure 20. *Representative specimen of material STAd (band A, α =22.5).*

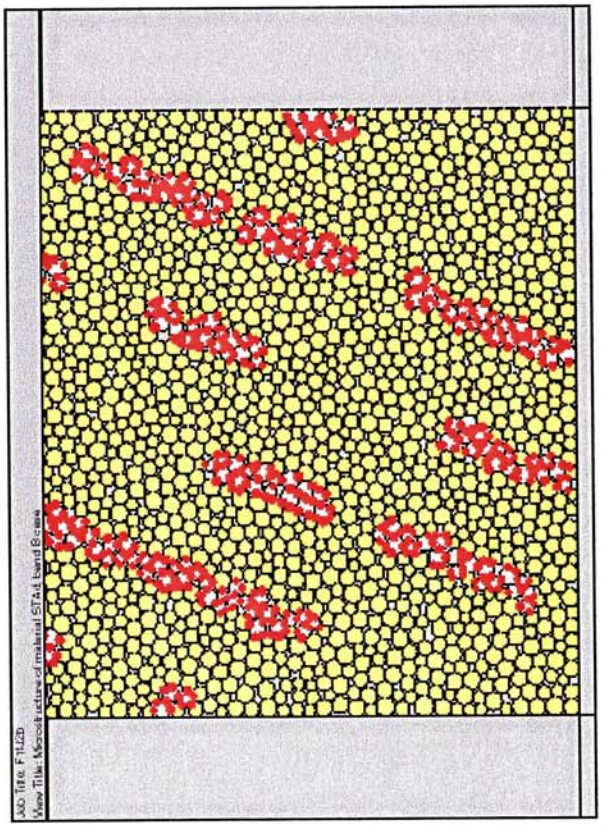

Figure 21. *Representative specimen of material STAd (band B, α =22.5).*

The resulting modulus variations for material STAd are shown in Figures 22 and 23. The effect of band geometry on reproducibility of the results is illustrated in Figure 22, which depicts the modulus results for the five different original specimens. The average response that is representative of material STAd is shown in Figure 23, which depicts the average modulus for each set of tests. These results indicate that the discrete anisotropic material exhibits the correct form of modulus anisotropy, in that the modulus decreases for increasing values of α and begins to stabilize for large values of α greater than about 60 degrees. This behaviour is as expected from the discussion in Section 2.2.2. The modulus is too low for $\alpha>12$, however, it should be possible to achieve a better fit by choosing a different set of band-characterization parameters.

The resulting strength variations for material STAd are shown in Figures 24 and 25. The effect of band geometry on reproducibility of the results is illustrated in Figure 24, which depicts the peak-strength results for the five different original specimens. The average response that is representative of material STAd is shown in Figure 25, which depicts the average values of both peak strength and crack-initiation stress for each set of tests. These results indicate that the discrete anisotropic material exhibits the correct form of strength anisotropy, in that the strength is largest for $\alpha=0$, declines rapidly until $\alpha=30$, and then remains nearly constant for $\alpha>30$. Thus, material STAd provides a good match of strength anisotropy, but underestimates the modulus for $\alpha>12$. It should be possible to improve the fit to the modulus anisotropy without degrading the fit to the strength anisotropy by choosing a different set of band-characterization parameters.

This additional calibration step was not performed, because time and budget constraints forced us to focus our efforts upon completing the test-hole simulations. Also, when material STAd was assigned to the fine test-hole model, it became apparent that greater near-field resolution is required to provide an adequate representation of the discrete banding (see Figure 26, which uses the same plotting convention as do Figures 20 and 21 and also includes a set of dashed circles at 10 mm intervals).

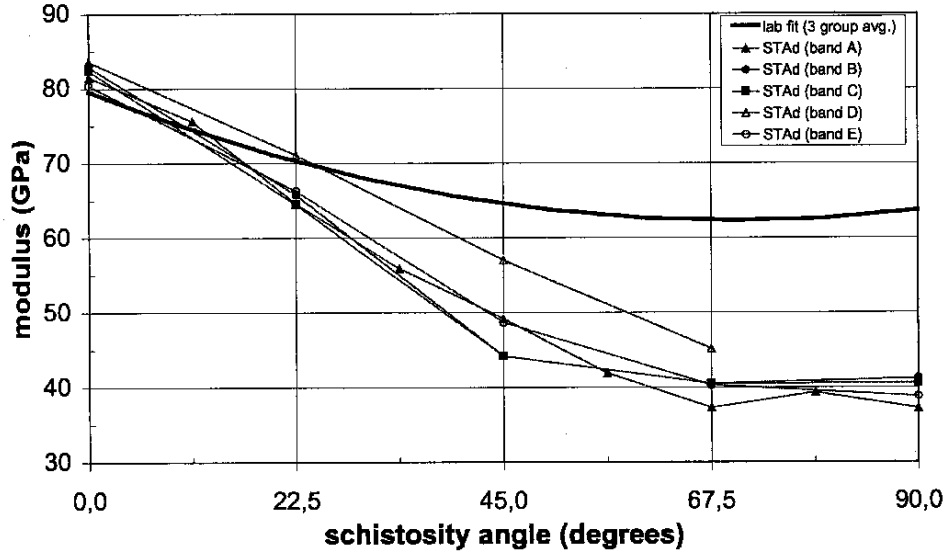

Figure 22. *Variation of modulus with schistosity angle (effect of band geometry; discrete anisotropic material STAd).*

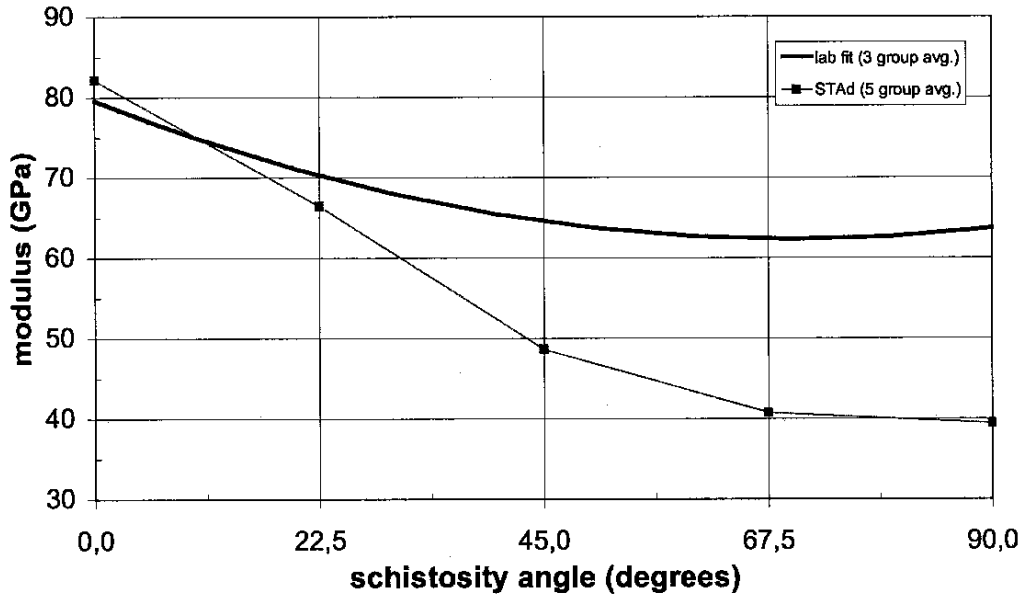

Figure 23. *Variation of modulus with schistosity angle (discrete anisotropic material STAd).*

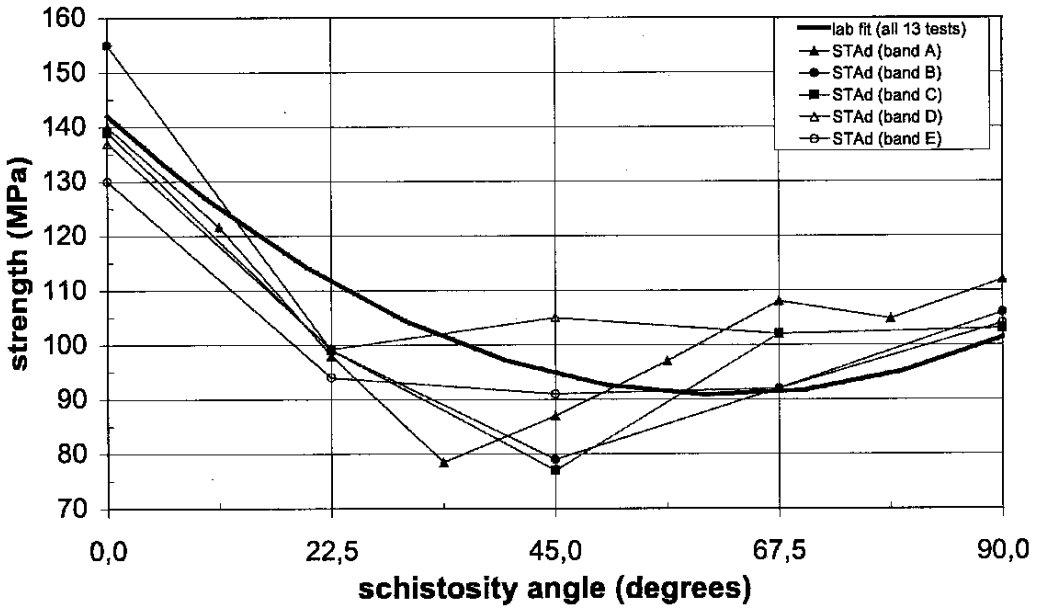

Figure 24. *Variation of strength with schistosity angle (effect of band geometry; discrete anisotropic material STAd).*

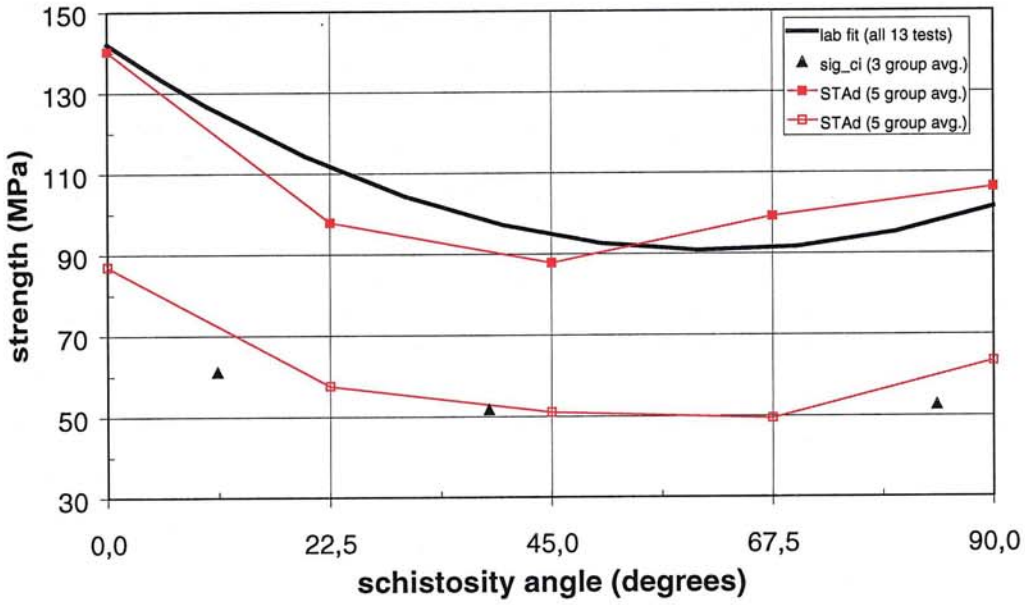

Figure 25. *Variation of strengths with schistosity angle (discrete anisotropic material STAd).*

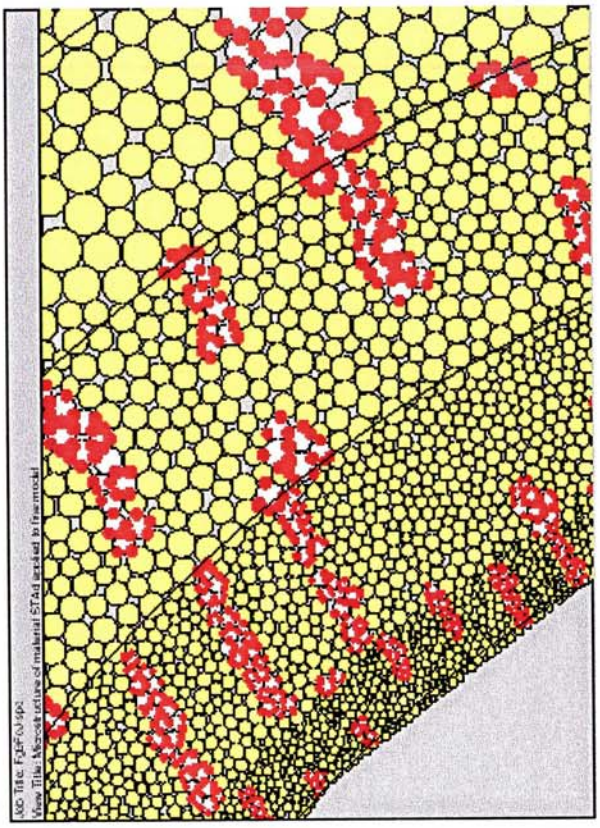

Figure 26. *Discrete anisotropy material STAd applied to the fine-resolution test-hole model.*

2.5 FAILURE PATTERNS OF SYNTHETIC SPECIMENS

The damage existing in some of the synthetic specimens that were subjected to biaxial and Brazilian testing is presented in this section. All damage plots correspond with either the pre-peak state, the peak state or the post-peak state for which the axial stress is equal to $0.80\sigma_f$. The damage plots are overlaid upon a plot of the axial stress versus axial strain, or axial force versus axial strain for the Brazilian tests. The crack distribution is depicted in these plots using the convention described in Appendix A.

2.5.1 Isotropic Materials

The damage evolution in the two lower-bound isotropic materials with different bond-failure modes, materials STL and TL, is shown in Figures 27 to 36.* For both materials, a macroscopic failure plane has developed that cuts across the biaxial-test specimen, and this failure plane forms in the post-peak region of the stress-strain curve — very little cracking is present in the specimen at peak load. It appears that a set of secondary microcracks oriented parallel with the loading direction is also forming on either side of this failure plane. Such behaviour was also observed in the laboratory samples. Note that these secondary microcracks do not form during Brazilian tests. Also, the failure plane is much better developed in the STL than in the TL material. This is reasonable, because the STL material allows micro-shear failures to occur along the plane, whereas the TL material must accommodate the shearing motion by forming a much larger-scale pattern of enechelon microcracking. Similar behaviour is being exhibited by the test-hole models that utilized materials STL and TL, especially with respect to development of the "shear band" failure mode (see Section 3.2).

* The results are presented for packing C, because for this packing, the failure plane has developed in the middle of the specimen away from the platens. For some of the other packings, the failure plane developed nearer to the platens, which obscured the behavior described here (see Figure 37).

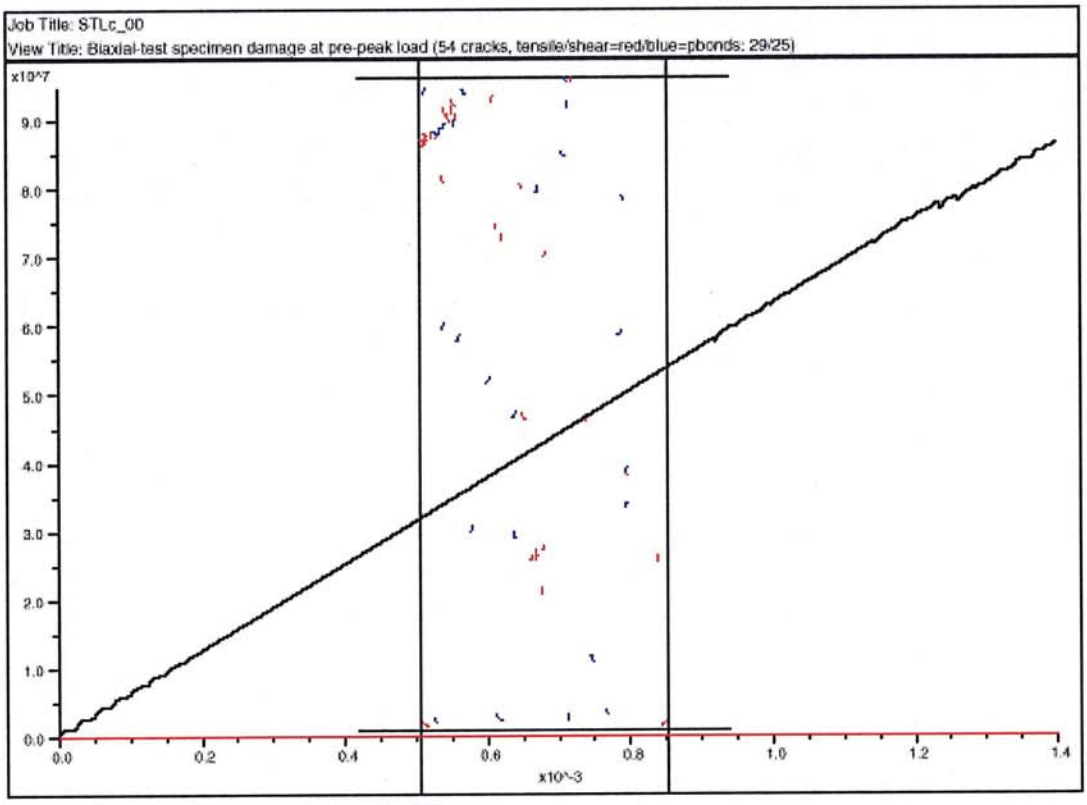

Figure 27. *Damage in biaxial-test specimen at pre-peak load (lower-bound isotropic material STL, pack C, strain of 0.14 percent).*

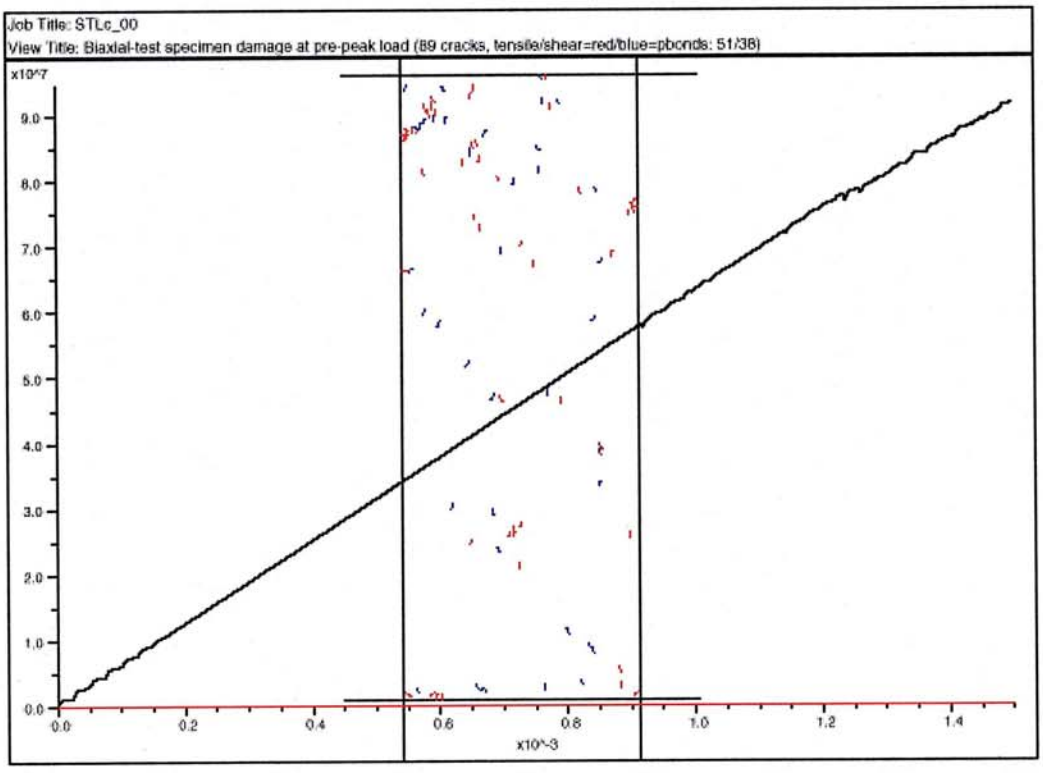

Figure 28. *Damage in biaxial-test specimen at pre-peak load (lower-bound isotropic material STL, pack C, strain of 0.15 percent).*

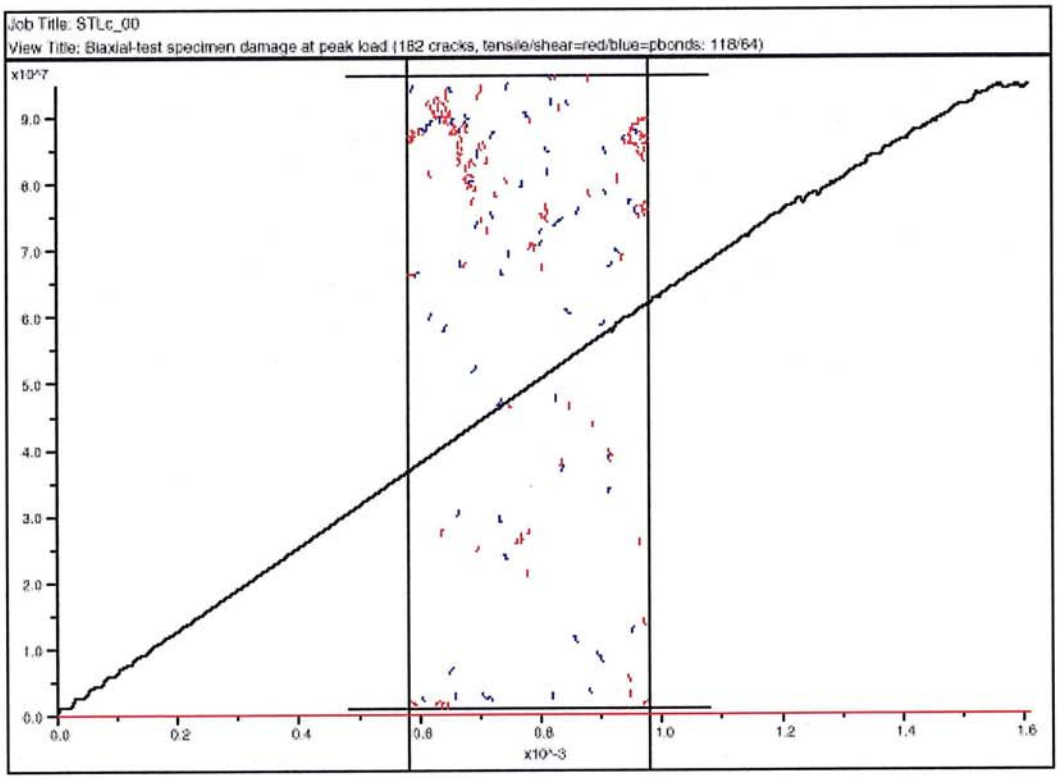

Figure 29. *Damage in biaxial-test specimen at peak load (lower-bound isotropic material STL, pack C).*

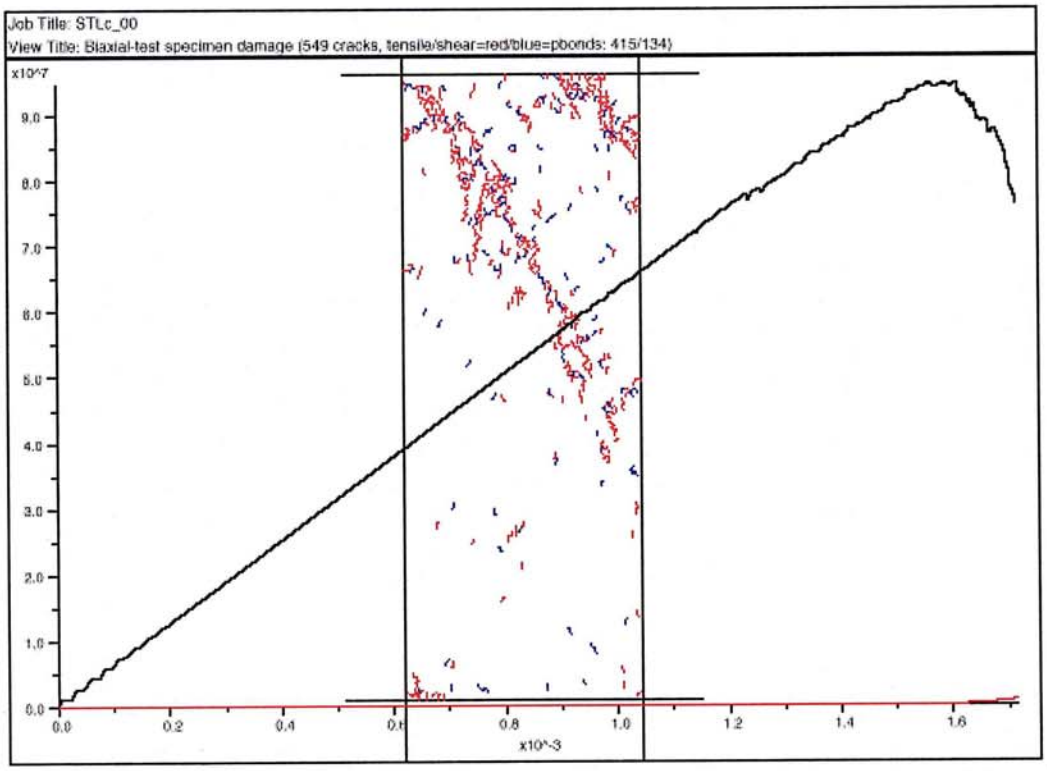

Figure 30. *Damage in biaxial-test specimen at post-peak load (lower-bound isotropic material STL, pack C).*

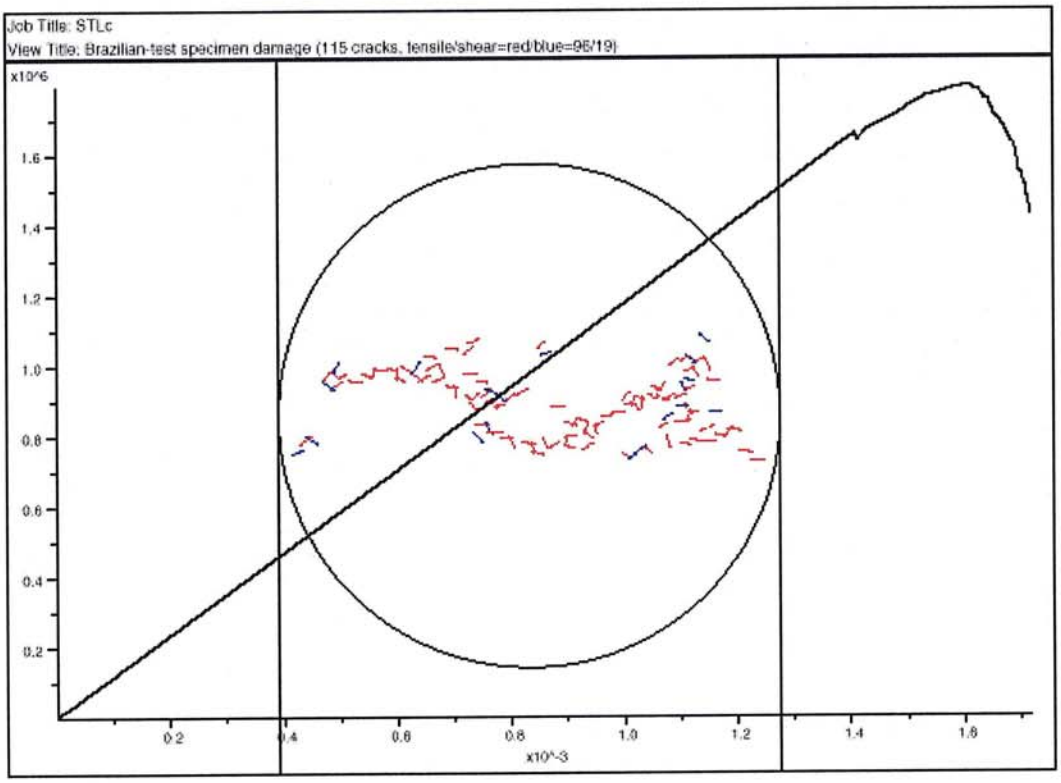

Figure 31. *Damage in Brazilian-test specimen at post-peak load (lower-bound isotropic material STL, pack C).*

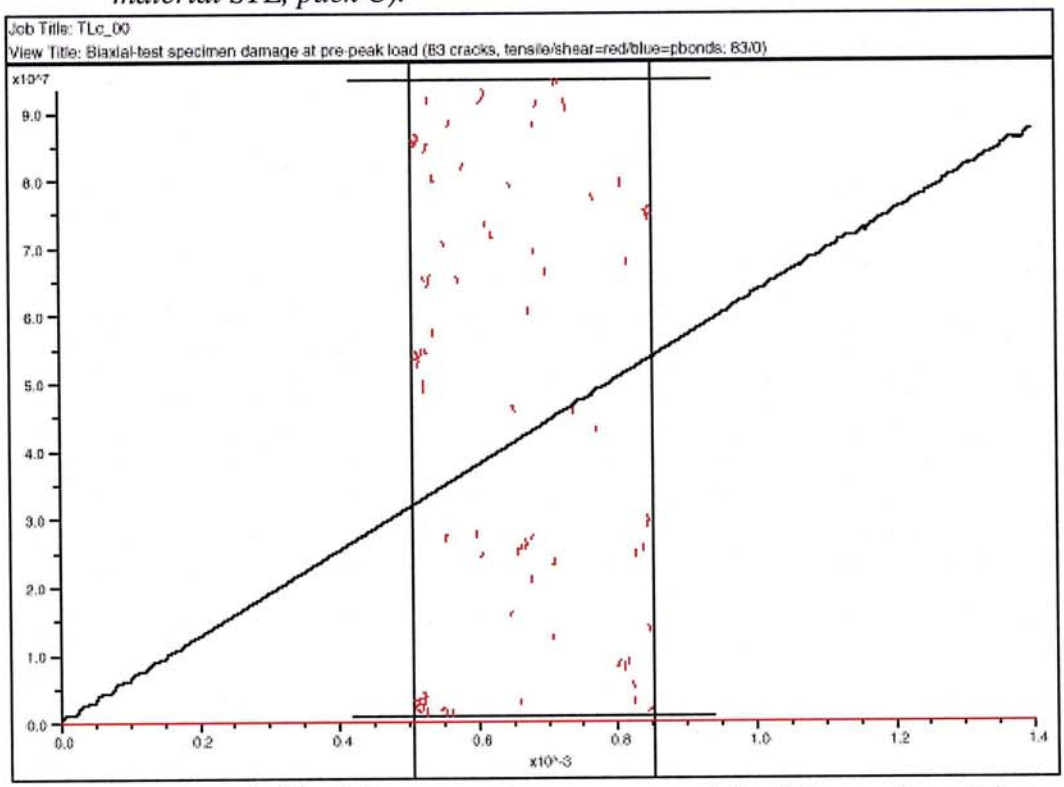

Figure 32. *Damage in biaxial-test specimen at pre-peak load (lower-bound isotropic material TL, pack C, strain of 0.14 percent).*

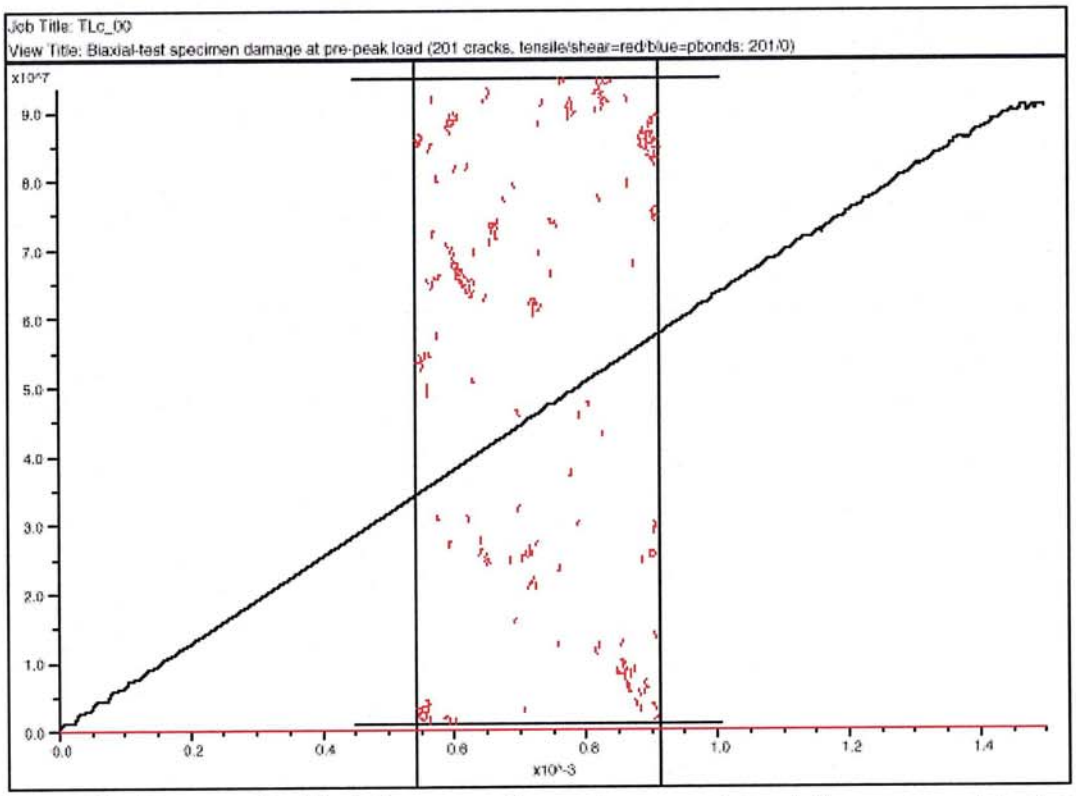

Figure 33. *Damage in biaxial-test specimen at pre-peak load (lower-bound isotropic material TL, pack C, strain of 0.15 percent).*

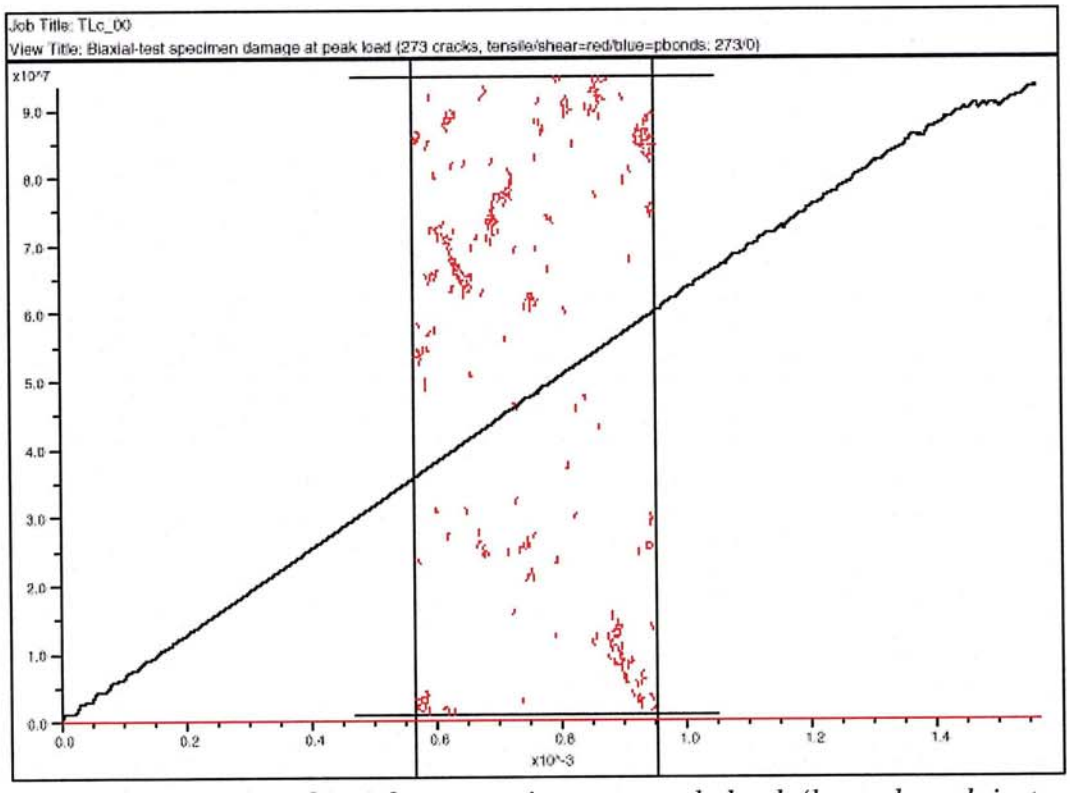

Figure 34. *Damage in biaxial-test specimen at peak load (lower-bound isotropic material TL, pack C).*

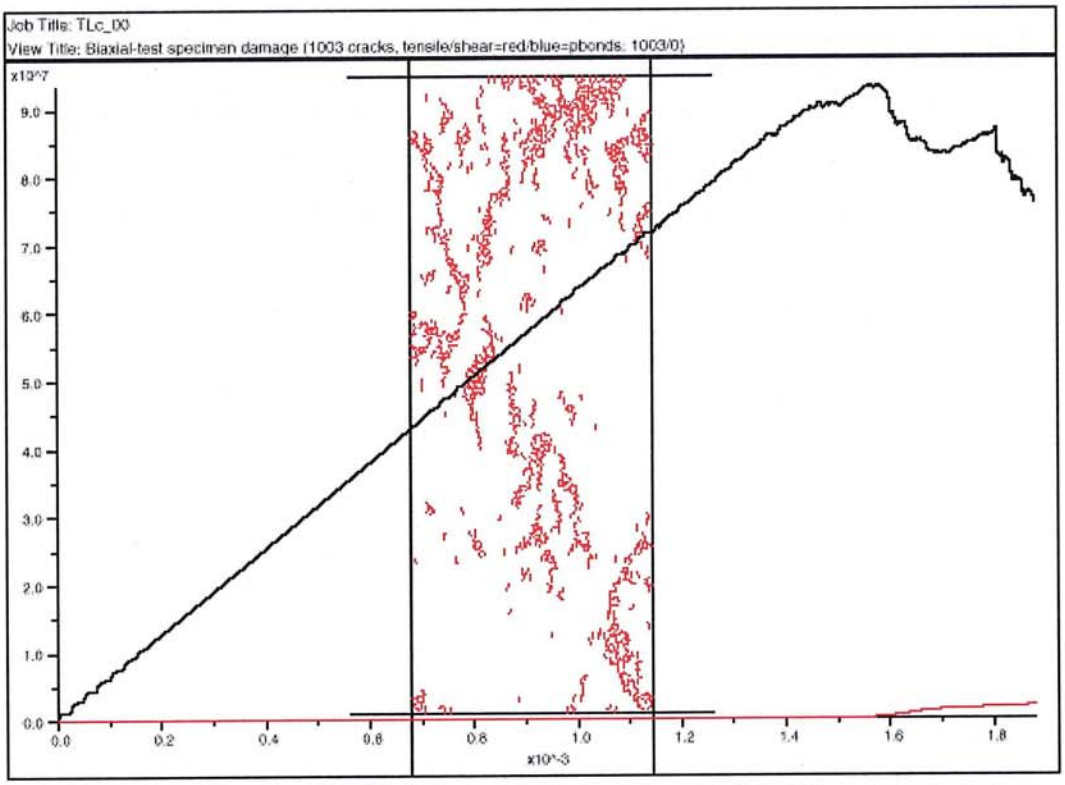

Figure 35. *Damage in biaxial-test specimen at post-peak load (lower-bound isotropic material TL, pack C).*

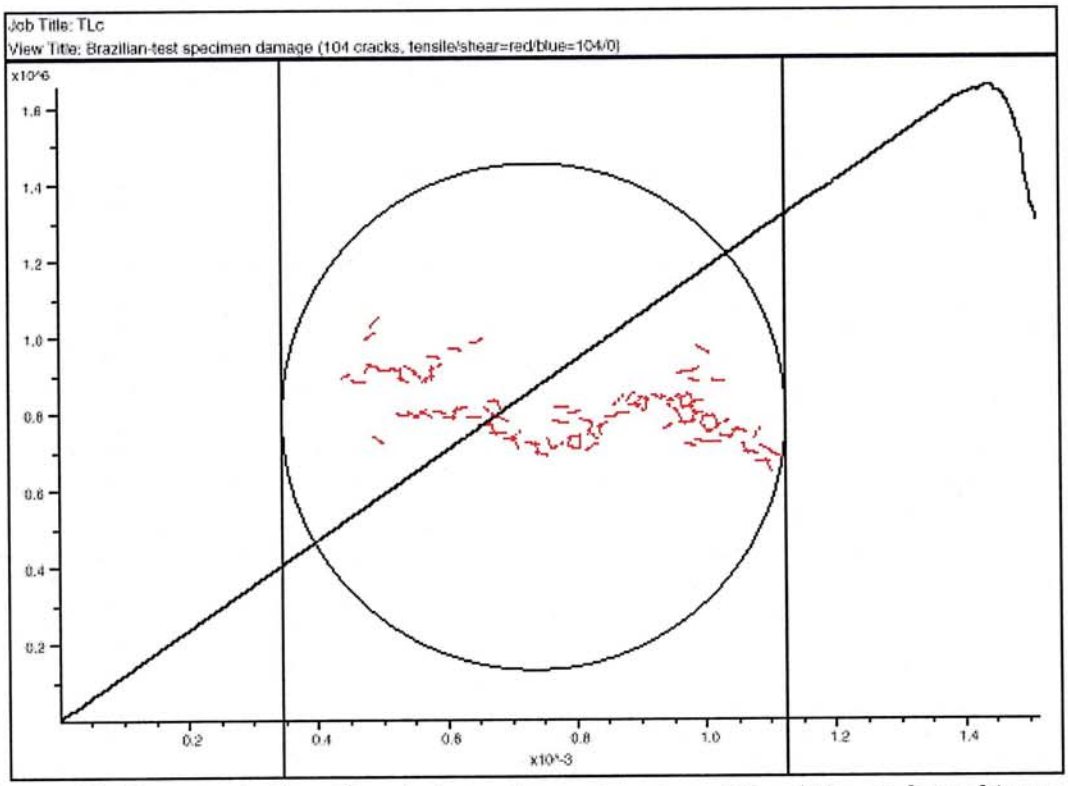

Figure 36. *Damage in Brazilian-test specimen at post-peak load (lower-bound isotropic material TL, pack C).*

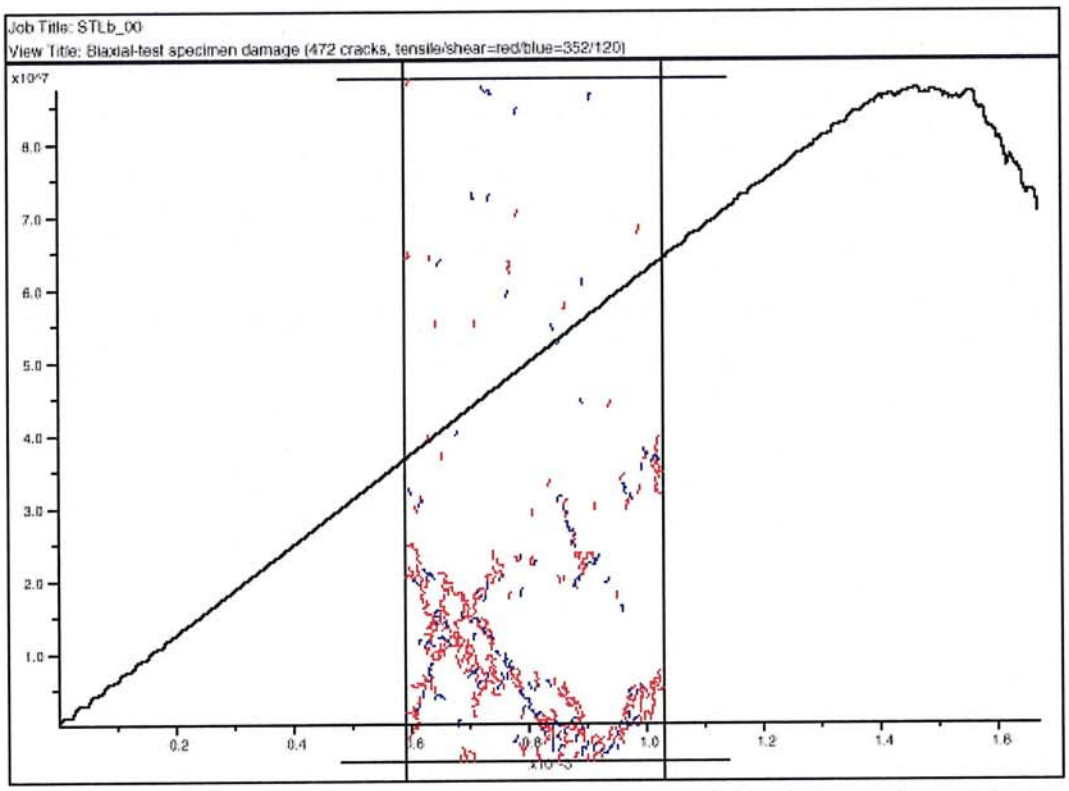

Figure 37. *Damage in biaxial-test specimen at post-peak load (lower-bound isotropic material STL, pack B).*

2.5.2 Smeared Anisotropic Material

The damage existing in the smeared anisotropic material STAs for five different values of schistosity angle is shown in Figures 38 to 42. The schistosity direction is depicted in these plots by the orientation of the three lines at the specimen center. A qualitative appraisal of these plots indicates that some of the damage may be localizing into macroscopic fractures that are aligned perpendicular to the schistosity direction. This is to be expected, because the strengths of this set of parallel bonds have been reduced by a greater amount than other sets by the smeared anisotropy installation procedure. (Refer to the blue bonds in Figure 5.) Similar behaviour is being exhibited by the test-hole models that utilized material STAs (note the macroscopic fractures that have formed on the left side of Figure A.44, the right side of Figure A.46 and the right side of Figure A.39). It should be noted that this behaviour differs from what was observed in the laboratory samples, wherein the damage tended to localize into macroscopic fractures that were aligned parallel with the schistosity direction. Such a response is exhibited by the discrete anisotropic material STA during biaxial testing (compare Figures 40 and 45).

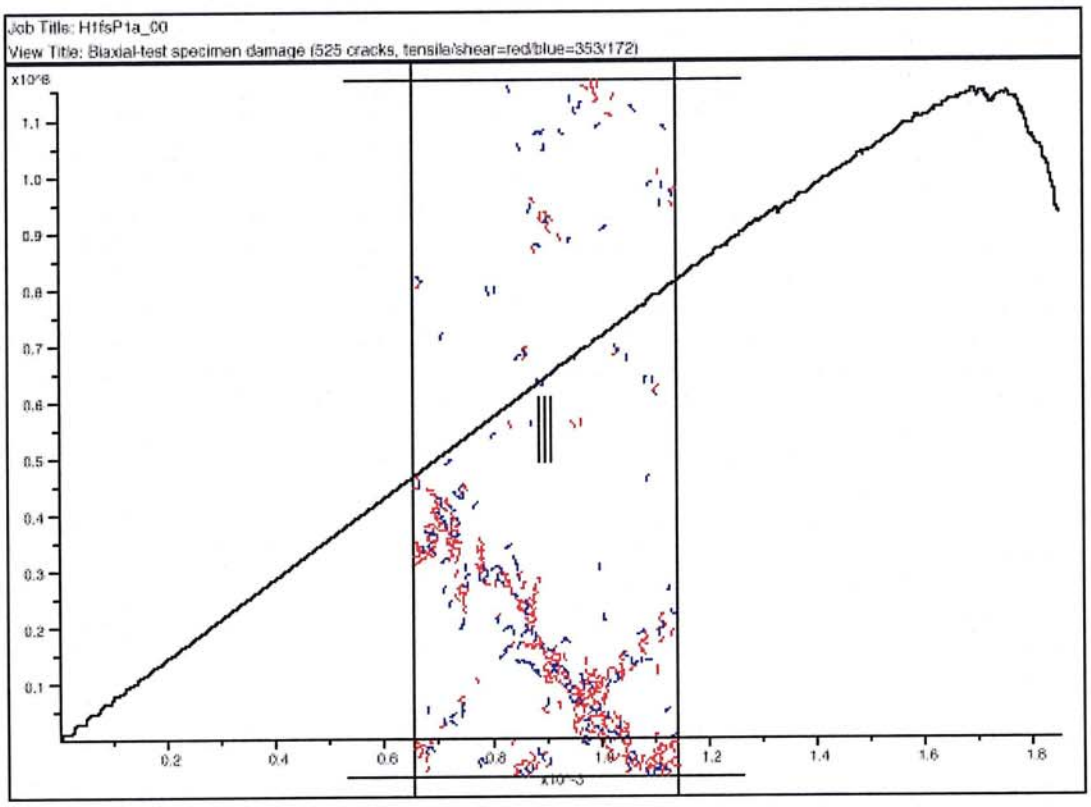

Figure 38. *Post-peak damage in biaxial-test specimen (smeared anisotropic material STAs, pack A, α =0).*

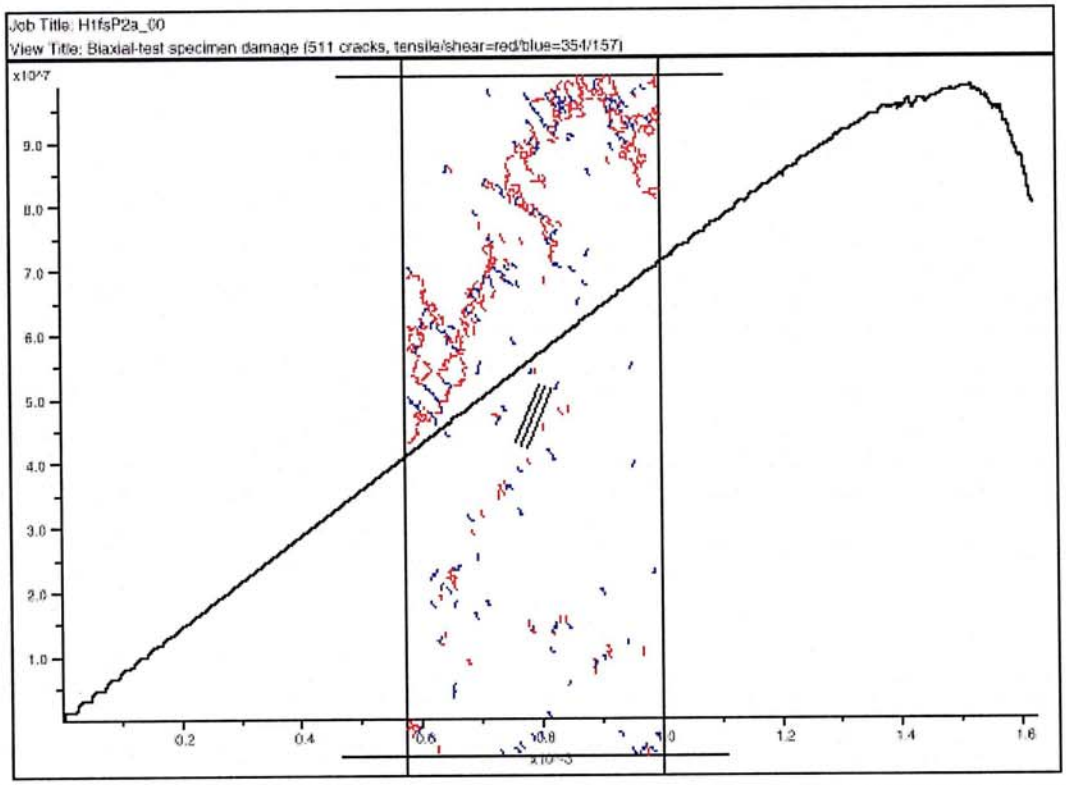

Figure 39. *Post-peak damage in biaxial-test specimen (smeared anisotropic material STAs, pack A, α =22.5).*

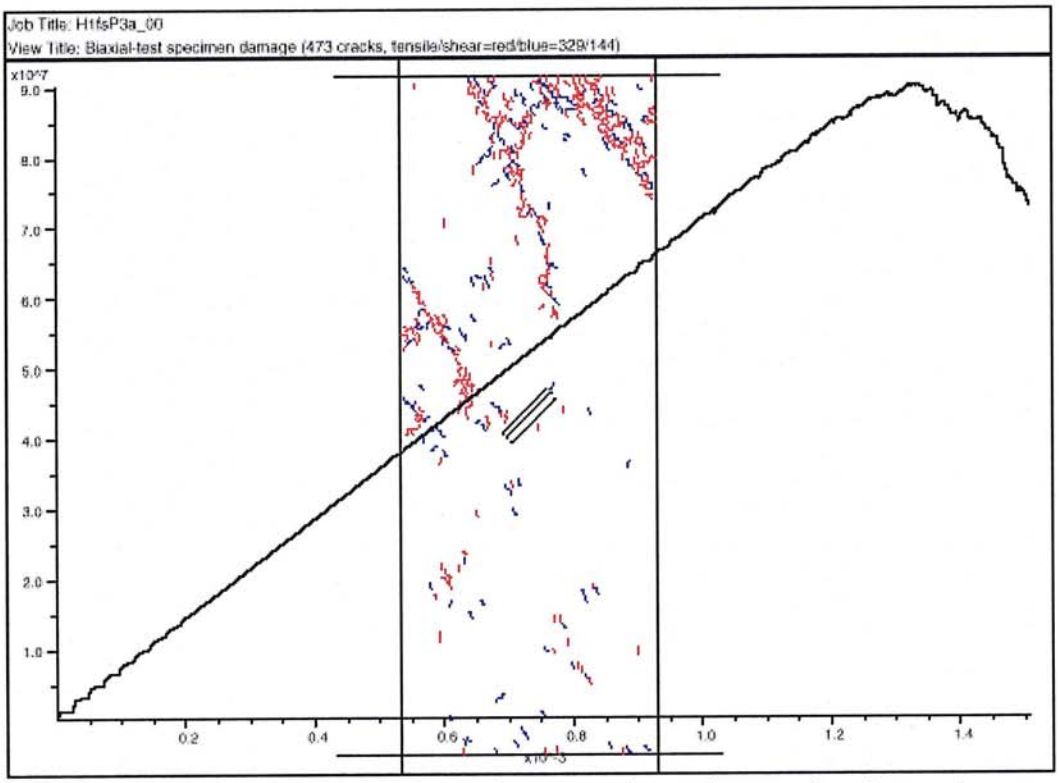

Figure 40. *Post-peak damage in biaxial-test specimen (smeared anisotropic material STAs, pack A, α =45).*

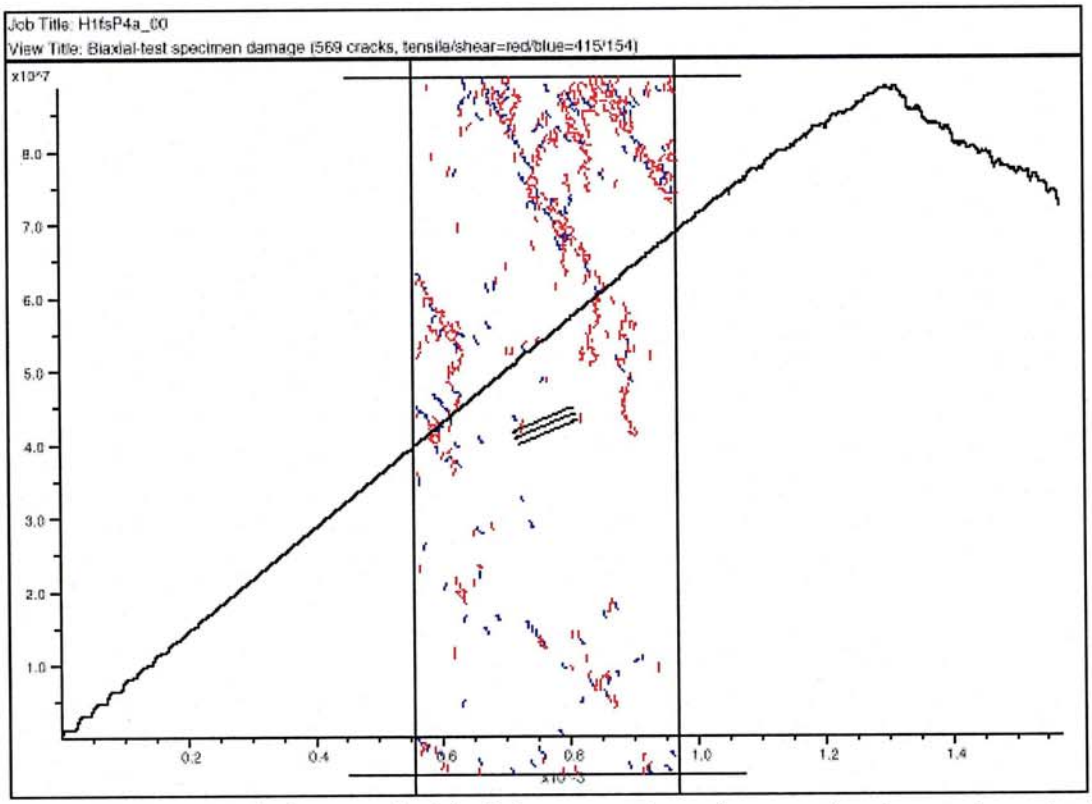

Figure 41. *Post-peak damage in biaxial-test specimen (smeared anisotropic material STAs, pack A, α =67.5).*

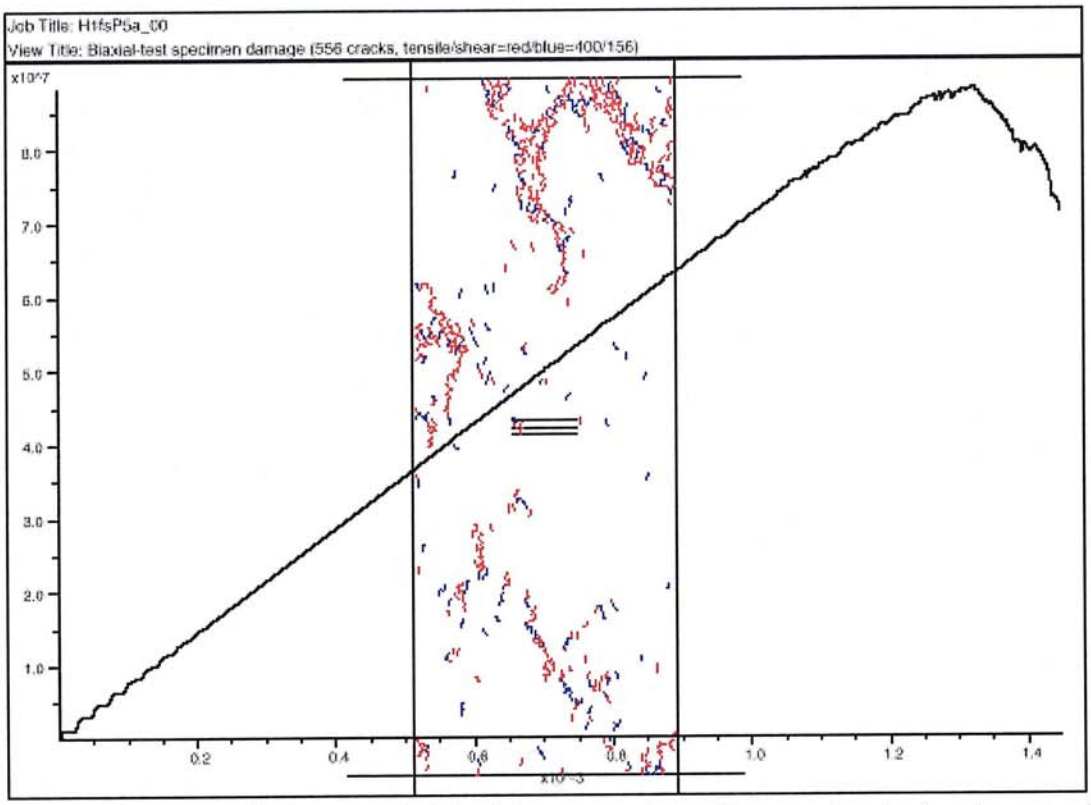

Figure 42. *Post-peak damage in biaxial-test specimen (smeared anisotropic material STAs, pack A, α =90).*

2.5.3 Discrete Anisotropic Material

The damage existing in the discrete anisotropic material STAd for five different values of schistosity angle is shown in Figures 43 to 47. The discrete bands are depicted in these plots by the set of green filled circles, which indicate the intact parallel bonds comprising the band material. When subjected to uniaxial compression, material STAd exhibits failure patterns that have two primary directions: one is parallel with the specimen (and loading) axis, and the other one is approximately parallel with the schistosity planes. The microcracks are localizing within the bands, and then bridging between band segments in an enechelon pattern that is parallel with the specimen axis. This behaviour is consistent with our understanding of what has been observed in the laboratory tests; however, most of these specimens exhibit a plastic-like behaviour after peak load is reached, and this differs from the more brittle behaviour observed in the laboratory tests. The plastic-like behaviour arises from the crack bridging that develops to join separate bands — notice that in Figure 44, which did not exhibit crack bridging, the response is brittle.

In Section 2.2.2, we argued how the existence of an alternate failure mode for large values of α (perhaps 60 degrees or more) could lead to the strength anisotropy exhibited by the gneissic tonalite. The behaviour exhibited by material STAd supports this hypothesis. For large values of α, a set of secondary cracks that are aligned parallel with the loading direction emanate from the bands and bridge between them until a failure mechanism forms across the entire specimen (see Figures 46 and 47). For smaller values of α (but $\alpha>0$), the damage localizes within a single band, and the secondary

cracking is minimal (see Figures 44 and 45). For the special case of $\alpha = 0$, the cracking does not localize within a single band, but rather bridges between bands in the process of forming a diagonally oriented failure plane.

The following facts and hypotheses are based upon the results of a series of runs for which the discrete anisotropy parameters were varied.

1. The stress-strain response can be clearly divided into pre- and post-peak stages. During the pre-peak stage, almost all cracking remains within the band segments, and this cracking is a mixture of both tensile and shear micro-failure modes. The peak is marked by a drastic increase in the rate of tensile cracking, while the rate of shear cracking is unaffected. During the post-peak stage, secondary cracking commences in which tensile cracks form enechelon patterns within the base material, and a mixture of tensile and shear cracking continues to occur within the band segments. In summary, throughout an entire unconfined biaxial test, a mixture of tensile and shear cracks are forming within the band segments, but after the peak, a large number of tensile cracks begin to form within the base material and to coalesce into enechelon patterns that are parallel with the loading direction.

2. We postulate that it is the initiation of this "coalescent" matrix cracking that controls the peak strength. This leads to the following open question. What is the initiation mechanism for such cracking, and how is it affected by the anisotropy parameters (band thickness, spacing, stiffness, strength, etc.)?

3. We have examined the effect of varying the stiffness of the band material by running cases in which the value of E_f was set equal to 0.60, 0.20 and 0.05. Our observations follow.

For a relatively stiff band material, we reproduce the strength anisotropy observed in foliated rocks such as slates. This appears to be the result of intense localization along a single band when the bands are oriented at about 30 degrees; for other angles, the cracking localizes into many bands.

As the band material is softened, the strength increase for $\alpha > 30$ is reduced such that the strength for $\alpha = 90$ is less than the strength for $\alpha = 0$. Also, the post-peak response becomes more plastic — i.e., the tensile cracks form and coalesce within the base material in a stable fashion, in which localizations do not span the entire specimen, and thus, a greater number of these macro-fractures form throughout the specimen. This leads to the following open question. *How does this change in failure mechanism reduce the strength increase for $\alpha > 30$?* A closer comparison of synthetic and laboratory failure patterns may help to answer this question.

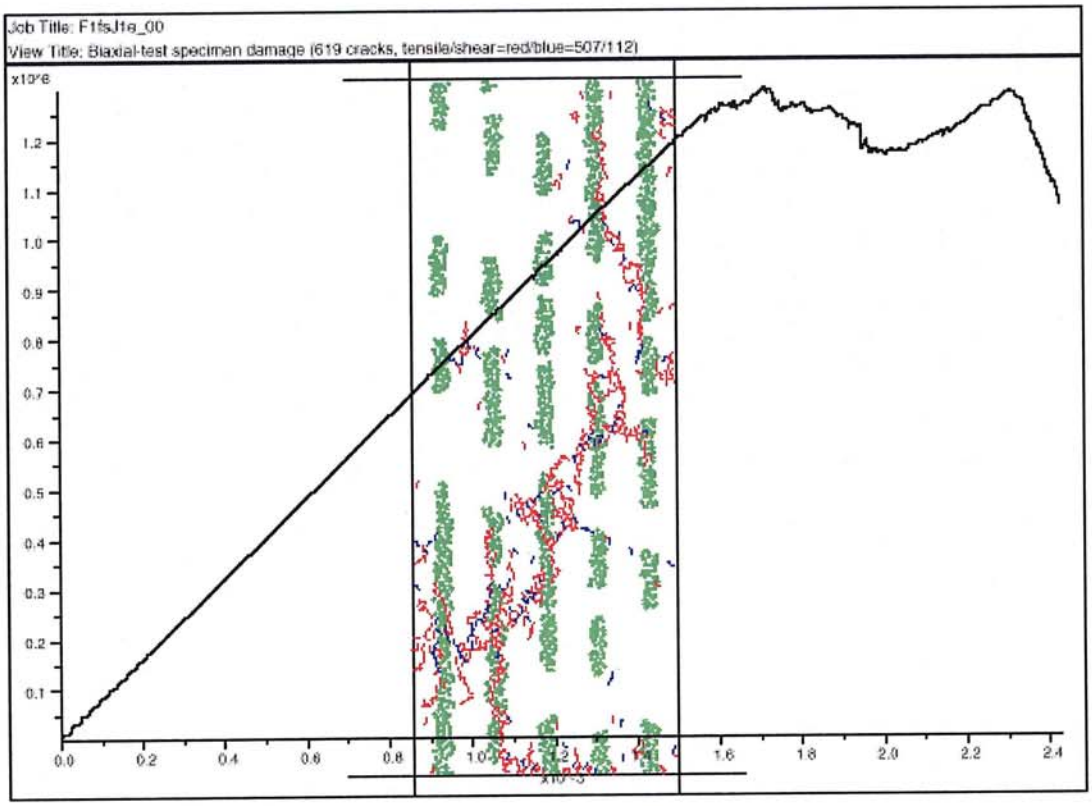

Figure 43. *Post-peak damage in biaxial-test specimen (discrete anisotropic material STAd, band E, α =0).*

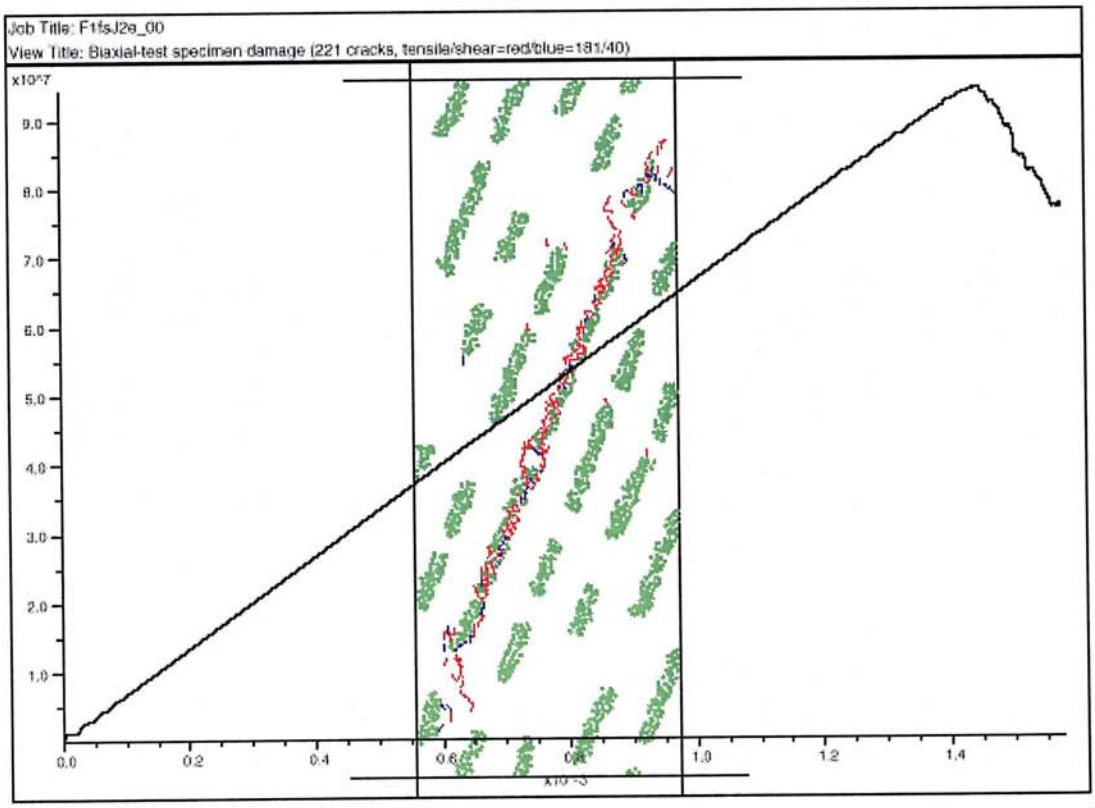

Figure 44. *Post-peak damage in biaxial-test specimen (discrete anisotropic material STAd, band E, α =22.5).*

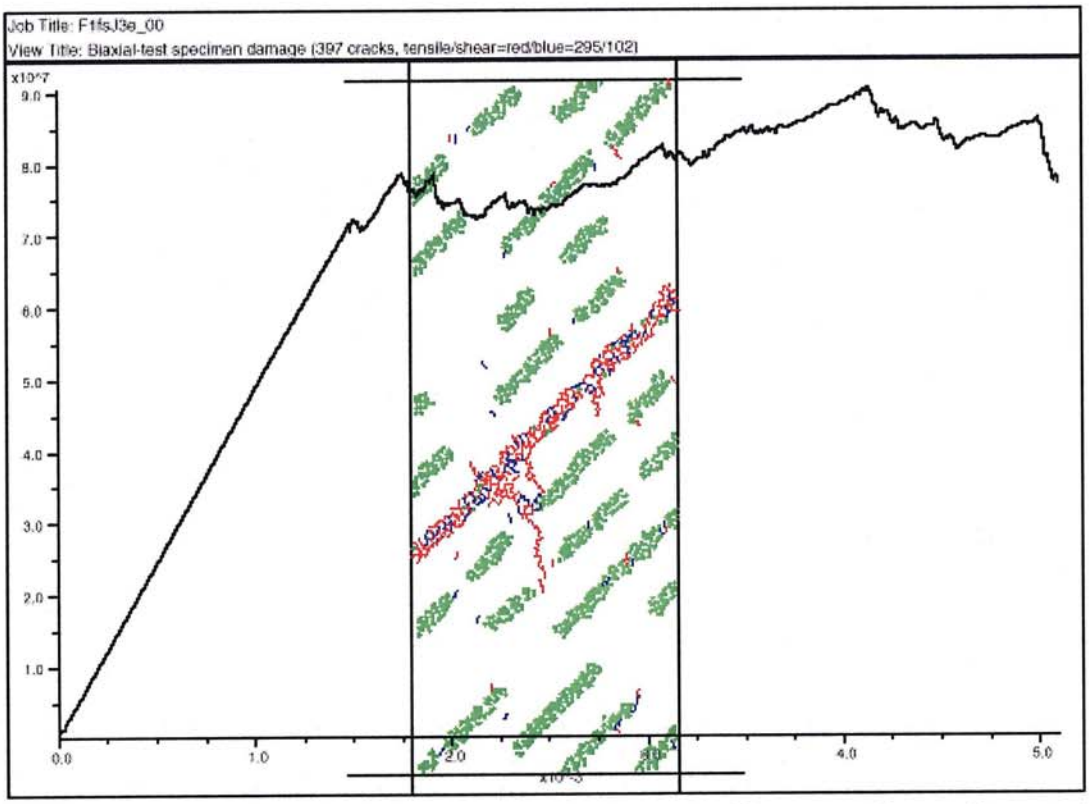

Figure 45. *Post-peak damage in biaxial-test specimen (discrete anisotropic material STAd, band E, α =45).*

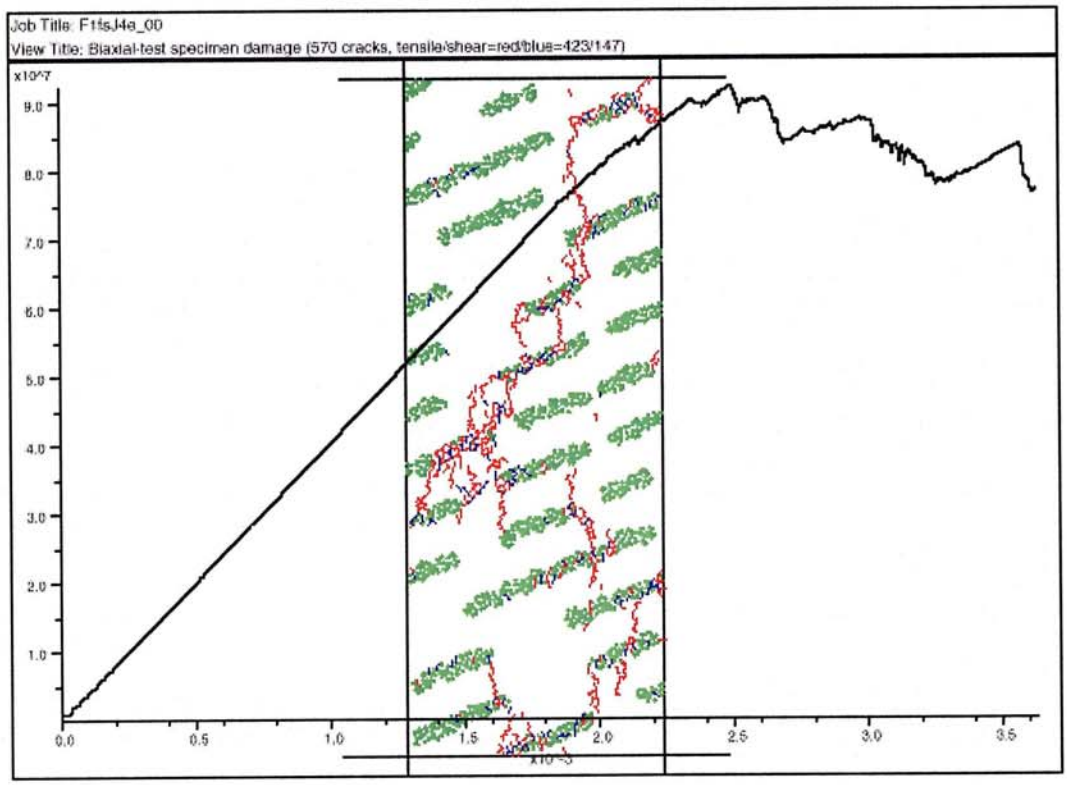

Figure 46. *Post-peak damage in biaxial-test specimen (discrete anisotropic material STAd, band E, α =67.5).*

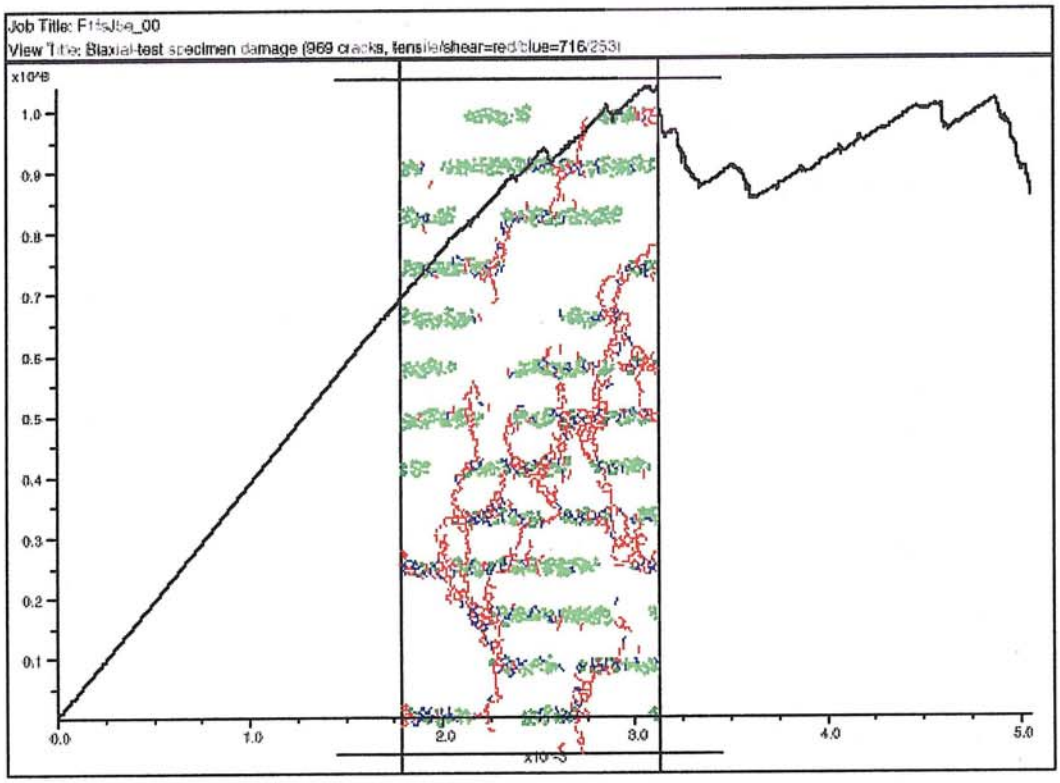

Figure 47. *Post-peak damage in biaxial-test specimen (discrete anisotropic material STAd, band E, α =90).*

3 PREDICTION OF DAMAGE ADJACENT TO THE TEST HOLE

A collection of FISH functions, referred to as a FISH environment, has been developed to support modelling of the test-hole boundary-value problem. The environment allows one to simulate the excavation of both the test hole and the slots, followed by the application of the pressure loading on the slot walls caused by the grout expansion. Throughout the simulation, the model boundaries move so as to approximate the behaviour of an elastic rock mass of infinite extent with specified in-situ stresses. Both coarse- (approximately 13,000 particles) and fine-resolution (approximately 40,000 particles) models have been constructed. Six of the best-fit materials (isotropic: STU, TU, STL, TL; smeared anisotropic: STAs, TAs) have been assigned to these models, and damage predictions for grout pressures of 40, 50, 60, and 70 MPa have been generated.

3.1 TEST-HOLE MODEL DESCRIPTION

3.1.1 Geometry and Boundary Conditions

The PFC ^{2D} cross section is assumed to lie halfway down the test hole at a depth of 250mm from the surface of the deposition hole, and to be oriented perpendicular to the test-hole axis. The PFC ^{2D} xy-axes are oriented such that the x-axis is horizontal, and the y-axis is aligned with the true up-direction of the test-hole. The PFC ^{2D} cross section is assumed to be oriented perpendicular to the schistosity planes (see Figure 4), and these planes are oriented at an angle of 30 degrees counter-clockwise from the positive x-axis.

The PFC ^{2D} model represents the original stress state existing in the rock mass before excavation of the test hole and slots by assuming that the test hole is infinitely long and lies within an infinite elastic rock mass (with elastic constants G =23.2 GPa and ν=0.25) that is subjected to in-situ stresses (Autio, 1999c) of

$$\begin{aligned} \sigma_{xx} &= 9 \text{ MPa} \\ \sigma_{yy} &= 2 \text{ MPa} \\ \sigma_{xy} &= 0.1 \text{ MPa} \end{aligned} \qquad (20)$$

These stresses are assumed to be the actual stresses present in the rock mass at the above location —i.e., they account for the presence of the deposition hole and the research tunnel, which serve to modify the stresses from their true, undisturbed in-situ values.

The geometry and boundary conditions of the test-hole models are shown in Figure 48. The test hole is circular with a radius of 50 mm. Two slots are placed symmetrically above and below the test hole. Each slot is straight and oriented horizontally, with a width of 520 mm, a thickness of 50 mm, and an offset from the test-hole center of 350 mm.

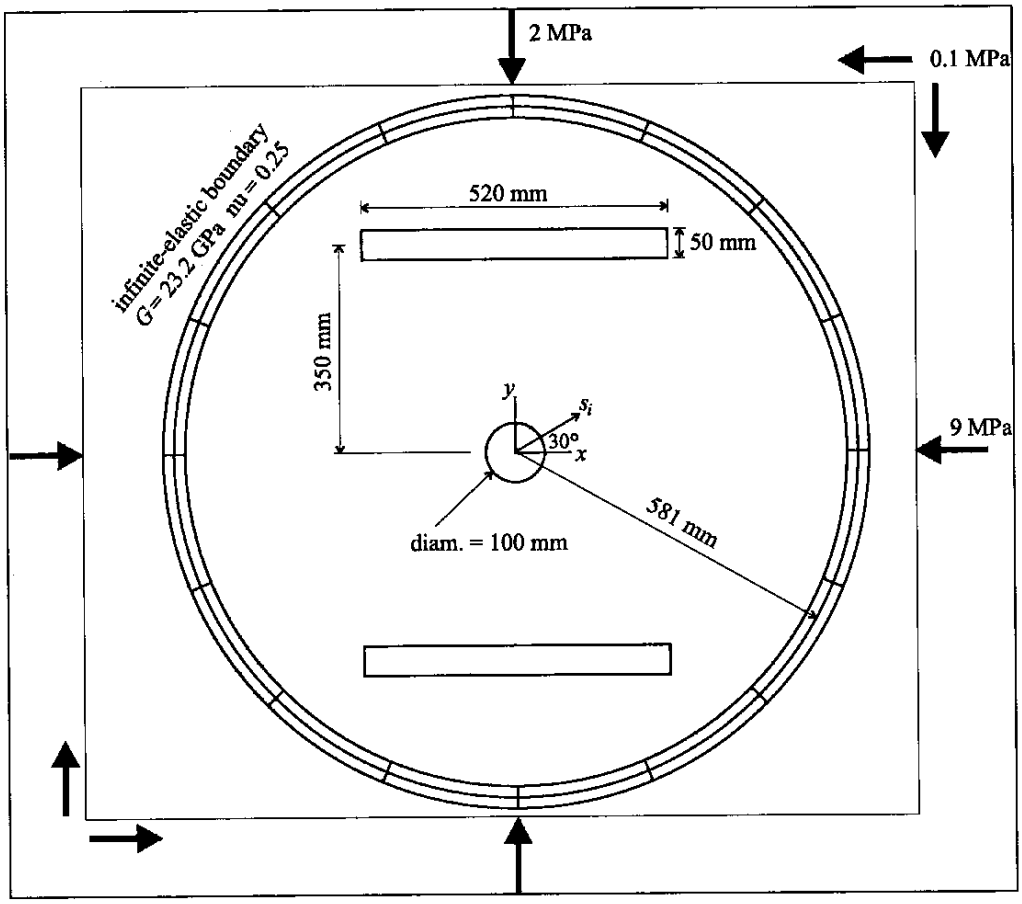

Figure 48. *Geometry and boundary conditions of the test-hole models.*

An infinite-elastic boundary (IEB) algorithm is employed such that only the near-hole region need be included in the model. The IEB operates as a numerical servo-mechanism, controlling the velocities of a thin layer of particles at the model's circular boundary, in order to satisfy the known force-displacement relation existing at the boundary of a circular hole in a homogeneous, isotropic, linear and elastic medium of infinite extent. Use of the IEB assumes that all nonlinear behaviour (in this case, microcracking) remains within the IEB boundary. A description of the IEB algorithm is given in Potyondy et al.(1997). For all test-hole models, the IEB control annulus is comprised of 16 zones with a thickness of 37.5 mm, the IEB gain parameter β is set equal to 1/300, and the displacement field corresponding to the analytical solution is recomputed every step (N_B=1).

3.1.2 Coarse- and Fine-Resolution Models

In a PFC ^{2D} model, damage takes the form of broken bonds, which are considered to represent microcracks that have formed within the rock. The size of each microcrack is equal to the average diameter of the two previously bonded particles (see Figure 5); therefore, the particle size dictates the model resolution —i.e., the smallest increment of damage that can be represented. Because the objective of this work is to predict the damage that will form adjacent to the test hole, the test-hole models consist of a graded assembly of particles with the smallest particles being adjacent to the test hole. The particle grading is achieved by generating a set of annuli (of increasing thickness) about the test hole. Within each annulus, the particle radii form a nearly uniform distribution bounded by R_{min} and R_{max} such that the ratio R_{max}/R_{min} =1.66. The value of R_{min} differs for each annulus, increasing as one moves away from the test hole.

A near-field region of the test-hole model is defined by a circle whose center coincides with the test-hole center, and whose radius is equal to two times the test-hole radius. All particles lying within this circle are considered to be part of the near-field region, while all particles lying outside of this circle are considered to be part of the far-field region. Thus, the near-field region extends a distance of one hole radius into the rock surrounding the test-hole.

The effect of model resolution upon the damage patterns that form within the near-field region is investigated by constructing a coarse- and a fine-resolution model. The coarse and fine models are designated as Fc and Ff, respectively. These two models differ primarily in their resolution in the near-field region; both models have approximately the same particle-size distribution in the far-field region (compare Figures 55 and 56), but the fine model has a greater number of smaller particles in the near-field region than does the coarse model. These differences in resolution are evident in Figures 49 to 52, which depict the particles in the near- and far-field regions for both the coarse and the fine models. The resolution differences are quantified in Figure 53, which lists the number of particles (Nballs) and the average particle size (R_avg) that lie within different annuli (designated as r_in and r_out). The average particle size in the inner 10 mm annulus is 0.73 mm and 0.22 mm for the coarse and fine models, respectively.

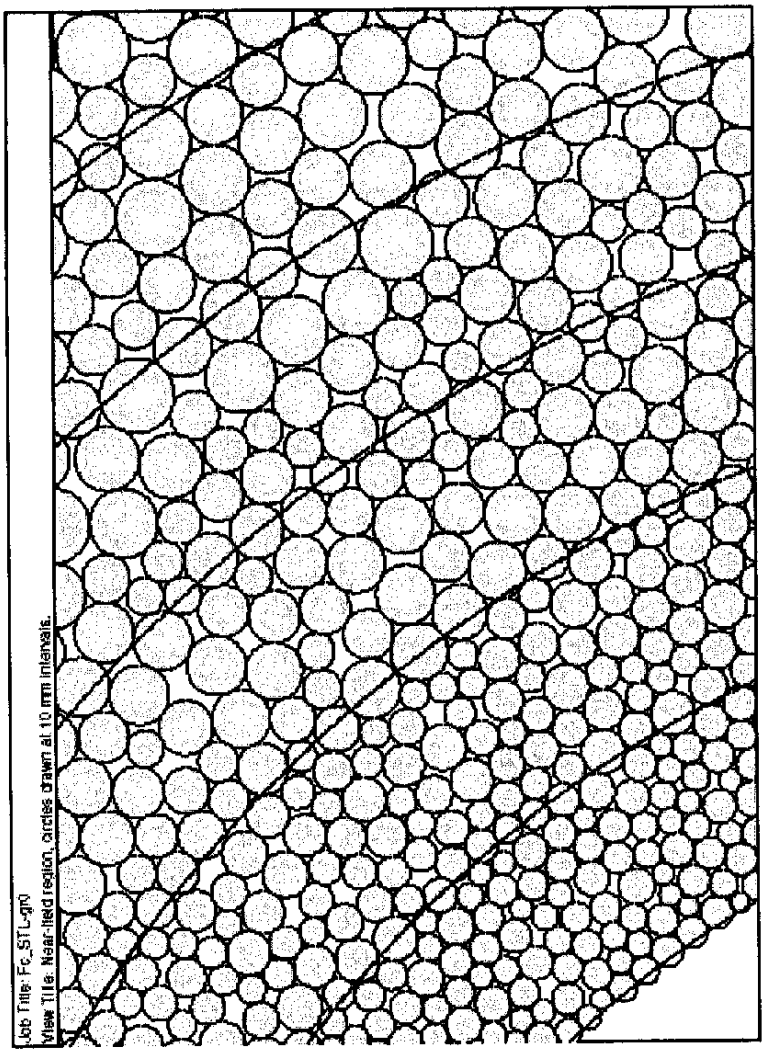

Figure 49. *Particles in near-field region of coarse-resolution test-hole model.*

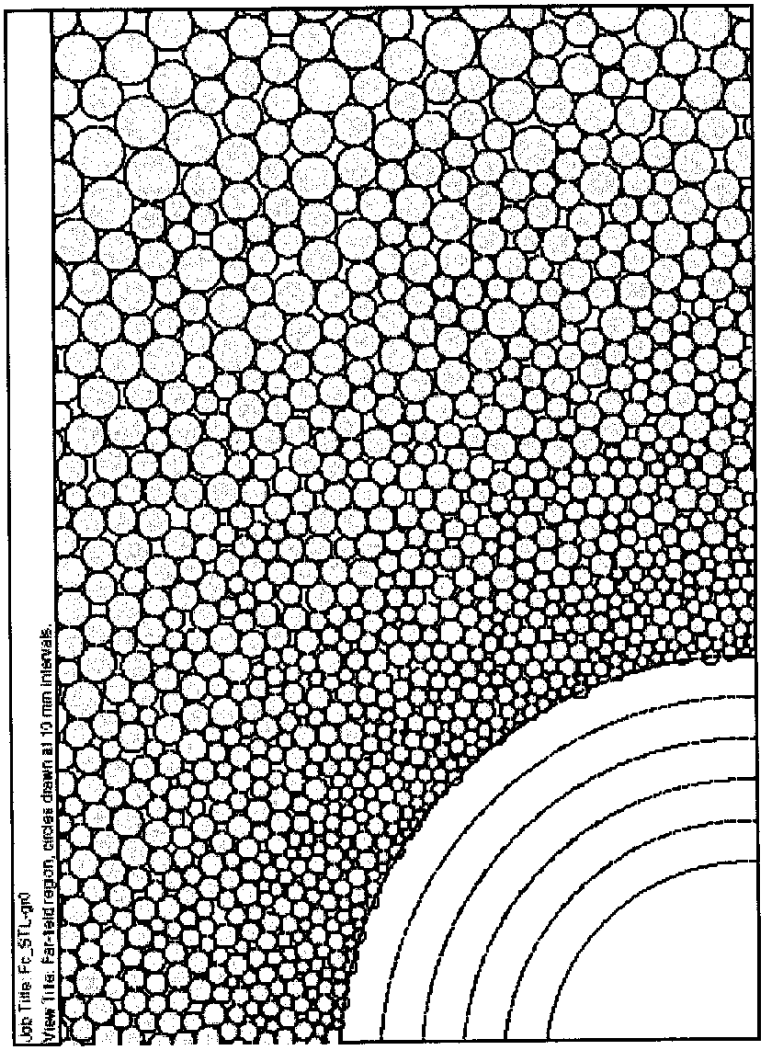

Figure 50. *Particles in far-field region of coarse-resolution test-hole model.*

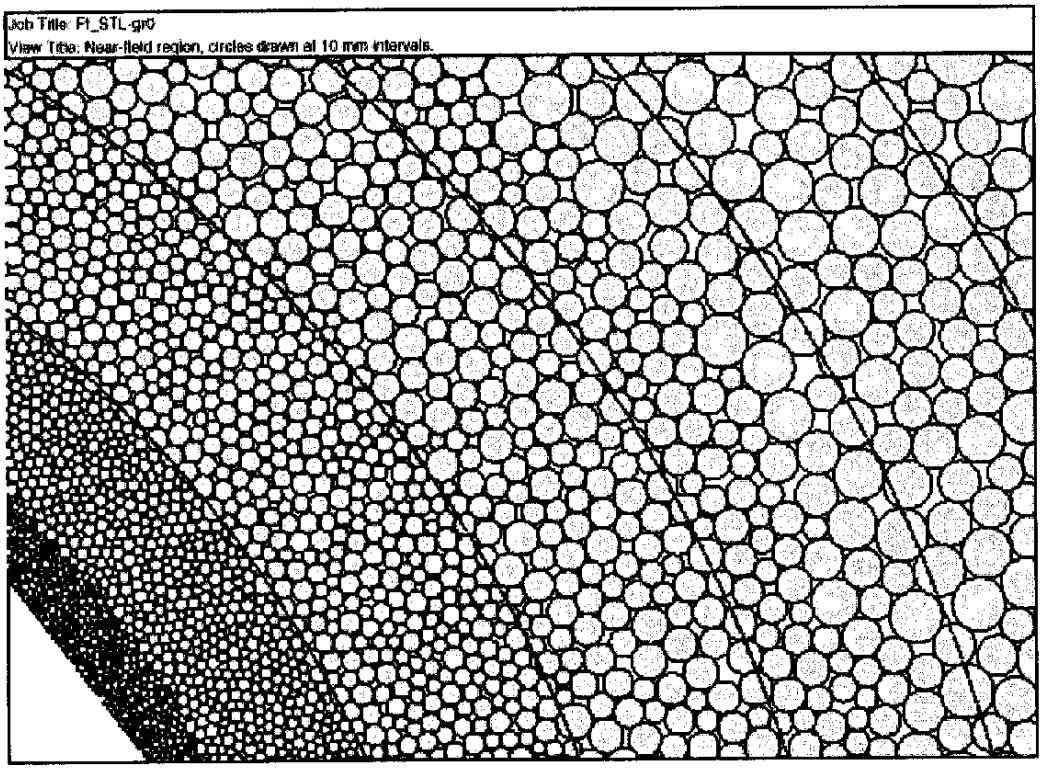

Figure 51. *Particles in near-field region of fine-resolution test-hole model.*

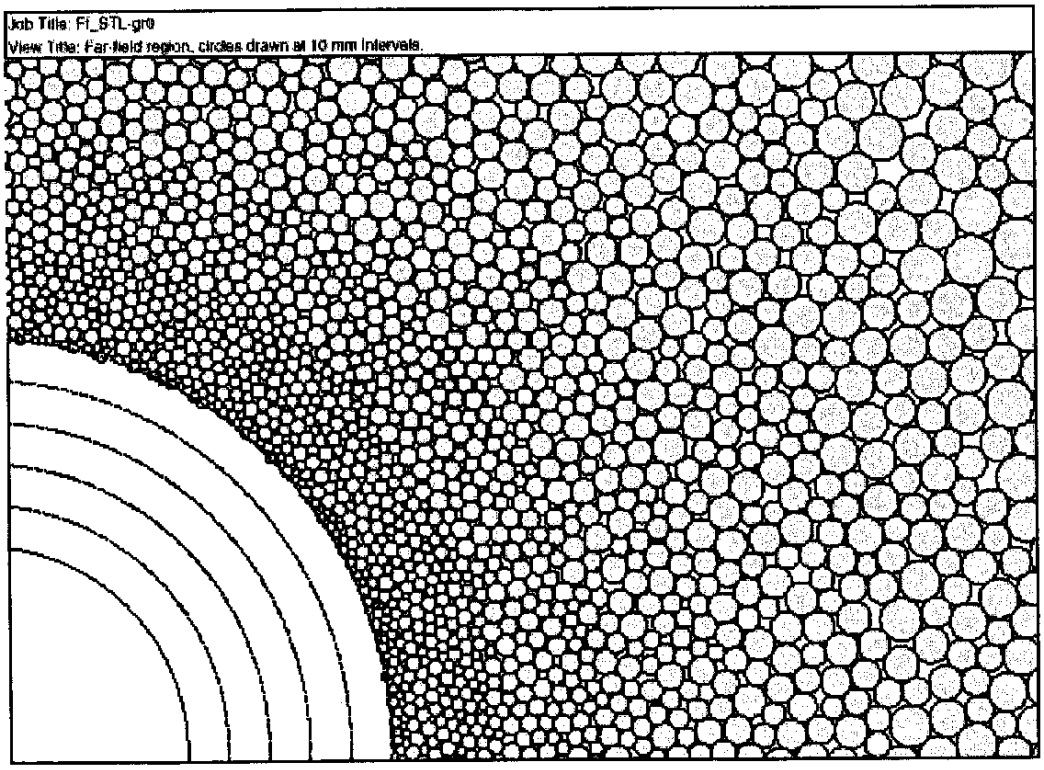

Figure 52. *Particles in far-field region of fine-resolution test-hole model.*

Fc	coarse-resolution model, particle-size distribution				
r_in (mm)	r_out (mm)	R_avg (mm)	Nballs ( )	Nsum ( )	Npercent (%)
0	60	0.73	1716	1716	12.9
60	70	0.94	1201	2917	21.9
70	80	1.18	883	3800	28.6
80	90	1.33	782	4582	34.5
90	100	1.56	639	5221	39.3
100	300	3.27	5434	10655	80.1
300	600	8.70	2640	13295	100.0

Ff	fine-resolution model, particle-size distribution				
r_in (mm)	r_out (mm)	R_avg (mm)	Nballs ( )	Nsum ( )	Npercent (%)
0	60	0.22	18419	18419	46.5
60	70	0.46	5084	23503	59.4
70	80	0.71	2469	25972	65.6
80	90	0.85	1898	27870	70.4
90	100	1.10	1304	29174	73.7
100	300	2.68	7606	36780	92.9
300	600	8.42	2820	39600	100.0

Figure 53. *Particle-size distributions in the test-hole models.*

3.1.3 Modelling Sequence

The modelling sequence mimics the rock genesis followed by test-hole and slot excavation and grout pressurization. It consists of the following five steps.

1. Create the rock mass. A square sample, consisting of a bonded particle assembly with low locked-in stresses, is created using the specimen-genesis procedures described in Section 2.3. During creation of the square sample, a circular hole is kept open by the presence of 24 adjoining wall segments; thus, no particles are generated in the test-hole proper.

2. Install in-situ stresses within the rock mass. All walls are deleted. Then, the in-situ stress state of Eq. (20) is installed throughout the square sample using the stress-installation procedure from Section 3.7 of the FISH in PFC^{2D} volume of Itasca (1999). The iterative procedure operates by moving all particles, fixing the boundary particles (here designated as those lying along the outer four edges of the square sample and those lying along the circular boundary), freeing the interior particles and allowing static-equilibrium conditions to develop. During each iteration, the applied particle displacements are computed from the strain increment that is related by linear elasticity to the stress increment needed to reach the target stress. The iterations continue until the target stress is achieved.

3. Install the IEB servo-mechanism. A circular sample is created by deleting all particles in the square sample that lie outside of the inscribed circle that just fits within the square region. A thin layer of boundary particles, the velocities of which will be controlled by the IEB algorithm, is identified. During this step, the boundary particles surrounding the circular hole are kept fixed.

4. Excavate test hole and both slots. The excavation process is simulated by (a) setting all bond strengths equal to 10,000 times their current values, (b) removing the fixity constraint on the boundary particles surrounding the circular hole and deleting the particles that lie within the slots, (c) allowing the stresses throughout the model to redistribute, (d) restoring all bond strengths to their initial values at the start of excavation and (e) allowing any cracks to form and the stresses to again redistribute. This procedure ensures that the strain energy removed from the system by the excavation process does not produce dynamically induced cracking. Note that the model is forced to behave elastically during this excavation-induced motion, and only after a static-equilibrium condition has been reached are the bonds allowed to fail.

5. Apply grout-induced pressure loading to the slot walls. The grout-induced pressure is assumed to be distributed uniformly over all four straight walls of each slot. The pressure loading is applied to the particle assembly by first defining a grid that surrounds each slot, and then distributing the total force acting on the boundary of each grid cell to all particles within the cell. Each such particle receives an applied external load directed outward from and perpendicular to the boundary.

3.1.4 Typical Model Responses

The typical behaviour of the test-hole models is described here using the coarse-resolution model of material STL with a grout pressure of 40 MPa as the representative case. The behaviour is described for each step of the modelling sequence from Section 3.1.3.

1. Create the rock mass. A square sample with side length of 1.2 m containing a total of 13,979 particles and 27,326 parallel bonds was created. At this stage, the model is densely packed and well-connected — 13 particles have two bonded contacts, and the remaining 13,966 particles have three of more bonded contacts — and has a locked-in isotropic stress of less than 1 MPa.

2. Install in-situ stresses within the rock mass. The uniformity of the stress state throughout the sample is demonstrated by the following stresses (σxx, σyy, σxy) computed by four measurement circles of 275 mm radius placed symmetrically about the test hole in the four quadrants (at 45, 135, 225 and 315 degrees ccw from the x-axis) at a radial distance of 350 mm from the test-hole center. The stresses (in MPa units) are {-8.8, -2.0, 0.03 }, {-8.8, –2.0, 0.03 }, {-9.2, –2.0, 0.14 }, and {-9.1, –1.9, 0.20}. These stresses compare favourably with the target stress state of Eq. (20). Also, no cracks have formed as a result of the installation of the in-situ stresses.

3. Install the IEB servo-mechanism. After trimming the sample into a circular shape, the coarse model contains a total of 13,548 particles. Also, there are a total of 261 particles within the IEB control annulus, which has a thickness of 37.5 mm. The particles lying within the control annulus near the top slot are shown in Figure 55.

4. Excavate test hole and both slots. The dynamic response of the coarse model to excavation is evident in Figure 54, which plots the radial displacements (inward motion is negative) of four particles on the test-hole boundary (at 0, 90, 180 and 270

degrees ccw from the x-axis). There is a horizontal contraction and vertical expansion that arise from the in-situ stresses. Also, no cracks have formed as a result of the excavation.

5. Apply grout-induced pressure loading to the slot walls. The grid used to distribute the pressure loading to the particles adjacent to the top slot is shown in Figures 55 and 56. These figures also depict the IEB control annulus and the particles contained therein. Notice that the coarse and fine models have similar resolution in the far-field region near the slots.

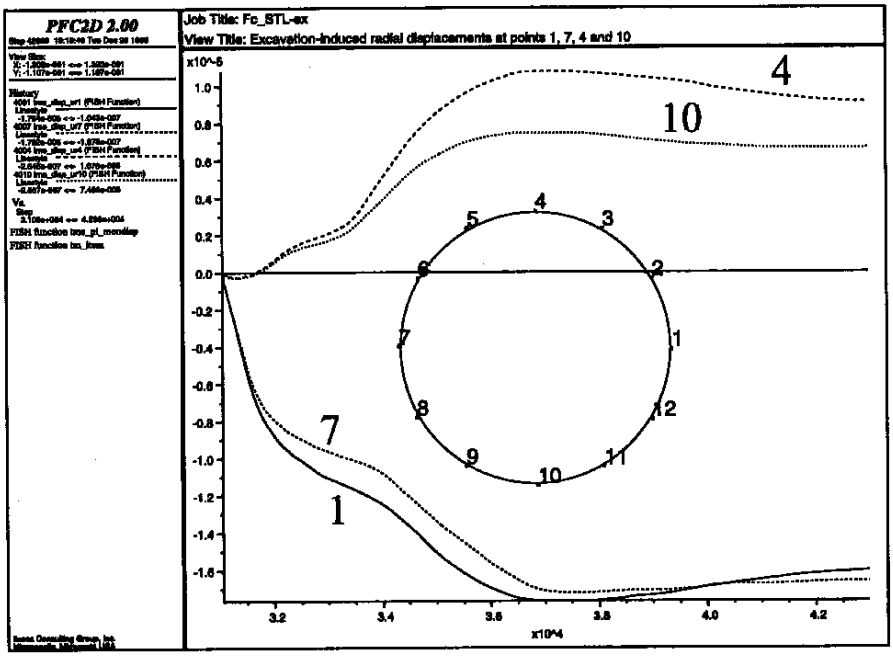

Figure 54. *Excavation-induced radial displacements of test-hole boundary (isotropic lower-bound material STL; coarse).*

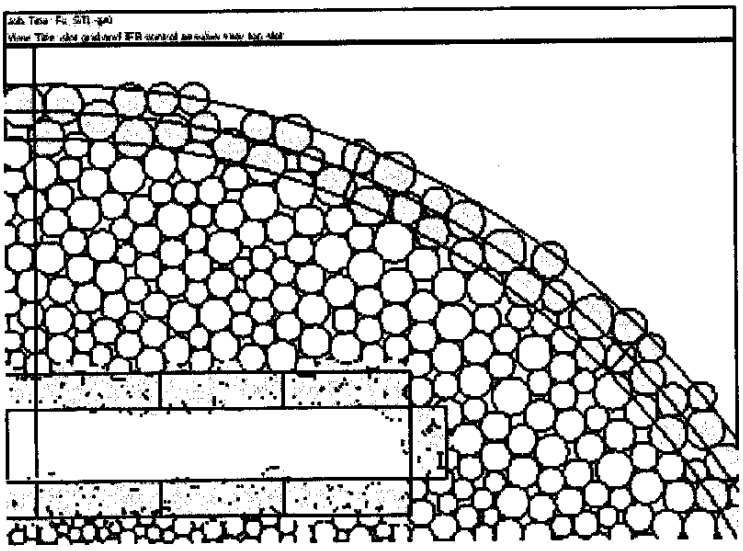

Figure 55. Particles near top slot in coarse model.

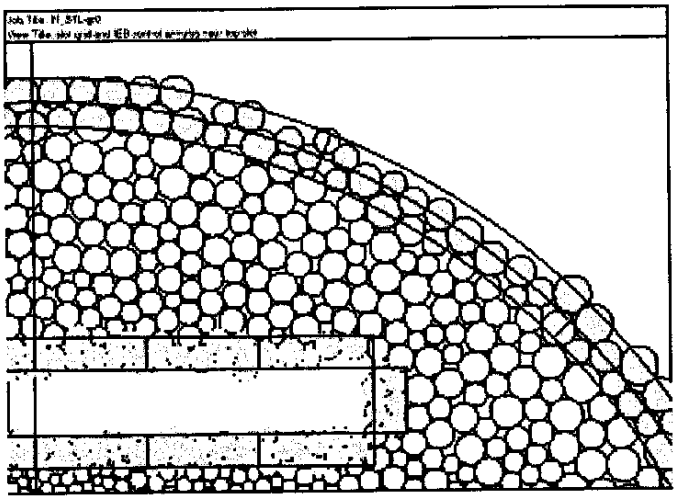

Figure 56. Particles near top slot in fine model.

The dynamic response of the coarse model to slot pressurization is evident in Figure 57, which plots the radial displacements (inward motion is negative) of three particles on the test-hole boundary (at 0, 90 and 270 degrees ccw from the x-axis). There is a horizontal expansion and vertical contraction that arise from the slot pressurization. The radial displacement of the point on the left side of the test-hole boundary is not shown, because damage is beginning to form at this location (see Figure A.9), and the particle being monitored has broken free from the rest of the assembly.

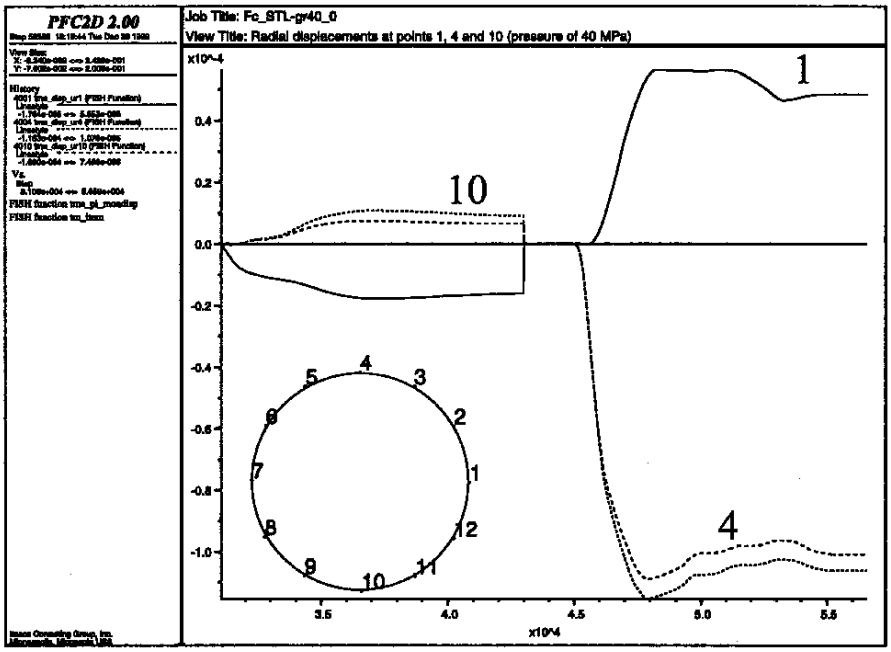

Figure 57. *Pressurization-induced radial displacements of test-hole boundary (isotropic lower-bound material STL; coarse; 40 MPa).*

The slot surface displacements have also stabilized as can be seen in Figure 58, which plots the vertical displacements (expansive motion is positive) of four particles that lie along the x =0 line on the top and bottom surfaces of each slot. The inner surfaces have expanded by 0.22 mm, and the outer surfaces have expanded by 0.36 mm. Such a differential expansion is reasonable, because the symmetry along the y =0 line is similar to an infinite-stiffness boundary, whereas the other boundary is at infinity because of the IEB. Also, stiffness is proportional to AE/L , and the effective L is greater for the outer surfaces.

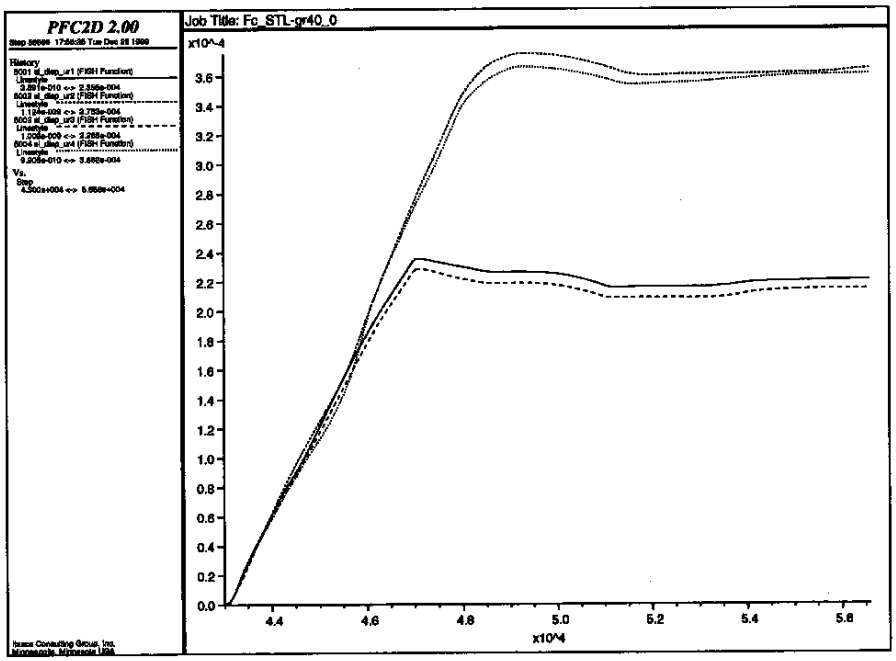

Figure 58. *Pressurization-induced expansive displacements of slot boundaries (isotropic lower-bound material STL; coarse; 40 MPa).*

A total of 65 cracks have formed throughout the entire model, but note that 30 of these cracks are emanating from the slot tips. Damage existing on the right side of the top slot is shown in Figure 59. Note that all of these cracks are the result of micro-tensile failure, and that similar cracking is occurring at all slot tips for pressures greater than or equal to 40 MPa for most of the models examined as part of this study. The far-field damage plots (such as Figure A.15) in Appendix A provide examples of such cracking for a pressure of 70 MPa.

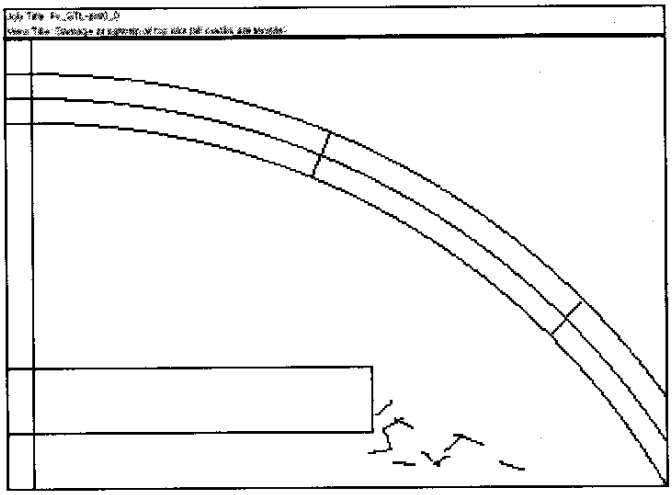

Figure 59. *Damage near top slot (isotropic lower-bound material STL; coarse; 40 MPa).*

The force distribution throughout the coarse model is shown in Figures 60 and 61. The force distribution is depicted in these two plots using the convention described in Appendix A. In Figure 60, we see the compressive zone that forms between the two slots, and the tensile zones that form at each slot tip. In Figure 61, we see how the presence of the test hole creates a compressive zone at each side of the test hole and a tensile zone above and below the test hole. It is these compressive and tensile loads which produce sidewall breakout and radial tensile fractures, respectively.

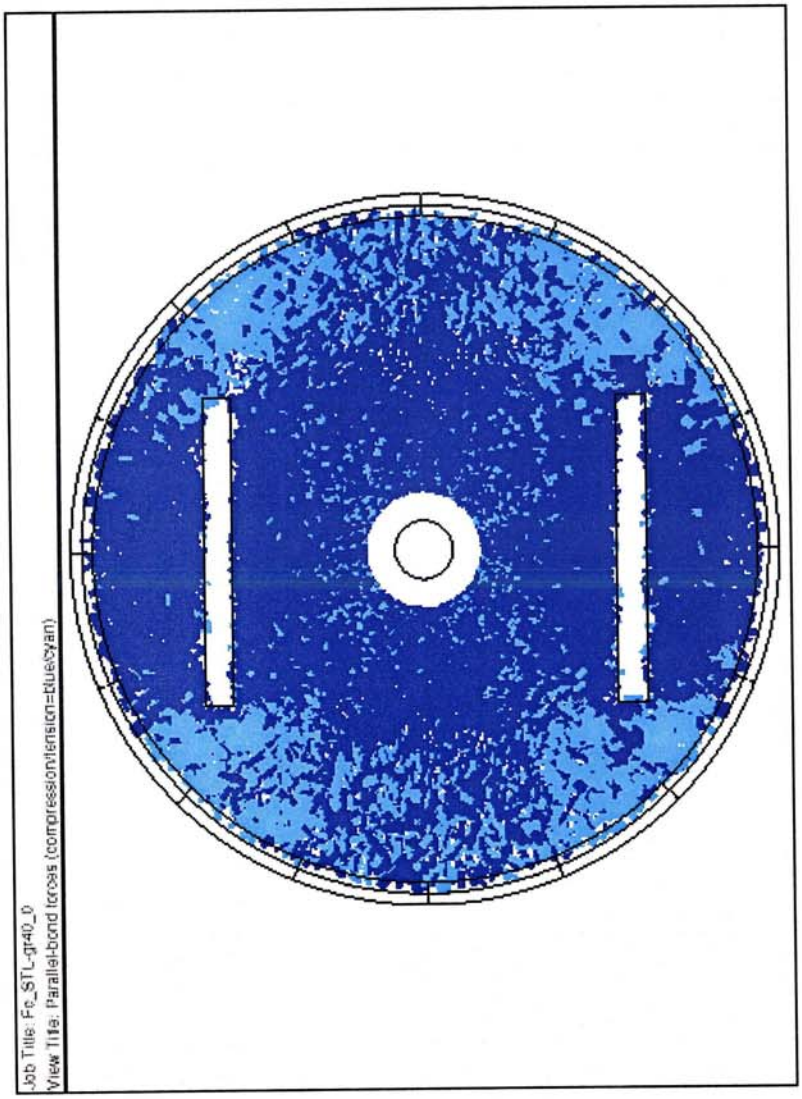

Figure 60. *Force distribution in far-field region (isotropic lower-bound material STL; coarse; 40 MPa).*

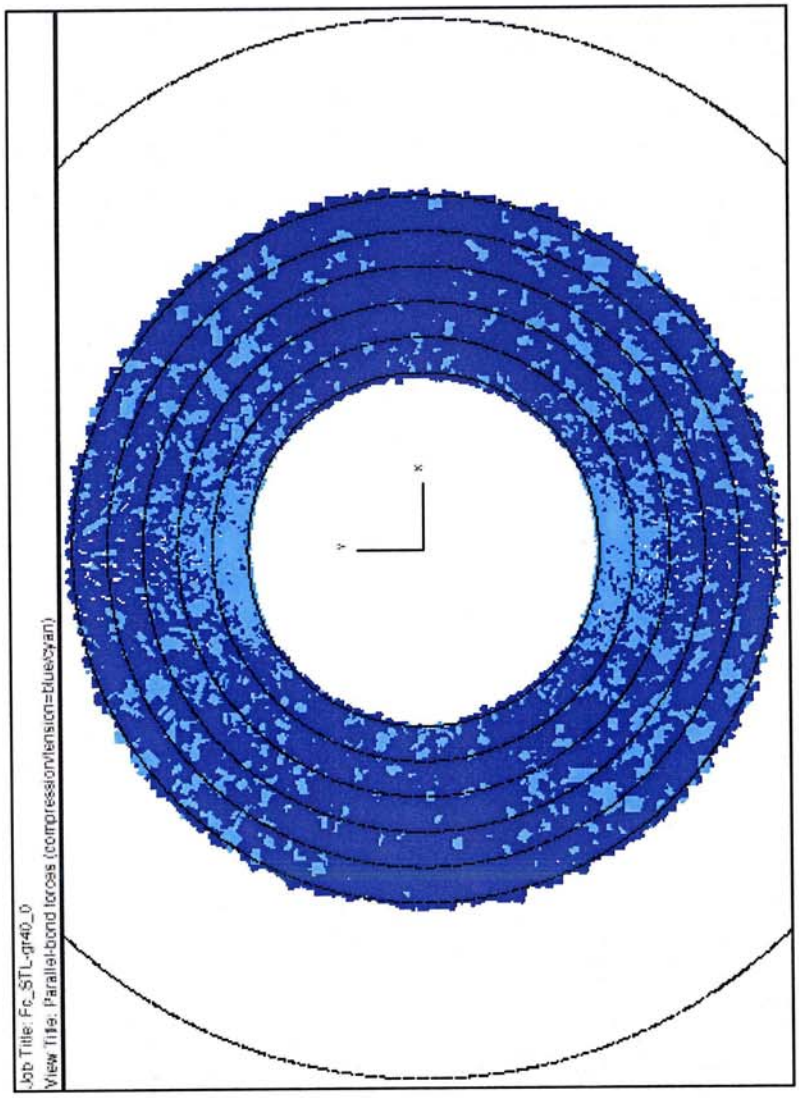

Figure 61. *Force distribution in near-field region (isotropic lower-bound material STL; coarse; 40 MPa).*

3.2 DISCUSSION OF SIMULATION RESULTS FOR TEST-HOLE MODELS

The primary results of the test-hole simulations consist of test-hole damage plots, which depict the damage that has formed adjacent to the test hole. All of these color plots are contained in Appendix A. The naming conventions employed to describe both the plotting representations and the various test-hole models are also described in the Appendix.

Here we discuss the simulation results, making liberal reference to the plots contained in the Appendix. Overall, the results show that significant breakout notches (at the sides of the test hole) exist at a slot pressure of 60 MPa, and that radial tensile fractures (extending from the top and bottom of the test hole) have also formed at this pressure.

This observation applies to the results for the lower-bound isotropic materials and the smeared anisotropic materials, but does not apply to the results for the upper-bound isotropic materials, which developed only minor amounts of damage. The observation is supported by Figures A.11, A.18, A.25, A.32, A.39, A.46 and A.49.

Various aspects of the physical and numerical processes are examined below in detail. Observations are given first, followed by hypotheses (printed in an italic font); thus, objective information is separated from subjective information.

Three types of damage are considered. These are defined as follows.

(a) A "notch" is the triangular region of intense cracking (sometimes bounded by discrete fractures) that emanates from each side of the test hole. It evolves from the microcracks that form parallel with the compressive hoop stress induced at each side of the test hole. The compressive forces generated by the slot pressurization interact with the circular test hole to produce a zone of compression on the lateral faces of the test hole.

(b) A "tensile fracture" is a macroscopic crack that emanates from the top and/or bottom of the test hole and extends radially toward the corresponding slot. Each tensile fracture is comprised of many microcracks that have localized into a single macroscopic crack. It evolves from the microcracks that form perpendicular to the tensile stress induced above and below the test hole. The compressive forces generated by the slot pressurization interact with the circular test hole to produce a zone of tension above and below the test hole.

(c) A "shear band" is the elongated cluster of cracks that emanates from the apex of one or both notches and extends approximately vertically. It evolves from a band or "cloud" of microcracks. The formation of this band seems to be related to a punching-type failure occurring at the top and/or bottom of the test hole, in which the applied load tries to drive an intact rectangular region of material into the unloaded region surrounding the test hole. This unloaded region encompasses the notch tips and results from the presence of the notches, which are much more compliant than the surrounding. In-Situ Failure Test 79 rock and therefore shed load deeper into the rock away from the test hole. The micro-failure mode within the shear band need not be of a shearing type; many tensile microcracks may combine in an enechelon fashion to accommodate the macroscopic shearing motion and thereby produce the shear band.

3.2.1 Effect of Model Resolution

In general, the coarse-resolution models produce both less well-developed, smaller notches and shorter tensile fractures than do the fine-resolution models. This observation is supported by comparing the following three pairs of Figures: (A.11 and A.18), (A.25 and A.32) and (A.39 and A.46).

One explanation for the effect of particle size on the extent of fracturing is that the apparent fracture toughness of a particle assembly is larger for an assembly comprised of larger particles. It can be shown that for a constant micro-tensile strength, fracture

toughness is proportional to the square root of particle radius. Although the concept of fracture toughness is inappropriate for a region of space containing many microcracks, it is relevant when significant force amplification is caused by stresses acting on a macroscopic crack comprised of several adjacent microcracks.

The calibration process did not consider fracture toughness, and no experimental value was provided. Therefore, even if the above explanation involving fracture toughness is valid, there is no way to say, given current knowledge, whether the coarse or the fine model is more realistic.

3.2.2 Effect of Bond-Failure Mechanism

We investigate here the effect of bond-failure mechanism upon damage formation. We compare the different behaviours exhibited by test-hole models that were assigned materials in which only tensile bond failure is allowed and materials in which both shear and tensile bond failure are allowed. The former materials are denoted by T and the latter by ST.

Both the notch region and the tensile fractures for fine-resolution models, of both the T and ST materials, are generally similar (compare Figures A.32 and A.18); however, the notches appear to be less well-developed for the T material in the sense that they do not form sharp, well-defined tips as they do for the ST material. Also, the total number of microcracks in the near-field region is greater for the T material than for the ST material for corresponding pressures. For pressures of 40, 50, 60 and 70 MPa, the T material contains 397, 1690, 3800 and 5547 microcracks while the corresponding ST material contains 375, 1584, 3267 and 5096 microcracks.

One explanation for this lack of well-defined tips in the T material is as follows. Assume that the macroscopic boundary conditions are causing the material to fail in a region shaped as a well-defined, sharp-tipped notch — i.e., the material "wants" to fail into such a shape. The ST material can accommodate this shape much more easily than can the T material, because a string of shear microcracks can form along the notch outline in the ST material. Notice the strings of aligned blue microcracks in Figures A.17 and A.18 that outline the notch, and the lack of such strings in Figures A.31 and A.32. In the T material, the localized shearing deformation along the notch outline must be accommodated by the formation of sets of tensile cracks, which requires that additional deformation occur. But the additional deformation is causing the T material to fail elsewhere within the notch — not along the notch outline. This hypothesis is supported by the fact that for corresponding pressures, the total number of microcracks in the near-field region is greater for the T material than for the ST material.

Shear bands are seen to extend from one notch apex for the T material but not for the ST material (compare Figures A.35 and A.21). Internally, the shear band consists of several enechelon micro-bands.

It is difficult for classical shearing failure to occur in a PFC material because of the "bumpy" nature of potential shearing surfaces — i.e., the apparent friction coefficient is very large. Hence, macroscopic shearing deformation is best accommodated by micro-tensile failure occurring across several sets of enechelon cracks. The micro-tensile

strength of the T material is less than that of the ST material to ensure that both materials possess the same unconfined compressive strength. Thus, the enechelon shear mode of failure will occur more readily in the T material than in the ST material.

3.2.3 Effect of Material Representation

We investigate here the effect of material representation upon damage formation. We compare the different behaviours exhibited by test-hole models that were assigned both upper- and lower-bound isotropic materials (denoted by U and L) and smeared anisotropic materials (denoted by A).

The U materials exhibit minor amounts of damage at a slot pressure of 60 MPa (see Figures A.3 and A.7). Both the notch region and the tensile fractures for fine-resolution models, of both the A and L materials, are generally similar (compare Figures A.18, A.32 and A.46).

We deduce from the similarity of the notch regions produced by the L and A materials that a type of "weakest-link" concept applies. Given that material strength varies with angle of loading, there appears to be freedom for local failure modes to align in the weakest direction, while preserving the overall mechanism (and region) of failure. This is clearly the case within each notch where extensive microcracking occurs, and different patterns of microcracks (arising from different directional strengths) can combine to produce similar end results — i.e., similar notch regions.

If the weakest-link concept is correct, then the L materials are much closer to reality than the U materials for the following reason. The notch size and shape is governed by the strengths in the weakest directions, and these low strengths are matched only by a lower-bound isotropic material; the upper-bound isotropic material is simply too strong. Also, there is little point in trying to refine the representation of anisotropy, because the notch regions formed by any anisotropic material will resemble those of a lower-bound isotropic material. However, the detailed microcrack pattern within each notch will differ for the two materials. We expect that a properly formulated and calibrated anisotropic material would exhibit detailed microcrack patterns that better resemble the actual patterns that occur in the physical rock.

It is not possible to make a good comparison of shear-band formation, because such bands do not form until the pressure reaches 70 MPa (see Figures A.21 and A.35 and the discussion in Section 3.2.2), and results are not available for the fine-resolution model of material A at a pressure of 70 MPa. Shear bands have not formed in any of the fine-resolution models when the pressure is 60 MPa. However, the coarse-resolution material A at 70 MPa pressure exhibits shear-band failure that is much more extensive than that of the corresponding coarse-resolution material L (compare Figures A.52 and A.28).

The reason for this greater amount of shear-band failure in the anisotropic material is not clear. The effect may not be of any consequence in the current study, given that failure in the fine models occurs at lower loads.

3.2.4 Time Evolution of Cracking

The time evolution of the crack development up to a slot pressure of 50 MPa for the fine-resolution test-hole model that has been assigned the lower-bound isotropic material STLis shown in Figures 62 to 64. In these three plots, the cracks are drawn in 16 shades of grey such that those that formed early are drawn in light colors, while those that formed late are drawn in darker colors. (Note that the fully white cracks correspond with the state of damage when the pressure was equal to 40 MPa.) One can correlate the relative developmental stages of the tensile fractures and the notches (see Figure 62), and the respective notches (see Figure 63). The tensile fractures form at about the same time as the notches are developing, and the shear bands form well after the notches have developed. Also, the progressive nature of the cracking process that produces the right notch is shown in Figure 64.

As the notch grows and becomes more compliant, it sheds load deeper into the rock, which in turn triggers further notch development via the formation of fractures that run almost parallel with the test-hole surface and eventually intersect the surface producing slab-like pieces.

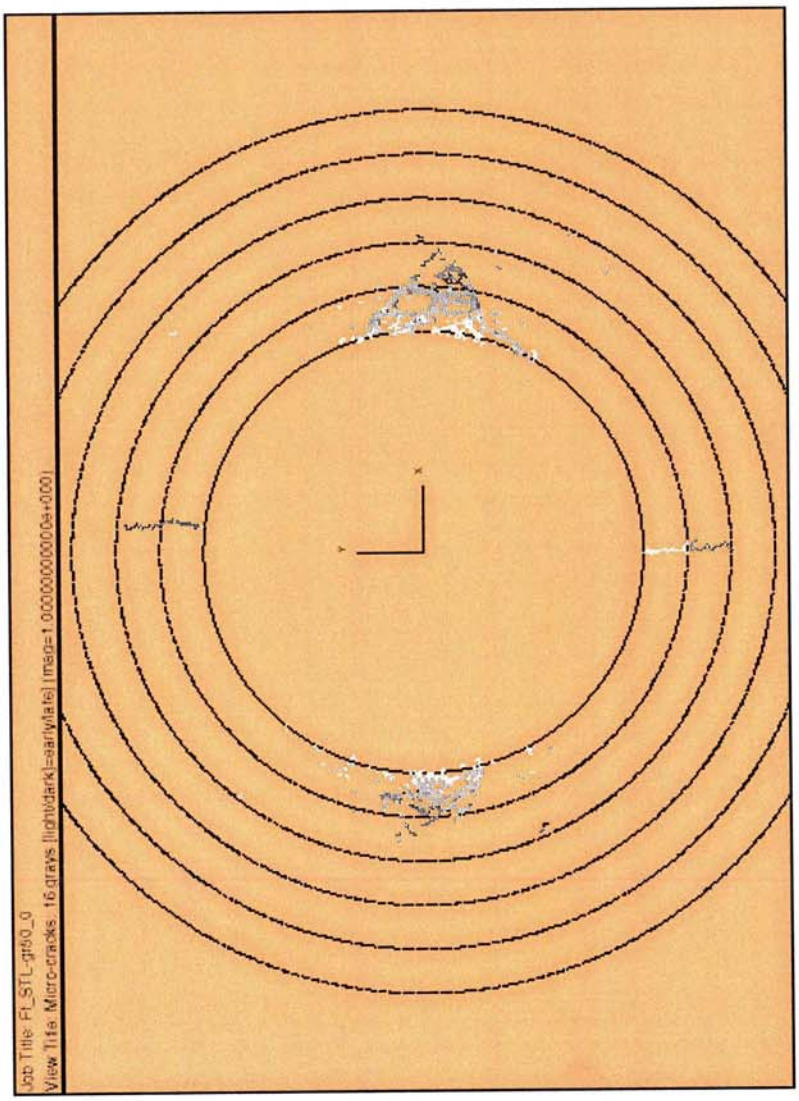

Figure 62. *Time evolution of cracking in near-field region (isotropic lower-bound material STL; fine; 50 MPa).*

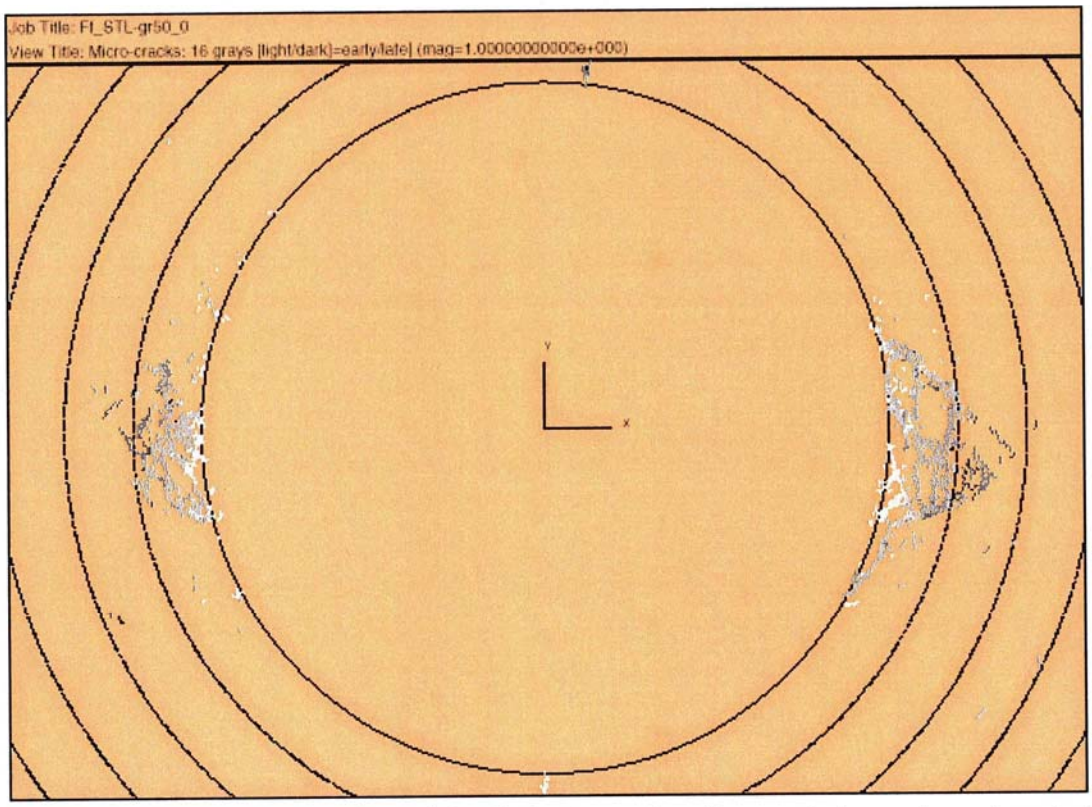

Figure 63. *Time evolution of cracking in both notches (isotropic lower-bound material STL; fine; 50 MPa).*

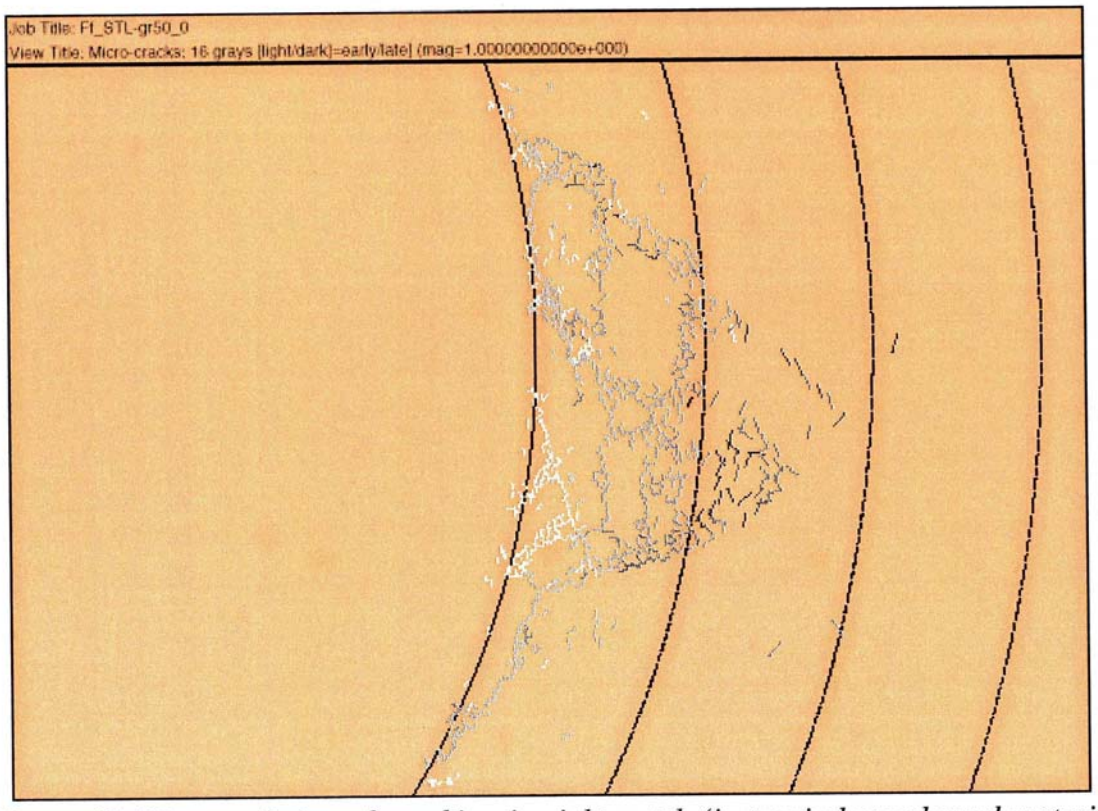

Figure 64. *Time evolution of cracking in right notch (isotropic lower-bound material STL; fine; 50 MPa).*

3.3 CONCLUSIONS REGARDING DAMAGE FORMATION

Our best guess as to the extent and type of damage that will exist when the slot pressures have reached 60 MPa is provided by the fine-resolution test-hole model that has been assigned the lower-bound isotropic material STL. The damage plot is given in the Appendix as Figure A.18.

We expect that well-developed lateral notches and vertical tensile fractures will exist when the slot pressures have reached 60 MPa. Material in the notches will be essentially unloaded (see Figures 65 to 67 — the plotting conventions are described in Appendix A), and may or may not fall out, depending on minor experimental details. Localized cracking will also be observed at the ends of the slots. In addition to the notches and tensile fractures, "shear bands" may extend vertically from one or both of the notch tips; however, the presence (or absence) of shear bands depends on details of the micromechanics that are unknown.

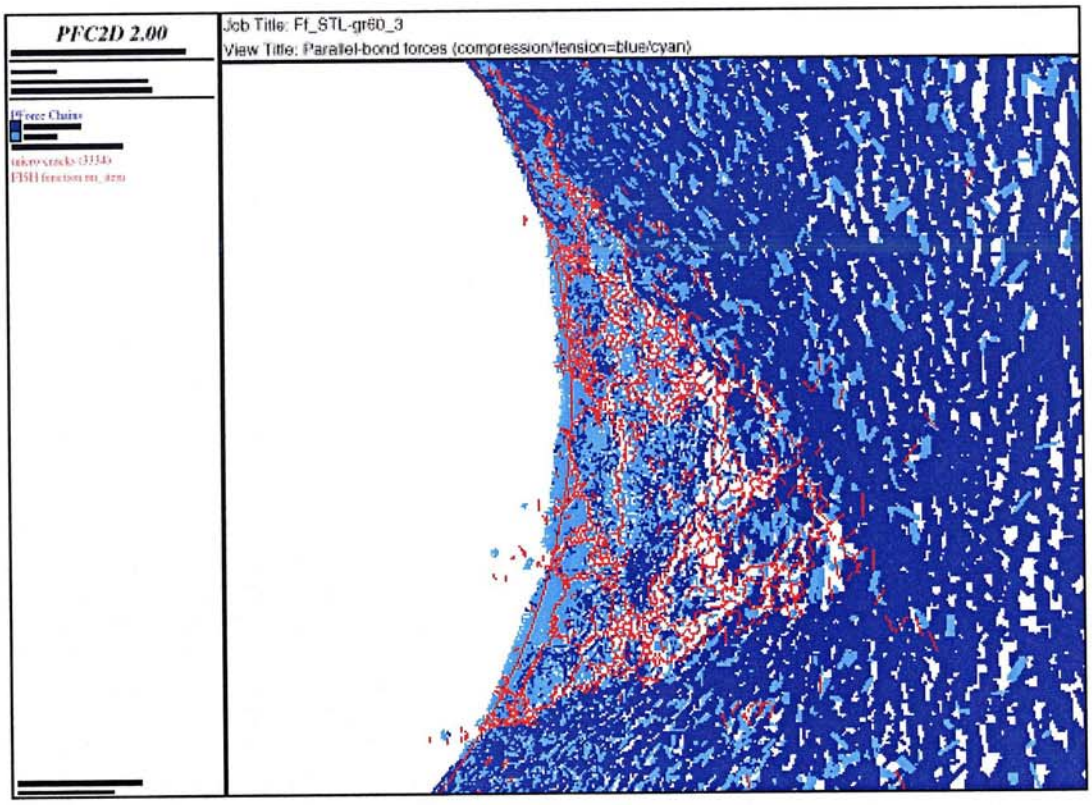

Figure 65. *Force distribution (pbonds) near right notch and all cracks (isotropic lower-bound material STL; fine; 60 MPa).*

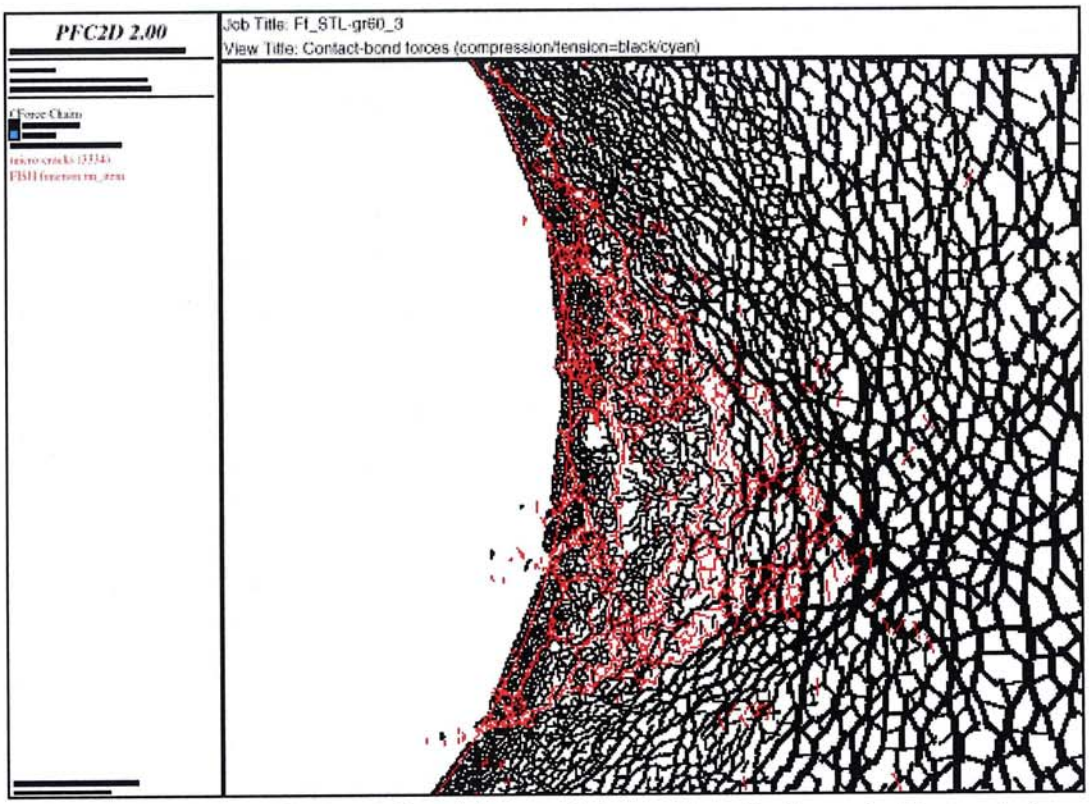

Figure 66. *Force distribution (cbonds) near right notch and all cracks (isotropic lower-bound material STL; fine; 60 MPa).*

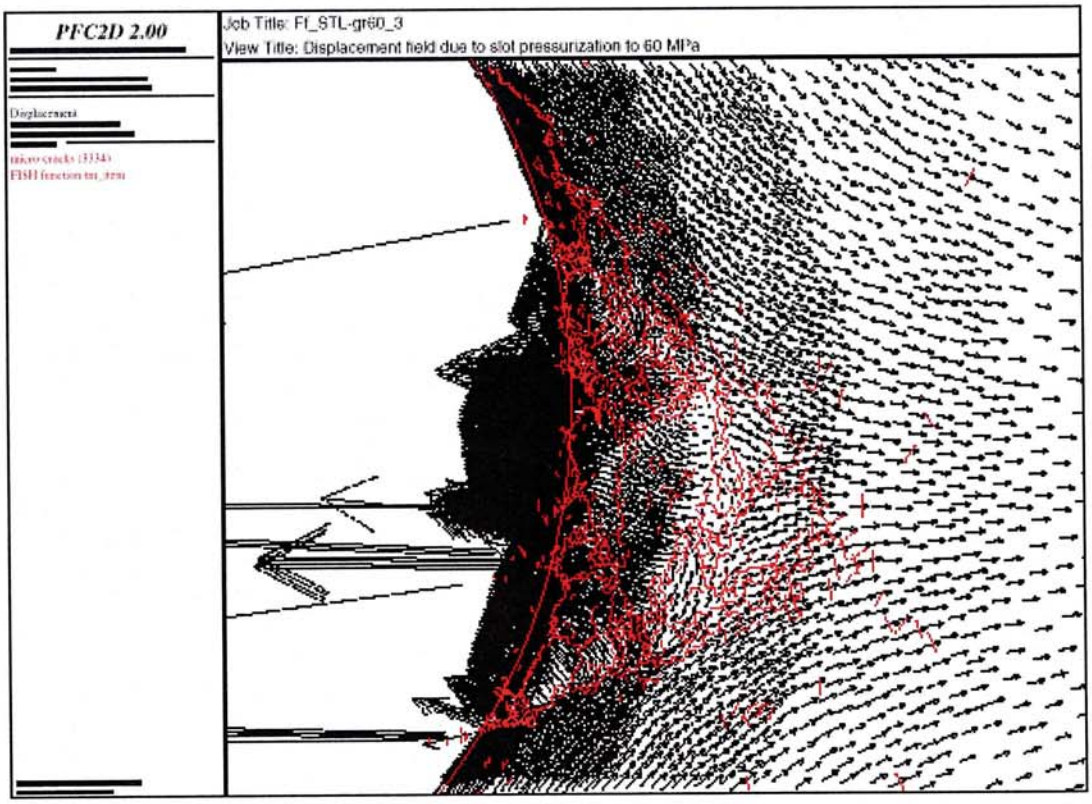

Figure 67. *Displacement field (induced by slot pressurization) near right notch and all cracks (isotropic lower-bound material STL; fine; 60 MPa).*

4 OVERALL CONCLUSIONS

The results of this work demonstrate that plausible predictions of excavation-induced damage formation can be made by employing the PFC ^{2D} Model for Rock. The predictions provide information about the detailed distribution of microcracks, including microcrack intensity, location and orientation as well as the time evolution of such damage. The failure mechanisms exhibited by the PFC ^{2D} model include the formation of notches (in compressive regions) and tensile fractures (in tensile regions) adjacent to the excavation. Our best guess as to the extent and type of damage that will exist when the slot pressures have reached 60 MPa is provided by the fine-resolution test-hole model that has been assigned the lower-bound isotropic material STL.

The accuracy of such damage predictions hinges upon how closely the synthetic material reproduces the physical mechanisms that drive the failure processes. At present, we lack a clear understanding of the details of these physical mechanisms and, thus, are forced to construct PFC ^{2D} materials that reproduce our best hypotheses of the relevant mechanisms. We also lack a clear understanding of what constitutes the relevant set of laboratory-scale properties to which the PFC ^{2D} material must be calibrated. At present, well-documented procedures exist to calibrate a PFC ^{2D} material to match elastic modulus, crack-initiation stress and unconfined compressive strength; additional procedures have been developed as part of this work to match the observed anisotropy in modulus and strength exhibited by gneissic tonalite. However, our current understanding of the calibration process is still incomplete — i.e., we still do not know how to construct a PFC material that reproduces a given strength envelope or one that reproduces a given ratio of unconfined compressive strength to Brazilian tensile strength. It is not clear how the strength envelope and Brazilian tensile strength of the synthetic material influence the damage that forms adjacent to an excavation; however, we can speculate that the tensile fractures that formed in the present simulations may have occurred at a larger loading than they will in the real rock, because the Brazilian tensile strengths of our synthetic material are approximately three times larger than those of the gneissic tonalite (Autio, 2000).

Further development of the PFC ^{2D} Model for Rock will require detailed comparison of model damage predictions with laboratory and field observations. As part of the current project, it is expected that after the physical test has been completed, the microcracking and failure patterns adjacent to the test hole will be studied in detail (by impregnating the rock with resin and studying overcored sections) and compared to the simulation results. This comparison may help us to determine what constitutes the relevant set of laboratory-scale properties to which the PFC ^{2D} material must be calibrated. In cases where large, discrete fractures develop, it would be beneficial to extend the calibration to include matching the fracture toughness. Matching the strength envelope (the increase in strength with confinement) would also increase our confidence in the PFC ^{2D} damage predictions because of the known sensitivity of rock strength to confinement.

All further development should be guided by focusing on exactly what one wishes to predict with the model, and then determining what are the set of laboratory-scale properties that influence the failure mechanisms occurring in the physical rock that are most relevant to making such predictions. The PFC ^{2D} Model for Rock is, at best, an analogue system, and it is unlikely that it can ever be made to reproduce all rock properties; therefore, the selection of the relevant properties must guide all predictive efforts.

The following caveats should be kept in mind when comparing the damage predictions with the damage formed during the physical test.

1. All simulations performed as part of this study were two-dimensional; thus, the damage patterns produced by the PFC ^{2D} models are assumed to be what would occur on a planar slice perpendicular to the test hole and away from the test-hole surface. The real deformation field is three-dimensional, and the failure observed at the test-hole surface may differ considerably from what occurs further into the rock. It is by no means clear that plane-strain conditions will develop half-way down the test hole (at only five test-hole radii into the rock mass), and it is possible that such three-dimensional effects may produce a different damage pattern. Our successful experience at predicting excavation-induced damage surrounding the excavations at the Canadian URL does not guarantee the fidelity of the present predictions, because the URL excavations were long relative to their effective radii; thus, plane-strain conditions probably developed in these excavations.

2. In the test-hole models, we are not representing the exact nature of the grout loading. We have modelled the slots as straight and have assumed that the grout produces a uniform loading upon the slot surfaces. In the actual test, the slots will be curved and will consist of a row of nine 40 mm diameter holes spaced 26 mm apart (Autio, 1999c). This more complex loading condition was not modelled, because the stiffness of the bridging material between the holes will affect the response, and the test-hole models would require significant refinement in the slot regions to capture this effect. We have assumed that straight slots will produce an equivalent loading upon the test hole, although the exact nature of this equivalence is unknown. Also, we anticipate that cracks will form in the bridging material between the nine holes, thus affecting the stress distribution in a way that will be difficult to determine.*

* * Autio (2000) adds the following information. "We modeled the difference between the two types of slots (open slot and row of holes) and found that the stress field around the test hole is almost identical in both cases when the expanding pressure is adjusted accordingly. We also found in the field test that the bridging between the holes takes place at low stress levels. Therefore the slot type does not affect the stress distribution.".

REFERENCES

Autio, J., E. Johansson, T. Kirkkomäki, M. Hakala and E. Heikkilä (1999a) "In Situ Failure Test in the Research Tunnel at Olkiluoto," Saanio & Riekkola, Consulting Engineers, Working Report Version 29.04.1999 to Posiva Oy, Helsinki, Finland, April.

Autio, J., E. Johansson and P. Somervuori (1999b) "Modelling of an In-Situ Failure Test in the Research Tunnel at Olkiluoto," Saanio & Riekkola, Consulting Engineers, Working Report Version 21.01.1999 to Posiva Oy, Helsinki, Finland.

Autio, J. (1999c) Personal communication of 20 October 1999.

Autio, J. (2000) Personal communication of 29 February 2000.

Bates, R. L., and J. A. Jackson. (1984) Dictionary of Geological Terms, Third Edition. New York: Doubleday Dell Publishing Group.

Cundall, P. A., D. O. Potyondy and C. A. Lee (1996) "Micromechanics-Based Models for Frac-ture and Breakout Around the Mine-By Tunnel," in Proceedings of the Excavation Disturbed Zone Workshop, Designing the Excavation Disturbed Zone for a Nuclear Repository in Hard Rock. 1996 Canadian Nuclear Society International Conference on Deep Geological Disposal of Radioactive Waste, Winnipeg, Canada, September 1996, pp. 113–122. J. B. Martino and C. D. Martin, Eds. Toronto: Canadian Nuclear Society.

Cundall, P., and D. Potyondy (1999) "The PFC Model for Rock — Phase A: Fundamental Investigations," Itasca Consulting Group, Inc., Accepted proposal to Atomic Energy of Canada Limited (AECL), May.

Everitt, R. A., P. Gann and D. M. Boychuk (1993) "Mine-by Experiment Data Summary: Part 7 —Geological Setting and General Geology," Atomic Energy of Canada Limited, Report RC-1080, COG-93-251.

Goodman, R. E. (1980) Introduction to Rock Mechanics. New York: John Wiley & Sons.

Haimson, B. C., and I. Song (1993) "Laboratory Study of Borehole Breakouts in Cordova Cream: a Case of Shear Failure Mechanism," Int. J. Rock Mech. Min. Sci. & Geomech. Abstr., 30(7), 1047–1056.

Itasca Consulting Group, Inc. (1997) FLAC ^{3D} (Fast Lagrangian Analysis of Continua in 3 Dimensions), Version 2.0. Minneapolis, Minnesota: ICG.

Itasca Consulting Group, Inc. (1999) PFC ^{2D} (Particle Flow Code in 2 Dimensions), Version 2.0. Minneapolis, Minnesota: ICG.

Jaeger, J. C., and N.G.W. Cook. (1979) Fundamentals of Rock Mechanics, Third Edition. London: Chapman and Hall Limited.

Potyondy, D. O., P. A. Cundall and C. Lee (1996) "Modeling Rock Using Bonded Assemblies of Circular Particles," in Rock Mechanics Tools and Techniques (Proceedings of Second North.In-Situ Failure Test 92 American Rock Mechanics Symposium —NARMS'96, Montréal, Canada, June 1996), pp. 1937– 1944. M. Aubertin, F. Hassani and H. Mitri, Eds. Rotterdam: A. A. Balkema.

Potyondy, D. O., P. A. Cundall and B. Damjanac (1997) "Modeling of Notch Formation in the URL Mine-By Tunnel: Phase III—Damage Mechanisms Leading to Notch Formation," Itasca Consulting Group, Inc., Report to Atomic Energy of Canada Limited (AECL), December.

Potyondy, D. O. and P. A. Cundall (1998) "Modeling Notch-Formation Mechanisms in the URL Mine-By Test Tunnel Using Bonded Assemblies of Circular Particles," Int. J. Rock Mech. & Min. Sci., Special Issue (Proceedings of Third North American Rock Mechanics Symposium — NARMS'98, Cancun, Mexico, June/July 1998), 35(4–5), Paper No. 067.

Potyondy, D. O., and P. A. Cundall (1999) "Modeling of Notch Formation in the URL Mine-By Tunnel: Phase IV—Enhancements to the PFC Model of Rock," Itasca Consulting Group, Inc., Report to Atomic Energy of Canada Limited (AECL), March. Issued as Ontario Hydro Nuclear Waste Management Division Report No. 06819-REP-01200-10002-R00.

Potyondy, D. O., and C. E. Fairhurst (1999) "The Value of Numerical Modeling in Understanding the Complete Load/Deformation Behaviour of Cohesive-Frictional Materials," in Nondestructive and Automated Testing for Soil and Rock Properties, ASTM STP 1350, pp. 290–299. W. A. Marr and C. E. Fairhurst, Eds. West Conshohocken, Pennsylvania: American Society for Testing and Materials.

Read, R. S., and C. D. Martin (1996) "Technical Summary of AECL's Mine-by Experiment, Phase 1: Excavation Response," Atomic Energy of Canada Limited, (Whiteshell Laboratories, Pinawa, Manitoba R0E 1L0), Report AECL-11311, COG-95-171, February.

APPENDIX A: TEST-HOLE DAMAGE PLOTS

The results of the test-hole simulations are presented here in the form of test-hole damage plots. These plots provide information about the intensity, location and orientation of the microcracks (and possible coalescence into macro-fractures) that have formed in the various test-hole models for grout pressures of 40, 50, 60 and 70 MPa. The results are discussed in Section 3.2.

A.1 Plotting Conventions

The crack distribution, force distribution and particle-displacement field are depicted in all color plots using the following conventions.

- The crack distribution is depicted as bi-colored lines (in which red represents tension-induced parallel-bond failure for which bond normal strength has been exceeded and blue represents shear-induced parallel-bond failure for which bond shear strength has been exceeded) lying between the two previously bonded particles with a radius equal to the average radius of the two previously bonded particles. The cracks are oriented perpendicular to the line joining the centers of the two previously bonded particles. In some plots, when the failure mode is not being emphasized, all cracks are drawn in red. Also, the total number of cracks is listed in the view title of most color plots.

- The force distribution is depicted by drawing each parallel-bond force as two bi-colored lines (in which cyan (light blue) represents tension and dark blue represents compression) through each parallel-bond location and oriented in the direction of the bond force, with a thickness proportional to force magnitude. An applied moment modifies the plot such that compression and tension at the bond periphery is indicated by the color of the two lines. The load being carried at a parallel-bonded contact is shared between that which is carried in the bond material itself (referred to as a parallel-bond force) and that which acts between the two overlapping particles (referred to as a contact force). The contact forces are depicted as a single line (in which cyan represents tension and black represents compression) through each contact location and oriented in the direction of the contact force, with a thickness proportional to force magnitude.

- The particle-displacement field is depicted as a vector field. Each vector originates at a particle center, is oriented in the displacement direction, and has a length that is proportional to the displacement magnitude.

All damage plots depict the crack distribution existing in a particular model at a particular grout pressure. The view title lists the model description using the naming convention described in Section A.2, and also lists the total number and type of cracks existing within a distance of 275 mm into the rock surrounding the test hole — note that this total does not include the cracks that may have formed at the slot tips.

A set of dashed circles has also been added to the plots to serve as a scaled reference. There are four different views: three near-field views (labeled as view 1, 2 and 3) and a far-field view. In the near-field view 1, a set of five dashed circles spaced at 10 mm intervals and an additional dashed circle at 100 mm into the rock have been added. In the near-field views 2 and 3, the dashed circles are spaced at 50 mm intervals into the rock. In the far-field view, an outline of the test hole, the two slots and the IEB control annulus have been added. And finally, the schistosity direction is depicted in each of the plots for the smeared anisotropic material by the orientation of a set of parallel lines at the test-hole center.

A.2 Model Naming Conventions

The following naming convention is employed to describe the different test-hole models. Each test-hole model is given a name of the form **A_B-C**, in which **A** ={Fc, Ff} denotes the model resolution, either *coarse* or *fine*; **B** = {STU, TU, STL, TL, STAs, TAs} denotes the material type (The naming convention for material type is given in the third paragraph of Section 2.0 and is repeated below.); and **C** ={gr40, gr50, gr60, gr70} denotes the grout pressure in units of MPa. Thus, for example, the fine-resolution instance **(Ff)** of the lower-bound isotropic material in which both shear and tensile bond failure may occur **(STL)** at a grout pressure of 60 MPa **(gr60)** would be designated as **Ff_STL-gr60**. Note that the additional number following the pressure designation indicates the successive states for which SAV-files were produced in the process of cycling each model to achieve quasi-static equilibrium conditions. All damage plots correspond with states for which quasi-static equilibrium conditions have been obtained.

The following naming convention is employed to describe the different best-fit materials. Each *PFC* [2D] material is given a name of the form **AB**, in which **A** ={ST, T} denotes the bond-failure mode, either *shear & tensile* or *tensile only*; and **B** ={As, Ad, U, L} denotes the material representation, either *smeared anisotropic*, *discrete anisotropic*, *upper-bound isotropic*, *or lower-bound isotropic*. Thus, for example, the lower-bound isotropic material in which both shear and tensile bond failure may occur would be designated as **STL**, while the corresponding upper-bound isotropic material would be designated as **STU**, and the corresponding smeared and discrete anisotropic materials would be designated as **STAs** and **STAd**, respectively.

A.3 Simulation Results

The results from a total of nine different test-hole models are presented here in order to investigate the effects of model resolution, material representation, and bond-failure mechanism upon the resulting damage patterns. Six of the best-fit materials (isotropic: STU, TU, STL, TL; smeared anisotropic: STAs, TAs) have been assigned to these models, and damage predictions for grout pressures of 40, 50, 60, and 70 MPa are presented. These six models are all coarse resolution. In addition, the results for three fine-resolution models of materials STL, TL and STAs are also presented

The best way to obtain damage predictions for the various grout pressures would be to progressively increase the applied pressure until the final target pressure is obtained. Thus, in each case, we would first apply the lowest pressure (40 MPa) and bring the model to a state of static equilibrium for which all of the stresses have been redistributed and no further cracking occurs. Then the pressure would be increased to the next higher value, and again the model brought to a state of static equilibrium. The large times required for each model to reach the static-equilibrium state made it prohibitive to utilize such a procedure. Instead, each model was brought to its excavated state, and then four separate loadings were applied (of 40, 50, 60 and 70 MPa) so that each of these four models could be cycled to static equilibrium separately on a separate machine, thereby allowing the computation of damage to be done in parallel.

The details of the final damage patterns are sensitive to load path, and to the way in which the stresses redistribute in response to accumulating damage. The parallel-loading procedure utilized for these runs introduces slightly different loading paths for each of the models in which the final pressures were different. This, in turn, produces slight differences in damage patterns formed in each of the models at "equivalent" pressures. That is, the initial location of a crack at an early stage in a high-loading case may not be the same as the location of the final crack in a low-loading case. This can be seen by comparing the tensile crack that is emanating from the top of the test hole in Figures A.17 and A.18. By carefully overlaying these two plots, one finds that the crack path for the model loaded to 50 MPa is slightly to the right of the crack path for the model loaded to 60 MPa.

Steps have been taken (similar to those described in step 4 of the modeling sequence in Section 3.1.3) to minimize the differences, which arise from the slight stress overshoot that occurs because of the dynamic propagation of the compressive stress wave throughout each model. However, the fact that equivalent crack locations differ slightly for different pressures of the same model indicates that these dynamic effects have not been fully eliminated. Nonetheless, we believe that these dynamic effects influence the damage patterns in only a minor way, and thus, do not effect the discussion of the results or the conclusions drawn from the results.

A.3.1 Isotropic Upper-Bound Material STU (coarse)

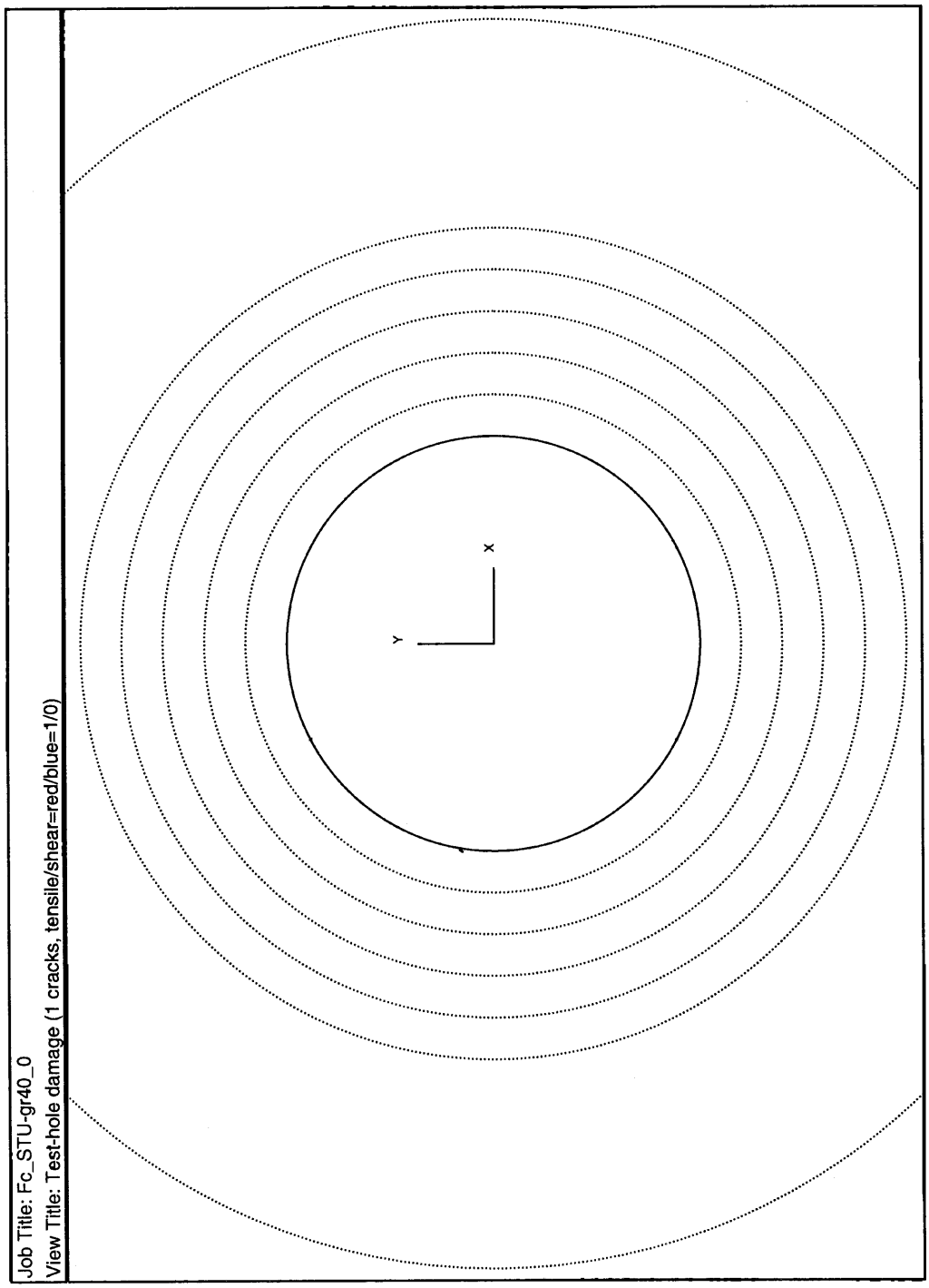

Figure A.1 Near-field damage, view 1 (isotropic upper-bound material STU; coarse; 40 MPa)

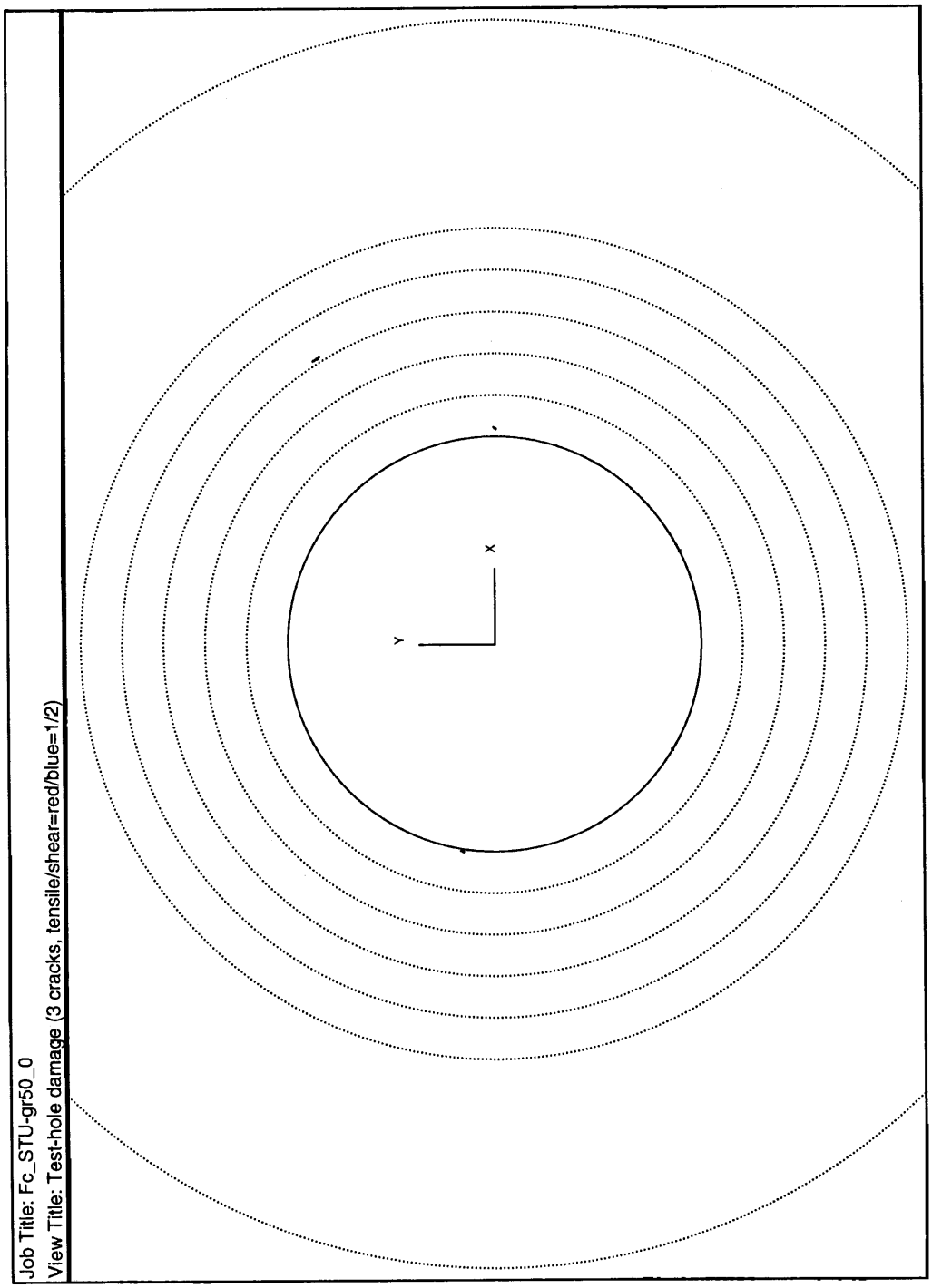

Figure A.2 ***Near-field damage, view 1 (isotropic upper-bound material STU; coarse; 50 MPa)***

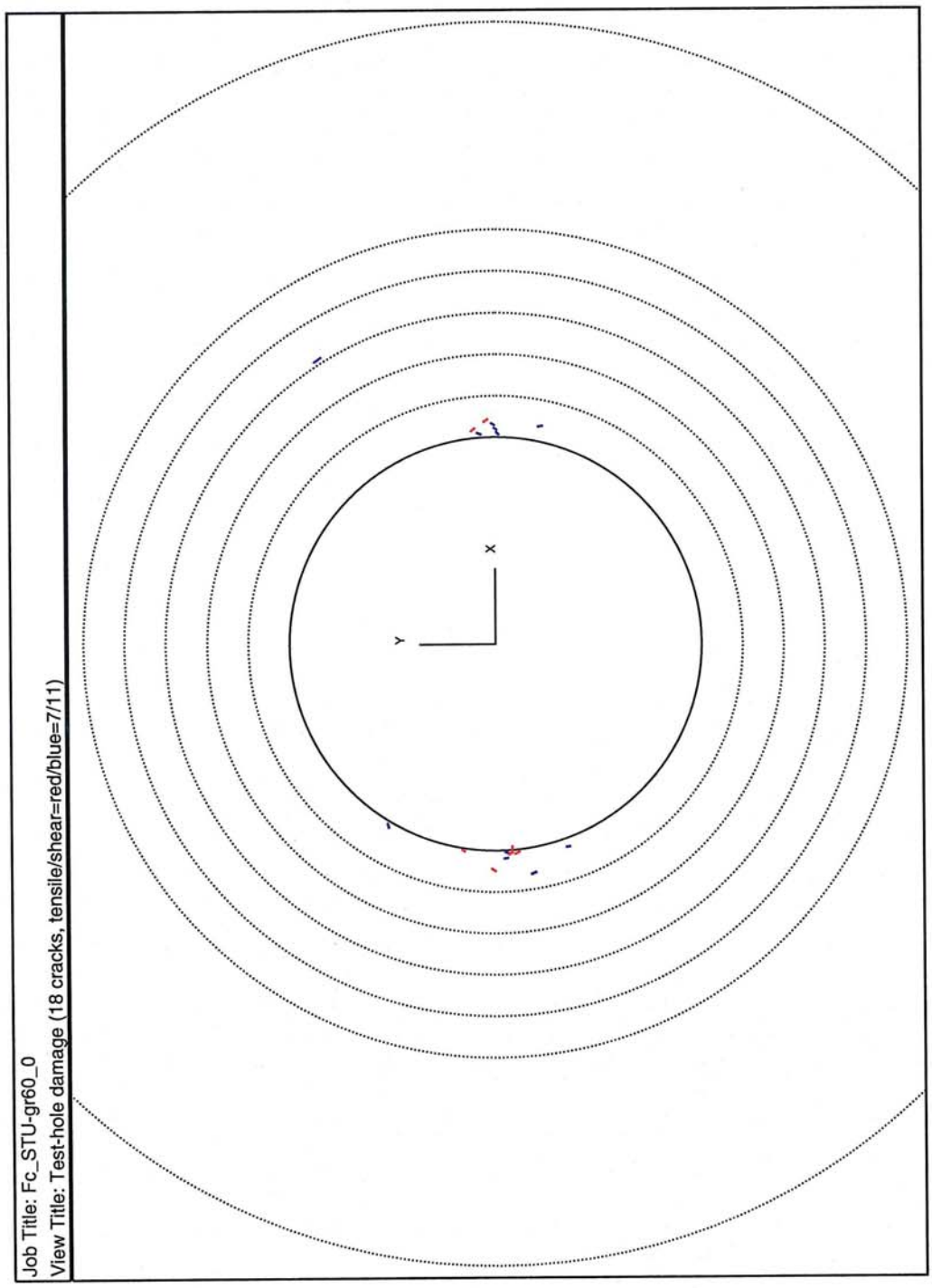

Figure A.3 Near-field damage, view 1 (isotropic upper-bound material STU; coarse; 60 MPa)

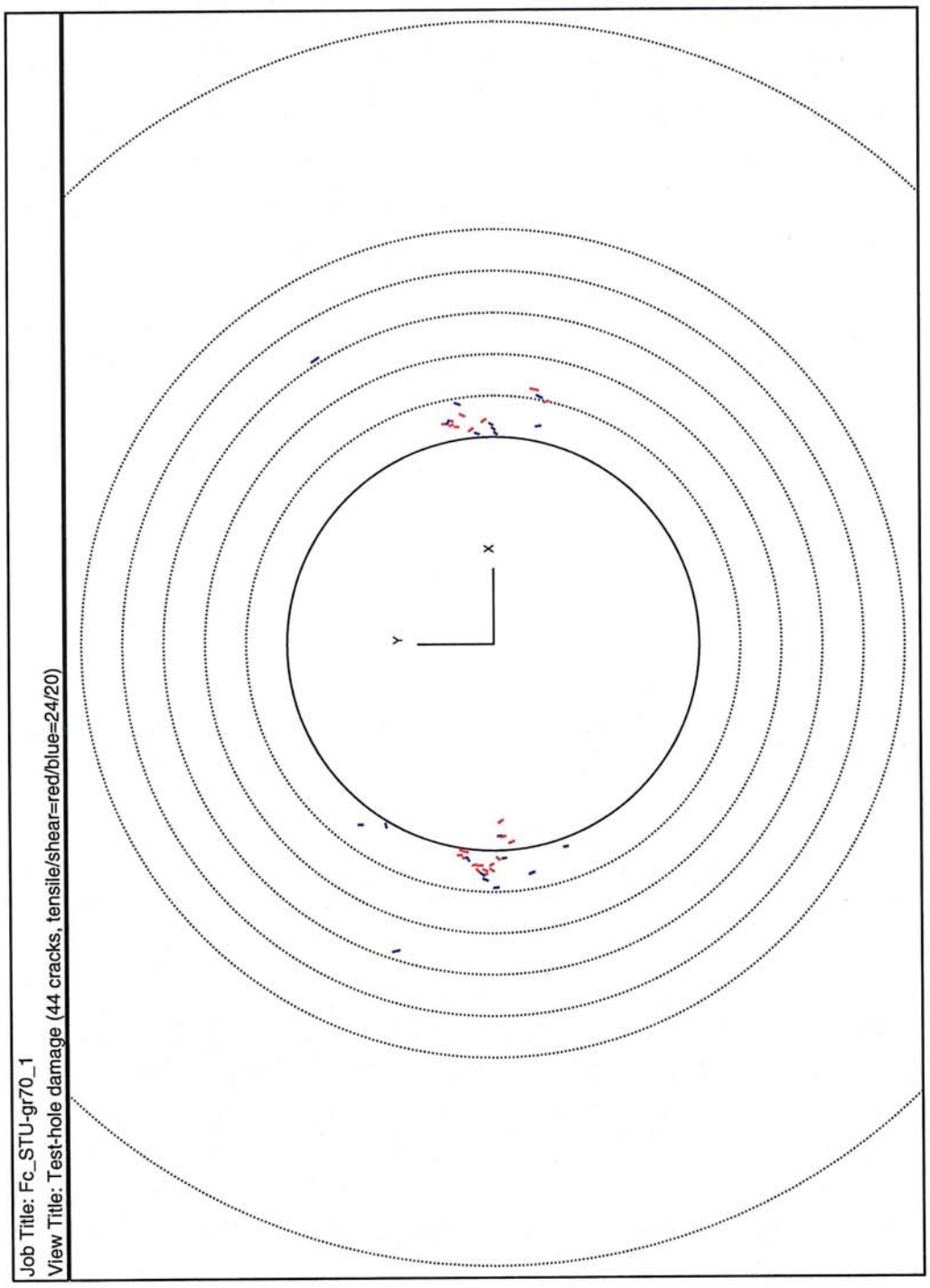

Figure A.4 Near-field damage, view 1 (isotropic upper-bound material STU; coarse; 70 MPa)

A.3.2 Isotropic Upper-Bound Material TU (coarse)

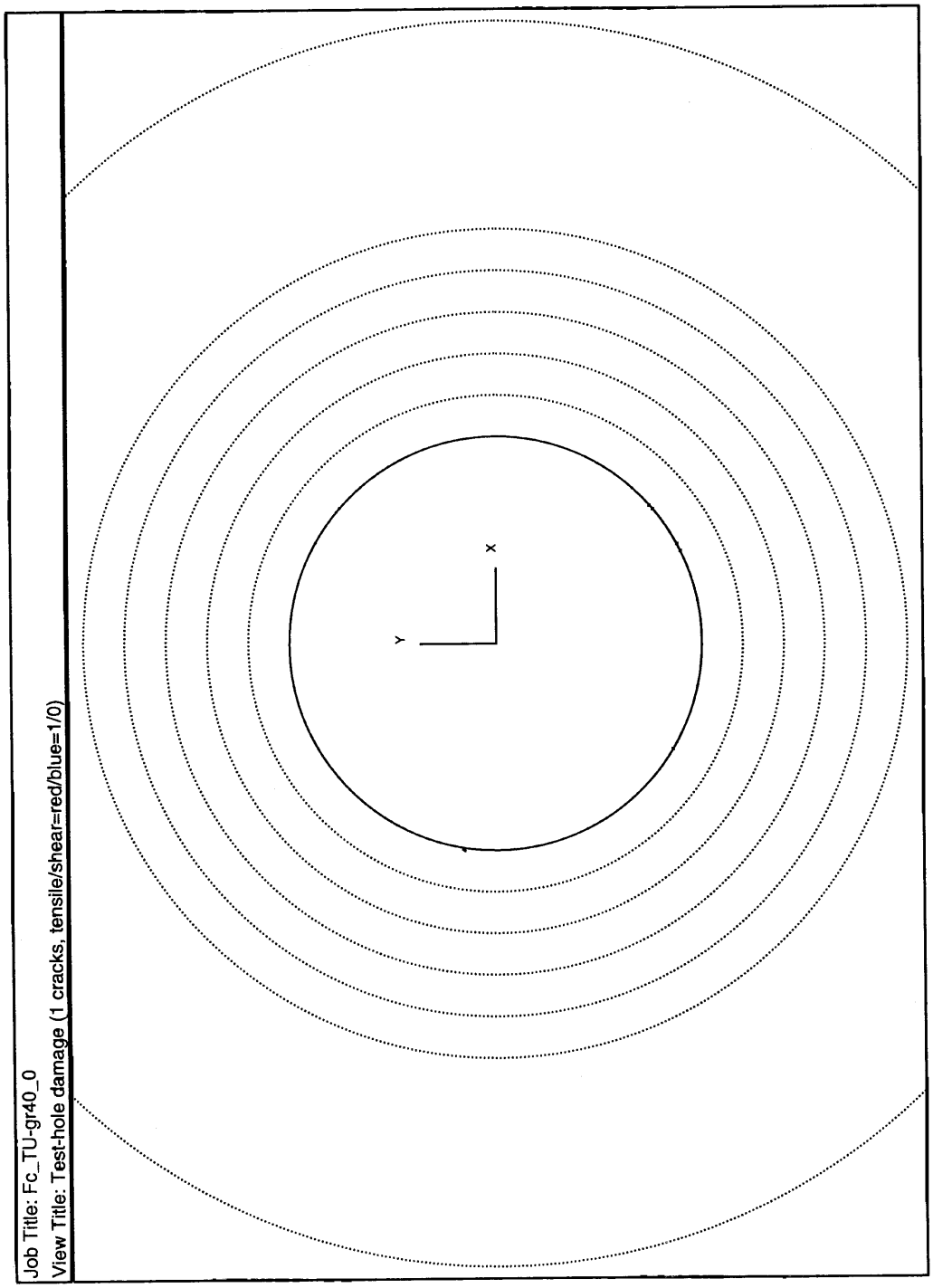

Figure A.5 Near-field damage, view 1 (isotropic upper-bound material TU; coarse; 40 MPa)

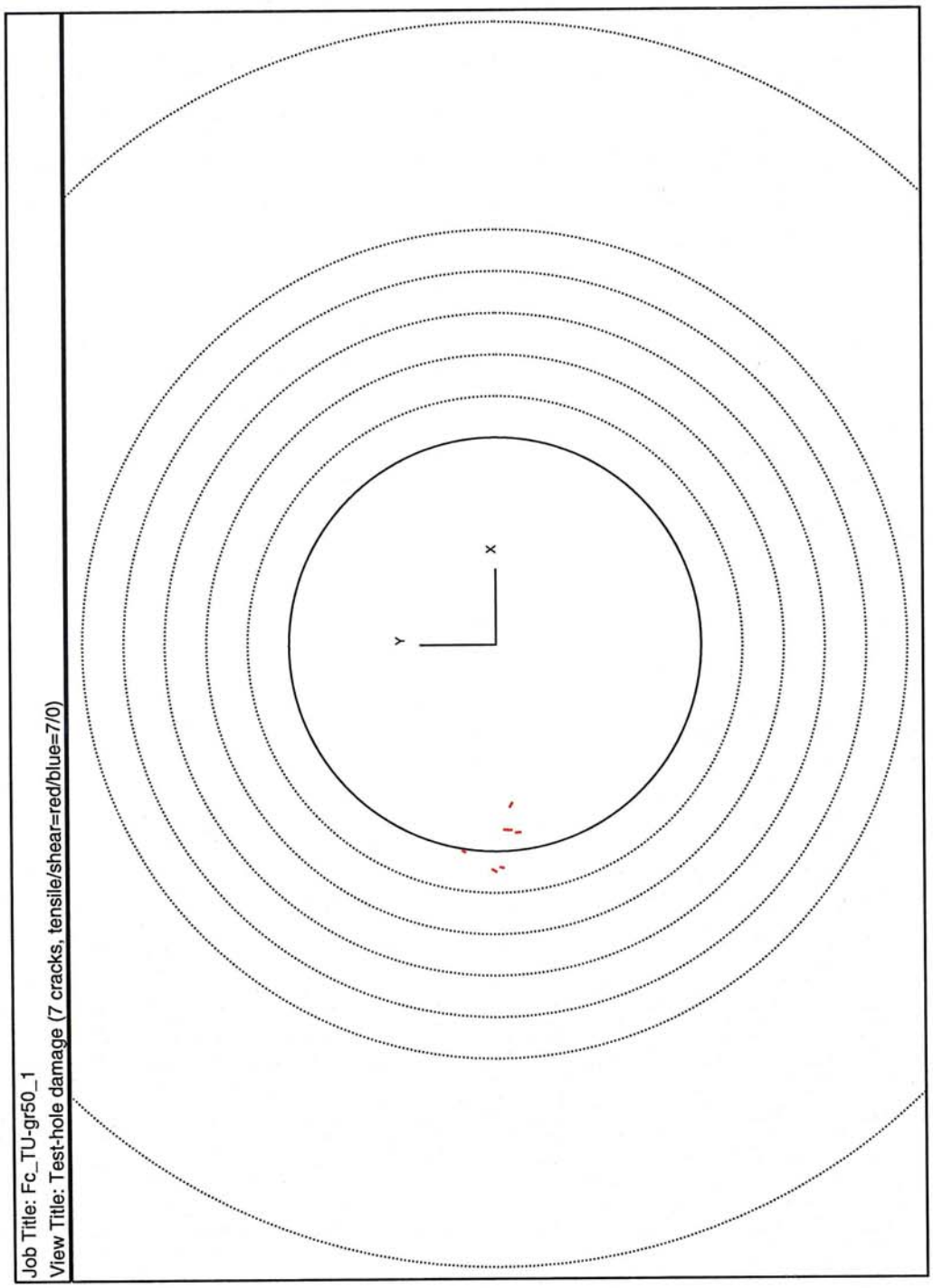

Figure A.6 Near-field damage, view 1 (isotropic upper-bound material TU; coarse; 50 MPa)

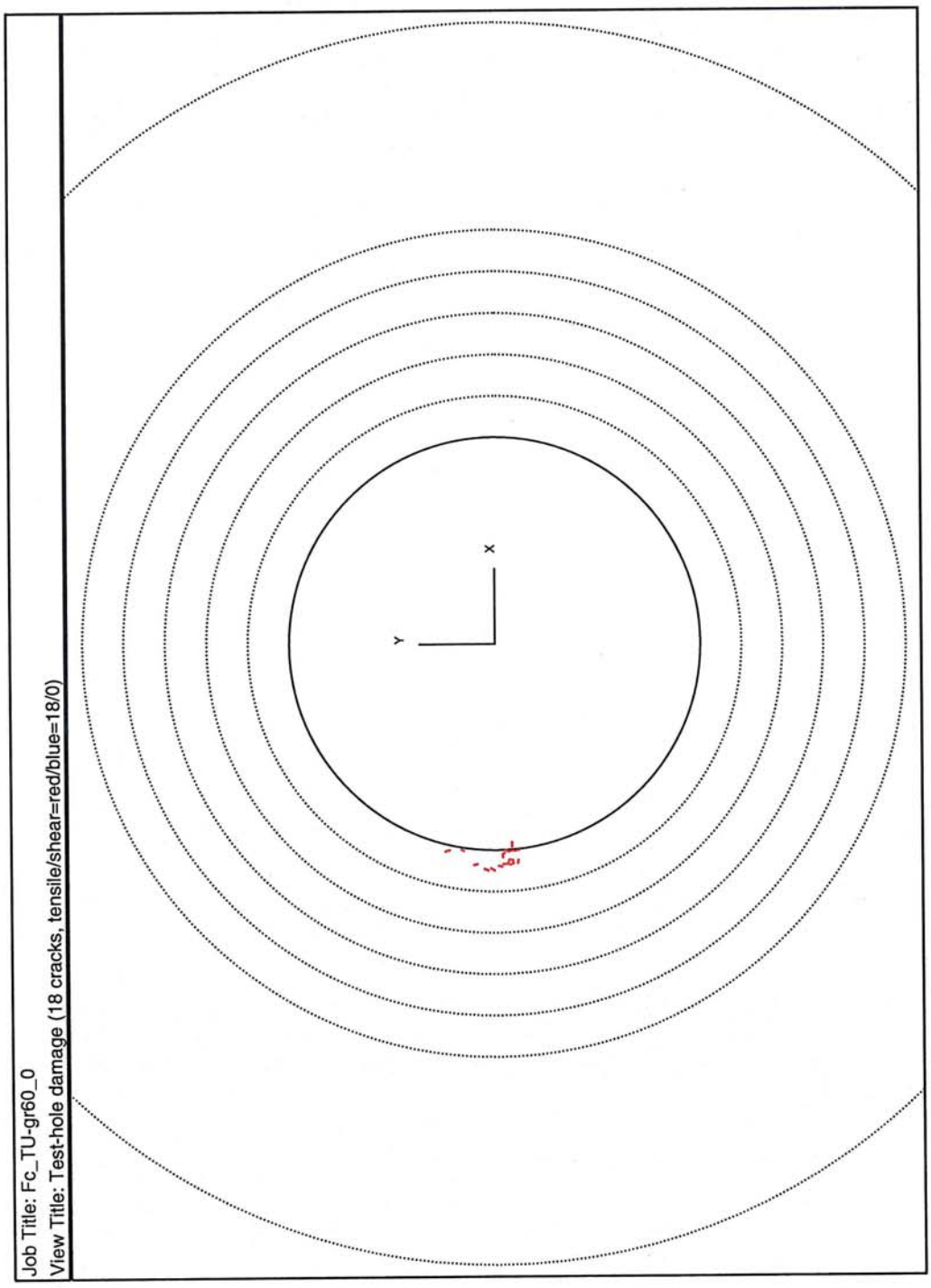

Figure A.7 Near-field damage, view 1 (isotropic upper-bound material TU; coarse; 60 MPa)

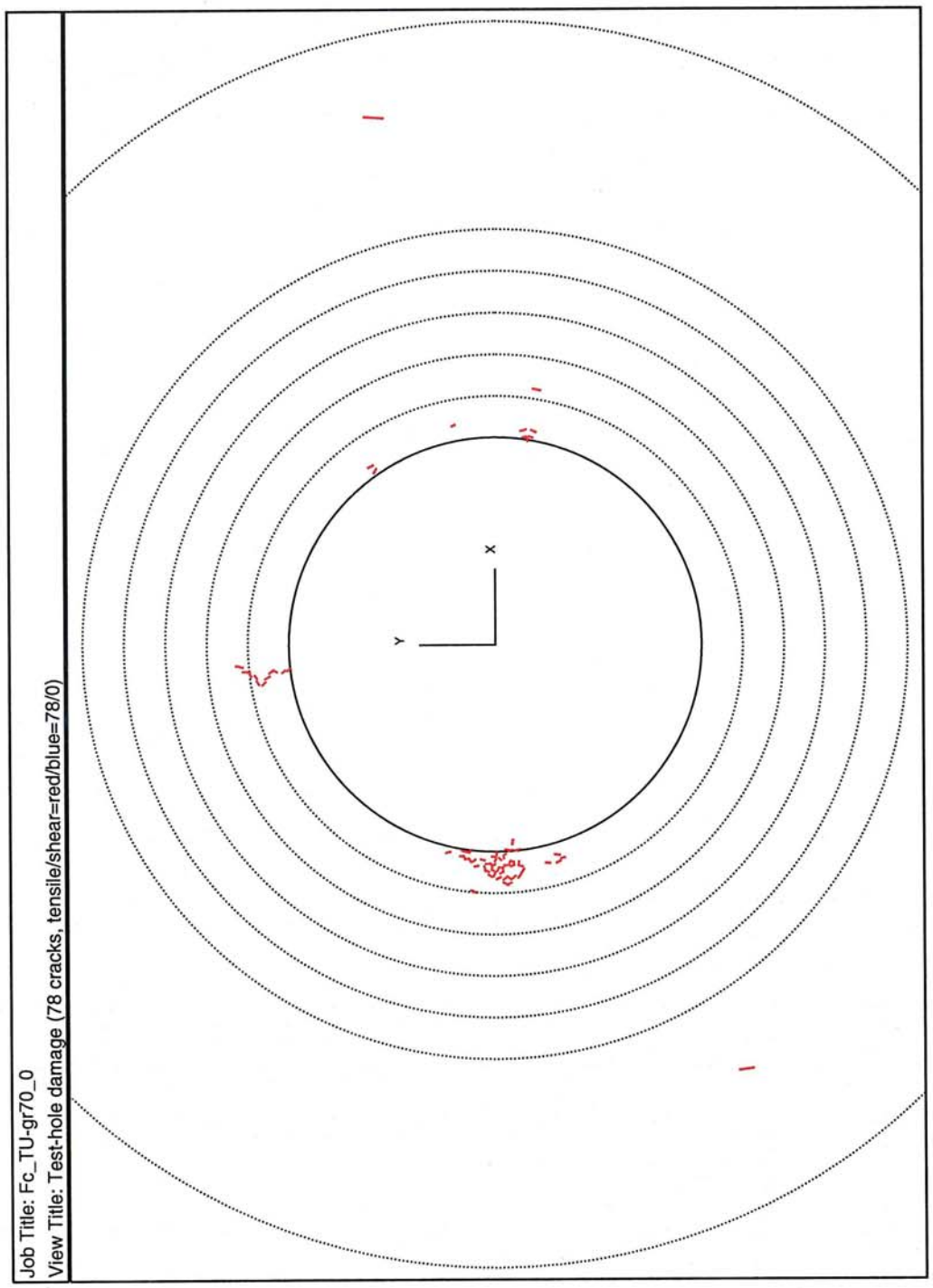

Figure A.8 Near-field damage, view 1 (isotropic upper-bound material TU; coarse; 70 MPa)

A.3.3 Isotropic Lower-Bound Material STL (coarse)

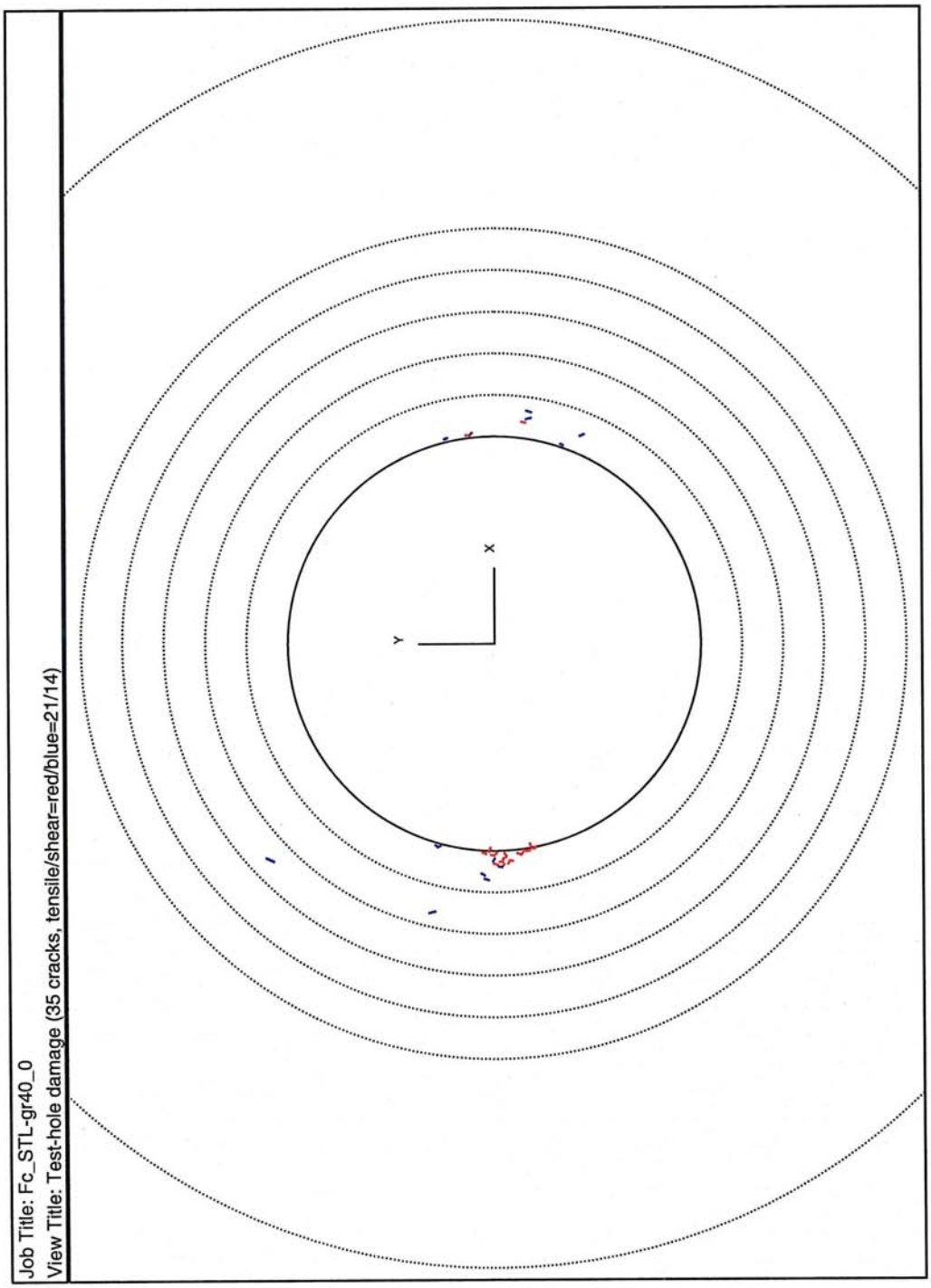

Figure A.9 Near-field damage, view 1 (isotropic lower-bound material STL; coarse; 40 MPa)

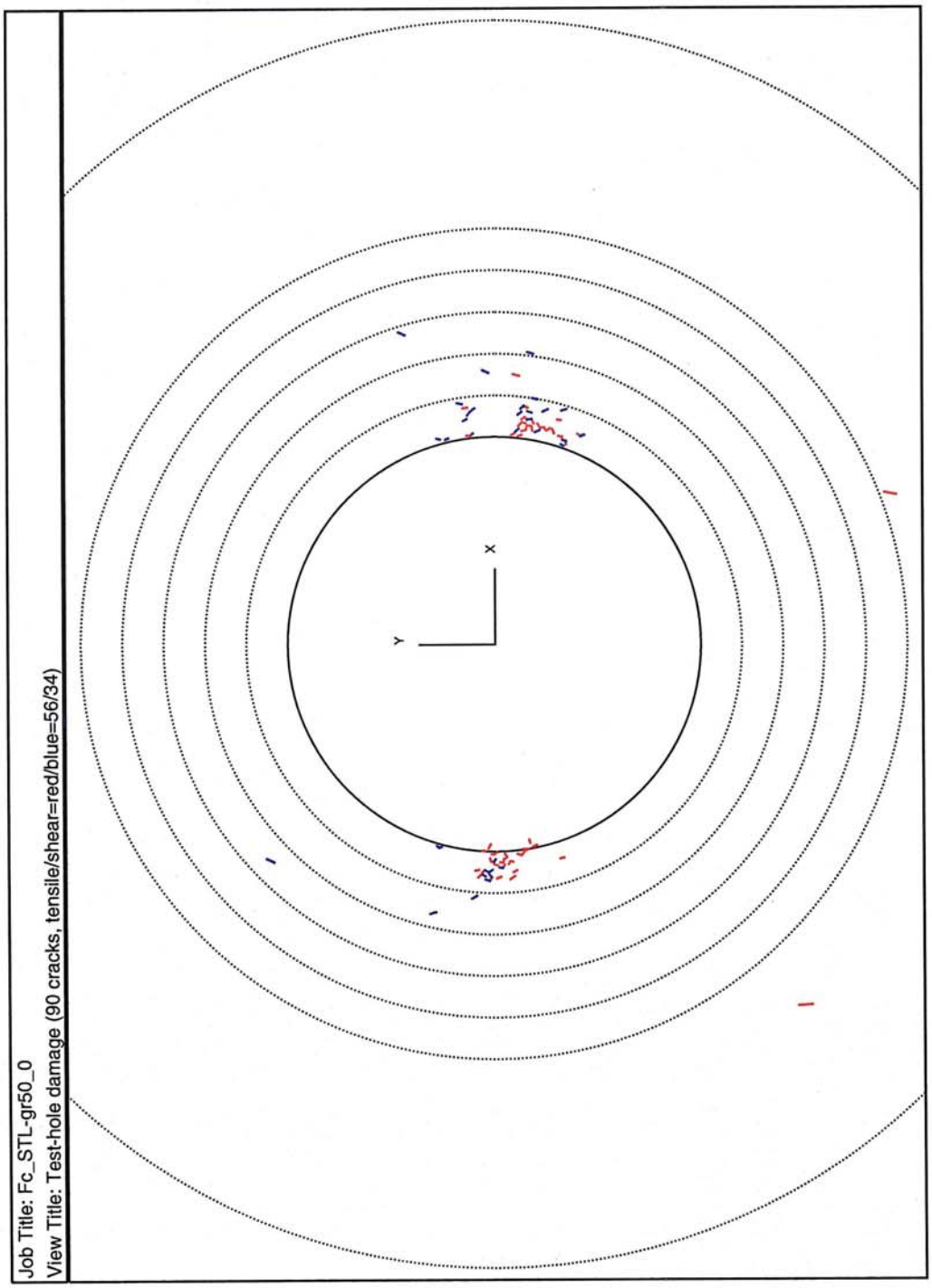

Figure A.10 Near-field damage, view 1 (isotropic lower-bound material STL; coarse; 50 MPa)

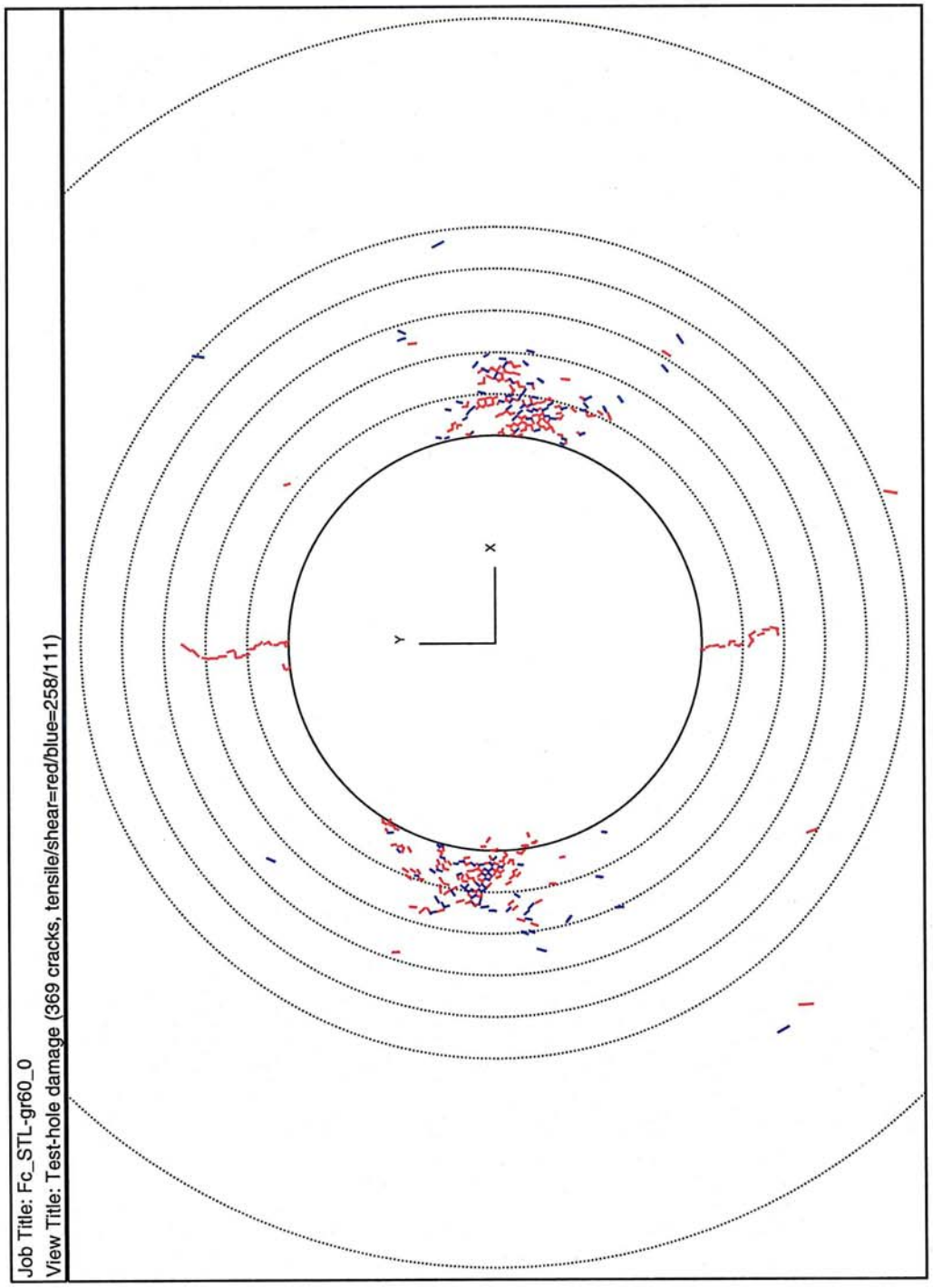

Figure A.11 Near-field damage, view 1 (isotropic lower-bound material STL; coarse; 60 MPa)

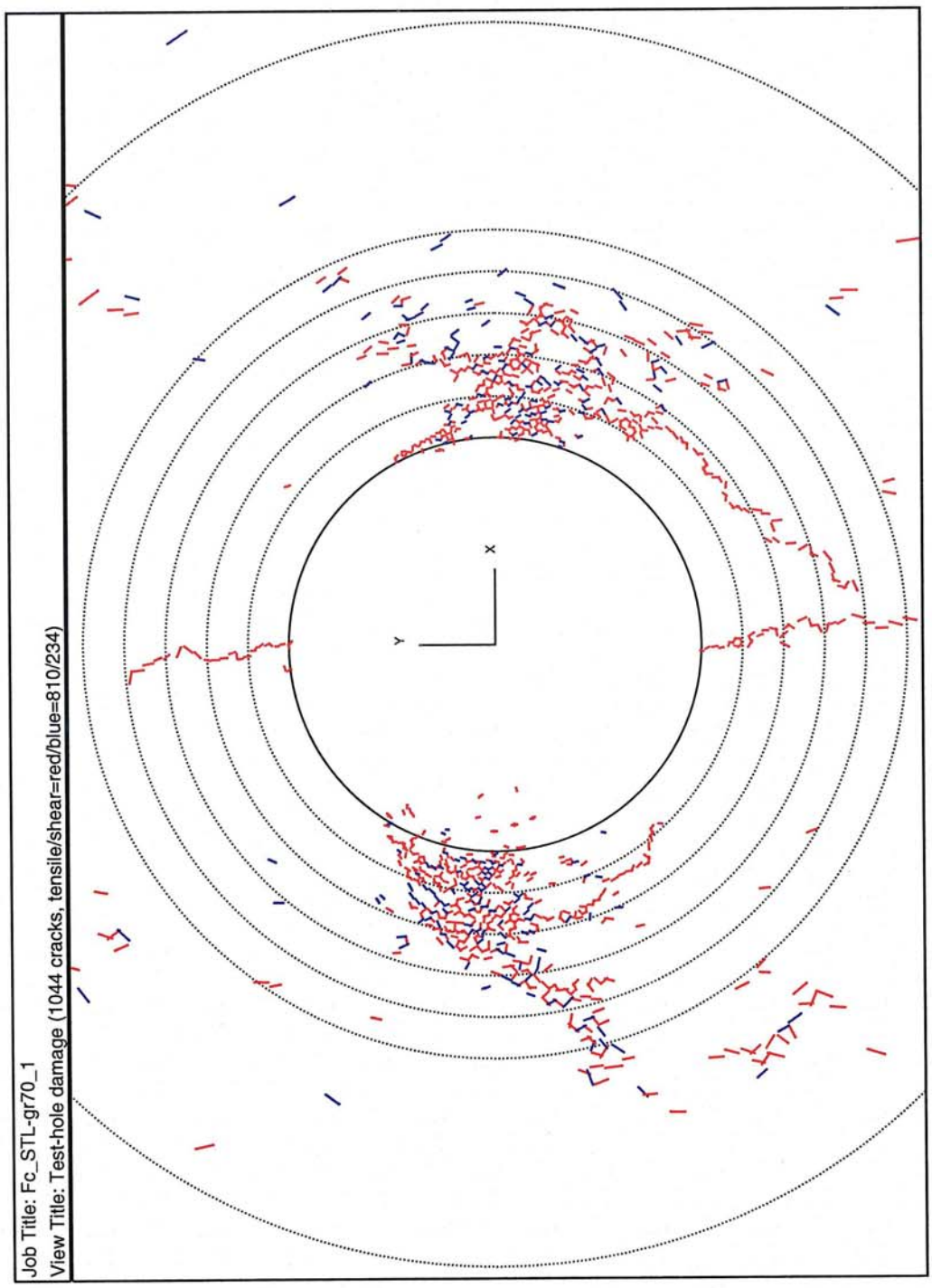

Figure A.12 Near-field damage, view 1 (isotropic lower-bound material STL; coarse; 70 MPa)

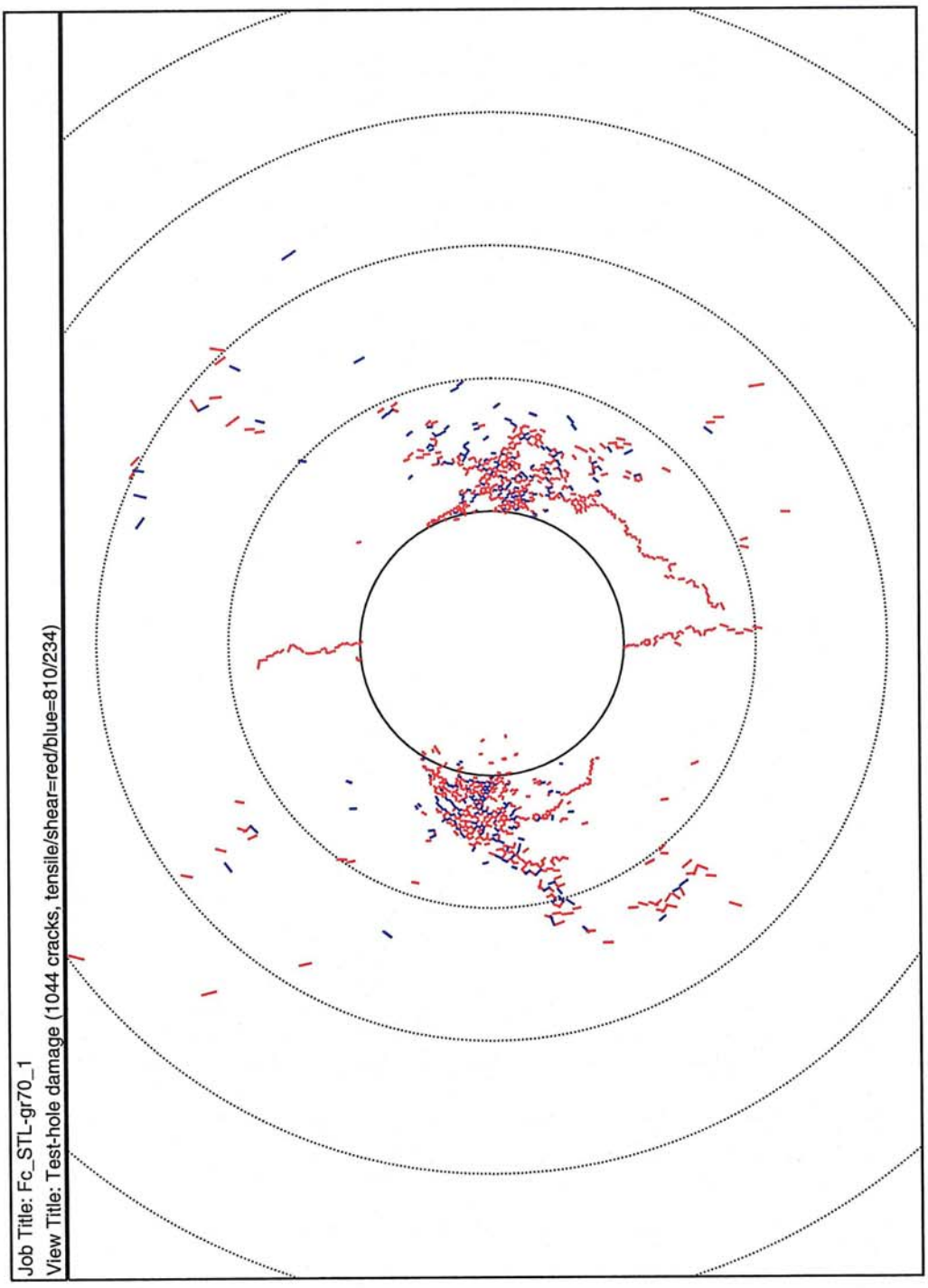

Figure A.13 Near-field damage, view 2 (isotropic lower-bound material STL; coarse; 70 MPa)

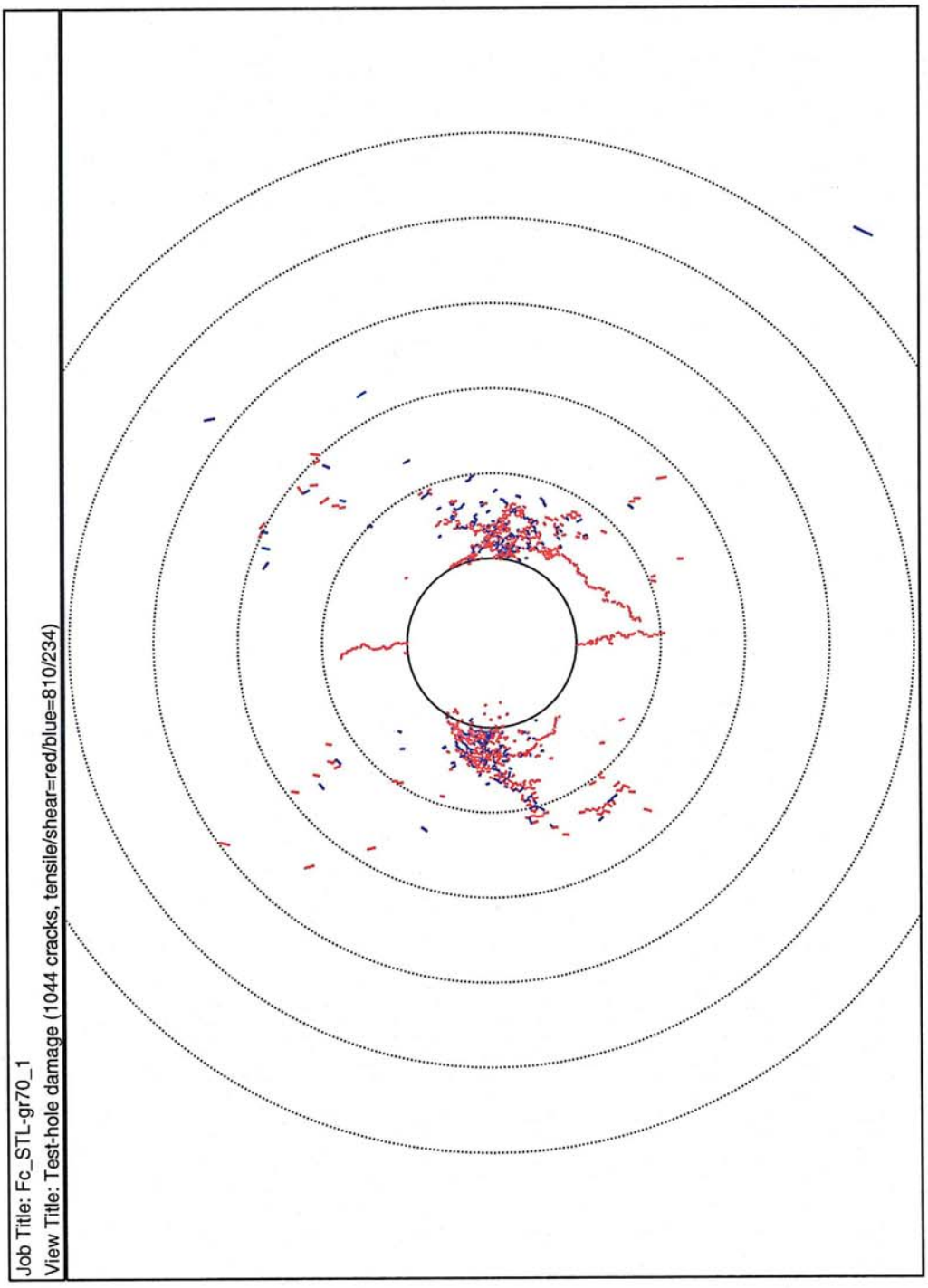

Figure A.14 Near-field damage, view 3 (isotropic lower-bound material STL; coarse; 70 MPa)

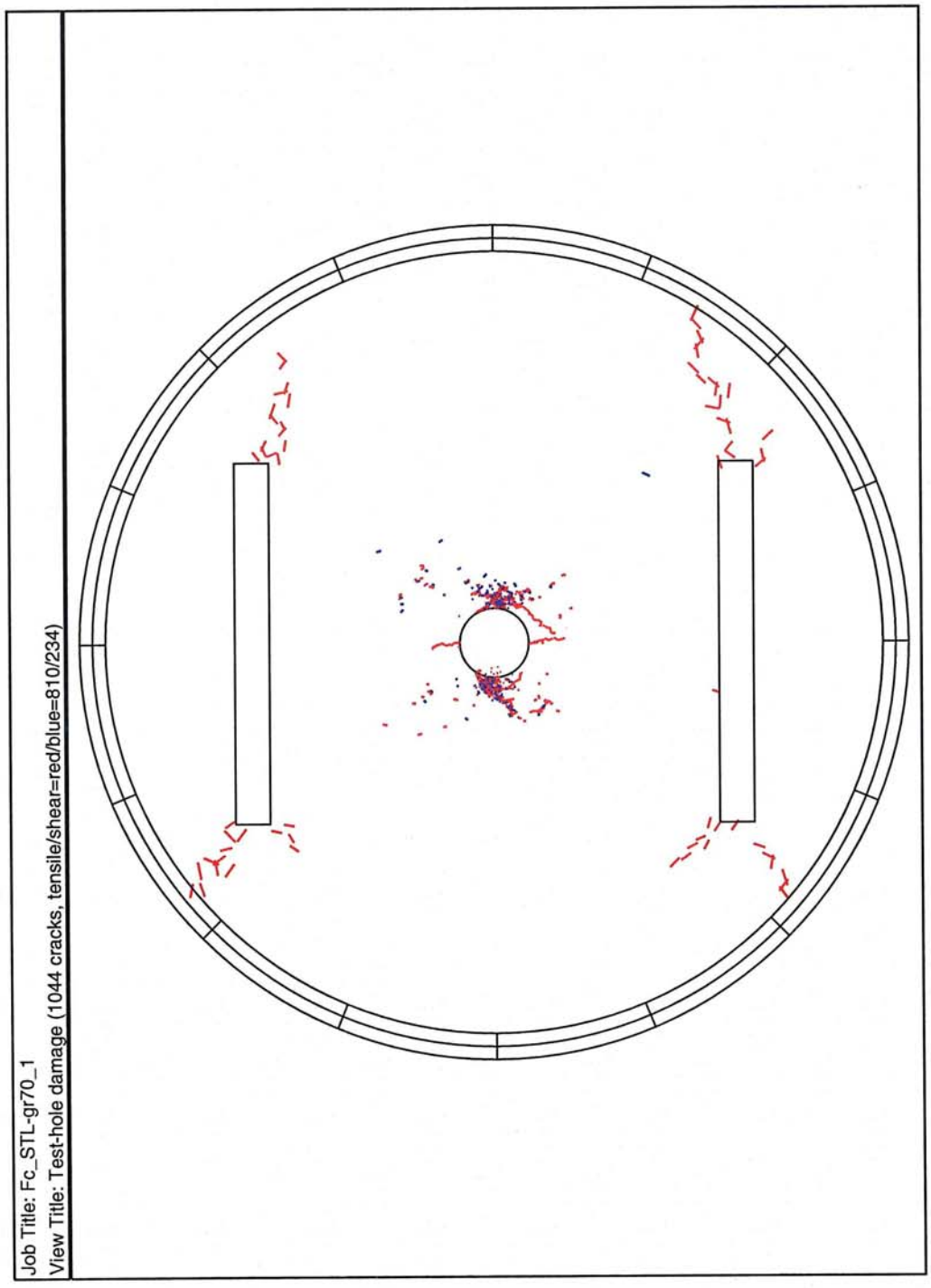

Figure A.15 Far-field damage (isotropic lower-bound material STL; coarse; 70 MPa)

A.3.4 Isotropic Lower-Bound Material STL (fine)

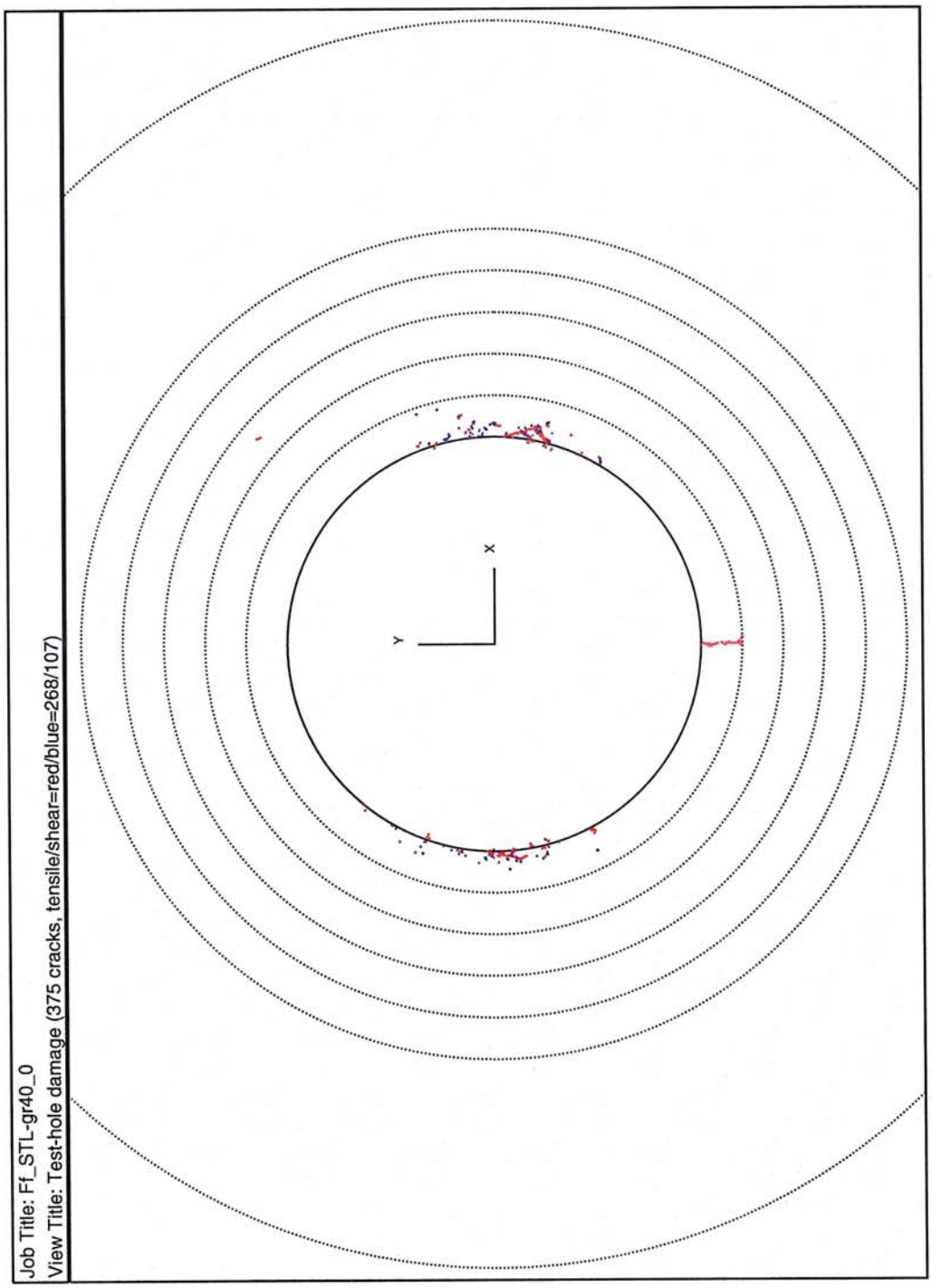

Figure A.16 Near-field damage, view 1 (isotropic lower-bound material STL; fine; 40 MPa)

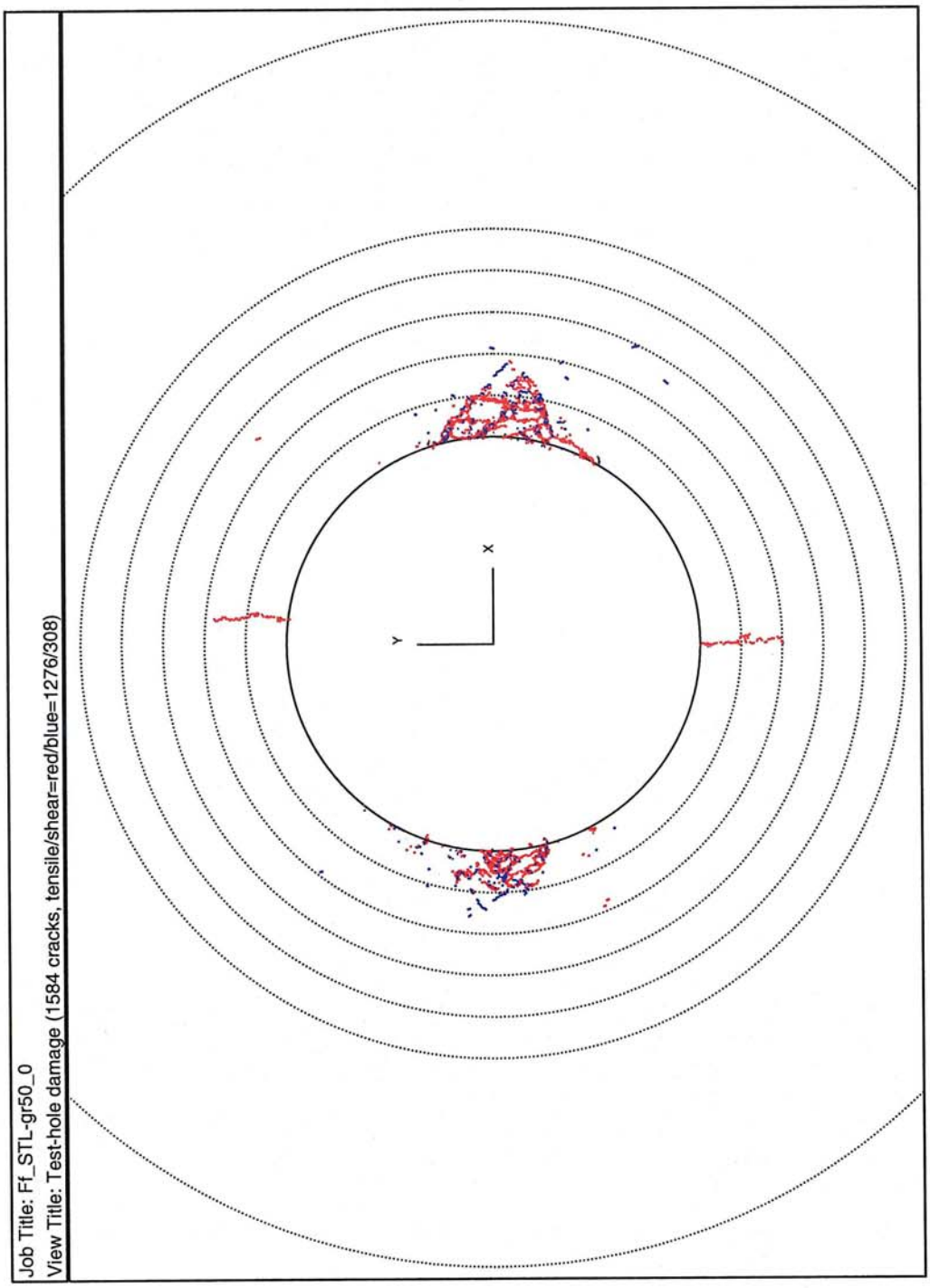

Figure A.17 Near-field damage, view 1 (isotropic lower-bound material STL; fine; 50 MPa)

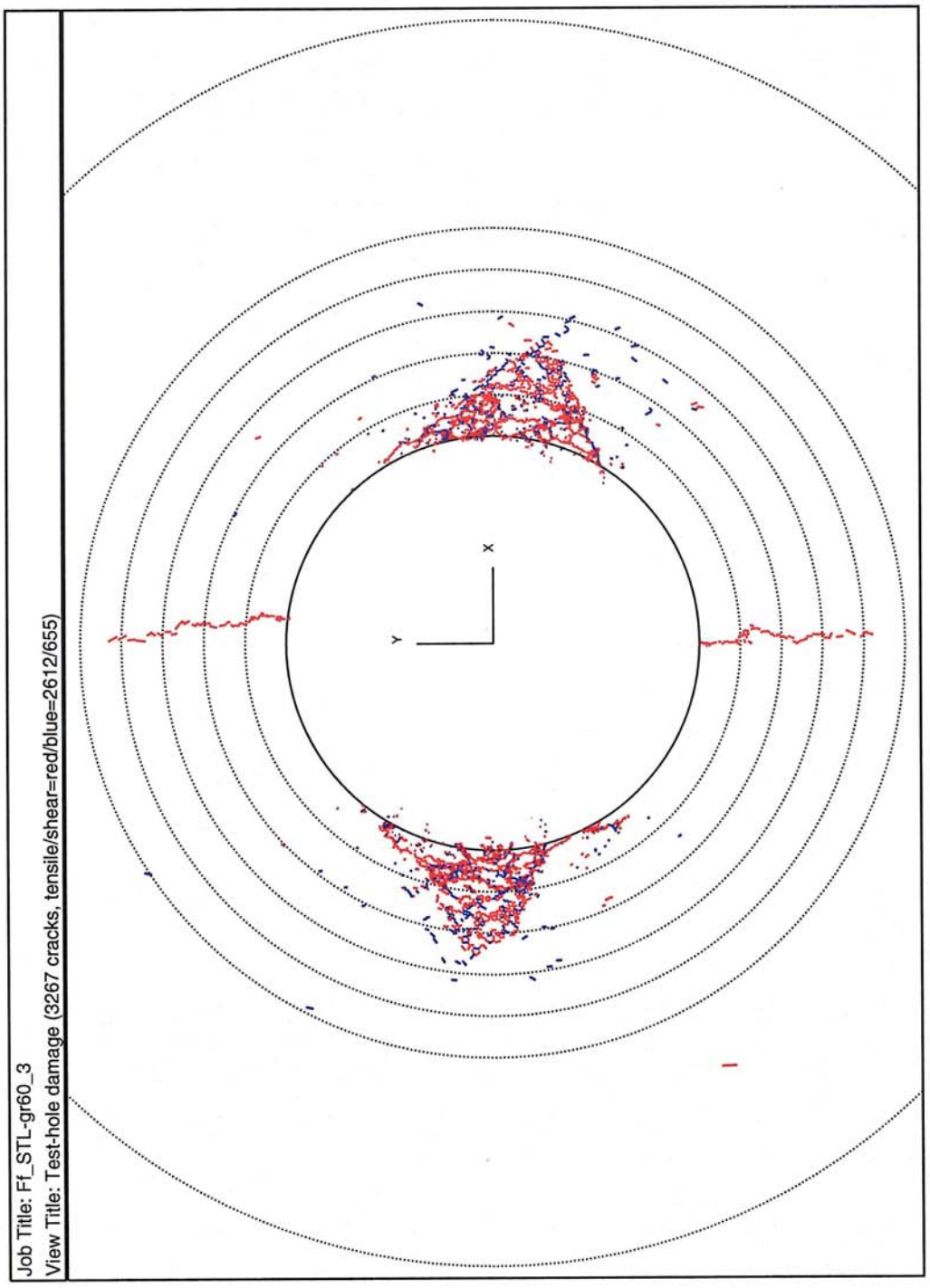

Figure A.18 Near-field damage, view 1 (isotropic lower-bound material STL; fine; 60 MPa)

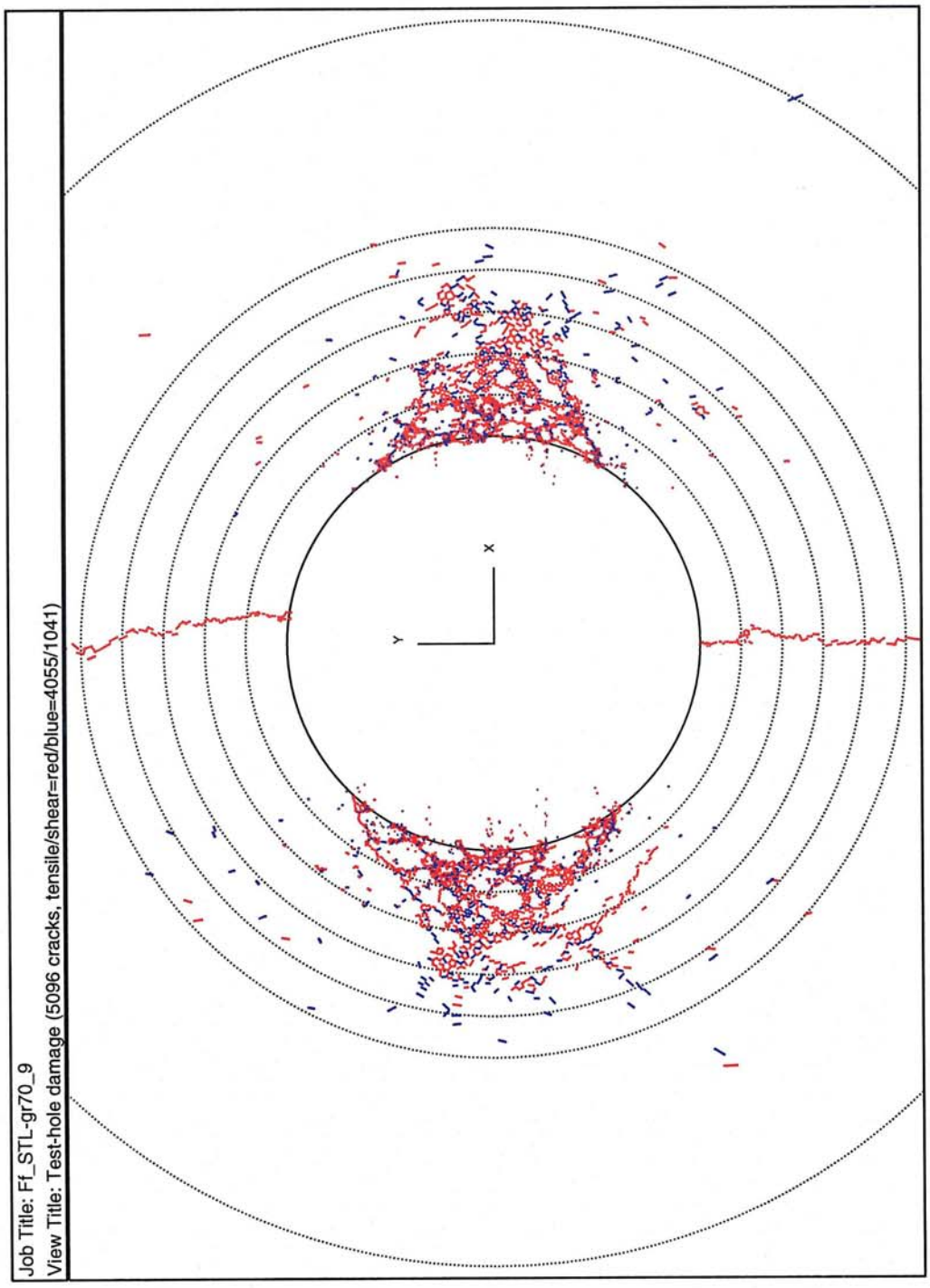

Figure A.19 Near-field damage, view 1 (isotropic lower-bound material STL; fine; 70 MPa)

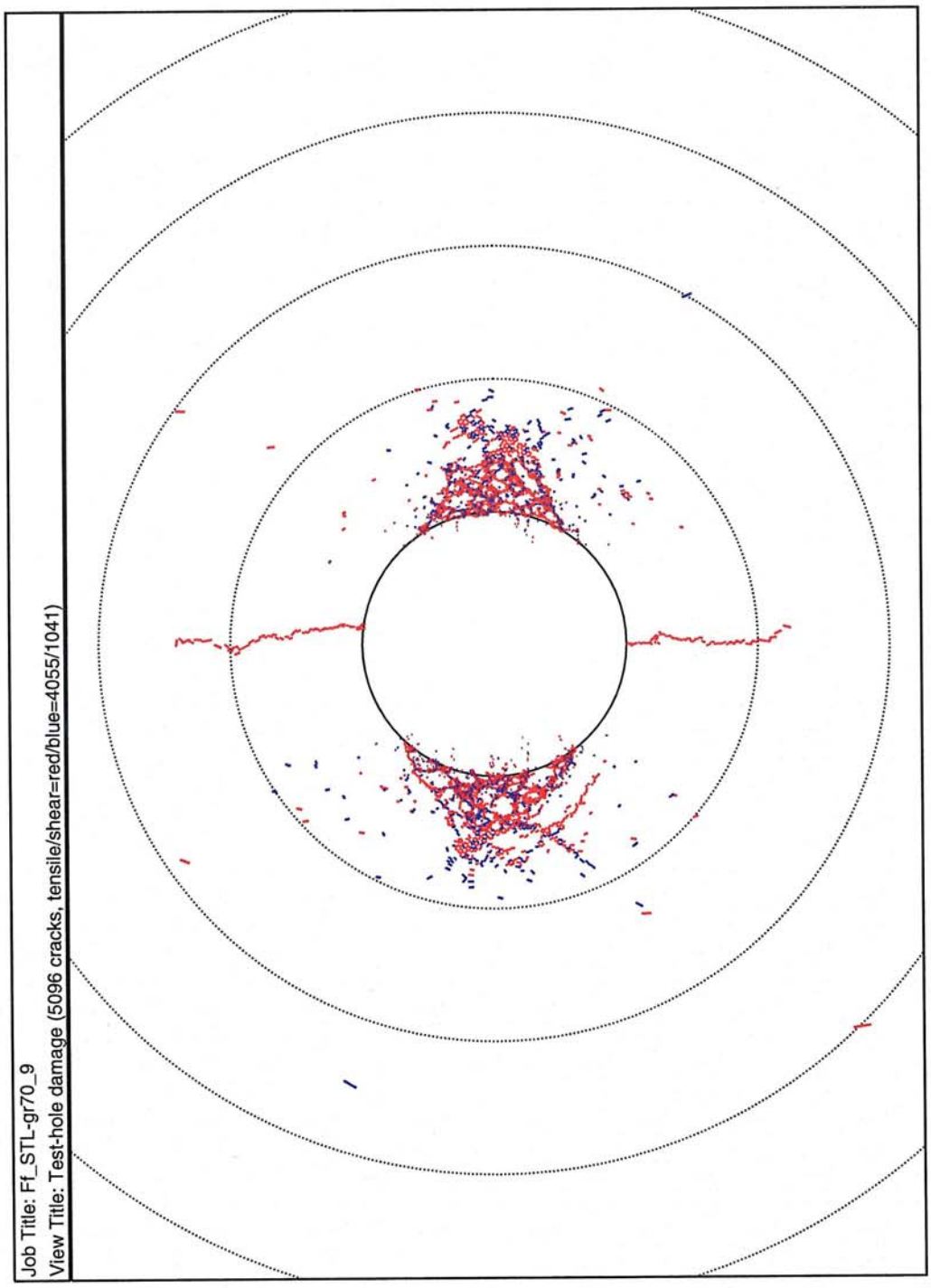

Figure A.20 Near-field damage, view 2 (isotropic lower-bound material STL; fine; 70 MPa)

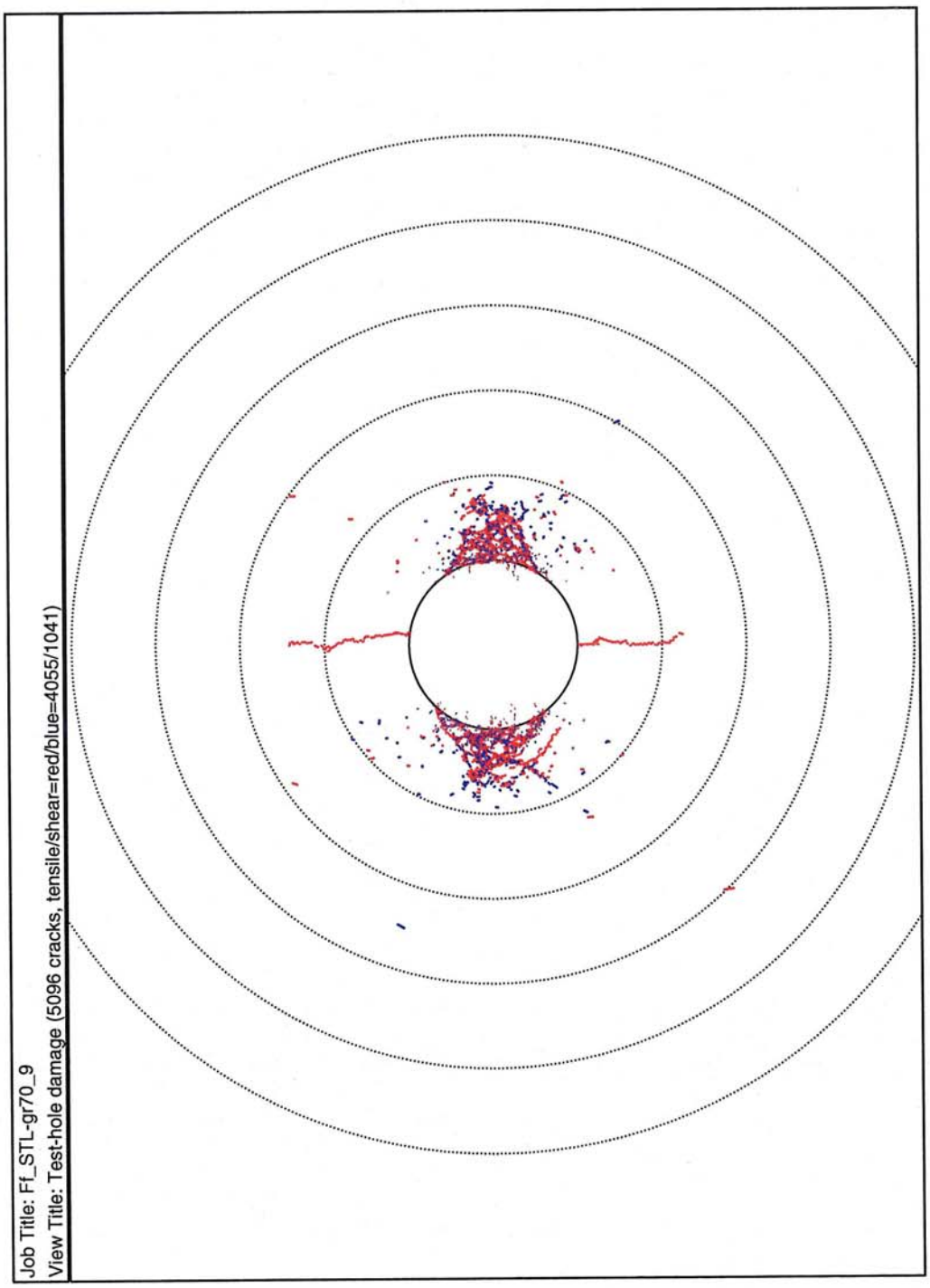

Figure A.21 Near-field damage, view 3 (isotropic lower-bound material STL; fine; 70 MPa)

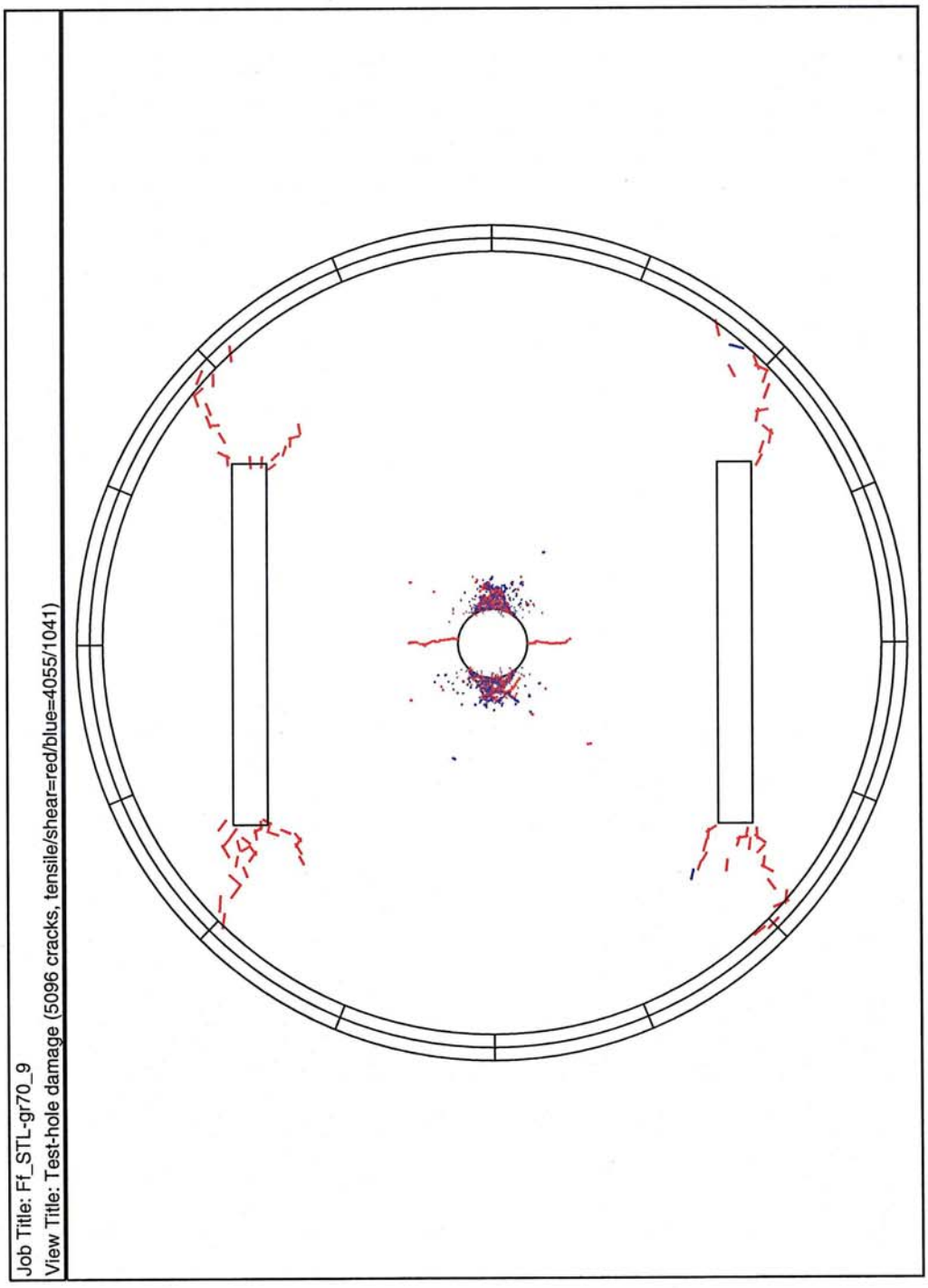

Figure A.22 Far-field damage (isotropic lower-bound mat. STL; fine; 70 MPa)

A.3.5 Isotropic Lower-Bound Material TL (coarse)

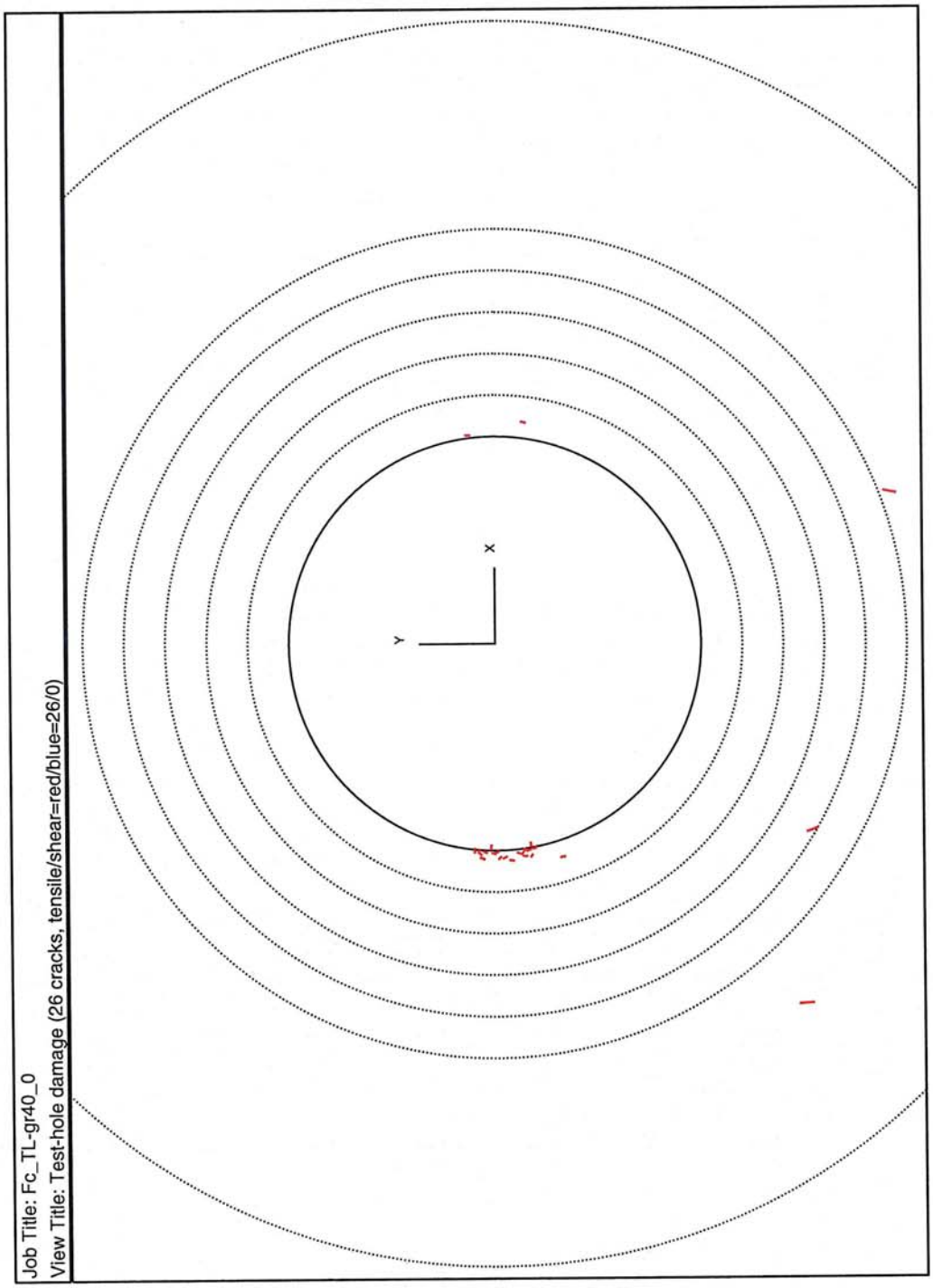

Figure A.23 Near-field damage, view 1 (isotropic lower-bound material TL; coarse; 40 MPa)

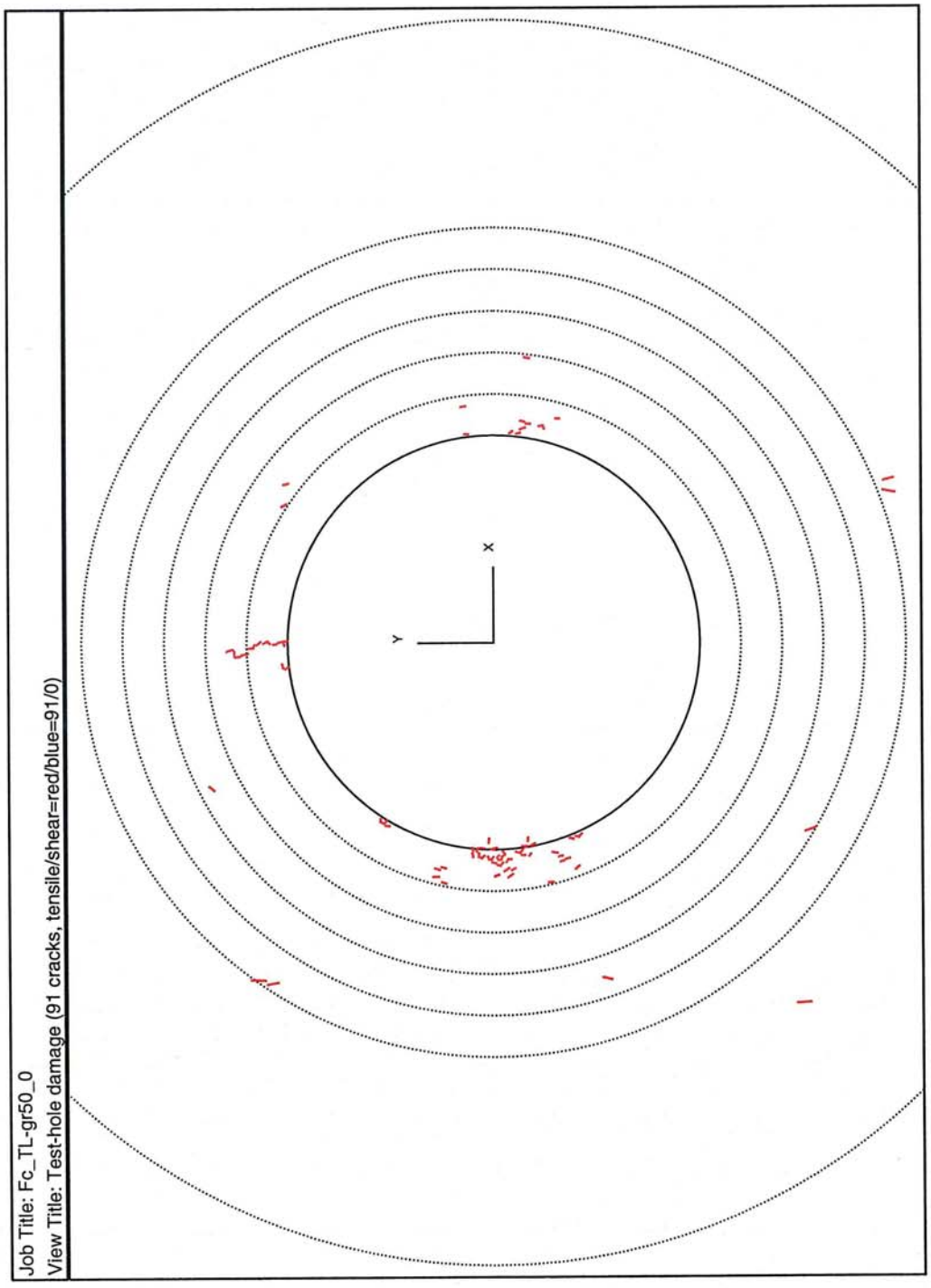

Figure A.24 Near-field damage, view 1 (isotropic lower-bound material TL; coarse; 50 MPa)

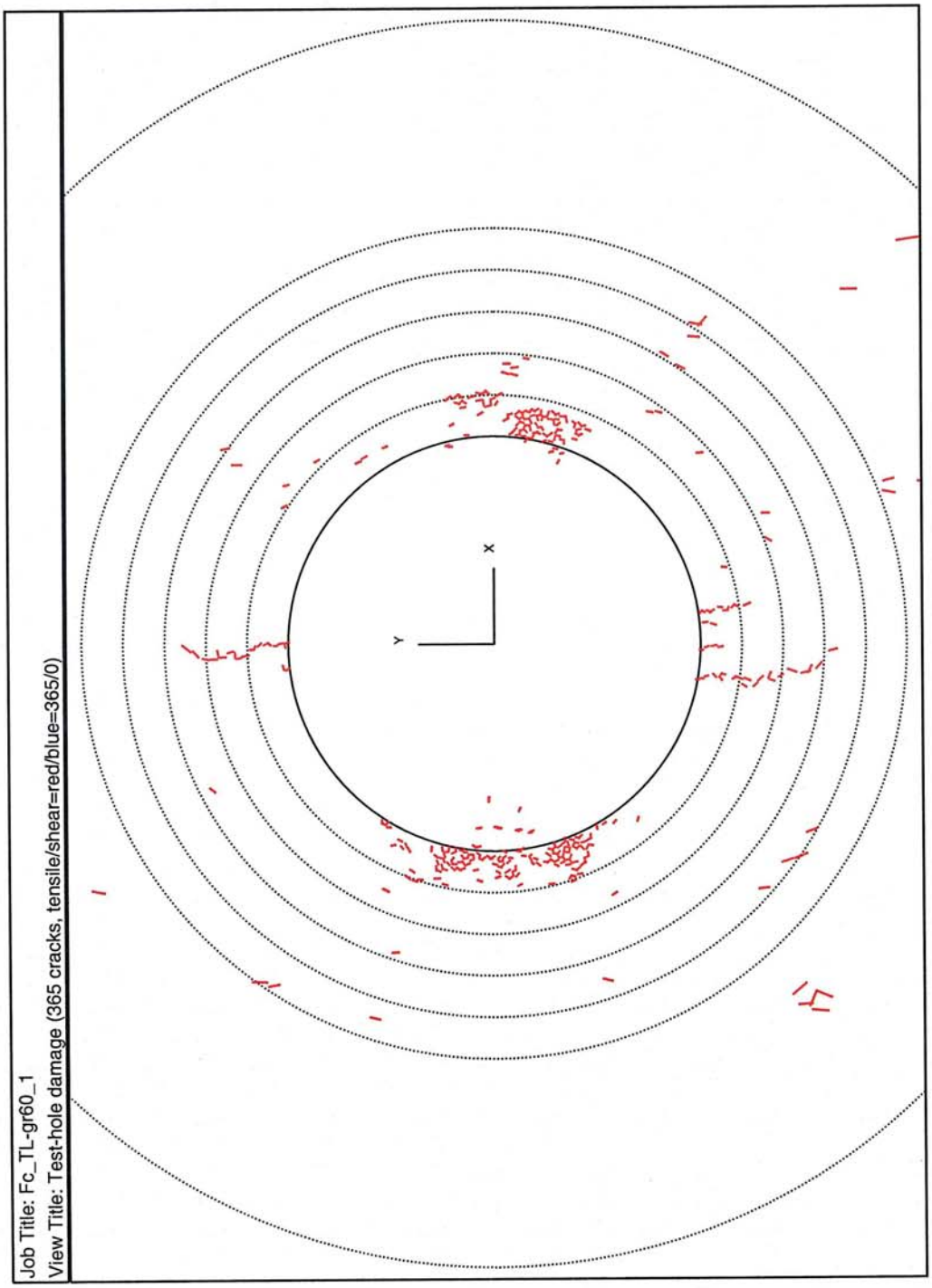

Figure A.25 Near-field damage, view 1 (isotropic lower-bound material TL; coarse; 60 MPa)

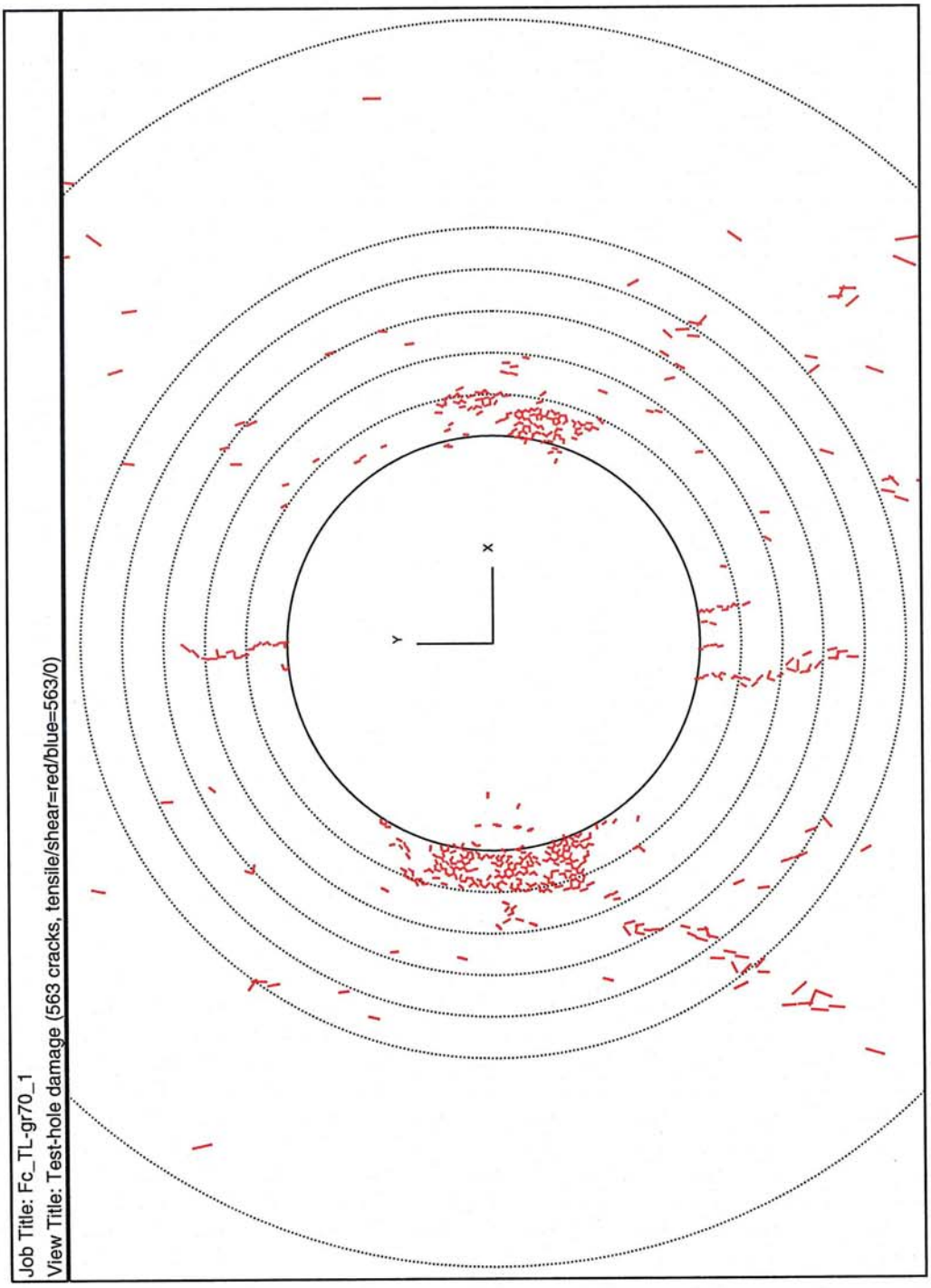

Figure A.26 Near-field damage, view 1 (isotropic lower-bound material TL; coarse; 70 MPa)

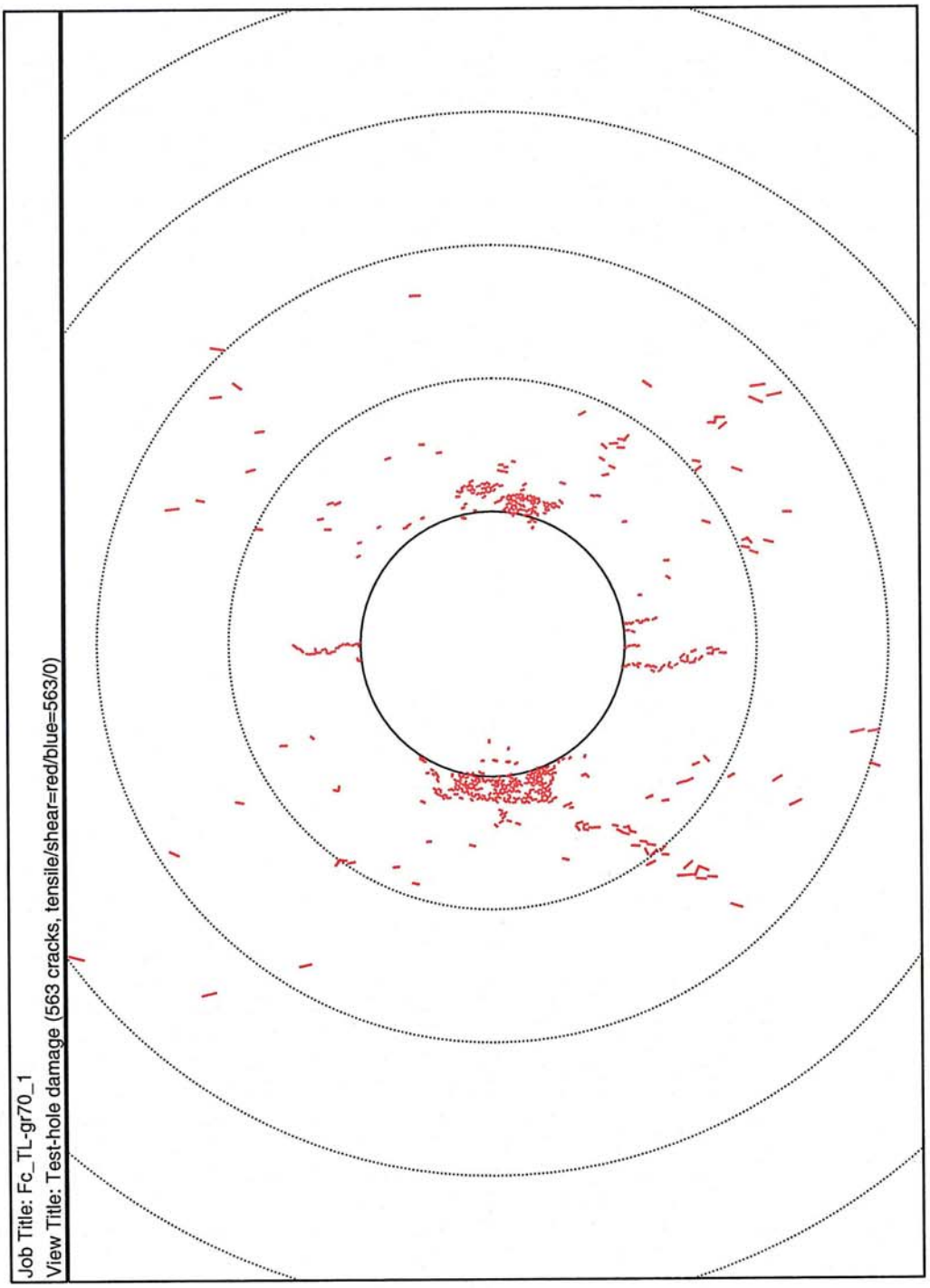

Figure A.27 Near-field damage, view 2 (isotropic lower-bound material TL; coarse; 70 MPa)

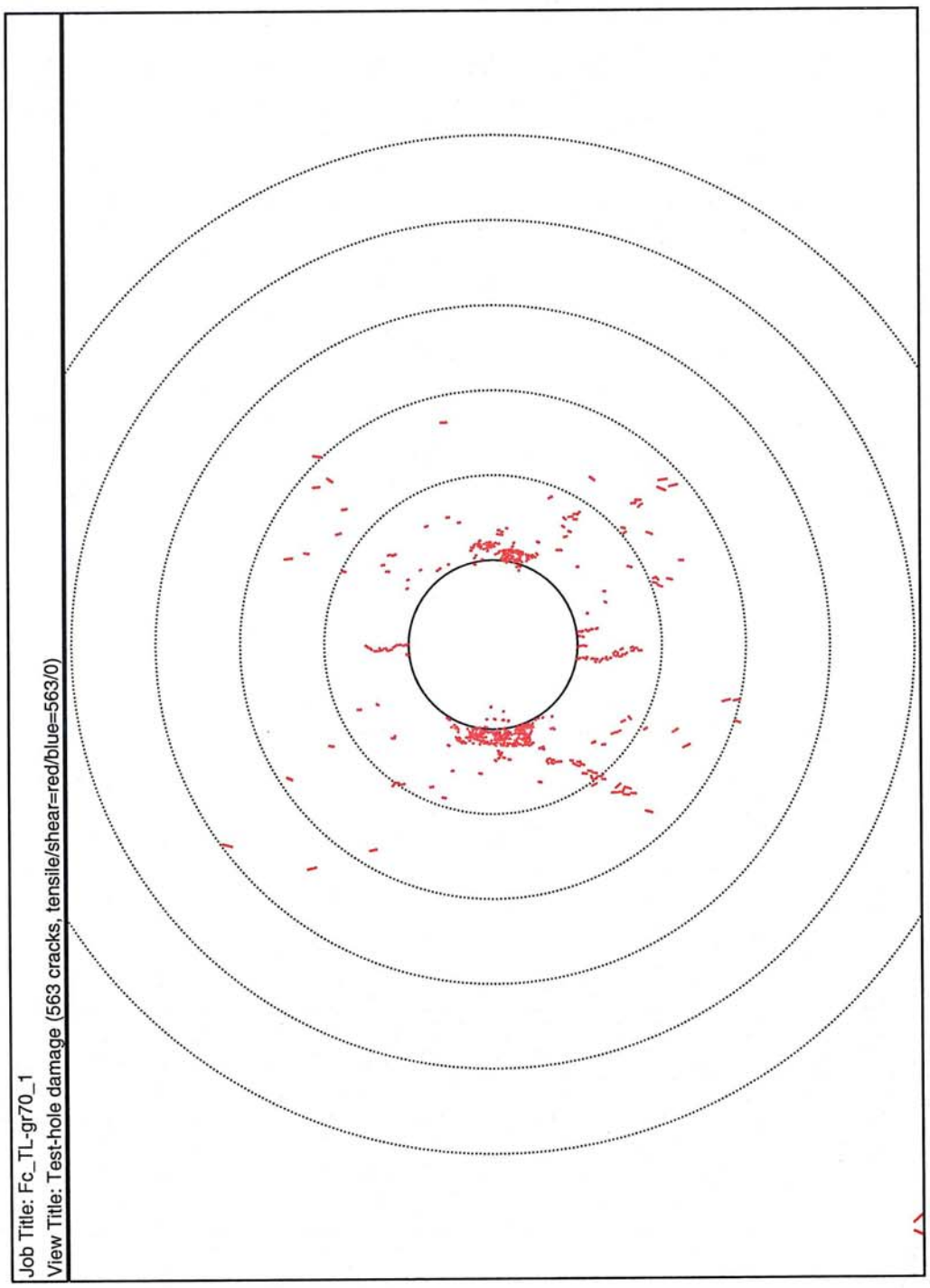

Figure A.28 Near-field damage, view 3 (isotropic lower-bound material TL; coarse; 70 MPa)

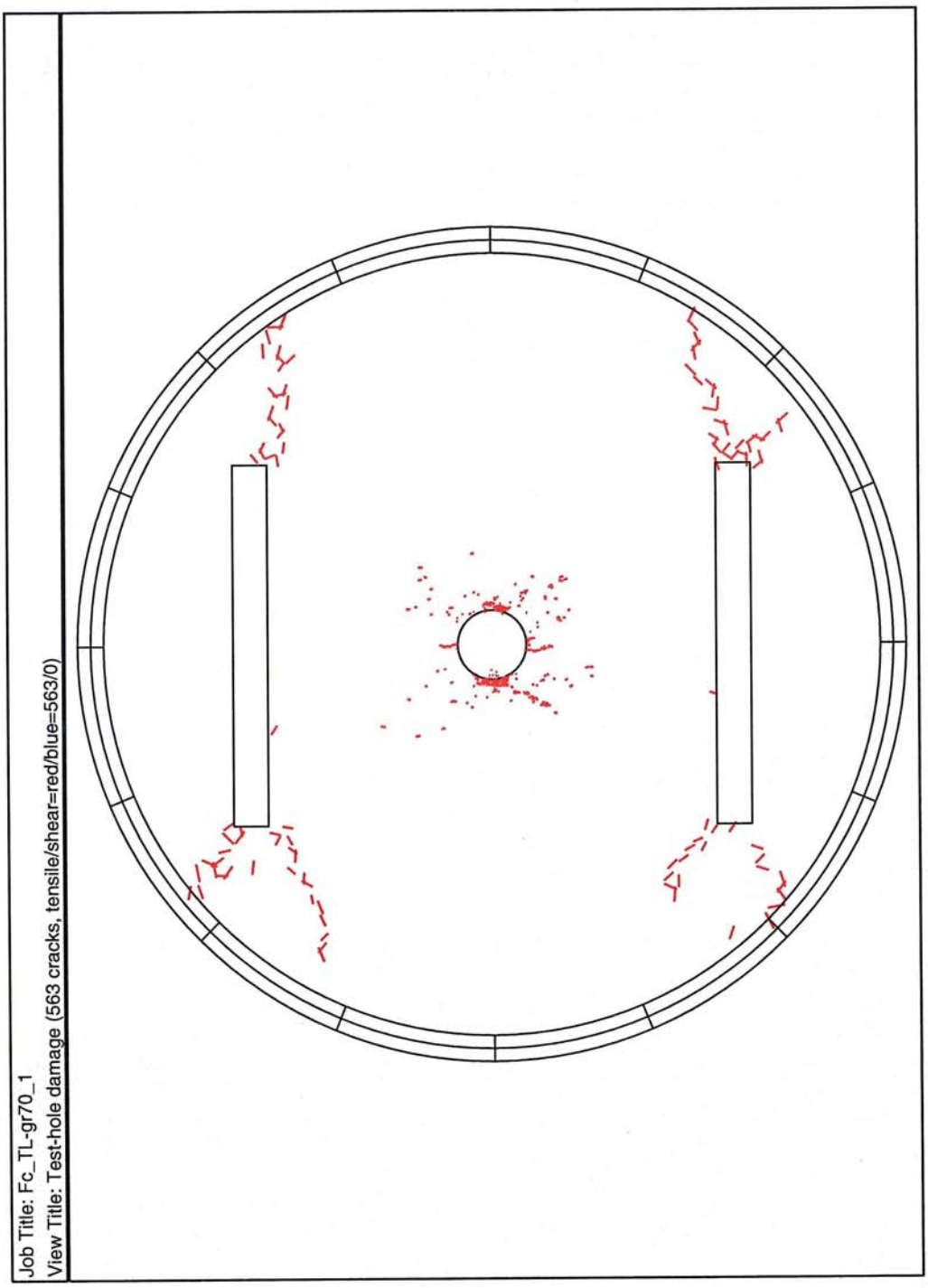

Figure A.29 Far-field damage (isotropic lower-bound material TL; coarse; 70 MPa)

A.3.6 Isotropic Lower-Bound Material TL (fine)

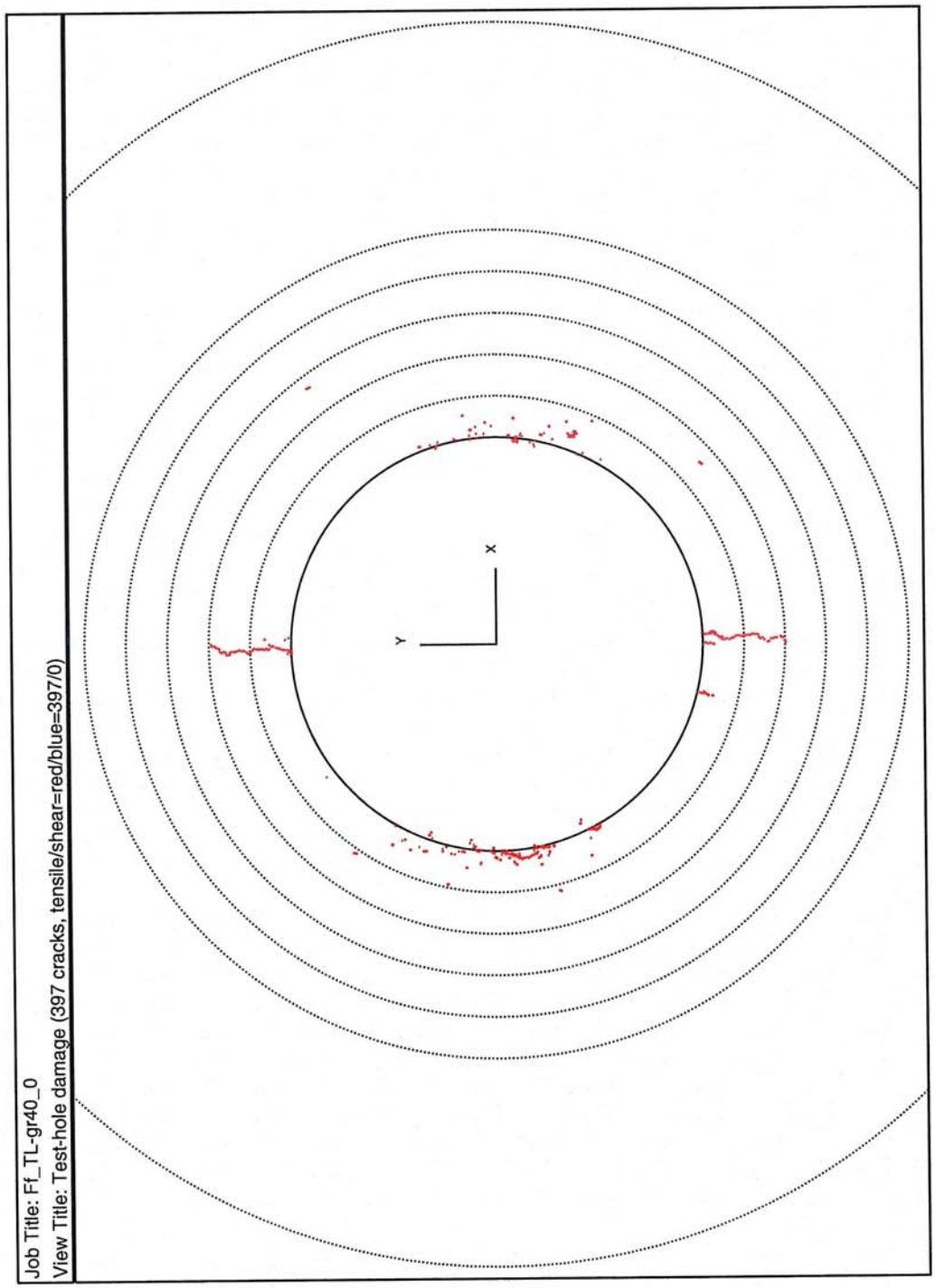

Figure A.30 Near-field damage, view 1 (isotropic lower-bound material TL; fine; 40 MPa)

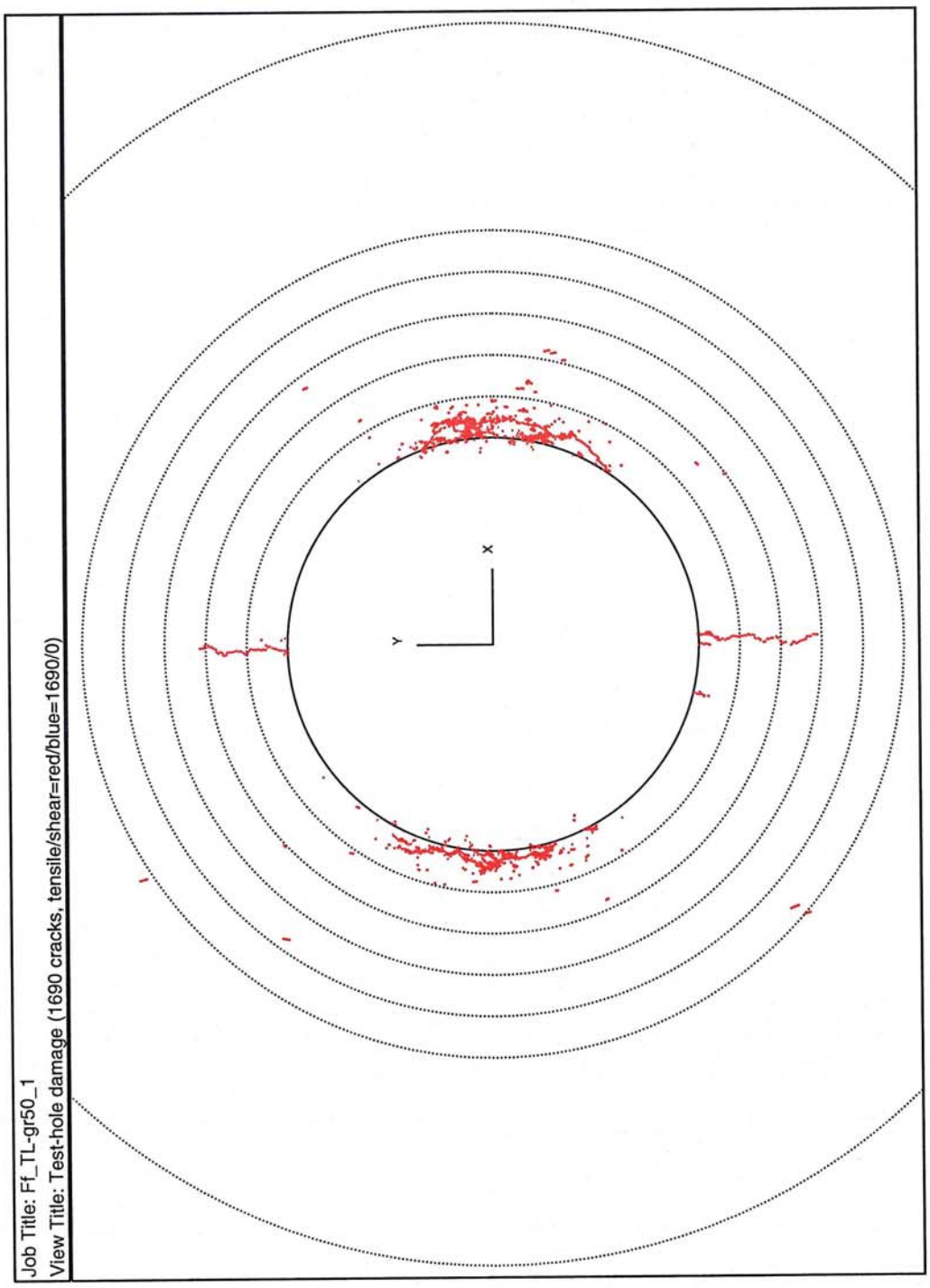

Figure A.31 Near-field damage, view 1 (isotropic lower-bound material TL; fine; 50 MPa)

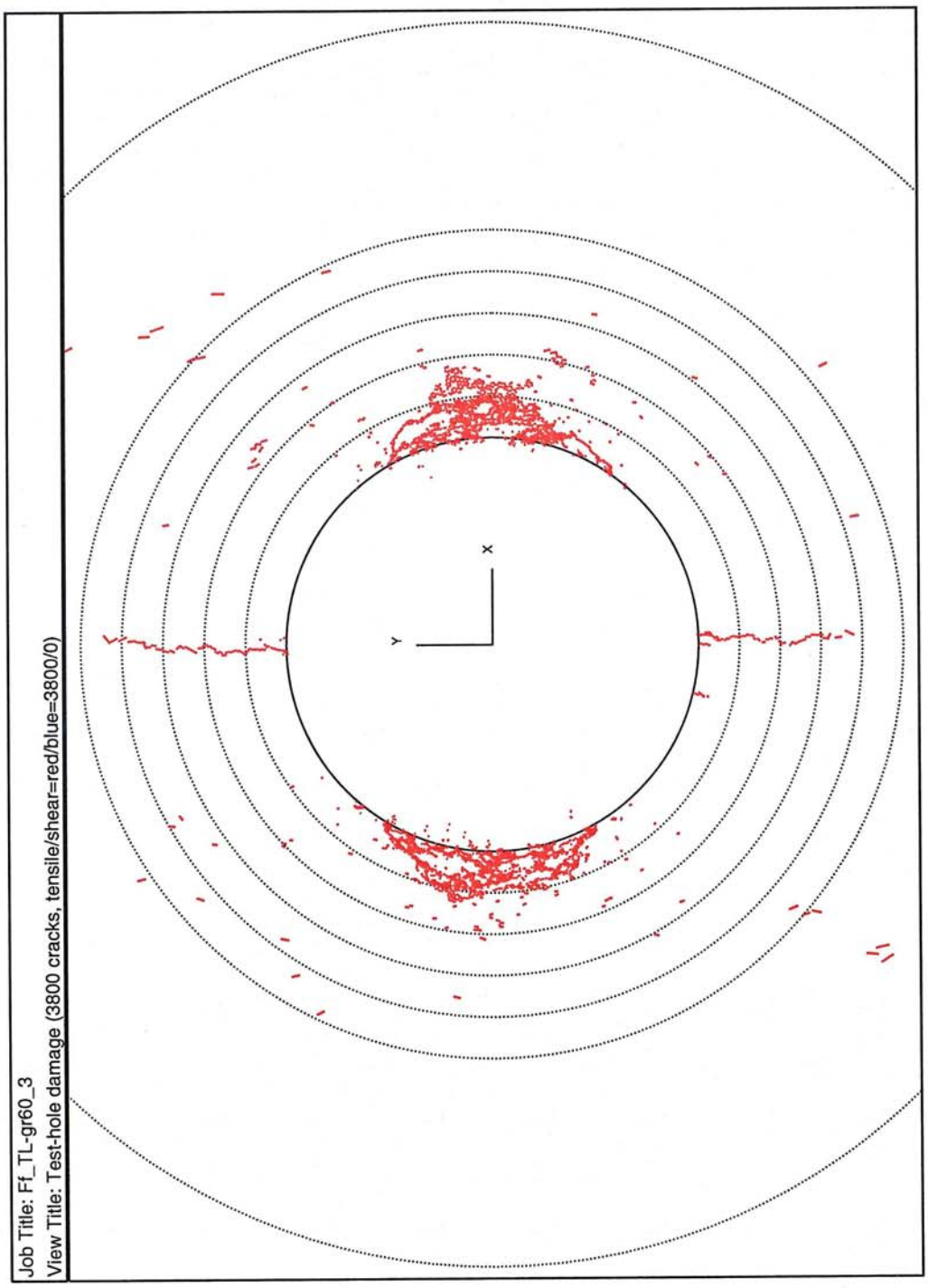

Figure A.32 Near-field damage, view 1 (isotropic lower-bound material TL; fine; 60 MPa)

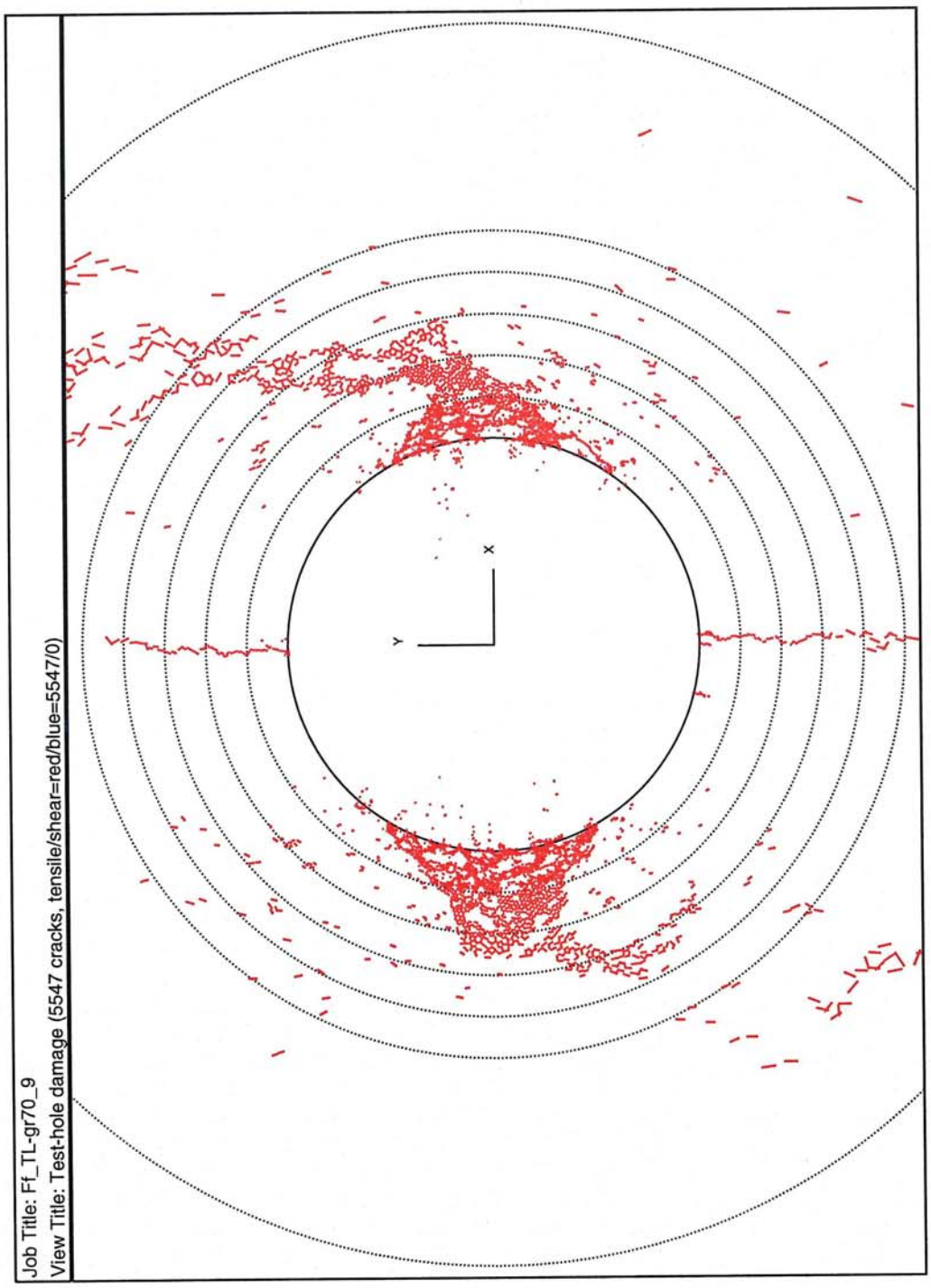

Figure A.33 Near-field damage, view 1 (isotropic lower-bound material TL; fine; 70 MPa)

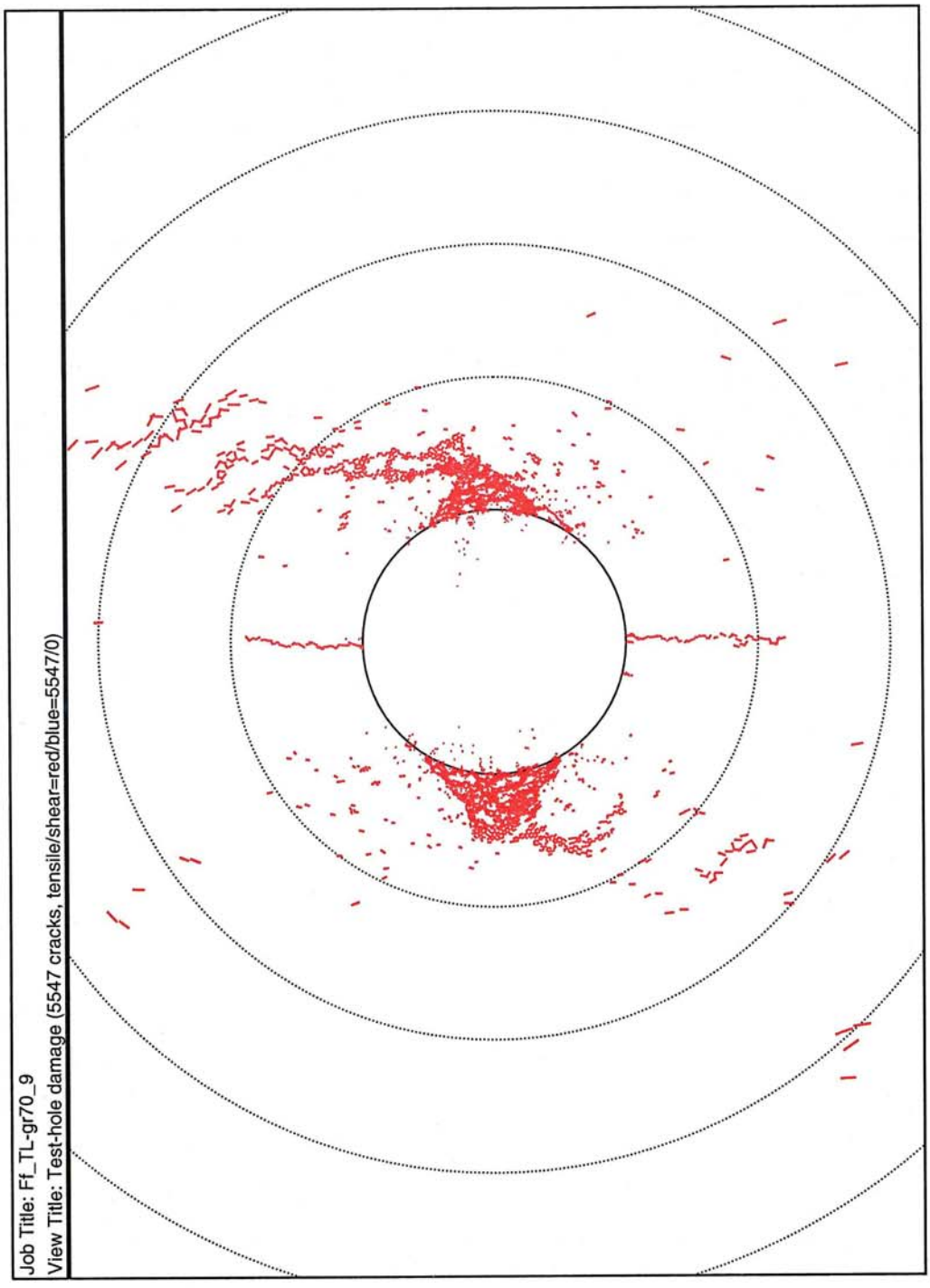

Figure A.34 Near-field damage, view 2 (isotropic lower-bound material TL; fine; 70 MPa)

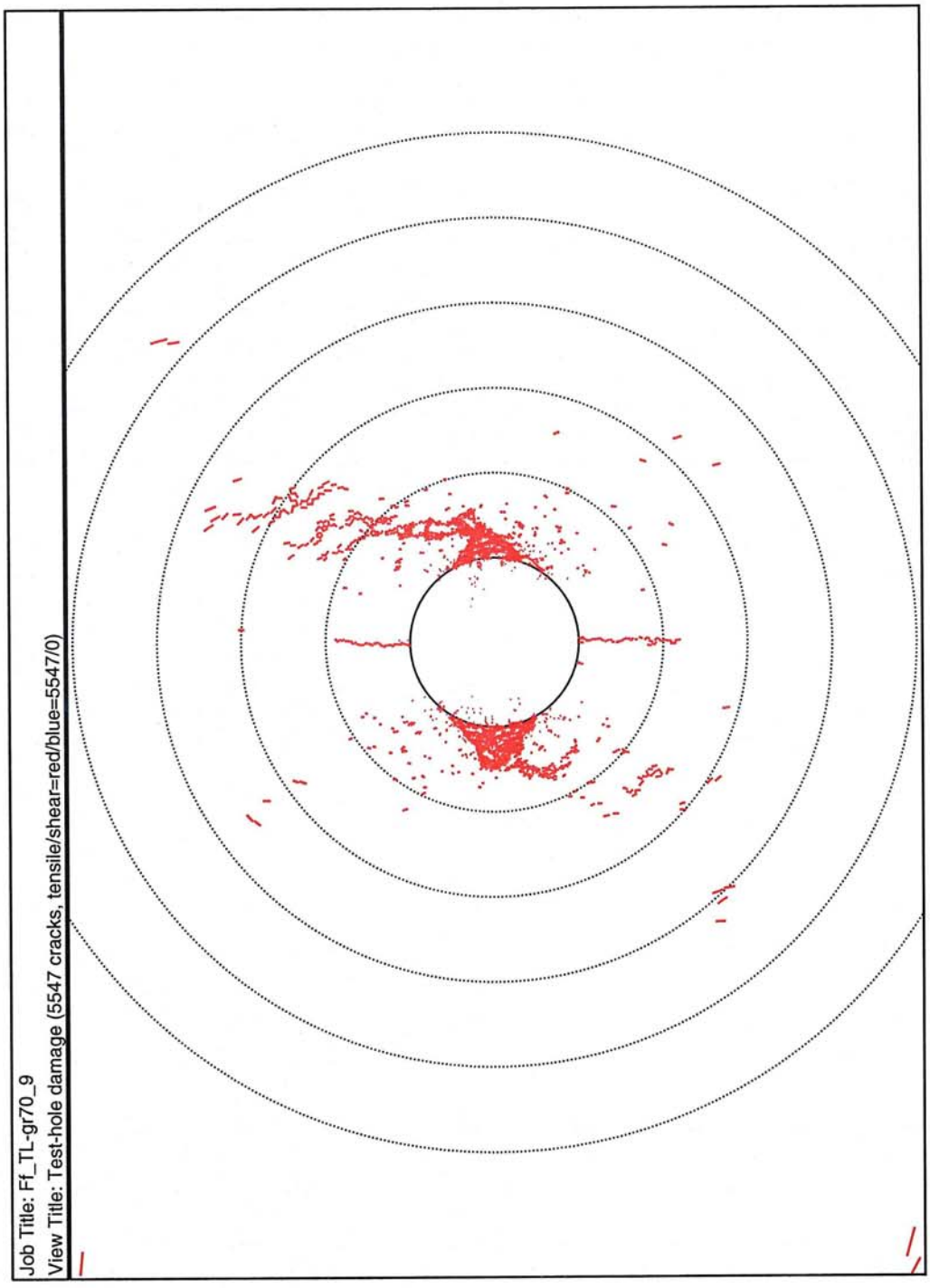

Figure A.35 Near-field damage, view 3 (isotropic lower-bound material TL; fine; 70 MPa)

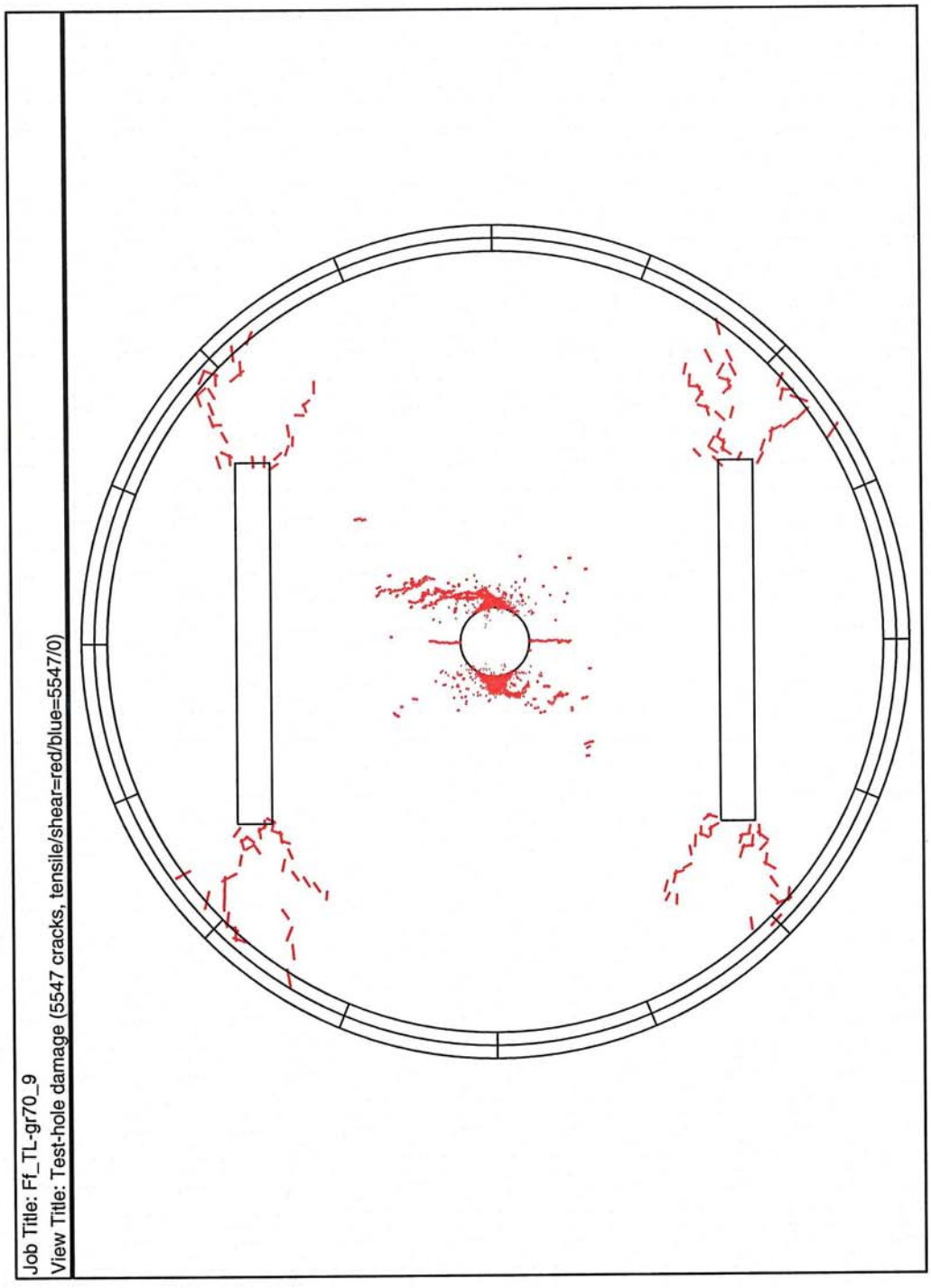

Figure A.36 Far-field damage (isotropic lower-bound mat. TL; fine; 70 MPa)

A.3.7 Smeared Anisotropic Material STAs (coarse)

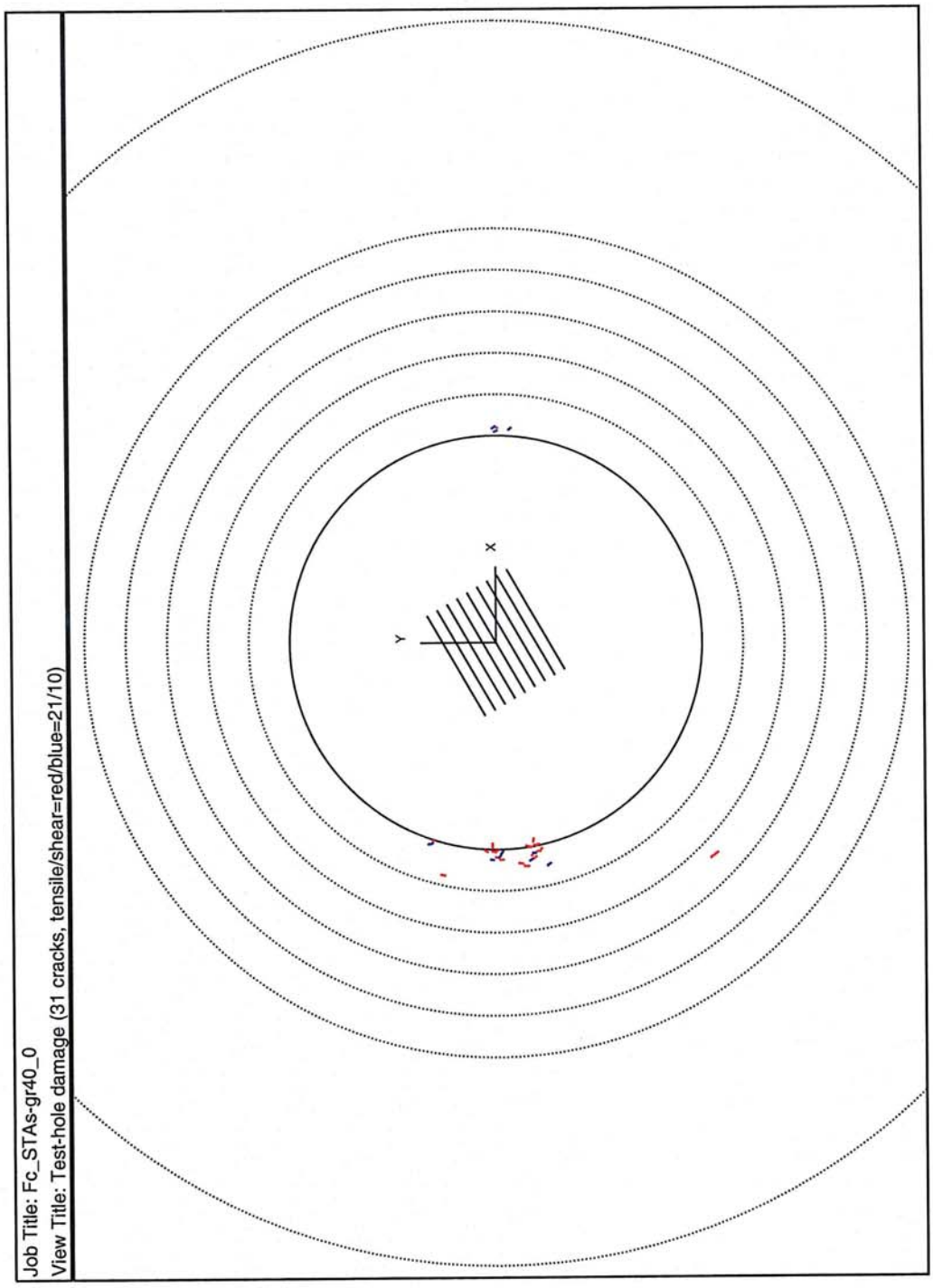

Figure A.37 Near-field damage, view 1 (smeared anisotropic material STAs; coarse; 40 MPa)

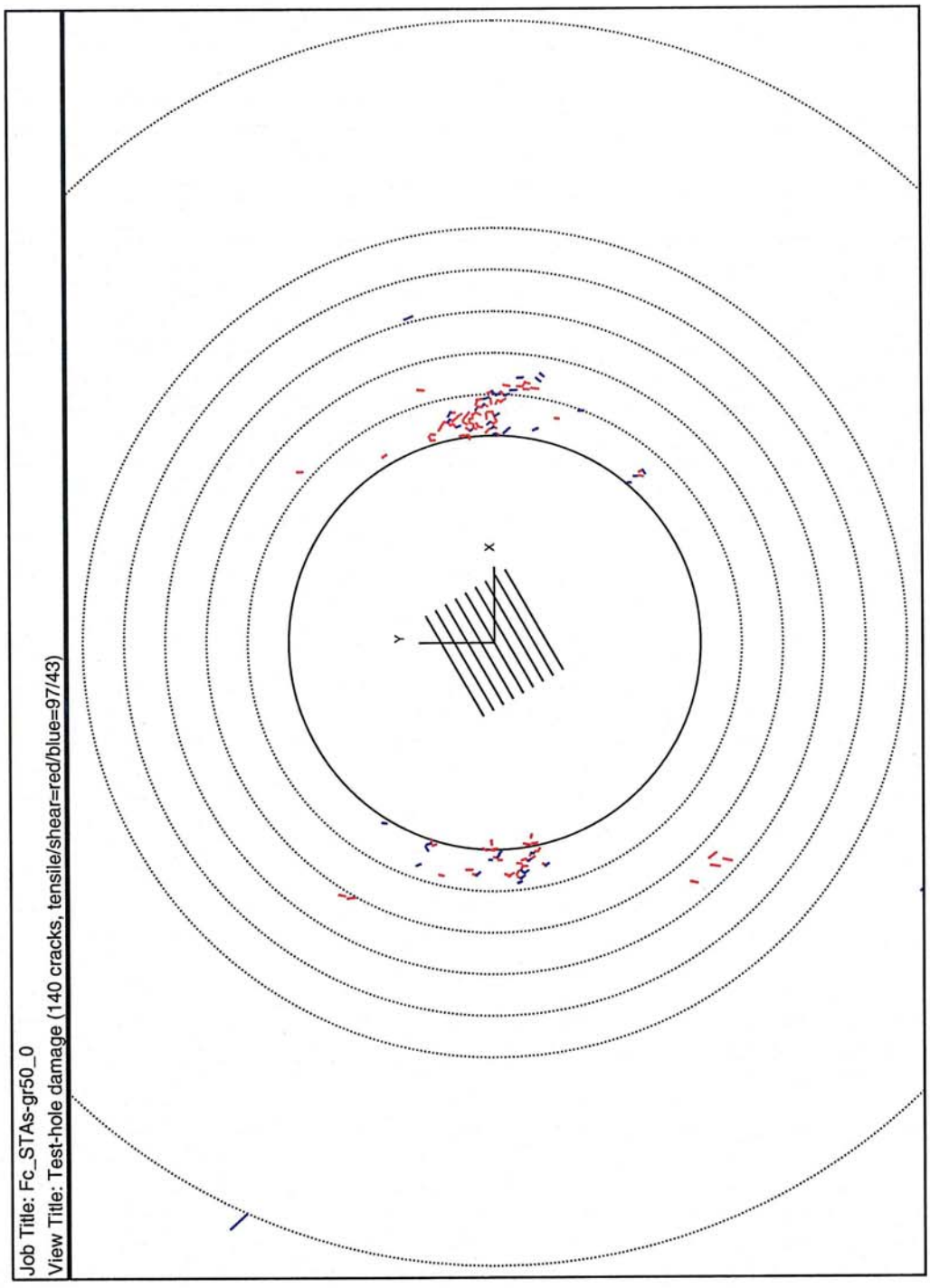

Figure A.38 Near-field damage, view 1 (smeared anisotropic material STAs; coarse; 50 MPa)

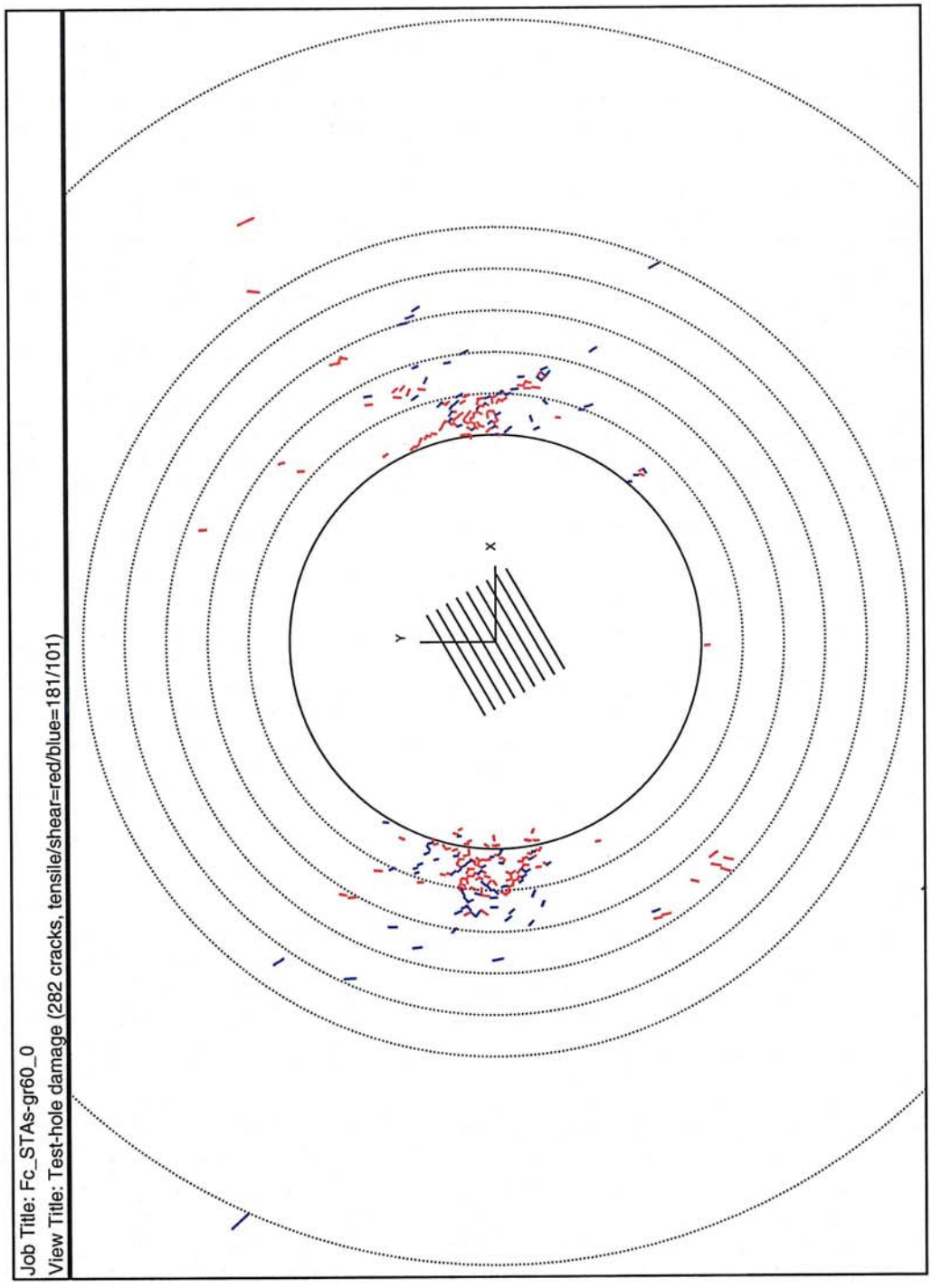

Figure A.39 Near-field damage, view 1 (smeared anisotropic material STAs; coarse; 60 MPa)

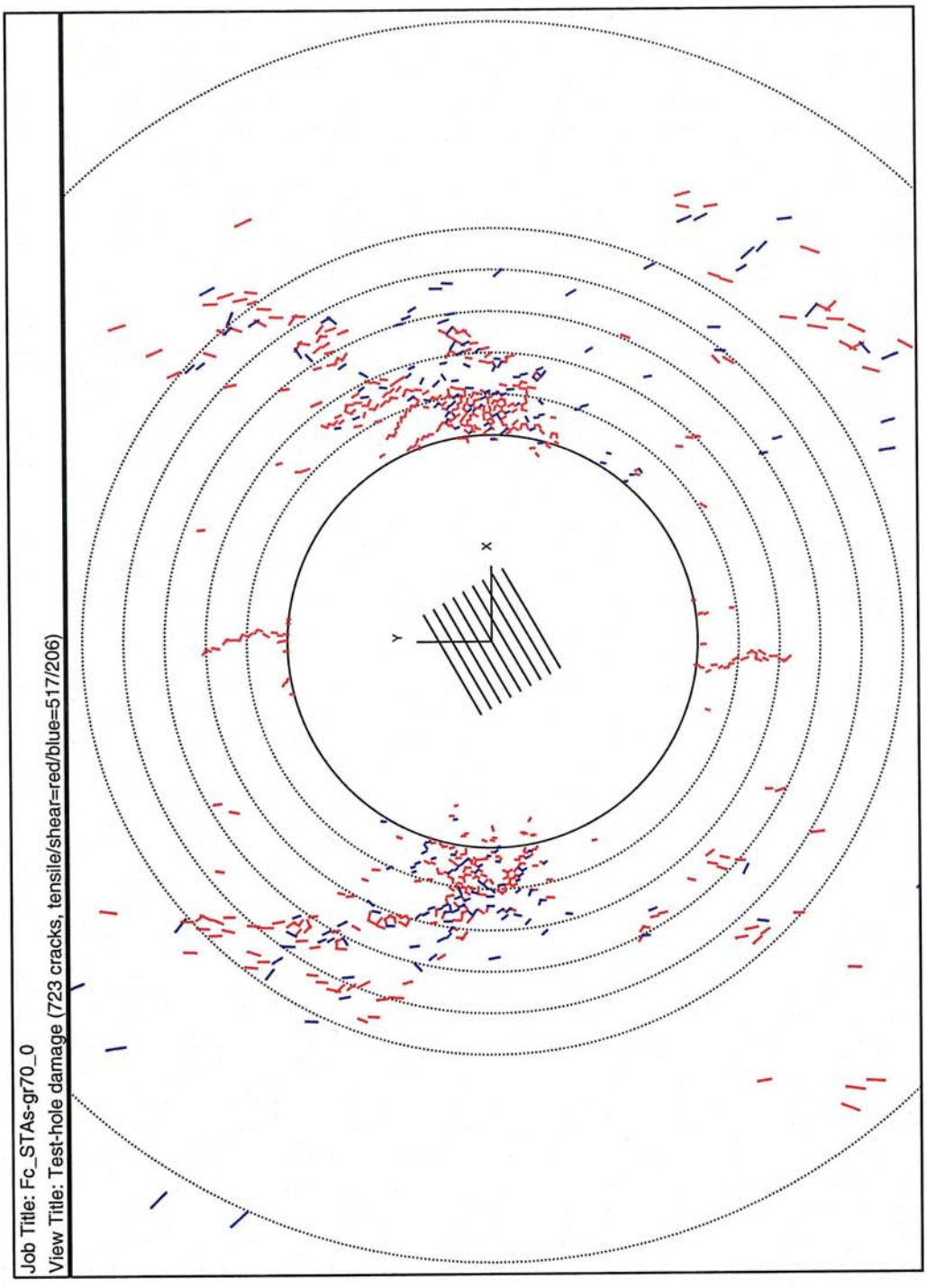

Figure A.40 Near-field damage, view 1 (smeared anisotropic material STAs; coarse; 70 MPa)

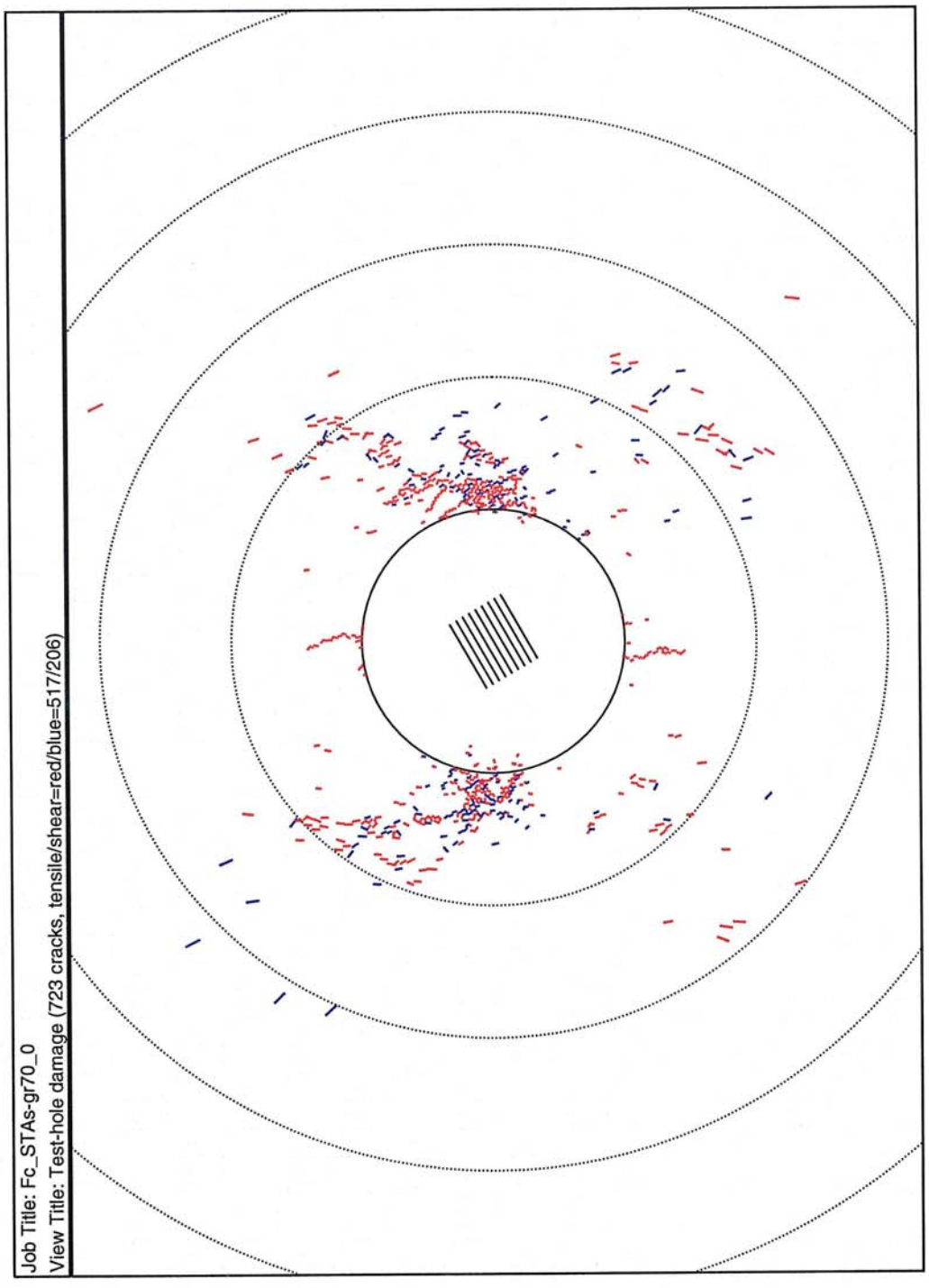

Figure A.41 Near-field damage, view 2 (smeared anisotropic material STAs; coarse; 70 MPa)

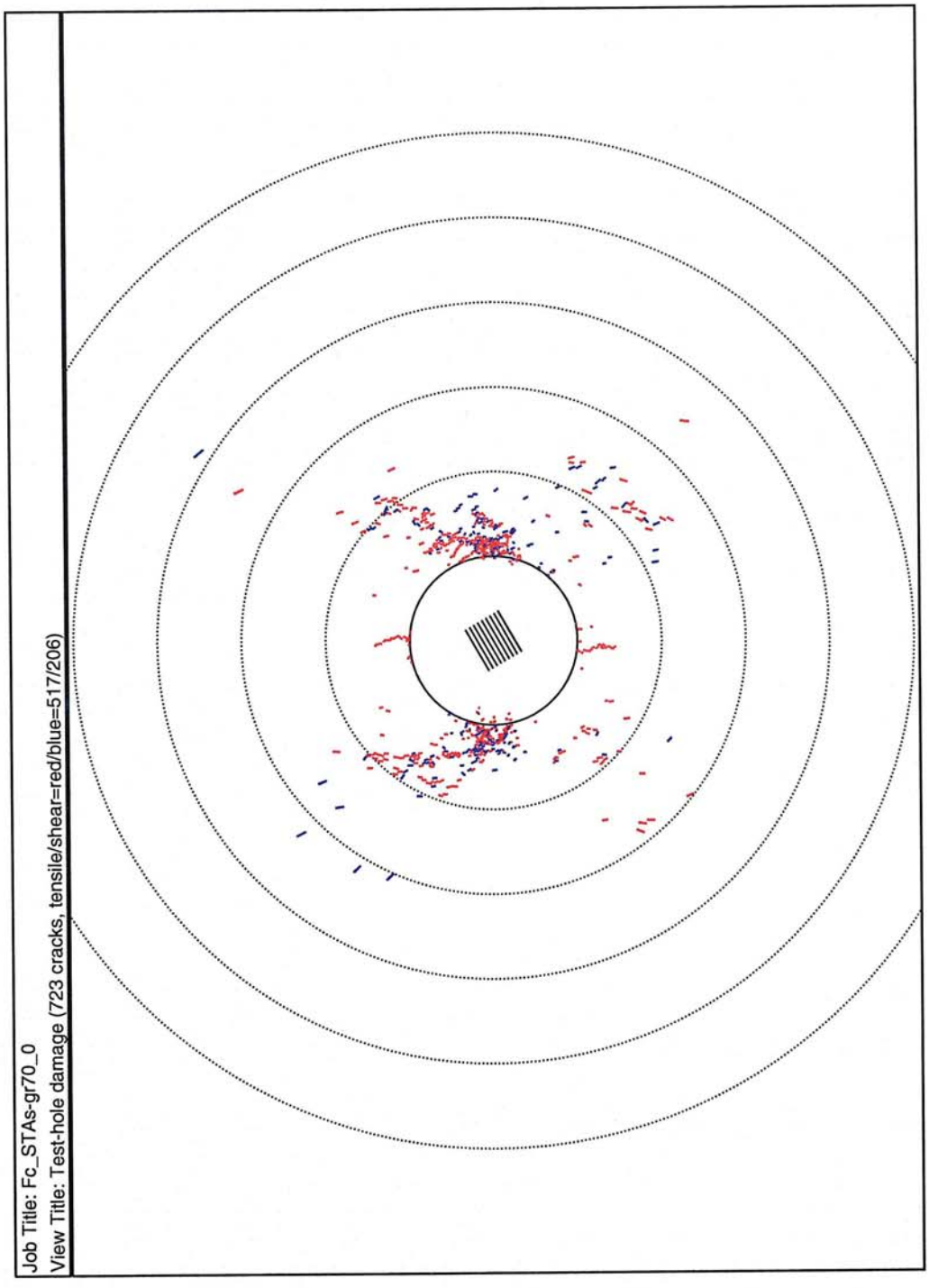

Figure A.42 Near-field damage, view 3 (smeared anisotropic material STAs; coarse; 70 MPa)

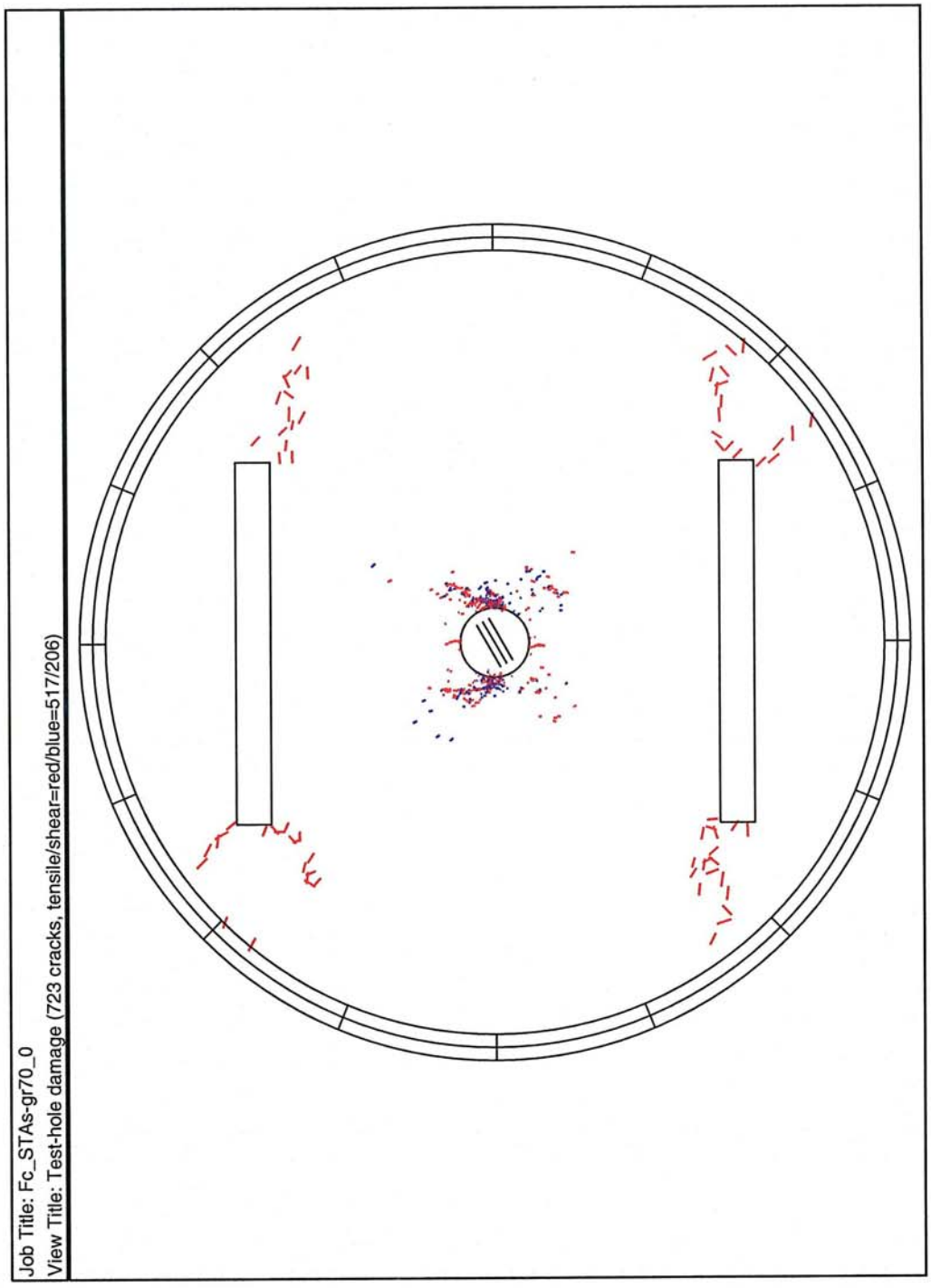

Figure A.43 Far-field damage (smeared anisotropic material STAs; coarse; 70 MPa)

A.3.8 Smeared Anisotropic Material STAs (fine)

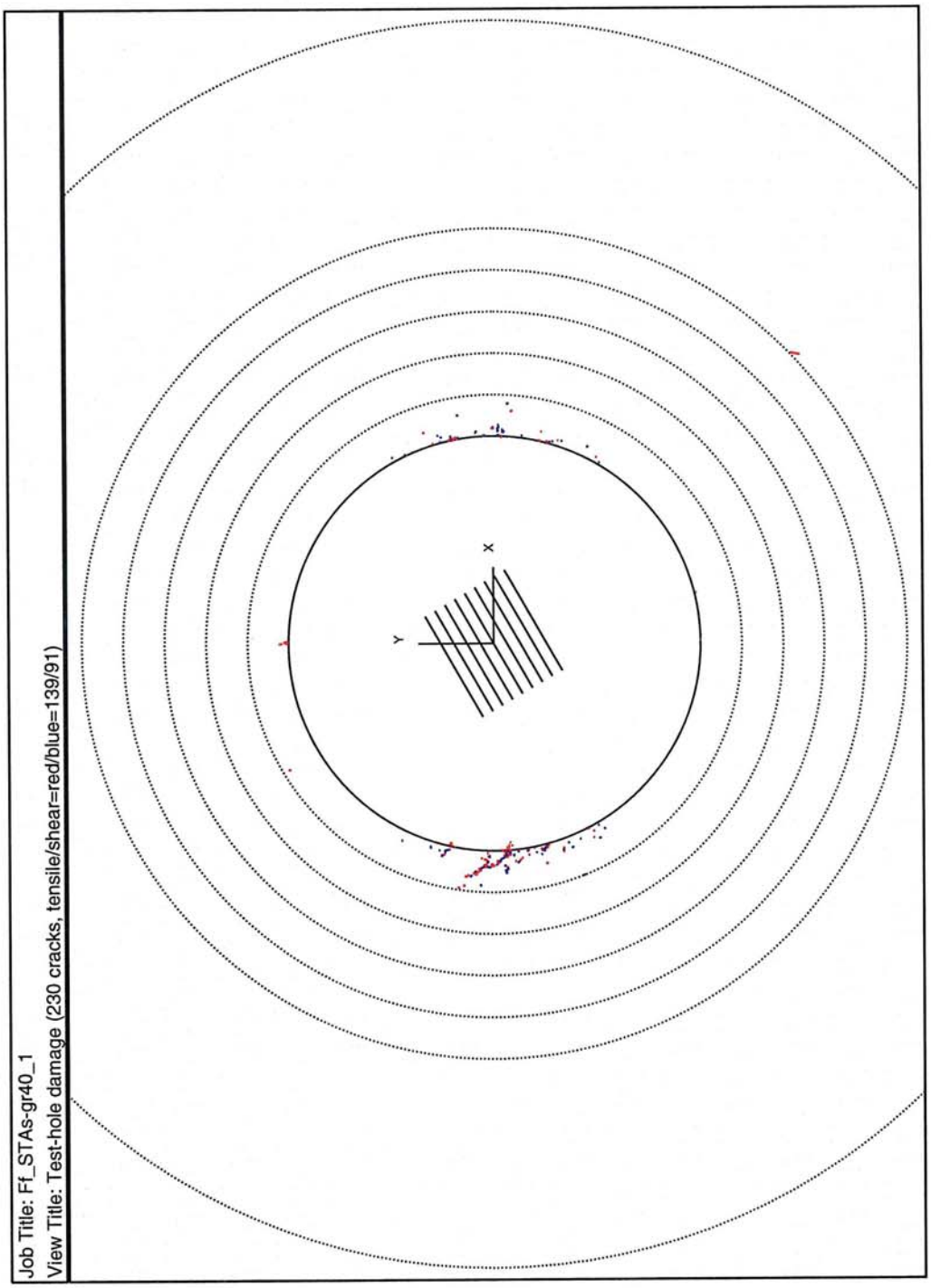

Figure A.44 Near-field damage, view 1 (smeared anisotropic material STAs; fine; 40 MPa)

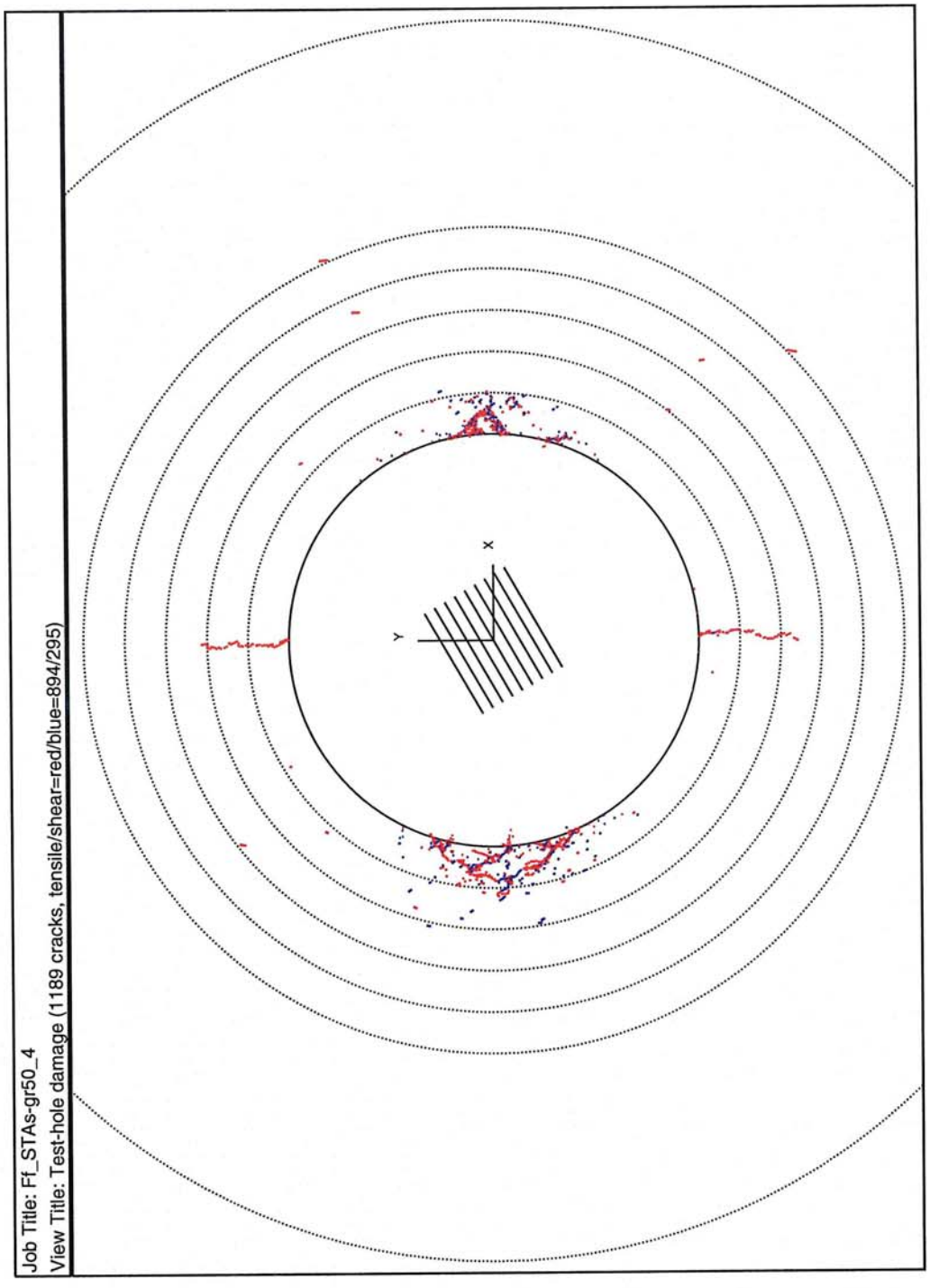

Figure A.45 Near-field damage, view 1 (smeared anisotropic material STAs; fine; 50 MPa)

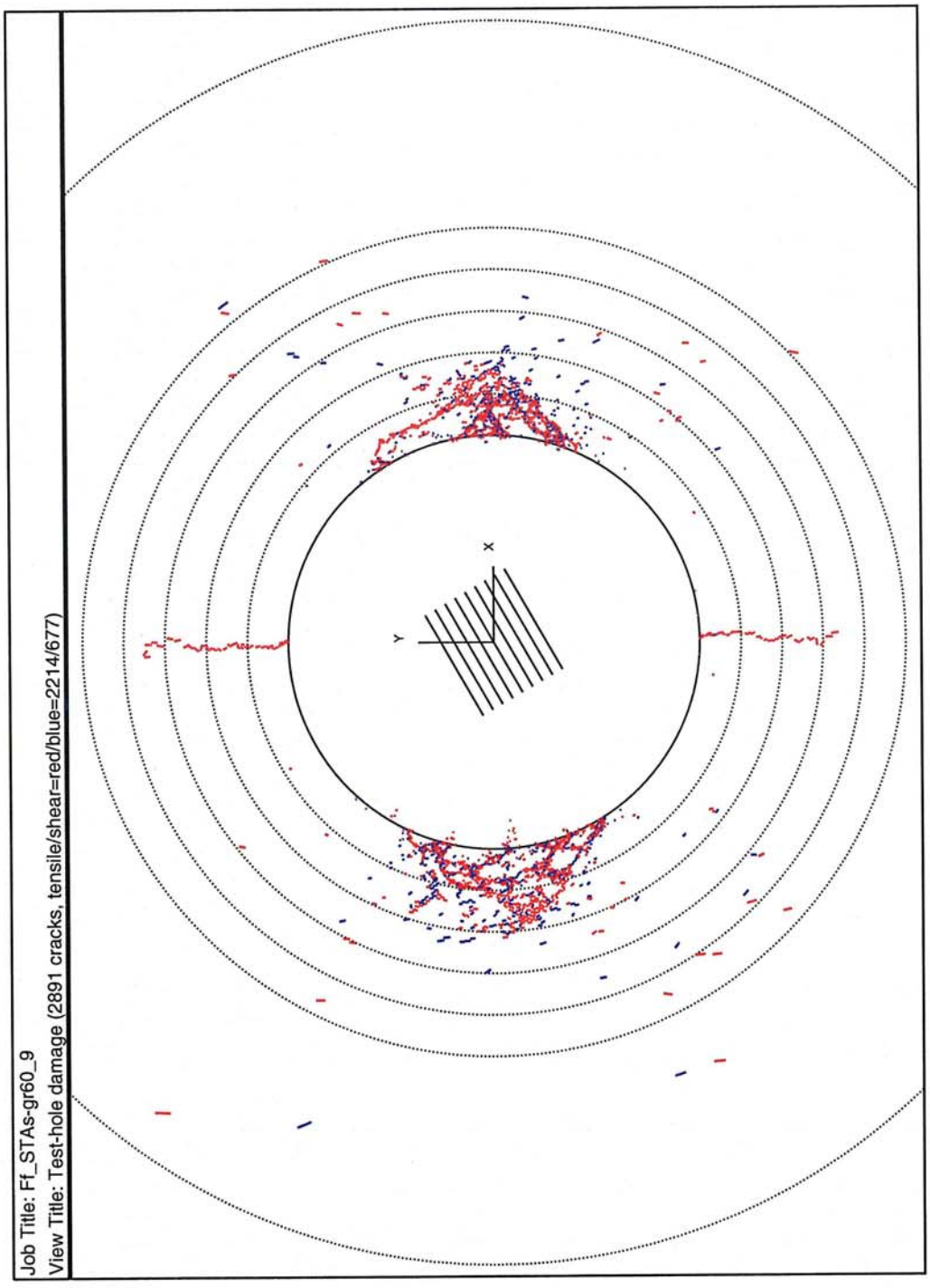

Figure A.46 Near-field damage, view 1 (smeared anisotropic material STAs; fine; 60 MPa)

A.3.9 Smeared Anisotropic Material TAs (coarse)

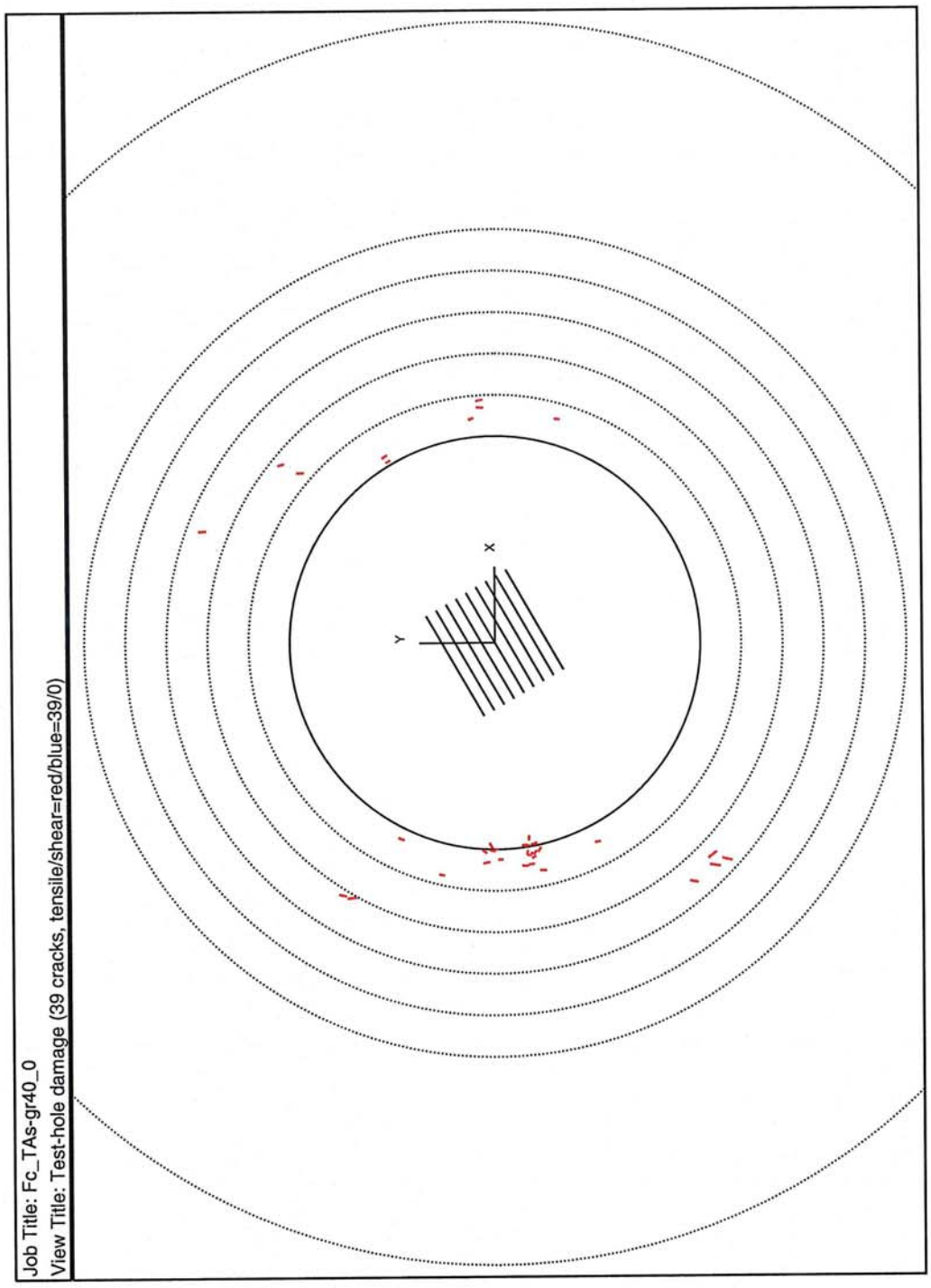

Figure A.47 Near-field damage, view 1 (smeared anisotropic material TAs; coarse; 40 MPa)

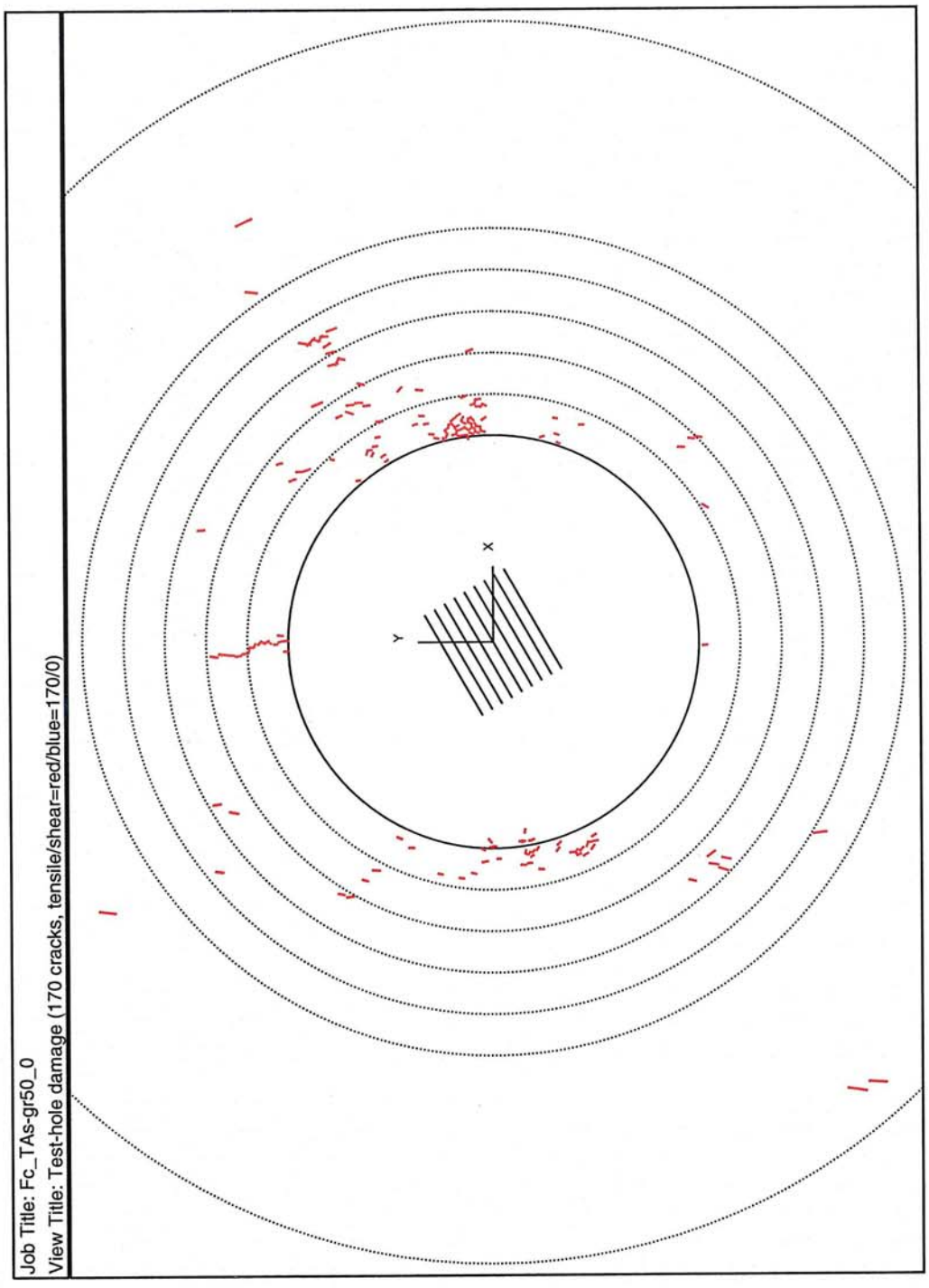

Figure A.48 Near-field damage, view 1 (smeared anisotropic material TAs; coarse; 50 MPa)

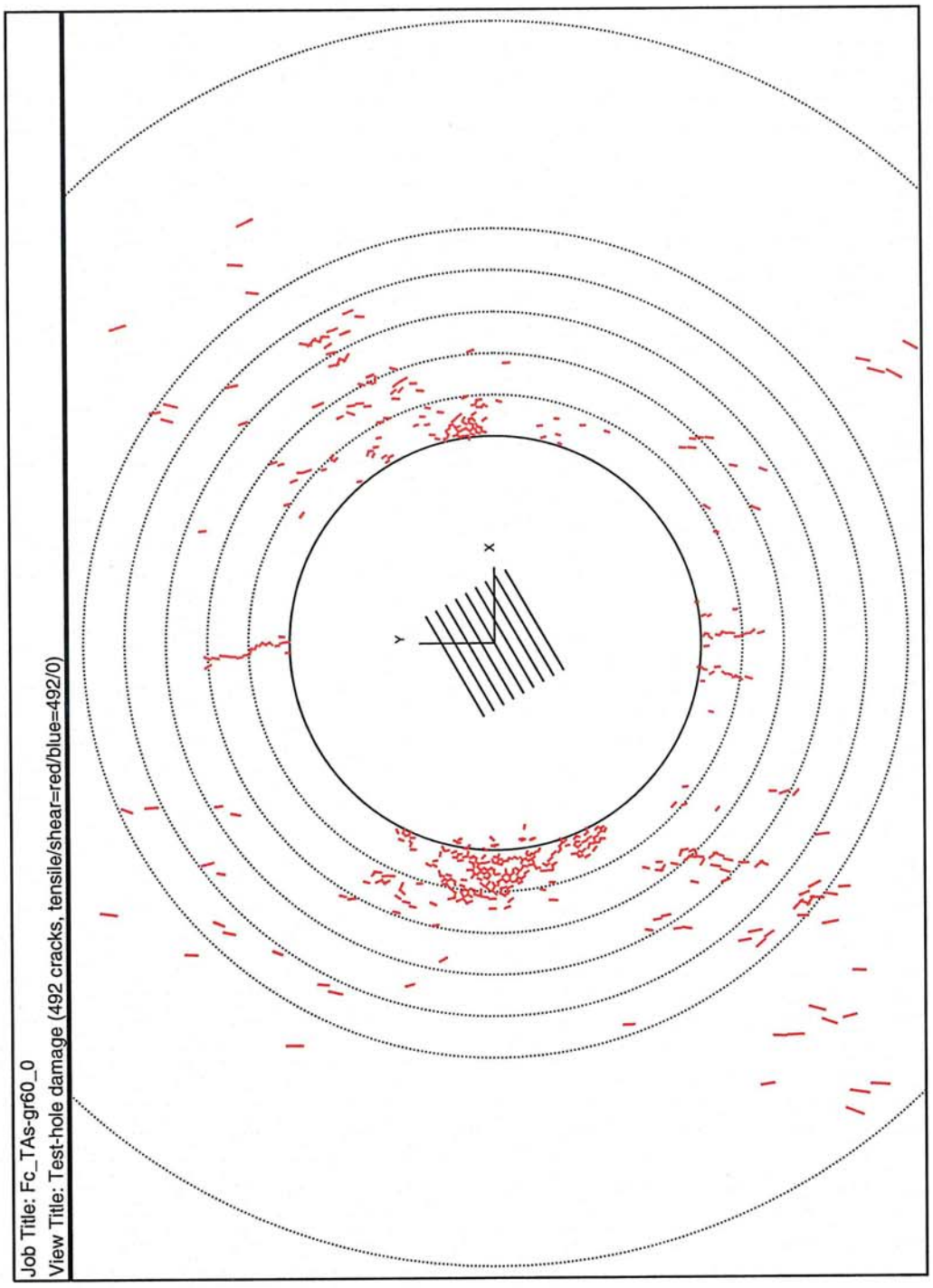

Figure A.49 Near-field damage, view 1 (smeared anisotropic material TAs; coarse; 60 MPa)

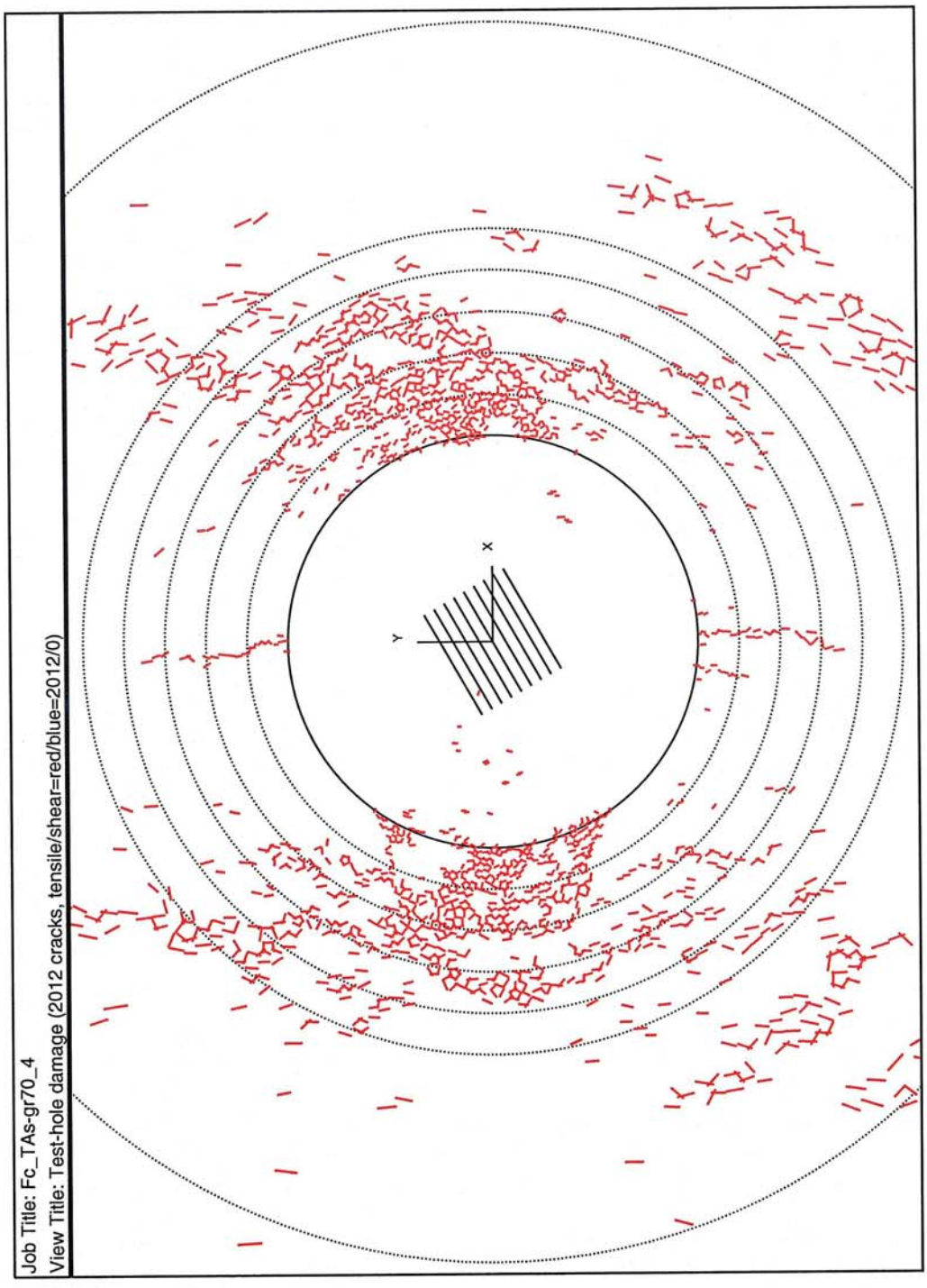

Figure A.50 Near-field damage, view 1 (smeared anisotropic material TAs; coarse; 70 MPa)

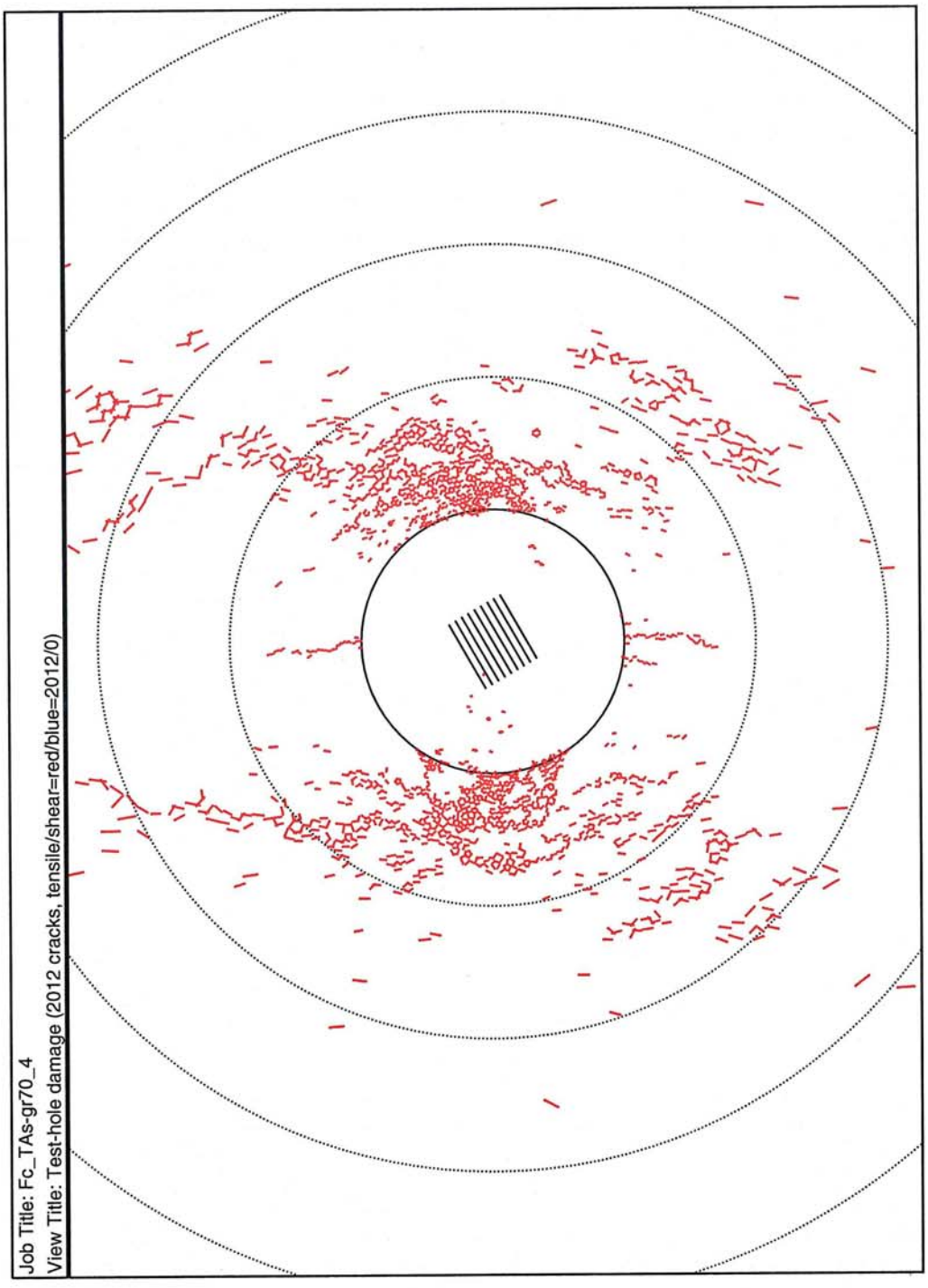

Figure A.51 Near-field damage, view 2 (smeared anisotropic material TAs; coarse; 70 MPa)

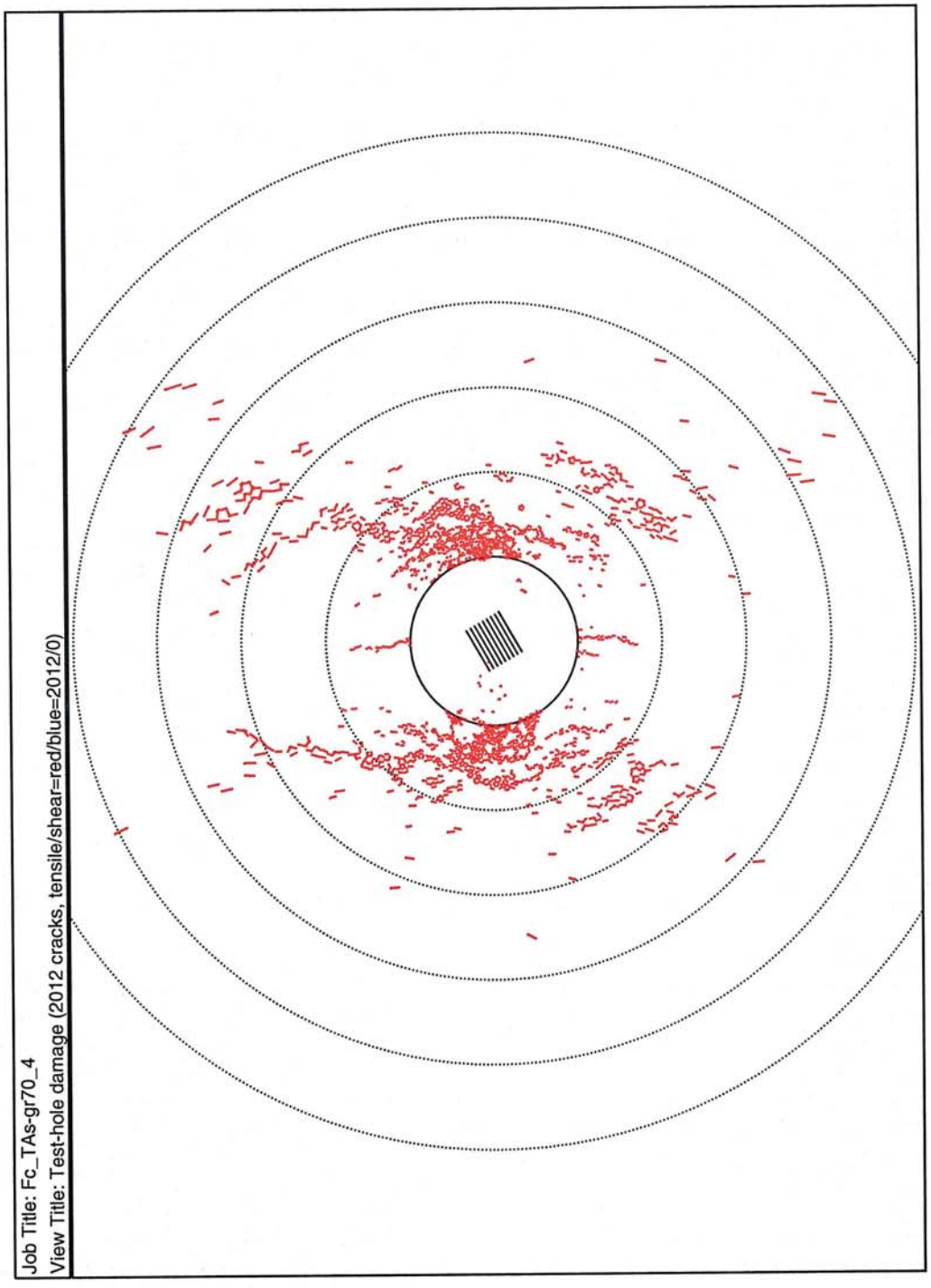

Figure A.52 Near-field damage, view 3 (smeared anisotropic material TAs; coarse; 70 MPa)

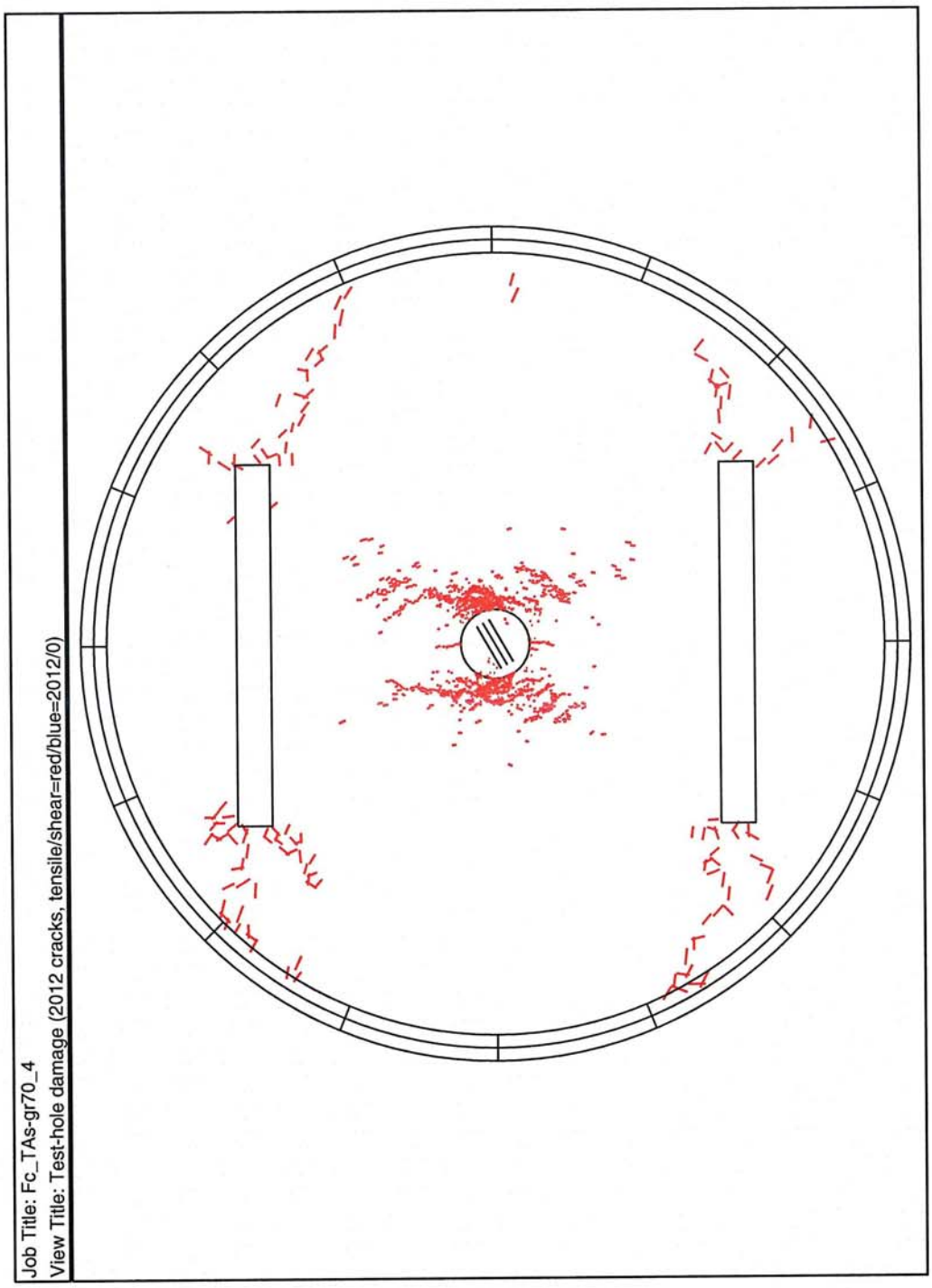

Figure A.53 Far-field damage (smeared anisotropic material TAs; coarse; 70 MPa)